Numerical Investigation of Chaotic Advection in Three-Dimensional Experimentally Realizable Rotating Flows

A Thesis
Presented to
The Academic Faculty

by

Tahirih C. Lackey

In Partial Fulfillment
of the Requirements for the Degree
Doctor of Philosophy in the
School of Civil and Environmental Engineering

Georgia Institute of Technology
November 2004

Numerical Investigation of Chaotic Advection in Three-Dimensional Experimentally Realizable Rotating Flows

Approved by:

Dr. Fotis Sotiropoulos, Advisor

Dr. Aris Georgakakos

Dr. Roman Grigoriev

Dr. Phil Roberts

Dr. Donald Webster

November 16, 2004

DEDICATION

This thesis is dedicated to my family: To my parents, Dr. Hilliard L. Lackey III and Mrs. Lillian T. Lackey; to my sister and brothers, Dr. Katrina Lackey Davis, Hilliard L. Lackey IV, and Darryl Lackey; to my grandmothers, Mrs. Louise Troupe and Mrs. Cora Long; to my brother-in-law Dennis and my sister-in-law Tracy ; to my nieces, Jasmine and Jada, and my nephew Hilliard Lackey V, I just want to say thank you so much for supporting me in all that I've done and for your unconditional love. Last but not least I would like to thank God for always giving me what I need.

ACKNOWLEDGEMENTS

I would like to thank my advisor Dr. Fotis Sotiropoulos for his guidance and unending patience with the progress of this work as well as my thesis committee: Drs. Aris Georgakakos, Roman Grigoriev, Phil Roberts, and Donald Webster for their advice. I would also like to thank the members (passed and present) of the Civil and Environmental Engineering Computational Fluid Dynamics Group at Georgia Institute of Technology, with special thanks to Liang Ge and Casey Jones for their continuous assistance with this research. Finally, I would like to express gratitude to Steven Bourne, Amy Tidwell, and the Baha'i communities of Atlanta and College Park, GA for their moral support. Thanks also for funding from the National Science Foundation Career grant CMS-9875691.

TABLE OF CONTENTS

LIST OF FIGURES

SUMMARY

In many engineering applications involving mixing of highly viscous fluids or mixing at micro-scales, efficient mixing must be accomplished in the absence of turbulence. Similarly in geophysical flows large-scale, deterministic flow structures can account for a considerable portion of global transport and mixing. For these types of problems, concepts from non-linear dynamical systems and the theory of chaotic advection provide the tools for understanding, quantifying, and optimizing transport and mixing processes. Advances in the theory of chaotic advection for flows of engineering relevance, however, have been hindered by the lack of experimentally realizable, three-dimensional, test-bed flows. In this thesis chaotic advection is studied numerically in three, steady, experimentally realizable, three-dimensional flows: 1) steady vortex breakdown flow in a cylindrical container with bottom rotating lid, 2) flow in a cylindrical container with exactly counter rotating lids, and 3) flow in a new model stirred-tank with counter-rotating disks. For all cases the three-dimensional Navier-Stokes equations are solved numerically and the Lagrangian properties of the computed velocity fields are analyzed using a variety of computational and theoretical tools.

For the flow in the interior of vortex breakdown bubbles it is shown that even though from the Eulerian viewpoint the simulated flowfields are steady and nearly axisymmetric the Lagrangian dynamics could be chaotic. Upstream originating particles enter the bubble from the downstream saddle focus, could recirculate in its interior for arbitrarily long times and the rate at which they exit is a fractal curve known as the Devil's staircase. Sil'nikov's mechanism is shown to play a critical role in breaking up

the invariance of the bubble and giving rise to chaotic dynamics. By examining the dynamics of a model dynamical system it is further shown that vortex breakdown bubbles occurring at sufficiently high swirl numbers exhibit integrable dynamics even when the advecting velocity field is three-dimensional. These findings resolve the decades-old controversy regarding the fundamental nature of vortex breakdown bubbles in confined swirling flows and establish for the first time a firm link between a simple Eulerian parameter, the swirl ratio, and the rate of chaotic stirring.

The computations for the steady flow in a cylindrical container with two exactly counter-rotating lids confirm for the first time the findings of recent linear stability studies. Above a threshold Reynolds number the equatorial shear layer becomes unstable to azimuthal modes and an intricate web of radial (cat's eyes) and axial, azimuthally-inclined vortices emerge in the flow. The flow becomes chaotic but contrary to intuition the stirring rate does not increase monotonically with Reynolds number. Above an optimal Reynolds number at which stirring rate is maximized the integrable (unmixed) part of the flow begins to grow and stirring rate declines. This remarkable finding, which has profound implications for designing and optimizing the performance of industrial mixing devises with rotating components, is explained in terms of a recently proposed theory of chaotic advection. Using these fundamental insights, a new stirring tank device with exactly counter-rotating disks is proposed as an alternative to the widely used in industrial applications co-rotating stirred tanks. Numerical simulations show for the first time that counter rotation of the middle disk in a three-disk stirred tank can create a flow with large chaotic regions without the need to resort to commonly employed in practice exotic impeller designs to break the symmetry and integrability of the flow.

The results of this thesis serve to demonstrate that fundamental studies of chaotic mixing are not only important from a theoretical standpoint but when the findings of such studies are properly exploited they can potentially lead to valuable technological breakthroughs.

CHAPTER 1

INTRODUCTION

The importance of mixing in science and engineering studies is based on the simple fact that mixing is everywhere. Weather patterns and oceanic flows, the behavior of gases and nutrients in the atmosphere, hydro turbines and combustors, convective mixing in our lungs, and many more examples force us to try to understand mixing so that we might understand our own bodies as well as our environment. However, mixing is usually associated with turbulent flows. When we think of fast fluid mixing, ideas immediately turn to rapid agitation and vigorous churning. However, an equally important engineering question is: How do fluids mix in the absence of turbulence?

There are many cases in both industry and nature in which non turbulent mixing is required and utilized. In the food and material processing industries, efficient mixing of highly viscous fluids can be accomplished using mixing devices that generate complex, large-scale, vortical structures (stirring tanks, static mixers, etc.). Similarly mixing of passive scalars in micro-mixing devices used in MEMS relies exclusively (due to the very low Reynolds numbers) on stirring due to large-scale, organized vortical structures in the flow. Even in turbulent geophysical flows in the ocean and the atmosphere, organized vortical structures are known to play a significant role in affecting global transport processes. Large-scale transport in and out the polar vortex, for instance, has

been suggested as an important mechanism for the chemical processes that contribute to the depletion of ozone in the atmosphere. To understand this counter-intuitive notion of efficient, rapid mixing without turbulence, we must first comprehend more clearly the term "mixing".

The homogenization of a scalar tracer by a flow field (what we usually call "mixing") occurs in two inter-related albeit distinct phases: 1) *stirring*, the mechanical process which creates material interface via repeated stretching and folding of material lines; and 2) actual *mixing*, which is, in fact, the molecular process via which the scalar diffuses across the so created material interface. Both stirring and mixing are integral components of the homogenization process but the former is commonly studied in the absence of the latter. That is, the scalar tracer is assumed to be passive or non-diffusive and to move along fluid trajectories without engaging in random Brownian motion. Under this assumption the motion of the scalar tracer in the flow is governed by the following advection equations:

$$\begin{aligned} \frac{dx}{dt} &= u(x, y, z, t) \\ \frac{dy}{dt} &= v(x, y, z, t) \\ \frac{dz}{dt} &= w(x, y, z, t) \end{aligned} \tag{1.1}$$

where *x*, *y*, and *z* are the Cartesian coordinates of the particle position and u, v, and w are the components of the flow velocity field, which for generality is assumed to be three-dimensional and time dependent. The above equations can be found in any introductory fluid mechanics textbook. Their solutions are the particle paths or particle trajectories of the flow field and are commonly used to visualize a flow and analyze its characteristics

from the so-called Lagrangian viewpoint. With this information, we can apply the concepts of dynamical systems to understand fluid stirring.

From a dynamical systems vantage point, a system of ordinary differential equations such as that given by equations (1.1) comprises a finite-dimensional dynamical system. The variables x, y, and z are now quantities defining the *state* of the system within its *phase space*. This realization, which was first made by Aref (1984) in his now seminal paper, has profound implications insofar as the understanding of the stirring process is concerned. Mathematicians since the time of Poincarè have known, for instance, that even very simple dynamical systems—i.e. systems whose right hand side are simple deterministic functions of space and time—can exhibit under certain conditions solutions with rich chaotic dynamics. The term *chaotic* here implies that two solutions (or *orbits*) of equations (1.1) starting from two arbitrarily close points in phase space separate exponentially in time eventually becoming completely uncorrelated. When applied to the stirring of a passive tracer by a fluid flow, this idea raises the exciting possibility that even a deterministic velocity field could very effectively stir a passive tracer by transporting it along trajectories that wander chaotically throughout the flow domain—the phase space of the dynamical system governing the particle paths of the flow. Since efficient stirring is a prerequisite for rapid scalar homogenization, it thus follows that even a non-turbulent velocity field could yield rapid scalar mixing. This phenomenon has indeed been shown to occur, first by Henon (1966), Arter (1983), and Aref (1984) and subsequently by many others, and was dubbed by Aref (1984) as "chaotic advection"—the term Lagrangian turbulence is also used in the literature.

Chaotic advection plays a critical role in a variety of mixing problems encountered in engineering and geophysical applications and for that reason it has attracted considerable attention in recent years. Although a large number of experimental (Chaiken, Chevray, Tabor, and Tan 1986; Chien, Rising, and Ottino 1986; Leong and Ottino, 1989; Swanson and Ottino, 1990; etc.) and numerical (Aref 1984; Khakar, Rising, and Ottino 1986; Rom-Kedar, Leonard, and Wiggins 1990; Ghosh, Leonard, and Wiggins 1998; etc.) investigations of the phenomenon have been reported for two-dimensional flows, the characteristics of chaotic advection in three-dimensional (steady and unsteady) flows are still largely unexplored. This should be attributed to the lack of test-bed flowfields of engineering relevance that are amenable to both experimental and numerical investigations. Most of the existing studies in three dimensions have employed mathematical flow models, such as the ABC flow (Dombre, Frisch, Green, Henon, Mehr, and Soward 1986; Tang and Booz 1999), Beltrami flow in a sphere (Zheligovsky 1993), compressed helical flows (Goverukhin et al 1999), and steady Stokes flow within a spherical drop (Bajer and Moffatt 1990; Stone, Nadim, and Strogatz 1991). Studies with experimentally realizable, steady, three-dimensional flowfields have also been reported. Khakar, Frajione, and Ottino (1987) and Kusch and Ottino (1992) studied chaotic advection in a partitioned-pipe mixer. Jones, Thomas, and Aref (1989) proposed a twisted-pipe configuration, which exhibits chaotic particle paths. Ashwin and King (1997) studied the Lagrangian characteristics of non-axisymmetric Taylor-Couette flows between two concentric cylinders. In all these studies the flowfields were specified analytically by deriving approximate solutions of the Navier-Stokes equations. There have been only a handful of investigations, so far, that have employed numerically

generated three-dimensional flowfields. Hobbs and Muzzio (1997, 1998) studied in detail chaotic advection in a straight, helical static mixer. Fountain et al. (1998, 2000) studied numerically and experimentally chaotic advection in a container with an inclined rotating disk for Reynolds numbers in the creeping flow regime. Sotiropoulos et al. (2000, 2001) reported experiments and numerical simulations of the rich Lagrangian properties of vortex breakdown bubbles in a confined swirling flow. Recently studies have been performed to investigate the effect of chaotic mixing in stirring tanks (Alvarez et al 2002a, 2002b; Zalc et al 2001, 2002). Even fewer studies have been carried out in unsteady, three-dimensional, experimentally realizable flows. Cartwright, Feingold, and Piro (1996) were the first to investigate chaotic advection in unsteady spherical Couette flow. More recently, Mezić, Leonard, and Wiggins (1998) analyzed particle paths in a helical vortex filament embedded in an axisymmetric, time-dependent strain field—a flow that can be viewed as a model of a tip-vortex shed from a propeller.

1.1 Thesis Objective and Outline

This thesis seeks to make novel contributions in the study of chaotic advection in three-dimensional flows by investigating numerically its multiple facets in a series of experimentally realizable and engineering relevant flow fields. We consider three problems involving three-dimensional, rotating flows in confined cylindrical containers.

The first problem is flow in a cylindrical container with a rotating end-wall. The emphasis in this problem is on the Lagrangian dynamics in the interior of the steady vortex-breakdown bubbles that form along the axis of the container over a range of

governing flow parameters. Vortex breakdown is among the most widely studied fluid mechanics phenomena but the results reported in this thesis constitute the first comprehensive study of its rich Lagrangian dynamics. A unique feature of this flow, which distinguishes it from the second case we study in this work, is that the base axisymmetric flow is stable, at least from the Eulerian standpoint, to arbitrarily small, steady, non-axisymmetric modes. Yet within a certain range of governing flow parameters, even very small three-dimensional perturbations, which are bound to be present in any experimental realization of this flow, have a profound effect on the Lagrangian dynamics of this flow leading to a very rich, chaotically advected flow in the interior of steady, vortex breakdown bubbles. In this thesis, we demonstrate these complex phenomena and establish concrete links with the theory of dynamical systems, which allows us for the first time to explain and reconcile the vast disparity in complexity between the Eulerian and Lagrangian descriptions of such flows.

The second problem is flow in a cylindrical container driven by exactly counter-rotating endwalls—also known as the von Karman swirling flow, since a flow of this type was first studied by Theodore von Karman in 1921. Flows of this type have attracted considerable recent attention in the literature because they serve as a geometrically simple model of many geophysical, atmospheric, and industrial flows. Recent stability analysis studies have shown that three-dimensional modes are excited even in the steady flow regime due to instabilities that originate at the shear layer between the two counter-rotating swirling flows. In this thesis, we report the first fully three-dimensional solutions of the Navier-Stokes equations over a range of Reynolds numbers in the steady flow regime, elucidate the physics of the shear-layer induced instabilities, and explore the role

of these flow instabilities on the onset and intensity of chaotic Lagrangian stirring. The fact that steady, three-dimensional instability modes are excited in this flow over a broad range of Reynolds numbers, makes this case an excellent test bed for investigating one of the central theoretical questions in chaotically advected flows; namely, the role of Reynolds number on the intensity of chaotic stirring.

The third case is motivated by the lessons learned from the second case. It is designed to explore whether the inherent instability of the flow between counter-rotating disks can be exploited to improve the performance of industrial mixing devices, which rely on rotating impeller blades. Commonly such devices employ a series of co-rotating disks or impellers. In this thesis we propose a model device, which utilizes counter-rotating disks and carry out a series of computations to demonstrate the concept and explore its feasibility as an industrial mixer.

For all cases we solve numerically the three-dimensional, incompressible Navier-Stokes equations using a second-order accurate finite-volume method. The numerically generated flowfields are analyzed using techniques from dynamical systems to study the rich dynamics of particle paths in these flows and quantify Lagrangian transport and stirring efficiency. We pose and seek to answer important questions about the link of Eulerian features of the flow and Lagrangian dynamics, the role of governing flow parameters (such as Reynolds number, swirl ratio, aspect ratio, etc.) on mixing efficiency, and the formation and persistence of unmixed regions of the flow.

The following chapters give an outline of the thesis and summary of the major contributions:

Chapter 2: provides a look at fundamental concepts of dynamical systems in relation to fluid mechanics and describes the tools used in Lagrangian analysis of flows.

Chapter 3: reviews the previous research on chaotic mixing.

Chapter 4: describes the particle-tracking method used in this research.

Chapter 5: provides results for the container flow with rotating bottom lid and stationary top lid with emphasis on the rich Lagrangian properties of steady vortex breakdown bubbles.

Chapter 6: discusses the flow field and Lagrangian transport in a cylindrical container flow with exactly counter rotating lids.

Chapter 7: applies the concepts gained in Chapter 6 to flow in stirred tanks driven by three exactly counter-rotating disks.

Chapter 8: presents a summary of the work, major conclusions, contributions, and future research objectives.

CHAPTER 2

CHAOTIC ADVECTION & DYNAMICAL SYSTEMS: DEFINITIONS AND FUNDAMENTALS

Understanding the use of chaotic advection and dynamical systems to analyze and quantify mixing requires a basic background of certain fundamental concepts and tools. In this chapter, we present a brief review of theoretical work in the area of dynamical systems that is directly relevant to the understanding of chaotic advection in three-dimensional flows. The discussion in the first section is aimed at introducing the essential theoretical framework for interpreting our computational findings. The subsequent sections will build upon that framework and extend to the development and application of specific dynamical systems tools that can be applied to analyze and quantify Lagrangian transport.

2.1 Dynamical Systems Framework

To begin our discussion, consider a steady, axisymmetric, incompressible flow in the closed rotating cylinder shown in figure 2.1. The Lagrangian equations of motion for non-diffusive passive markers read in cylindrical polar coordinates as follows:

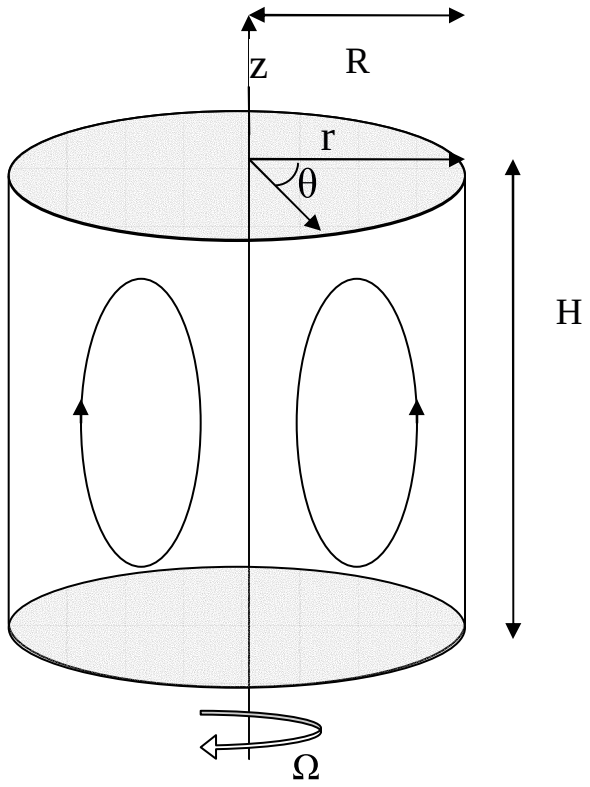

Figure 2.1 Flow geometry for steady, axisymmetric, incompressible flow in a closed rotating cylinder.

$$\frac{dx}{dt} = u_x(x,r) \qquad \frac{dr}{dt} = u_r(x,r) \qquad \frac{d\theta}{dt} = \frac{1}{r}u_\theta(x,r) \tag{2.1}$$

where u_x, u_r, and u_θ are the axial, radial, and azimuthal velocity components, respectively. The Stokes stream function, $\psi = \psi(x,r)$, can be employed to formulate the above equations as follows:

$$\begin{aligned} \frac{dx}{dt} &= \frac{\partial \psi}{\partial R} \\ \frac{dR}{dt} &= -\frac{\partial \psi}{\partial x} \\ \frac{d\theta}{dt} &= \Omega(x, R) \end{aligned} \tag{2.2}$$

where $R = r^2/2$ (Benjamin 1962), and Ω is the swirl velocity of the flow. From a dynamical systems point of view, the Stokes stream function is the Hamiltonian function and equations (2.1) comprise a one and a half degree of freedom Hamiltonian system. Solutions of these equations lie on invariant cylindrical or toroidal surfaces (the stream-surfaces of the axisymmetric flowfield) and, thus, chaotic advection is not possible (Holmes 1984; MacKay 1994; Mezić and Wiggins 1994) and the dynamical system given by equations. (2.1) is said to be *integrable*. A common example of invariant sets encountered in vortex-ring type flows are toroidal or donut-like stream-surfaces.

Consider now a flow domain foliated by a series of nested invariant toroidal surfaces such as the cylindrical container with rotating bottom lid seen in figure 2.1. A coordinate transformation can be introduced to take advantage of the toroidal structure of the flow (see figure 2.2). The variable *I* is a radial curvilinear coordinate measured from the circle that lies at the center of the toroidal structure and *I*=const. identifies a specific torus. The angular variable ϕ locates the particle on the cross-section of the torus while θ is the azimuthal coordinate as in the polar-cylindrical coordinate system. Using this notation, the Lagrangian advection equations (2.1) can be transformed as follows:

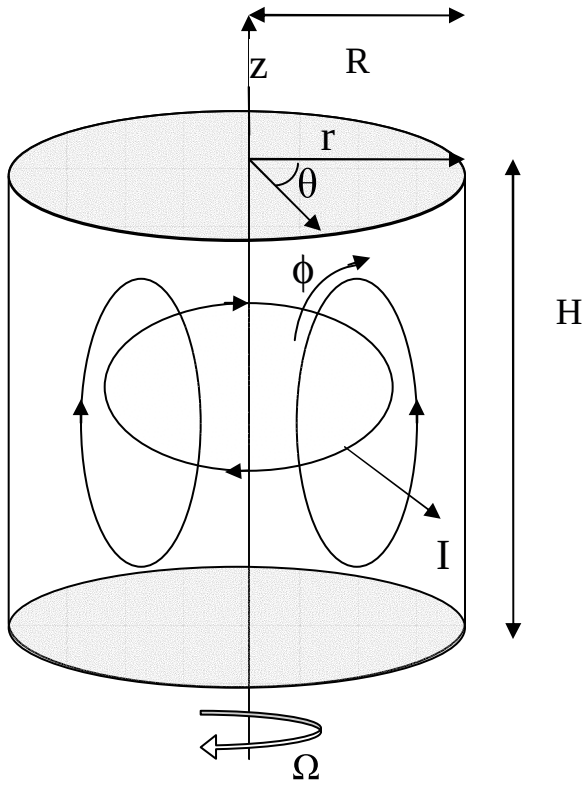

Figure 2.2 Coordinate transformation for steady, axisymmetric, incompressible flow in a closed rotating cylinder.

$$\begin{aligned} \frac{dI}{dt} &= 0, \\ \frac{d\phi}{dt} &= \Omega_{\phi}(I), \\ \frac{d\theta}{dt} &= \Omega_{\theta}(I), \end{aligned} \tag{2.3}$$

where Ω_θ, and Ω_ϕ are frequencies of rotation in the direction of θ and ϕ, respectively.

The fact that such a transformation exists for an axisymmetric, volume preserving flow has been rigorously shown by Mezić and Wiggins (1994). In the dynamical systems literature this transformation is known as the transformation in *action-angle-angle*

variables. The first equation in the system (2.3) expresses the fact that for an integrable flow a particle will remain confined on the same torus at all times. The other two equations govern the motion of the particle on its respective torus. We define the rotation number of a torus *f* as follows:

$$f = \frac{\Omega_\phi(I)}{\Omega_\theta(I)} \tag{2.4}$$

In general *f* can be either a rational or an irrational number. A particle moving on a torus with rational rotation number, say $f=q/p$, where *p* and *q* are prime numbers, will move along *periodic orbits* of period *p*. That is, such a particle will revisit the position where it started after rotating *p* times along the circumference of the torus and *q* times along the cross-section of the torus. A particle moving on a torus with irrational rotation number on the other hand may pass arbitrarily close from its initial location but will never exactly revisit it. We shall say that such a particle covers *ergodically* the entire torus. To summarize, an integrable vortex-ring type flow will be foliated by invariant rational and irrational tori on which particles remain confined. In such a case, scalar tracer homogenization can only occur via molecular action across tori and in general will take very long times.

Let us now examine how the above orderly picture changes if a small non-axisymmetric perturbation is imposed onto the base integrable axisymmetric flow. Under the action of a steady, three-dimensional perturbation of strength ε equations 2.3 can be formulated as follows:

$$\begin{aligned}
\frac{dI}{dt} &= \varepsilon g_I\left(I,\phi,\theta,\varepsilon\right), \\
\frac{d\phi}{dt} &= \Omega_\phi(I) + \varepsilon g_\phi\left(I,\phi,\theta,\varepsilon\right), \\
\frac{d\theta}{dt} &= \Omega_\theta(I) + \varepsilon g_\theta\left(I,\phi,\theta,\varepsilon\right),
\end{aligned} \tag{2.5}$$

where g_I, g_ϕ, and g_θ are the perturbation functions. For sufficiently small ε, equations 2.5 describe a mildly perturbed dynamical system, which could exhibit very complex dynamics even when $\varepsilon << 1$. The following sections will discuss the nature of the complexities and in the process also describe dynamical system tools that we can be used to visualize and quantify them.

2.2 Visualizing Rich Dynamics

2.2.1 Poincarè Maps

A powerful approach for visualizing rich dynamics is to construct a Poincarè map. In this section we discuss the construction of the Poincarè map and explain how it can be used to visualize various dynamically rich regions of the solutions of the perturbed equations (2.5). We begin by defining a diametral plane as the plane of section of the Poincarè map. Particles are distributed on the surface of section and their trajectories are integrated in time by solving equations. (2.5). Every time a particle crosses the plane of section we mark the position it intersected the plane by a dot. For the unperturbed system given by equations (2.1), this process will yield an image that is identical to the streamlines of the axisymmetric flow in a diametral plane (see figure 2.3). The picture

that will result for the perturbed system given by equations (2.5), however, could be drastically different even for small perturbation ε.

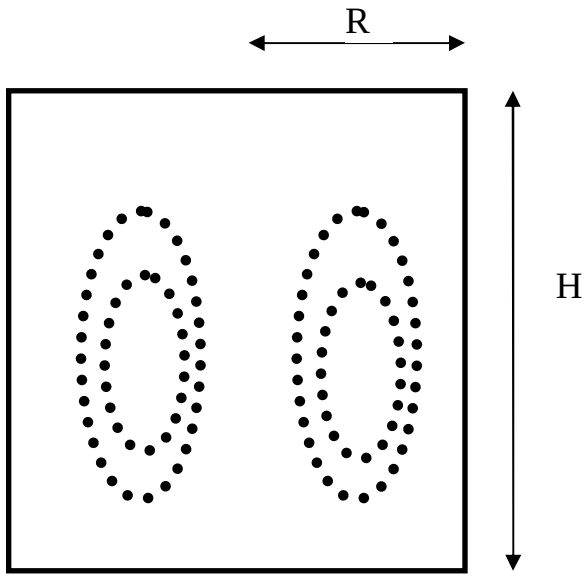

Figure 2.3 Poincarè map for unperturbed system given by equations 2.1.

According to the KAM (after Kolmogorov, Arnold and Moser) theorem (Arnold 1978; Moser 1968), under the action of a sufficiently small perturbation ε many of the invariant tori of the initial axisymmetric flow structure whose rotation number is sufficiently irrational will survive the perturbation and remain intact in the solutions of Eqns. (2.5). Such surfaces are called KAM tori and can be thought of as the remnants of the axisymmetric stream-surfaces of the flow. The term *sufficiently irrational* is meant in the sense that *f* satisfies the Diophantine condition

$$\frac{\Omega_\phi(I)}{\Omega_\theta(I)} - \frac{l}{k} \geq \frac{c}{k^\mu} \tag{2.6}$$

for $\mu > 2$ and for all integers k, l (Arnold 1978). Rational tori, on the other hand, will in general break upon perturbation into higher order tori (see for example figure 2.4) with chaotic regions in between. Such higher order tori are invariant sets of the flow in the sense that particles trapped within them can escape only via molecular action. We shall refer to such tori as unmixed or periodic islands the period of which is determined by the denominator p of f. The so described breaking of the torus is described by the Poincaré-Birkhoff theorem (Lichtenberg & Lieberman 1992).

The resulting Lagrangian structure of the flow is very complex as indicated by the 3D perspective shown in figure 2.5 from Helleman (1980). Invariant KAM-tori occupy the core of the toroidal structure surrounded by periodic islands and regions of chaos. Particles that lie on a KAM torus will appear in the Poincarè map as two, symmetrically located with respect to the centerline, closed circles—the intersection of the plane of section with the respective invariant tours. Particles that lie on an unmixed torus of period p will appear as two symmetrically located chains of p islands. Each island chain consists of a fixed elliptic point at its center surrounded by KAM-tori and is connected with adjacent islands with two fixed points of hyperbolic type, which give rise to chaotic trajectories via the transverse intersections of their stable and unstable manifolds. (see figure 2.4)

In addition to KAM-tori, which are impermeable barriers to transport, leaky or partial barriers to transport have also been shown to exist in mildly perturbed volume preserving dynamical systems (McKay, Meiss, and Percival 1984). Such surfaces can be

thought as tori with an intricate set of fractal windows—a Cantor set of openings—through which particles located on the torus could ultimately escape. Since by definition

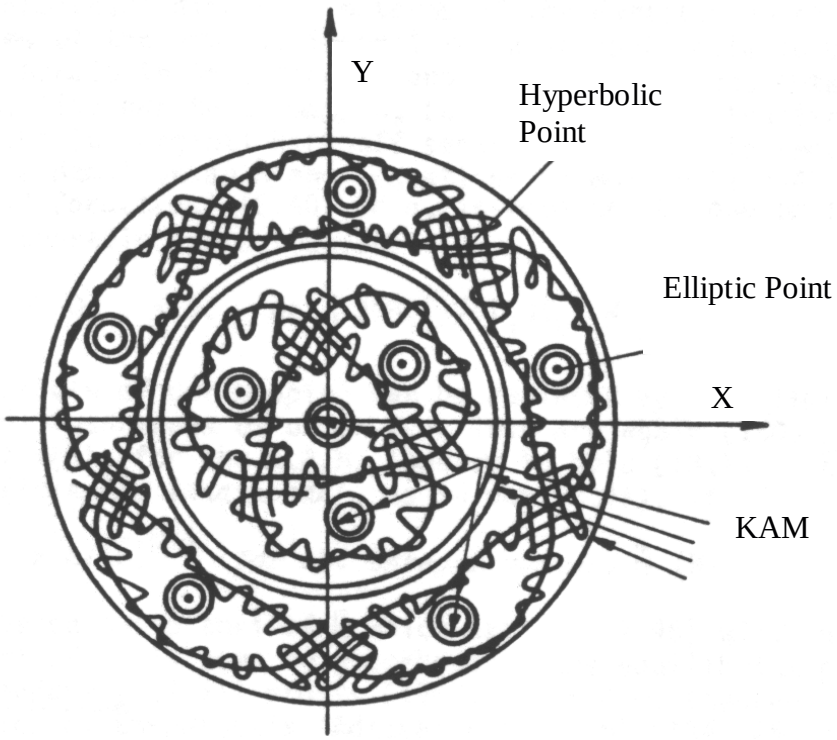

Figure 2.4 Two-dimensional view of perturbed tori structure

a Cantor set of openings consists of infinitely many openings whose size approaches zero, a particle trajectory initially located on a leaky torus may stay there for arbitrarily long times before it encounters a fractal opening and escapes. Such partial barriers to transport are known as Cantori and their presence further complicates the Lagrangian dynamics of a perturbed flow.

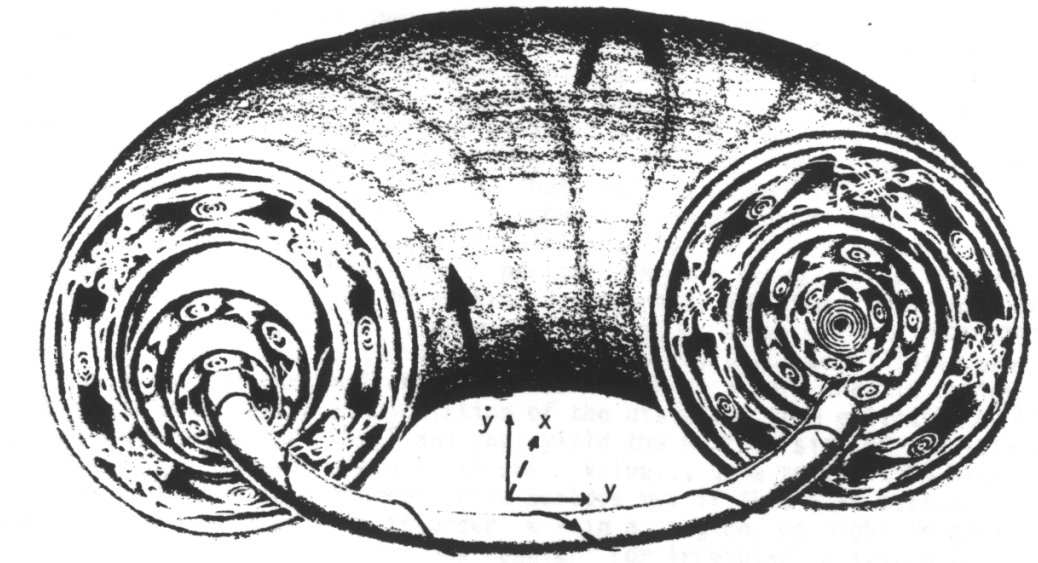

Figure 2.5 Three-dimensional perspective of perturbed tori (Helleman 1980).

2.2.2 Lagrangian Averaging

A difficulty when constructing Poincarè maps in complex, 3D flows stems from the fact that one often has to manually search through the entire flowfield for an appropriate set of initial conditions that elucidates the most important dynamical features of the flow. As discussed above, in a chaotically advected flow many high-period unmixed islands will in general exist embedded within areas of chaotic motion. The higher the period of these islands the more difficult it is to locate them in a Poincarè map.

An approach that remedies this situation relies on Lagrangian time averaging as proposed by Mezić (1994) and Mezić and Wiggins (1999). Lagrangian time averaging can be used to visualize the unmixed regions of the flow—known in the dynamical systems literature as *invariant sets* of the Poincarè map—and is described as follows.

Let f be some property of the flow, such as velocity, pressure, vorticity, etc.—for a steady, three-dimensional flow $f = f(x, y, z)$. Consider a particle that at $t = t_o$ is located at point $\boldsymbol{X_o} = (x_o, y_o, z_o)$, where $\mathbf{X}_o$ is the initial position vector. The trajectory of this particle is obtained by integrating in time Eqns. (1.1) and can be expressed as follows:

$$\mathbf{X} = \mathbf{X}(t, \mathbf{X_o}) = \left(x(t, \mathbf{X_o}), y(t, \mathbf{X_o}), z(t, \mathbf{X_o})\right) \tag{2.7}$$

where $\mathbf{X}$ is the solution of Eqns. (1.1) passing through $\mathbf{X}_o$ at $t = t_o$. As particle $\mathbf{X}_o$ wanders along its trajectory $\mathbf{X}$ through the flowfield, it samples different values of property f at every point it visits. We can then express f in terms of Lagrangian variables as follows:

$$f = f\left(\mathbf{X}(t, \mathbf{X_o})\right) \tag{2.8}$$

The above notation implies that f is a function of the position in the flowfield, which is currently occupied by the particle that at $t=t_o$ started at $\mathbf{X_o}$. The Lagrangian average of f, f_L^*, is the average over all possible values of f sampled by the particle as it moves along its trajectory and can be formally defined as follows:

$$f_L^*(\mathbf{X}_o) = \lim_{t\to\infty} \frac{1}{t} \int_0^t f(\mathbf{X}(t, \mathbf{X}_o)) \quad dt \tag{2.9}$$

As indicated by the above notation, for steady flow f_L^* is only a function of the initial position $\mathbf{X_o}$ of the particle. Therefore, every possible initial condition in the flow is associated with a unique Lagrangian average of f. The fact that for an incompressible

flow in a bounded domain the average in equation (2.9) exists follows directly from Birkhoff's ergodic theorem. Note that Birkhoff's ergodic theorem is valid for almost every initial condition (in the sense of measure theory) and thus its validity is not restricted only to chaotic or to regular regions of the flow.

Using the concept of Lagrangian averaging the unmixed regions in the flow can be visualized by the following procedure:

1) Define a set of initial conditions $\boldsymbol{X_o}$;
2) Compute the Lagrangian time averages of a chosen function f over the fluid particle trajectories (streamlines in a steady flow) originating from the points $\boldsymbol{X_o}$;
3) Map the so computed $f_L^*(\boldsymbol{X}_o)$ to $\boldsymbol{X_o}$ and plot the iso-contours of the resulting scalar field.

Ergodic theory can be used to rigorously show that the iso-contours of $f_L^*(\boldsymbol{X}_o)$ will indeed visualize the unmixed regions in the flow (invariant sets) (Petersen 1983). A heuristic argument that supports this proof can be given as follows. Consider an invariant torus in the flow embedded in a region of chaos. Initial conditions placed on this torus will explore only a small subset of the flow domain (the toroidal surface on which they are confined) and, thus, will sample only a small subset of all possible values of *f*. The Lagrangian average for all points on the torus should converge to the same value since these points will cover the torus ergodically. Points surrounding this torus on the other hand wander chaotically throughout the flow domain. Such points will cover ergodically the entire chaotically advected region of the flow and will, thus, sample a much larger subset of values of *f*. The resulting Lagrangian average for these points will, thus, be

considerably different than for the points on the torus and the iso-surfaces of $f_L^*(\boldsymbol{X}_o)$ will reveal the structure of the invariant torus.

An important aspect of the above method concerns the integration time required for the averages to converge to their mean value. It is knows that along chaotically advected trajectories convergence is extremely slow (Meiss 1994) and the trajectory integration needs to be carried out for millions of time steps. As shown in Mezić and Sotiropoulos (2002), however, along periodic trajectories convergence is very rapid, about t^{-1}. This property of periodic orbits suggest that Lagrangian averaging can be used to develop an efficient computational technique for identifying unmixed islands in complex, 3D flows. As shown in Mezić and Sotiropoulos (2002) this property was also exploited by Sotiropoulos et al. (2002) to develop the first non-intrusive experimental technique for visualizing in the laboratory unmixed islands in 3D swirling flows.

2.3 Quantifying Lagrangian Transport

The Poincarè map of the flow can provide a global qualitative picture of the richness of the dynamics of Eqns. (2.5) but can not quantify the intensity of Lagrangian transport in the chaotic areas of the flow, which as we discussed above is critical for developing measures of transport and mixing. In this section we discuss techniques for computing two quantities that can be used to obtain a quantitative description of the intensity of chaotic motion: 1) Lyapunov exponents, which describe the rate of divergence of nearby trajectories; and 2) the local stretching rate of material lines.

2.3.1 Lyapunov Exponents

Lyapunov exponents were proposed by Alexander Lyapunov in the late 1800's and by definition they measure the rate at which particle trajectories that start from infinitesimally close initial conditions will diverge apart. Since extreme sensitivity to initial conditions and the associated exponential separation in time of trajectories is the hallmark of chaos, Lyapunov exponents provide a natural way to quantify the intensity of chaotic transport and mixing in the flow. In this section we define the concept of Lyapunov exponents and outline a numerical technique for calculating them.

Consider the previously described flow. Recall that in the unperturbed, axisymmetric flow, tracer particles remain confined on their respective (invariant) stream-surfaces. Under these conditions, homogenization would be very slow as it could only occur via molecular mixing across adjacent tori. In a chaotically advected flow on the other hand, the break-up of many of the invariant toroidal surfaces creates a subset of the flow domain within which particles can wander chaotically and separate exponentially in time. The volume V_{chaos} of this subset of the flow domain is equal to the volume of the entire flow minus the volume occupied by impermeable barriers to transport such as KAM tori and unmixed island chains:

$$V_{chaos} = V_{flow} - V_{KAM\ tori} - V_{islands} \tag{2.10}$$

As discussed above, the Lyapunov exponents can be used to quantify the rate at which such exponential separation takes place (Wolf et al. 1985, Rosenstein et al 1992).

To define the Lyapunov exponents, consider an infinitesimal material sphere of radius $\boldsymbol{dr}$ centered at time $t = 0$ at the starting point of a particular fluid trajectory. Such

material sphere, therefore, contains a large set of initial conditions, which are arbitrarily close together. In general, the flow will stretch this material surface and deform it into a material ellipsoid. The volume of this ellipsoid at any given time t can expressed in terms of the lengths $\ell_i(t)$ of its three major axes (i = 1 to 3). A Lyapunov exponent λ_i can then be defined for each one of the three spatial directions to quantify the rate at which the ellipsoid expands or contracts in time along that direction as follows:

$$\lambda_i = \lim_{t\to\infty} \frac{1}{t} ln\left(\frac{d\ell_i(t)}{dr}\right) \tag{2.11}$$

It follows from the above definition that if all three Lyapunov exponents are zero then the initial material sphere preserves its shape and size at all times. If λ_i <0 then the initial sphere will be contracted exponentially in time along the i^{th} direction. Finally, if λ_i >0 then the initial sphere will be stretched exponentially in time along the i^{th} axis. Note that since for a volume preserving flow of a constant density fluid the initial size of any material volume must be preserved at all times, it can be shown that the summation of all thee Lyapunov exponents must be zero at all times (Ottino 1981). That is, if the material volume is stretched exponentially along one principal direction it must experience exponential contraction along some other direction in order for its volume to be conserved. In general, a flow region will be said to be occupied by chaotically advected trajectories if at least one of the three Lyapunov exponents is positive for every initial condition within that region.

It is readily apparent from the above discussion that after sufficiently long times, the size of the material ellipsoid will be controlled almost entirely by the value of the

largest positive Lyapunov exponent, which we shall denote as λ. It is, therefore, reasonable to assume that the state of a chaotic dynamical system in general and the intensity of stirring in a chaotically advected flow in particular could be described by the values of the largest positive Lyapunov exponent for all possible initial conditions (see Rosenstein et al. 1992). The largest Lyapunov exponent for a particular initial condition $\mathbf{X}_o$ can be calculated for a discrete dynamical system, such as the numerically calculated flowfields we are interested herein, via the following numerical procedure (Ottino 1981).

Consider a material point *A* located at $\mathbf{X}_o$ at time t_o and the nearby material point *B* located at $\mathbf{X}_o + \boldsymbol{\delta}_o$, where $\delta_o << 1$, at the same time (figure 2.6). Let $\boldsymbol{\delta}_k = \boldsymbol{\delta}(\mathbf{X}_o, t_k)$ denote the distance between these two material points at any later time $t = t_k$. Define the relative separation parameter φ_k at time $t = t_k$ between the two points as follows:

$$\varphi_k = ln \frac{|\boldsymbol{\delta}_k|}{|\boldsymbol{\delta}_o|} \tag{2.12}$$

Note that as a practical matter in chaotic regions of the flow φ_k will be become large in relatively short times due to the exponential separation of trajectories and consequently the positions of the two material particles will rapidly become uncorrelated. To remedy this situation we continue monitoring the separation of point B relative to point A up until their relative distance exceeds a prescribed maximum threshold. At that moment, we: 1) note the time t_k when this criterion is reached; 2) calculate φ_k using the above equation; 3) re-initialize the position of point B so that it is once again located at distance $\boldsymbol{\delta}_o$ from the current position of point *A*—that is, at the end of this step point *A* is located at $\mathbf{X}_k$ and point *B* is placed at $\mathbf{X}_k + \boldsymbol{\delta}_o$; and 4) start monitoring the relative separation of the two

points once again until the maximum distance is reached and the procedure is repeated from the first step in this list. After repeating this process N times for the trajectory of

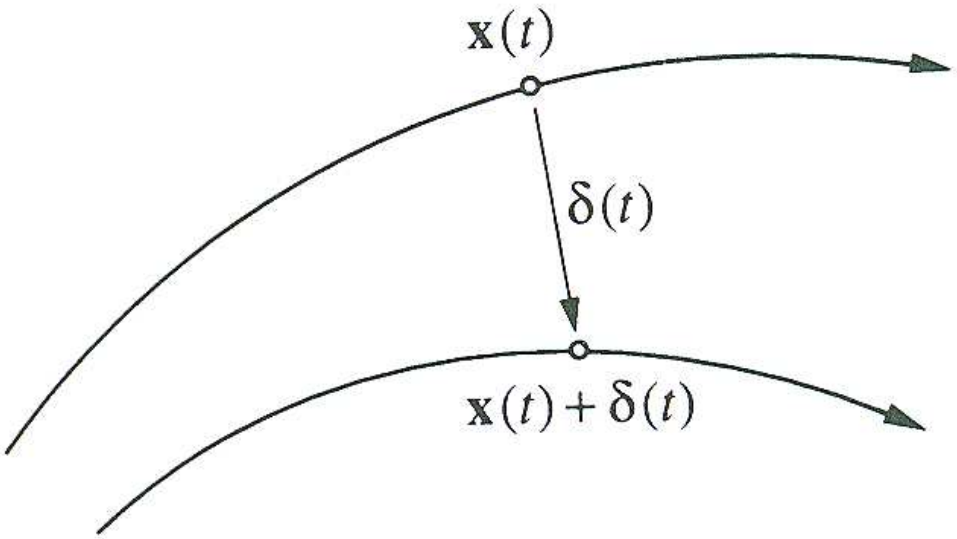

Figure 2.6 Separation of initial conditions with time.

point *A* we obtain a sequence of times t_1, t_2, t_3,...,t_N marking the instants in time when the position of point B had to be re-initialized relative to the position of point A. The maximum Lyapunov exponent for the trajectory originating from point A is then calculated as follows:

$$\lambda = \lim_{N \to \infty} \frac{1}{N} \sum_{k=1}^{N} \frac{\varphi_k}{t_k - t_{k-1}} \tag{2.13}$$

2.3.2 Local Stretching of Material Lines

The exponential separation of trajectories in chaotically advected flows is the result of continuous stretching and folding of material lines by the flow. Stretching and folding create material interface at spatial scales much smaller than the Eulerian scales of the flow and lead to scalar concentration gradients at scales sufficiently small for molecular diffusion to complete the mixing process. Therefore, calculating the length of stretch and the stretching rate of material lines is another useful tool for quantifying the intensity of chaotic transport and stirring in the flow.

The computation of the total length stretch requires knowledge of the instantaneous values of the velocity gradient. The length stretch denoted by $\Gamma(t)$ is defined exactly by

$$\Gamma \equiv \lim_{|dX|\to 0} \frac{|dx|}{dX} \tag{2.14}$$

where dX is the initial length of an infinitesimal filament and dx is its length at time *t*. One should note the similarity of the forms for this above equation with equation 2.11 from our discussion of the Lyapunov exponents. The value of $\Gamma(t)$ can be obtained numerically by integrating the following system of ordinary differential equations:

$$\dot{\mathbf{p}} = \mathbf{p} \cdot \nabla \mathbf{v} \tag{2.15}$$

where **p** is the infinitesimal material vector and **v** is the velocity vector. The length stretch is then

$$\Gamma(t) = \frac{|\mathbf{p}(t)|}{|\mathbf{p}(0)|} \tag{2.16}$$

The length stretch is therefore calculated at every time step. Using the velocity gradient, obtained by the flowfield, we follow a similar process as that used in the Lagrangian time average calculations to now create stretching maps. A set of initial conditions is chosen. Those particles trajectories are integrated throughout the system. Then, for every time t, we calculate the vector **p** by solving the system of equations given by (2.15). We calculate the length stretch Γ and map the values back to the initial conditions before plotting the iso-contours of the resulting scalar field.

Using this information for the instantaneous length stretch it is possible to calculate the average specific rate of stretch over time and eventually the average stretching efficiency (Khakhar et al 1987). For a continuous system the specific rate of stretching can be defined by

$$\gamma = \frac{D \ln \Gamma}{Dt} \tag{2.17}$$

The average specific rate of stretching α over time t corresponding to the initial position x_o and orientation m_0 is given by

$$\alpha(x_0, m_0) = \frac{1}{t} \ln \Gamma \tag{2.18}$$

If we remember from the previous section that the Lyapunov exponent of a trajectory is the rate at which particles separate, we can find the relationship between the average specific rate of stretching and the Lyapunov exponent.

$$\lambda \equiv \lim_{t\to\infty}\left\{\frac{1}{t}\int_0^t \frac{D\ln\Gamma}{Dt'}\,dt'\right\} = \lim_{t\to\infty}\left[\frac{1}{t}\ln\Gamma\right] \tag{2.19}$$

The Lyapunov exponent is then the long time average of the specific rate of stretching.

CHAPTER 3

LITERATURE REVIEW

In this chapter we review previous research in the area of chaotic advection. We review experimental, computational, and analytical studies in the context of both two- and three-dimensional flows. This chapter seeks to summarize the progress in the field, underscore its engineering significance, and the underlying significance of our contribution.

There have been several reviews of research performed in the area of chaotic advection, such as Aref's "The Development of Chaotic Advection" (2002) and "An Introduction to Chaotic Advection" (Cartwright et al 1999). Undertaking such a review, however, is difficult mostly because this field is almost organic in its growth due to new applications that seem to materialize every day. Also, reviews often tend to be skewed towards the research of the presenter and could not possibly exhaustively present *all* relevant contributions. Therefore, here we attempt to summarize the major contributions in the area of chaotic mixing in a systematic manner. First, we give a historical overview of the original studies of chaotic mixing, after which we discuss some of the subsequent studies of two-dimensional flows both experimental and numerical. Finally, we review the research in our area of emphasis: three-dimensional flows.

3.1 Historical Overview

The fundamental nature of mixing was first addressed more than a century ago by Osborne Reynolds. In his talk published in *Proceedings of the Royal Institution* (Reynolds 1893-1895), he remarks on the two step process of attenuation (or thinning of fluid layers) as well as folding, piling, and wrapping. These are keywords that we now readily refer to when addressing the ideas of chaotic mixing, although at the time this connection was not made. Approximately fifty years passed since Reynolds' remarkable insights until Carl Eckert, while working on problems of geophysical dynamics, suggested some important distinctions concerning the fundamental nature of mixing (1948). He expressed the idea that what was previously called mixing should instead be split into two categories: "stirring," which increases the material interface between a tracer and the fluid in which it is being mixed via the aforementioned stretching and folding process, and "mixing" the molecular process via which the tracer diffuses across the so created material interface. These fundamental concepts were both necessary building blocks for chaotic advection.

In 1955, Pierre Welander (Welander 1955) was the first to visualize the stirring of a blob of dye in a two dimensional, time dependent laminar flow. His work demonstrated clearly the processes of stretching and folding and their role to quickly homogenize the flow. Even though it is apparent that Welander understood some of the essential ideas leading to the (then still unborn) concept of advection and its use to enhance mixing, it was not until the mid 1960s when further progress was made in the field. At that time, Vladimir Arnold (1965) studied the integrability of three-dimensional Euler flows. Arnold describes a class

of non-integrable Euler flows called ABC flows (Arnold-Beltrami-Childress) or flows for which the vorticity and velocity vectors are parallel. A year later, M. Henon (1966) experimentally realized this flow based on the Arnold work, creating the first simulation of chaotic advection.

Nearly ten years later Shinji Nagata (1975) published the accumulation of twenty years worth of work, in a book in which he systematized all the knowledge of mixing in stirred tanks. Within this work he discusses the ring or doughnut-like structures that are not mixed with the other fluid areas for a long time. These same doughnut-like structures can now be recognized as the tori or non-chaotic regions of the flow.

It was almost another ten years before W. Arter (1983) approached the subject in a brief paper in which he investigated ergodic streamlines in steady convection. However the seminal contribution in the field that ignited what can now be considered one of the major research areas in fluid mechanics was the work of Hassan Aref (1984) who studied numerically the particle paths of the blinking vortex flow and described in detail the process of stirring by chaotic advection. Aref was not only the first to coin the term chaotic advection, but he also established the clear connection between the flow domain and the phase space of dynamical systems, thus, creating a clear and powerful link between fluid mechanics and dynamical systems. The result of this work had two effects: 1) a great increase in the study of flows using dynamical systems, and therefore the Lagrangian approach and 2) the key involvement of chaotic advection within the field of fluid mechanics and mixing.

3.2 Two Dimensional Flows

In this section we summarize some of the major experimental and computational contributions to chaotic advection in two-dimensional, low Reynolds number flows, which comprise the majority of works in the field following Aref's seminal paper. Even though chaotic advection is possible in two-dimensional time dependent flows as well as in three dimensional flows, it has been stated (Saatdjian and Leprevost 1998) that most experimental work has dealt with two-dimensional flows simply because the experimental apparatus is generally easier to build, cheaper to run, and the experiments are more straightforward to carry out.

Chaikan et al (1986) studied experimentally chaotic advection in time-periodic, Stokes flow between two eccentric rotating cylinders. Their research provides the first experimental verification of chaotic advection and was detailed over extended flow parameters. Within the same year Chien et al (1986) performed an experimental study of laminar mixing in two-dimensional cavity flows. Their work elucidated the stretching of material lines and the complete blob deformation in chaotic and periodic areas. Solomon and Gollub (1988) studied chaotic particle trajectories in time-dependent Rayleigh Bernard convection both experimentally as well as numerically. Leong and Ottino (1989) researched chaotic advection in a cavity flow and Swanson and Ottino (1990) investigated the phenomenon in a journal bearing flow. This last experiment also provided numerical calculations and employed dynamical systems tools such as Poincaré maps to verify and interpret the experimental results. Solomon et al (1994) studied the chaotic advection in an annular tank. In this work they found indication of anomalous diffusion, which quantifies

the irregular growth of particle displacement with time. Recently, Voth et al (2003) investigated an experimental setup in which the mixing rate is measured for a magnetically forced two-dimensional chaotic flow.

There is also a large body of numerical work within the realm of two-dimensional flows. The preference for two-dimensional to three-dimensional flows in numerical studies is based primarily on the computational complexities. Incompressible two-dimensional flows can be described through the stream function as a Hamiltonian system which makes the velocity field much easier to obtain than numerically solving the full three-dimensional Navier-stokes equations. Khakhar et al (1986) were among the first after Aref (1984) to capitalize on this technique. They revisited the 'Aref-blinking-vortex' flow and attempted to find and describe the mechanism responsible for mixing. Over the next decade the two-dimensional numerical studies included among others the works of Rom-Kedar et al. (1990), who researched chaotic mixing in unsteady vortical flow, Melesako and Peters (1996), who described methods for obtaining periodic points for Stokes flow in a rectangular cavity, and Saatdijan and Leprevost (1996 and 1998), who consider chaotic heat transfer in the annular region between two cofocal ellipses. Other studies in that time period included those by Barkley et al 1990, who also considered a complex annular geometry, Liu et al 1994, who studied stretching in chaotic cavity flows, and Cerbelli et al 2000, who investigated partially mixed structures evolving under the effects of time-periodic chaotic flows.

A separate but closely related research area deals with transport and mixing by large scale, coherent structures in atmospheric, oceanic, and geophysical flows. Although these flows are turbulent, organized, coherent motions have been shown to emerge and persist and

to account for a significant percentage of total scalar transport and mixing. Thus, the theoretical framework of chaotic advection can be very useful for understanding and quantifying large-scale transport in such flows. In tidal areas, anomalous diffusion has been discovered (Pasmanter 1988) as well as chaotic stirring, (Beerens et al 1994). Samelson (1996) presents a strong case for chaotic transport in his study of the Gulf Stream. Such large scale convection was further investigated by Joseph (1998) to describe the mixing and transport of passive particles in two-dimensional thermal convection. Binson and Swathi studied the Lagrangian particle transport in the Indian Ocean (1999). Pierce and Fairlie (1993), Pierrehumbert and Yang (1993), and Koshyk and Ngan (2000) contributed to the surge of research that addresses large-scale chaotic advection in the atmosphere.

3.3 Three-Dimensional Flows

Many three-dimensional studies have employed mathematical flow models, such as the Arnold-Beltrami-Childress (ABC) flow. The ABC flow is a 3-D periodic, incompressible and steady flow given by the sum of three parameterized Beltrami waves.

$$\begin{aligned} u &= A\sin z + C\cos y \\ v &= B\sin x + A\cos z \\ w &= C\sin y + B\cos x \end{aligned} \tag{3.1}$$

When A or B or C are zero then the flow is integrable. However when ABC ≠ 0 then non-integrable streamlines are possible. Dombre et al. (1986) sought to understand why

ABC flows display chaotic features and to develop criteria based on the analytic equations of when integrable and non-integrable streamlines might occur. To accomplish this, they studied the unstable periodic orbits and fixed points described by the equations. They found that when one of the parameters (A, B, or C) vanishes, for the integrable flow, perturbation techniques could be used to predict strong local resonances that develop. These resonances are able to disrupt the invariant surfaces to develop the chaotic flow for the non-integrable case. They also found that by studying the complex-time singularities of fluid-particle trajectories they could characterize non-integrable cases as having recursive clustering of these singularities. Tang and Booz (1999) further studied this flow by attempting to characterize the diffusion in chaotic as well as integrable cases of the system. They developed criteria of enhanced diffusion between the chaotic flow and KAM surfaces that exist at certain values of A, B, and C. They found that by considering the advection-diffusion equation, which they studied via a global Lagrangian coordinate transformation, they were able to express a finite time Lyapunov exponent in terms of two convergence functions. These functions were determined to be responsible for the spatio-temporal complexity of both the advective and diffusive transports. It was found in both integrable and chaotic flows that there exist both fast and slow diffusion. However for the integrable case, the fast diffusion is confined within KAM surfaces preventing enhanced mixing. This was a fundamental suggestion that for non-chaotic flows there is in fact intensive mixing occurring but that it is trapped within small-localized areas of the flow, preventing transport throughout the larger flow domain.

Using the basic ABC flow concept, other variations have also been studied. The Beltrami flow in a sphere, which is the spherical analogous of the ABC flow was

investigated by Zheligovsky (1993). Also, Goverukhin et al (1999) investigated chaotic advection of the ABC flow as a part of their research within the compressible flow regime, looking at the CABC (compressible ABC) flow. Here they describe why compressible helical flow is more chaotic than incompressible helical flow. Using Poincaré maps they consider the varying cell structures that result from alternating the coefficients. They found that there is much stronger global mixing in the compressible flow case and that very intricate cell structures develop.

The study of Stokes flow within a spherical drop by Bajer and Moffatt (1990) was the first example of a bounded steady three-dimensional Stokes flow with chaotic streamlines. In this work they show the step-by-step process of a single trajectory as it goes through what they termed a "trans-adiabatic drift" where particles that remained on a fixed periodic orbit for certain parameters begin to behave chaotically as the parameters are varied. They explain the dynamics of particle trajectories as they pass through previously impenetrable surfaces by stating that "*particles migrate from one adiabatic surface to another*." This research paved the way for the subsequent works by Stone et al (1991), Neishtadt et al (1998) and Kroujiline and Stone (1999). These studies extend the work of Bajer and Maffet (1990), by developing a detailed view of the periodic islands regions within the drop that are surrounded by the chaotic regions. Using Poincaré maps they characterized these effects by changing the vorticity magnitude and found that changing the vorticity magnitude alone does not guarantee rapid mixing. Stone et al (1991) reported the first detailed analysis of the flow at the onset of chaos.

Ashwin and King (1997) observed the existence of regions of chaotic mixing from a numerical study of the Lagrangian properties of the steady flow pattern of the

non-axisymmetric Taylor-Couette flow between concentric cylinders using the model of Davey, DiPrima & Stuard (1968) near the onset of wavy vortex instability. The flow pattern is formed by rotating the inner cylinder while keeping the outer cylinder stationary, causing the flow to become unstable to motion in the axial direction. This gives rise to Taylor vortex flow at a critical value of the Taylor number, which eventually develops (as the Taylor number is increased further) secondary instabilities in the form of wavy vortex flow where a wave-like disturbance propagates around the Taylor vortices. Rotating both cylinders develops many other variations of non-axisymmetric flows such as spirals, ribbons, and twisted vortices. The rotational symmetry of the basic flow pattern is broken by non-axisymmetric perturbations to the flow field. In this work they consider the non-axisymmetric modes of the wavy vortices, spirals, ribbons, and twisted Taylor vortices. They observed that for all non-axisymmetric modes with the exception of spirals, there existed regions of chaotic mixing within the fluid. They also developed parameter values where the studied flow patterns were observed to be stable, providing a possible guide to particle behavior in this type of flow.

Ashwin and King's work with wavy vortex Taylor-Couette flow was extended by Rudman (1998) who analyzed mixing in the flow with respect to the axial diffusion coefficient which was based on axial particle dispersion. He found that the coefficient does not increase monotonically with Reynolds number, which differed from previous assumptions. Also an effective Schmidt number of the chaotic fluid motion was defined which suggests that chaotic advection of fluid elements is an order of magnitude more important for mixing in wavy vortex flow than molecular viscosity. Rudolph et al (1998), in their analysis of this flow observed chaotic particle paths in wavy Taylor-Couette flow based

on the Taylor number. They also found that for a range of Taylor numbers ($131 \leq Ta \leq 253$) chaotic mixing would exist and increase as the Taylor number increased. Later, Yannacopoulos et al. (1998) went on to both study eccentric Taylor vortex flow based on the DiPrama and Stuart (1975) model and wavy Taylor vortex flow. They differed from many other studies, which focused on the Lagrangian perspective, by proposing an Eulerian diagnostic to pinpoint where chaotic streamlines might occur. They reported good correlation between the diagnostic and the particle orbits.

A significant body of work in three-dimensional flows has also been carried out using confined swirling flows in cylindrical containers. Fountain et al (1998) researched, experimentally, the chaotic mixing in a cylindrical container with a rotating angled impeller. As the angle of the impeller is increased, the symmetry breaks and chaotic regions begin to develop around the tori that form in the completely axisymmetric case where the impeller angle is zero. They found that increasing the Reynolds number reduced the order of tori formed in the flow but did not guarantee better mixing. In the work by Stokes and Boger (2000), mixing of viscous polymer liquids in a torsionally driven cavity was investigated. They studied the instabilities that occur with increasing Reynolds number and the effects of the elasticity of the fluid and also found results suggesting that Reynolds number has an effect in enhancing chaotic advection for extremely small Reynolds numbers of order one of the viscoelastic fluids. Sotiropoulos and Ventikos (2001) provide numerical results for the flow within steady vortex breakdown bubbles that form in a cylindrical container with rotating bottom lid and a stationary cover. They state that the basic axisymmetric flow is subject to instabilities which result in asymmetries in the vortex breakdown bubbles and

subsequent chaotic particle paths. The origin of these asymmetries was found to be linked to the stationary cover Ekman layer and the sidewall Stewartson layer.

A large portion of the work dealing with experimentally realizable three-dimensional flows has focused on chaotic mixing in industrial mixing devices. Khakhar et al (1987) studied analytically the so-called partitioned-pipe mixer. This mixer consists of a pipe, which contains a sequence of flat plate blades placed in alternating, mutually perpendicular directions. As flow passes through the pipe, these plates give rise to a secondary flow which causes mixing to occur. Khakhar et al (1987) varied the parameter β, which designates the mixing strength and is the product of the characteristic resident time and the cross-sectional shear rate. They found that as they increased this parameter, the areas of the flow occupied by chaotic mixing also increase in size. Using stretching ratios, they were able to develop distinct mappings of the unmixed flow regions. Kusch and Ottino (1992), experimentally also researched the partitioned-pipe mixer along with the eccentric helical annular mixer. They were able to visualize the existence of KAM-tubes surrounded by regions of chaotically advected fluid. From these experiments, they discovered that Reynolds number effects are far outweighed by the effect of the mixing strength parameter and that the system could therefore be completely characterized by β.

Much of the more recent work in the area of static mixers is due to Hobbs & Muzzio who studied mixing in a straight, helical static mixer. In this mixer, similar to the aforementioned portioned pipe, mixer elements are arranged in an alternating fashion along a pipe length. However instead of flat plates, the mixer elements are instead twisted in a helical manner. Hobbs and Muzzio present a series of papers in which they investigate techniques to study mixing using dynamical systems tools. These tools include Poincarè

maps (Hobbs and Muzzio 1997, 1998), stretching and curvature of fluid elements (Hobb and Muzzio 1998) and determining manifolds of hyperbolic points. A large portion of their research is centered on creeping and low Re number flows. Other contributors to the understanding of chaotic advection in static mixers include Byrde and Sawley (1997), who computed Poincarè maps that indicated global chaos and unmixed islands dependent on the Reynolds numbers, as well as Jones (2000), who numerically studied the invariant areas of the flow in the helical static mixer with two and six elements finding that coherent bands of unmixed particles existed for long times in the pipe.

Hydon (1994) studied, numerically, chaotic advection in a curved pipe in which he uses Poincarè sections to show particle trajectories that lie on KAM tori within islands in the flow. He goes on to describe the incredibly intricate systems of KAM-tori, cantori and unmixed islands that exist within the flow. In addition he finds that trapping behind cantori is modeled as a Levy walk, which suggests distinct chaotic flow characteristics to the trapping and releasing of particles in that region. Jones et al (1989) as well as Jones and Young (1994) studied chaotic advection in a twisted pipe flow. This geometry would later be used as the basis for micromixers. In the first paper, they show chaotic particle paths and work to determine the parameters that control fluid stirring. Using Poincaré maps as well as stretching maps they describe the unmixed regions of the flow. In the latter study, they continue the investigation using concepts of shear dispersion and anomalous diffusion. They consider not just the type of mixing that can occur, but also examine the effect of varying the type of tracer. In that work they look at the statistics of the axial dispersion of both diffusive and non-diffusive tracers in the system. Interestingly, they found that chaotic advection actually reduces the value of the dispersion coefficient of diffusive tracers. The reason

stated behind this observation, is that chaotic trajectories permit particles to more rapidly sample the axial velocity profile.

Chaotic advection in micro-scale mixing has become important in MEMS (Micro-Electro-Mechanical Systems) research, where the objective is to perform within the micro-channels of a chip some of the jobs usually accomplished with ordinary lab-scale equipment—the so-called lab-on-a-chip concept. Because of the small length scales, Reynolds numbers are small and the flow remains laminar. Therefore chaotic advection becomes a key factor for mixing. The first biofluidics stirrer based on chaotic advection (Evans et al 1997) was modeled on the pulsed source-sink flow of Jones and Aref (1988). A static mixer in the form of a C-shaped helical micromixer was developed by Liu et al (2000) as an alternative to the Evans active mixer. This serpentine formation was based on the Jones et al (1989) numerical studies of chaotic advection through a twisted pipe. In the experimental investigation, they develop images of reacted phenolphthalein as well as water-alcohol interfaces at points along the mixer. For this channel they find that, even at such small length scales, chaotic advection increases the stirring of the flow.

The effect of chaotic advection in heat transfer was investigated by Acharya et al (1992) and Castelain et al (1993). In their research, Acharya et al (1992) use a helically coiled tube as a means of heat transport. They calculate the temperature field numerically and show that chaotic mixing is responsible for an increase in convective heat transfer. Using experiments conducted with water on two coiled tube geometries, they find a distinct increase in the heat transfer coefficient due to chaotic mixing. Castelain et al (1993) perform experiments on hydrodynamic and heat transfer behavior of the flow in a twisted curved channel, using heat exchanger coils. They remark that the flow generates high stretching

and folding of material surfaces. Ultimately they show a 15-18% higher efficiency for the chaotic heat exchanger compared with a helically coiled tube heat exchanger.

Another area of study within the industrial mixers is flow in stirring tanks. Recently Alvarez et al (2002a, 2002b) and Zalc et al (2001, 2002) investigated chaotic mixing in impeller driven flows and explored the use of chaotic advection to enhance mixing. In this series of papers, they conduct experiments in which they look at low Reynolds number mixing (Re = 10 to 200) in a stirring tank with one or three impellers. What they find is that for the basic concentric disk flow, unmixed toroidal regions primarily exist above and below each disks and mixing is poor. However when impeller blades are added chaotic mixing behavior is created by small periodic perturbations as the passing impeller blades fold material lines repeatedly within relatively short times.

Finally, let us consider previous works on chaotic advection in unsteady, three-dimensional flows. The amount of research in this area is small, primarily because the computational cost of studying such flows is extremely expensive. Currently the research has been limited to four types of flows. These flows include unsteady spherical Coutte flow, flows near a helical vortex filament, three-dimensional periodic cavity flows, and flows within spherical droplets.

Cartwright et al (1996) performed the first study we will address. In this work, they consider biaxial unsteady spherical Couette flow. Spherical Couette flow is steady flow at low Reynolds numbers between coaxially-rotating concentric spheres. A fully, three-dimensional flow is established simply by using two different axes of rotation for the spheres and then becomes time-dependent by rotating the spheres periodically. They found that Hamiltonian chaos is produced by long-period flow and that the amount of chaos

increases as the period increases. The also discovered the possibility of resonance induced chaos for small periods when the axes-of-rotation of the two spheres are aligned.

Mezić et al (1998) investigated the helical chaotic particle motion near a helical vortex filament. In this analytical look at a helical vortex filament which is placed in a three-dimensional time periodic strain rate field, they utilize KAM theory to show the existence of invariant two dimensional helical cylinders in the flow that act as barriers to the transport of fluid. However, they found that there are chaotic fluid regions that allow for the exchange of fluid between the inside and outside of these barriers as the size of the perturbation (strain) increases.

Anderson et al (1999) researched three-dimensional non-periodic cavity flows. Based on the work of Aref (1984) they start from the basis of two-dimensional cavity Stokes flow, which predicts integrable streamlines for the steady case and chaotic flow for the time-periodic case. As the cavity flow is made three-dimensional, they develop a method for determining periodic structures. They discovered that periodic lines are observed for the three-dimensional cavity flows and that the structure of the lines can be extremely complex in geometry.

Finally we consider the research concerning flow in droplets. These investigations extend the work performed by Bajer and Moffat (1990) into the unsteady regime. Angiella and Brancher (2003) focused on a spherical drop moving in a uniform flow and assumed that an inner circulation in the form of Hill's spherical vortex ("dipole" flow) occurs within the drop. They further assumed that the symmetry of axis of this vortex rotates periodically around a radial axis. This type of rotation could be obtained in a laboratory by making a droplet fall in a uniform flow displaying a time-periodic direction. They used Poincarè

sections to show mixing within the droplet, finding that mixing efficiency is dependent on the scale of the frequency of rotation.

War and Homsy (2001, 2003) performed both a numerical and experimental investigation of the effect of mixing within a drop using time-dependent electric fields. Considering a drop of dielectric liquid settling in a second dielectric liquid, they imposed a time-dependent spatially uniform electric field, resulting in a periodic displacement of an internal stagnation disk in the drop. They visualized the complex structures that result by calculating Poincarè maps. They also determined the rate of mixing by calculating the largest Lyapunov exponent. Charge relaxation was found to be the most important of possible finite frequency effects, developing an overall decrease in the estimated volume mixed. Similarly, Paik et al (2003) researched experimentally rapid droplet mixers for digital microfluidic systems. They studied the effects of varying droplet aspect ratios on linear-array droplet mixers, proposing several mixing strategies based on the number of electrodes. They found an optimal aspect ratio for two and four electrode linear-array mixing and calculated mixing times.

Schatz and Grigoriev controlled mixing in droplets by optically manipulating surface tension in the system. They conceived that the mixing properties of flows in the microdroplets are governed by their symmetries which give rise to invariant surfaces. Therefore they developed a time-dependent method of switching the direction of the thermal gradients in the flow that would ensure that all the invariants were destroyed. Using Poincarè maps and video images, they illustrated the rapid breaking of invariant flow regions due to this method.

CHAPTER 4

PARTICLE TRACKING

Accurate particle tracking is a critical prerequisite for the analysis of Lagrangian dynamics in chaotically advected flows. Every dynamical systems tool we employ to visualize and quantify stirring (see Chapter 2) requires a distinctly meticulous approach to particle tracking. This is because by definition chaotic trajectories are extremely sensitive to initial conditions. Therefore even very small numerical errors may have a profound effect on the computed trajectory of a chaotically advected particle. Interestingly enough, most current particle tracking methods used by many researchers today seem to be dependent primarily on software developed for visualization of CFD flows. In some instances these algorithms are indeed accurate and computationally expedient. It will be shown in this chapter, however, that it is extremely important to carefully consider specific aspects of each computational situation, such as the grid topology and density for example, to develop the best possible particle tracking algorithm.

Assuming that the advecting velocity field is known at the nodes of the computational grid—either analytically or has been obtained via numerical solution of the Navier-Stokes equations—particle trajectories can be calculated by solving numerically equations. (2.1). Any numerical algorithm for integrating the particle

trajectory equations consists of three modules: 1) the particle location scheme, 2) the interpolation scheme, and 3) the temporal integration scheme. The first module needs to be performed at all instants in time except the very first time step when the initial particle positions are known. It entails searching the computational grid cells to identify where the particle is located. Once we find the grid cell, we can use the known velocity components at each node in the cell to interpolate the velocity at the location of the particle. After both the particle position and its velocity have been obtained, we can integrate the particle forward in time. Each one of these three steps involves numerical operations, which, if not carefully implemented, could introduce significant errors.

In the following sections we describe the particle tracking algorithm used in this work and carry out a series of numerical experiments to demonstrate the accuracy and computational efficiency of this algorithm.

4.1 Particle Location Scheme

Three-dimensional particle tracking in fine computational meshes can be extremely expensive computationally. That being said, often the most time consuming culprit is the particle location scheme. When searching for a particle throughout a computational grid, the algorithm has to look in each individual cell and apply a set of criteria to find the cell in which the particle is located. Without an "intelligent" particle location scheme, for grids that contain millions of grid nodes, one could spend minutes looking for a *single* particle—most of the dynamical systems tools used in this work require calculations which require tens of thousands of particles. The worst case scenario

is that the scheme searches through each and every grid cell before finding the correct one. It could theoretically take hours to perform a single time step and for the purpose of our calculations hundreds of thousands of time steps are required. Therefore much work has gone into finding the most efficient and intelligent location scheme possible.

When considering Cartesian or polar-cylindrical meshes, the location process is a rather straight forward task. This method is described in section 4.1.1. However developing an efficient searching algorithm that always returns the correct particle location in a three-dimensional curvilinear mesh (with arbitrarily skewed cells) is considerably more complicated. The location schemes can be classified into two different categories: volumetric and spatial. The volumetric schemes consider a three-dimensional cell and break that cell into smaller volumes based on some type of vector criteria. Given these smaller volumes, there are various ways in which a particle can be determined to exist within that cell. The spatial schemes characterize where a particle is located in relation to a grid node based on its position components.

There have been attempts at using both of these methods. Spatial schemes have been utilized by Zhou and Leschziner (1999) who developed a 2D particle-to-the left algorithm. This Zhou and Leschziner method defines an arbitrary 2D convex polygon by given the Cartesian coordinates (x,y) of its n vertices ordered anticlockwise (figure 4.1a). To determine if the particle is within the cell, move along the cell faces anticlockwise and check if the particle lies to the *left* of all the cell faces (figure 4.1b). This condition can be checked by looking at the z-component of the cross product between the cell face vector and the particle vector. A positive value indicates the particle is to the left-hand-side of the cell face and a negative value indicates that the particle is to the right-hand-side of the

cell face. The advantage of this method is that it is easy to implement. However it has some deficiencies. Firstly, it is not a very intelligent scheme and so that one might end up doing redundant searches each iteration or searching in regions far away from the particle position. In addition, for some cases this method can lead to a circular search of the particle around the target cell, which would trap the simulation within an infinite loop. Also, and most importantly for our work, its extension to 3D grids is extremely complex and difficult to implement. In this case the cell face is no longer a line segment but a set of vertices which suggests that it be called the particle-towards-the-inside algorithm. And the same deficiencies that exist in the 2D case are multiplied here. This original method was evaluated by Chen and Pereira (1999) and improved into a more intelligent scheme, so that after the initial location of a particle is tested to remain in that cell until it exits a cell face and then a focused testing is done to see which cell the particle has entered. However the other deficiencies to both algorithms still existed. Recently (Chorda et al 2002) there have been attempts to further improve the algorithms' extension to 3D grids by looking at the trajectory of the particle as it exists a cell face.

Based on the literature, volumetric schemes appear to be a more popular method of cell searching techniques. Perhaps this is due to difficulties of the spatial searching algorithms in handling adequately the 3D flow cases. One of the more popularly utilized methods is the tetrahedral decomposition method by Kenwright and Lane (1996) in which they break a grid cell into tetrahedron. They state that the core problem in particle tracking methods is to find the natural coordinates (i.e. the local non-dimensional coordinates for a cell: ξ_c,η_c,ζ_c) based on its given physical coordinates. Using the tetrahedral elements, the natural coordinates of the cell can be evaluated directly from the

physical coordinates or vice versa (see figure 4.2a). And once these natural coordinates are located, it is possible to determine if a particle is located within a tetrahedron by applying specified criteria. This method was considered for our work but found ultimately to be too expensive computationally. Each tetrahedron must be tested within the cell, during the search. Also, because there are possible gaps that can exist between the tetrahedron that form the cell, particles may be lost. This problem has been addressed by Kenwright and Lane (1996) in which they develop an alternating subdivision technique. They show that there are two ways of dividing the cell into tetrahedron and by alternating both ways, it is possible not to leave gaps in between the tetrahedral cells (figure 4.2b).

In what follows, we describe the two search techniques used in our research. The first is applicable to cylindrical-polar or Cartesian meshes and is a simple 1D directed search technique. The second technique is volumetric algorithm suitable for curvilinear meshes with skewed grid cells.

4.1.1 Method 1: 3-1D search technique

The first spatial search technique we discuss is applicable to polar grids (though it can be transformed quite easily to normal Cartesian grids). This method consists simply of three 1D searches. Given the r, y, and θ components of an initial particle position P, the particle is located by searching within each direction in succession. A sweep is performed between the boundaries of $r_{i=1}$ to $r_{i=imax}$, $y_{j=1}$ to $y_{j=jmax}$, and $\theta_{k=1}$ to $\theta_{k=kmax}$. To make this procedure even more efficient particle positions of the n^{th} iteration

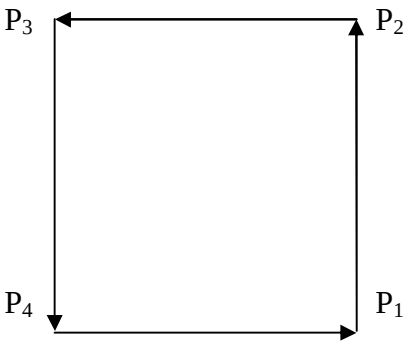

a)

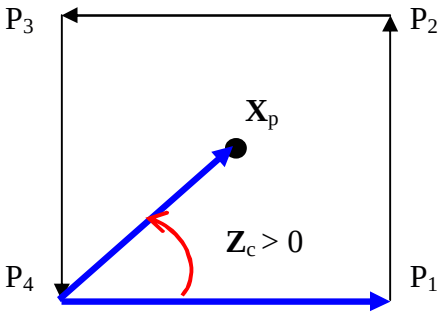

b)

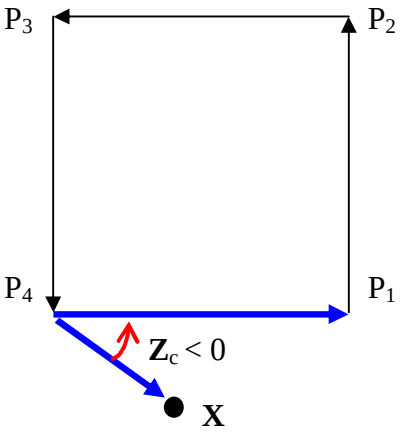

c)

Figure 4.1 Two-dimensional particle-to-the left scheme: (a) grid cell (b) particle in the cell (c) particle outside of the cell.

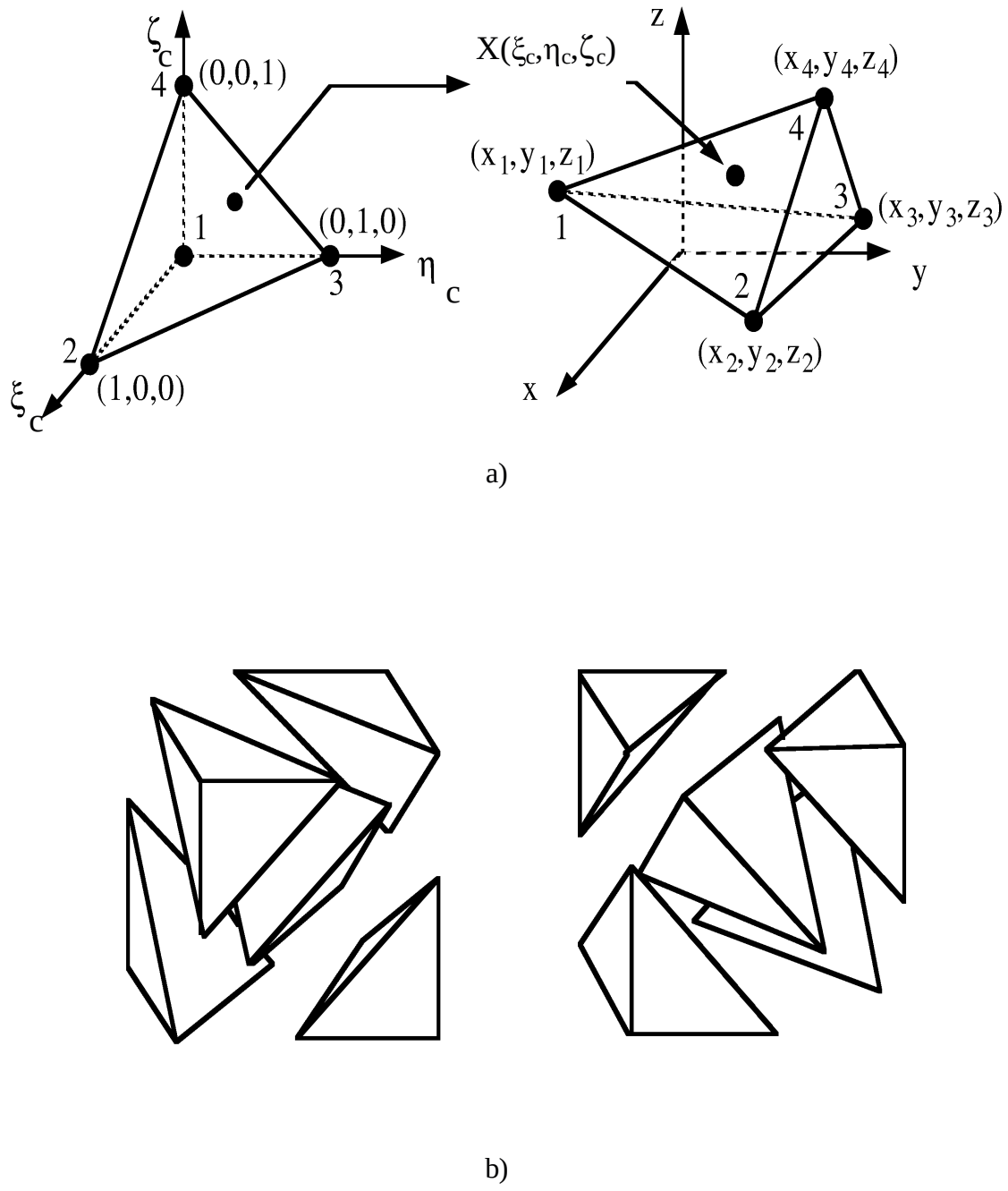

Figure 4.2 Tetrahedral particle location technique (Kenwright and Lane 1996): a) natural coordinate transformation b) tetrahedral cell subdivision.

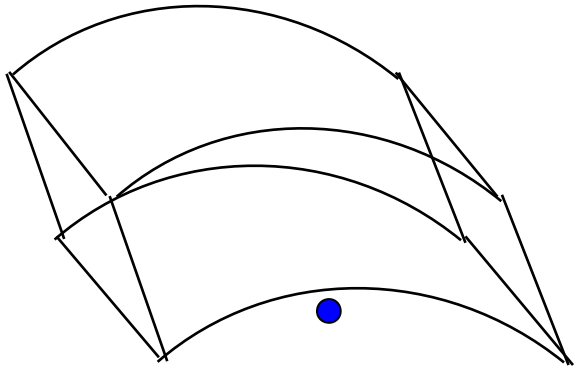

Figure 4.3 Particle existing outside of a skewed cell that location schemes may find inside cell.

are stored for the n+1 iteration so that the searching region is confined to the grid cells surrounding the particle position from the n^{th} iteration. Because each grid point is also defined by its radial, axial, and azimuthal position, this straightforward method is extremely fast and extremely accurate.

Besides the computational efficiency of using this technique, it may also be more accurate than techniques developed for skewed grid cells. This is because those calculations simplify the cell geometry (i.e. approximate curved cell boundaries with straight lines, see figure 4.3). Therefore it is possible that mathematically, particles may be lost or that particles which remain very close to curved walls may be found in

neighboring cells. However, with this straightforward method, particles are guaranteed to be located within the computational domain in their correct grid cell.

4.1.2 Method 2: Triple Product Technique

The next spatial searching technique employs a triple-scalar-product method (see Murman and Powell (1989) for the two-dimensional analogue of this procedure). We consider each grid cell to form a parallelepiped—the best case scenario is of course that the cell to be a cube, which would occur for equally spaced, non-skewed meshes. For every grid cell, there are six pairs of vectors ($\vec{a}_j$ and $\vec{b}_j$, j=1,6) defined by the diagonals of every one of the six faces comprising the quadrilateral cell. For every cell face, that is for every vector pair ($\vec{a}_j, \vec{b}_j$), we construct a third vector $\vec{c}_j$ defined by the particle location and the center-point of the cell face (i.e. the intersection of $\vec{a}_j$ and $\vec{b}_j$). In figure 4.4a we see that each vector trio forms in the best case (where a particle is located exactly in the middle of the cell) a pyramid-like structure. The volume of this pyramid can be obtained by:

$$V_{pyramid} = 1/3 \times A_{base} \times h_{perpendicular} \tag{4.2}$$

For a general cell, the base will be a parallelogram whose area is defined by the vector pair ($\vec{a}_j, \vec{b}_j$). The height can be acquired using the third vector $\vec{c}_j$. The volume of the pyramidal shape obtained will then be some constant multiplied by the triple scalar

product. This can be seen through a basic geometry concept, which defines the volume of a parallelepiped to be:

$$V = \vec{c}_j \cdot (\vec{a}_j \times \vec{b}_j) . \tag{4.3}$$

Using this idea, we can reasonably assume that the volume of the skewed pyramidal shapes is 1/6 the volume required to create a parallelepiped (see figure 4.4).

Now we can develop a criterion for particles existing in a particular cell. As we attempt to locate the particle in a cell, we create the six volumes based on each cell face. Then we define four grid points which make up the corners of the cell face as G_1 to G_4 (see figure 4.4c). Each grid point has an x_n,y_n, and z_n (where n=1,4) coordinate associated with it. The fifth point needed to complete the volume is the particle position P, and has coordinates (x_p,y_p,z_p). Therefore vector coordinates needed to obtain each of the six pyramidal volumes that make up a grid cell are:

$$\begin{aligned} a_{\vec{x}} &= \vec{x}_2 - \vec{x}_1 \\ b_{\vec{x}} &= \vec{x}_4 - \vec{x}_3 \\ c_{\vec{x}} &= \vec{x}_p - .25(\vec{x}_1 + \vec{x}_2 + \vec{x}_3 + \vec{x}_4) \end{aligned} \tag{4.4}$$

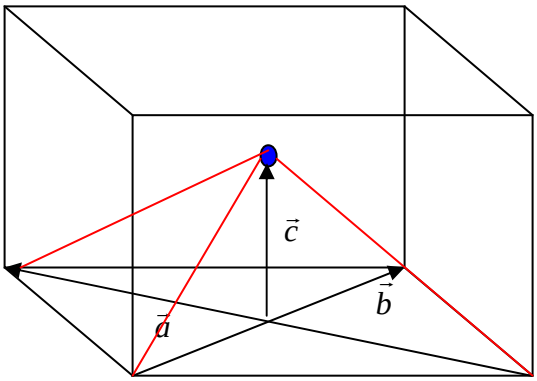

a)

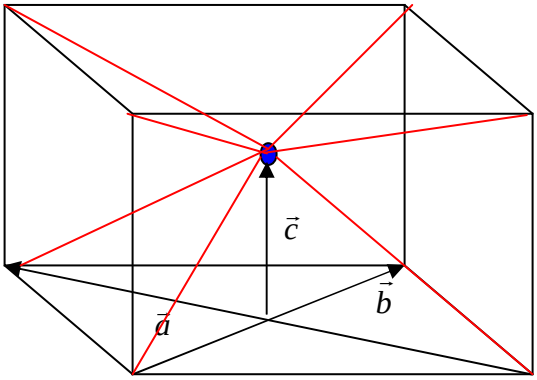

b)

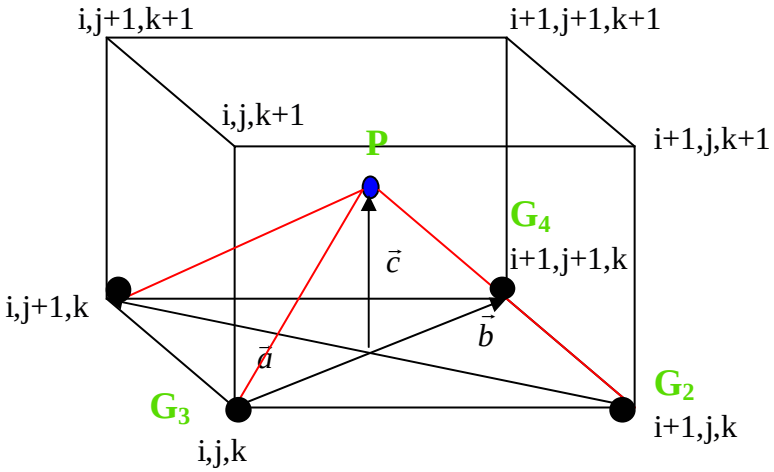

c)

Figure 4.4 Triple Product Technique for particle location

And the volume itself is calculated as:

$$V = a_x b_y c_z + b_x c_y a_z + c_x a_y b_z - c_x b_y a_z - b_x a_y c_z - a_x c_y b_z \quad (4.5)$$

From this we can say that if a particle exists in the cell each of the volumes for the six different cell faces obtained using the above definition will remain positive (V>0 for all j). If a particle is outside the cell, at least one of the volumes will be negative.

This technique has been tested on a variety of complex, three-dimensional geometries and has been found to consistently identify the correct cell. The benefits of the technique are that it is one of the best methods for skewed geometries. However the negative aspect of this method is that the location procedure may take a large amount of computational time. To enhance the efficiency of our particle location technique we once again employ localized searching based on previously found cell memory. For every iteration, we begin our search in the region where the particle was located in the previous iteration. This cuts down the computational time required to locate a particle radically.

4.2 Interpolation

After identifying the particle location we need to calculate its velocity by interpolation. Many interpolation techniques were considered in this work. Relatively straightforward procedures, based on simple averaging or weighted averaging such as the inverse distance method, were found inadequate as they consistently failed to resolve trajectories near critical points in the flow such as periodic (invariant) flow regions and

complex regions near saddle points. Another critical area is near grid boundaries, where poor interpolation of cell velocities may cause a large percentage of particles to "escape" from a contained flow. Similar inadequacies were found when using three consecutive linear interpolation steps, where linear interpolation takes place sequentially between the three pairs of opposite cell faces that comprise a computational cell. Finally, a tri-linear interpolation scheme was used because of its ability to resolve the complex structure of the velocity field. In this scheme the interpolated quantity is assumed to vary tri-linearly, as follows

$$u_j = (ax + b)(cy + d)(ez + f) \tag{4.6}$$

where u_j represents one of the eight nodal points of the cell. After some algebra:

$$u_j = A_1 xyz + A_2 xy + A_3 xz + yzA_4 + xA_5 + yA_6 + zA_7 + A_8 \tag{4.7}$$

The coefficients A_i are computed by solving an 8x8 linear system of equations that is formed when each of the nodal points of the cell is used to cast a similar equation.

$$\begin{bmatrix} x_1y_1z_1 & x_1y_1 & x_1z_1 & y_1z_1 & x_1 & y_1 & z_1 & 1 \\ x_2y_2z_2 & x_2y_2 & x_2z_2 & y_2z_2 & x_2 & y_2 & z_2 & 1 \\ x_3y_3z_3 & x_3y_3 & x_3z_3 & y_3z_3 & x_3 & y_3 & z_3 & 1 \\ x_4y_4z_4 & x_4y_4 & x_4z_4 & y_4z_4 & x_4 & y_4 & z_4 & 1 \\ x_5y_5z_5 & x_5y_5 & x_5z_5 & y_5z_5 & x_5 & y_5 & z_5 & 1 \\ x_6y_6z_6 & x_6y_6 & x_6z_6 & y_6z_6 & x_6 & y_6 & z_6 & 1 \\ x_7y_7z_7 & x_7y_7 & x_7z_7 & y_7z_7 & x_7 & y_7 & z_7 & 1 \\ x_8y_8z_8 & x_8y_8 & x_8z_8 & y_8z_8 & x_8 & y_8 & z_8 & 1 \end{bmatrix} \begin{bmatrix} A_1 \\ A_2 \\ A_3 \\ A_4 \\ A_5 \\ A_6 \\ A_7 \\ A_8 \end{bmatrix} = \begin{bmatrix} \vec{u}_1 \\ \vec{u}_2 \\ \vec{u}_3 \\ \vec{u}_4 \\ \vec{u}_5 \\ \vec{u}_6 \\ \vec{u}_7 \\ \vec{u}_8 \end{bmatrix} \tag{4.8}$$

A fast LU decomposition algorithm is used to invert this system. The benefits of using this method as opposed to other techniques such as Gaussian elimination is that the decomposition need only be computed once and then each velocity component can be solved based on that decomposition as opposed to having to solve the entire system once for each component.

For polar grid calculations this system must be solved in polar coordinates for better accuracy. This is because, due to symmetries that exist in the polar grid, the system of equations becomes ill conditioned and difficult to invert. Such an example is shown in figure 4.5. The shaded grid cell is bisected by a line at the 45 degree angle. Therefore at the grid nodes the (x,z) coordinates switch. That is, if one grid node is at position (x=4, z=5), then there will be a corresponding grid node at (x=5, y=z). Therefore, in the linear system (Eqn 4.8) two of the lines in the matrix will be the same. This makes the system ill-conditioned and impossible to invert to numerically. Similar symmetries exist at the 135, 225, 315 degree positions. In the case of grid cell faces bisected by the 135 and 315 angles, the nodes not only switch coordinates but also signs. However due to the nature of the equations this too results in the same problems. To remedy this situation, we assume that the quantity to be interpolated varies tri-linearly in polar-cylindrical coordinates. That is, by replacing x, y, z with the transformed coordinates r, y, θ, in Eqn 4.7, the symmetry problems are eliminated.

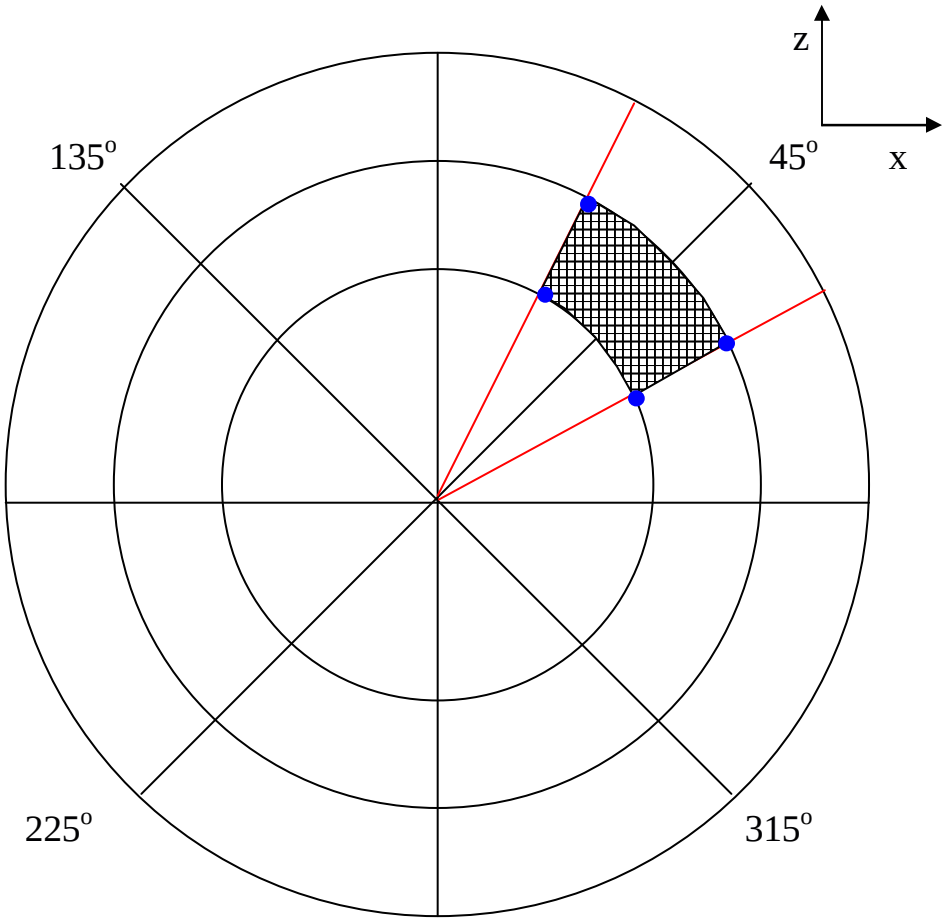

Figure 4.5 Example of bisecting symmetry for grid cell at 45 degree angle.

The interpolation algorithm is tested for accuracy using a simple analytical solution: solid body rotation of fluid in a closed cylindrical container rotating at constant angular velocity about its axis. Since the exact values for the velocity components are known analytically at each point in space, the accuracy of the interpolation method can be readily quantified as a percent error of the exact solution and monitored in time as the trajectory is calculated:

$$\%Error = \left| \frac{x_{calc} - \mathbf{x}_{exact}}{\mathbf{x}_{exact}} \right| * 100 \tag{4.9}$$

For all interpolation schemes tested, the integration of the particle path equations has been carried out using 4th order Runge-Kutta and a time step of 0.001.

Because the greatest possible error will exist where the grid is coarsest, i.e. near the walls, we look at a trajectory in that vicinity to evaluate the error. The results are presented in figure 4.6. Here we plot percent error with time as a particle initially placed close to the wall is advected through the flowfield using two different interpolation techniques. The first is a frequently suggested tri-linear method (hence forth called Method 1) but is developed by simply weighting the velocity at the particle position in a straight forward manner by the distance from the grid nodes (Yeung and Pope 1988):

$$\begin{aligned} u_{xyz} &= u_{000}(1-x)(1-y)(1-z) + u_{100}x(1-y)(1-z) \\ &+ u_{010}(1-x)y(1-z) + u_{001}(1-x)(1-y)z \\ &+ u_{101}x(1-y)z + u_{011}(1-x)yz + u_{110}xy(1-z) + u_{111}xyz \end{aligned} \tag{4.10}$$

The velocity u_{xyz} is the calculated velocity component at the (x,y,z) point in space located within the cell whose nodes are marked as shown in figure 4.7. The second interpolation scheme is the aforementioned more complex tri-linear method (eqn 4.7) implemented in cylindrical-polar coordinates (designated Method 2).

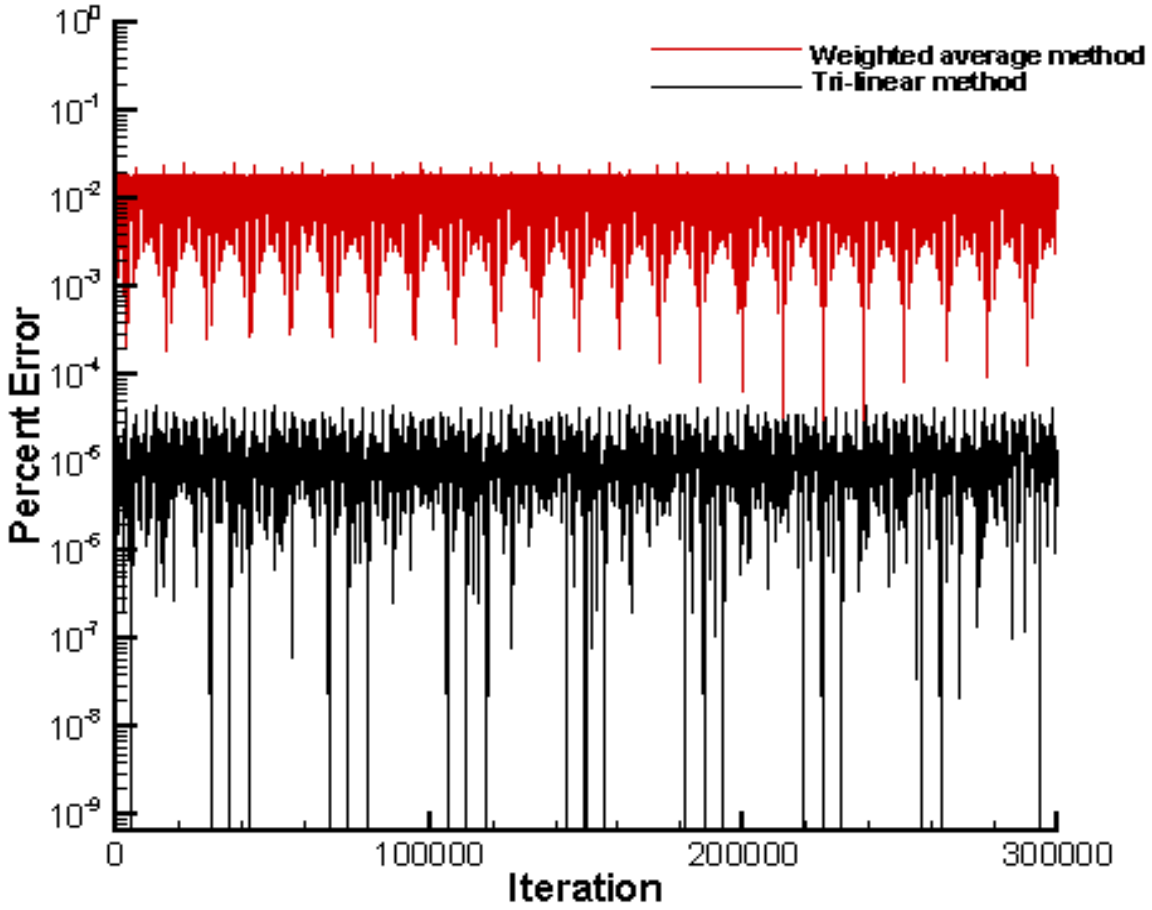

Figure 4.6 Percent error of a trajectory which covers an orbit for solid body rotation case for two different interpolation methods.

As seen in Fig. 4.6, there is an almost periodic trend in the error as the trajectory continues to cover the same circular orbit. However it is evident that there is a great difference in Method 1 and Method 2. The error obtained from using Method 1 is three orders of magnitude higher than that of Method 2. This is perhaps because Method 1 does not take into account adequately the curved structure of the grid. For many cases of particle tracking, it is possible that this method would be within acceptable criteria. When looking at the particle trajectories with the naked eye, they appear to be the same. However, for chaotic particle tracking this method may lead to unacceptably high numerical errors. The tri-linear method is, thus, selected as the interpolation scheme in our work as it consistently yields errors less than 10^{-5} percent.

It should be mentioned that a higher accuracy and much more expensive computationally scheme based on tri-cubic interpolation was also tested. In this case, three mesh cells in each spatial direction are involved in the approximation, which leads to a 4^3-term equation and requires the inversion of a 64x64 linear system. Provided that all other numerical parameters are kept the same, tri-linear and tri-cubic interpolation were found to yield practically identical trajectories.

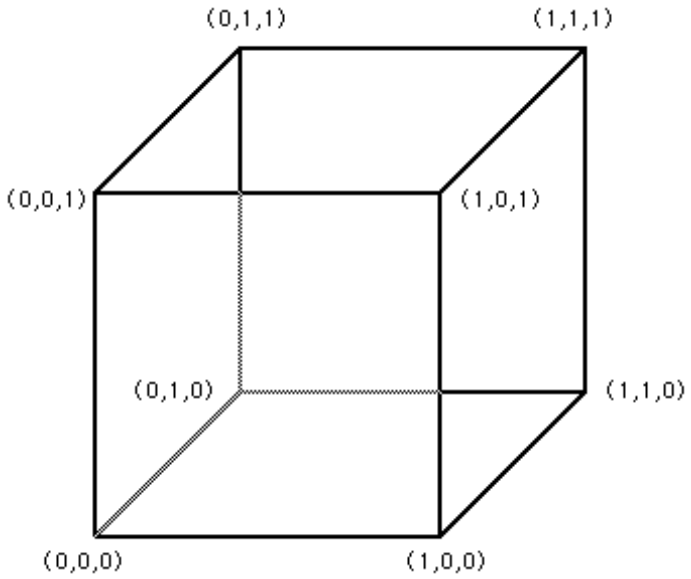

Figure 4.7 Cubic computational cell for method given by equation 4.10

4.3 Temporal Integration

Because many of the dynamical systems tools, such as Poincaré maps and Lagrangian time average maps, require long integration times, temporal accuracy is extremely important. After many time steps, even small numerical errors can lead to very large errors in a chaotically advected flow. In our analysis several integration methods were considered: 1st-order Euler, 2nd-order Predictor-Corrector, 3rd-order Runge-Kutta, and 4th-order Runge-Kutta. These schemes are summarized below as follows.

1^{st}-order Euler (E1)

$$\vec{x}_{i+1}^{k} = \vec{x}_{i}^{k} + \Delta t\vec{u}(\vec{x}_{i}^{k}) \tag{4.11}$$

2nd-order Predictor-Corrector (PC)

$$\vec{x}_{pred}^{k} = \vec{x}_{i}^{k} + \Delta t\left[\frac{3}{2}\vec{f}_1 - \frac{1}{2}\vec{f}_0\right] \tag{4.12}$$

$$\vec{x}_{i+1}^{k} = \vec{x}_{i}^{k} + \frac{1}{2}\Delta t[\vec{f}_1 + \vec{u}(\vec{x}_{pred}^{k})]$$

3nd-order Runge-Kutta (RK2)

$$\vec{r}_1 = \vec{u}\left(\vec{x}_{i}^{k}\right) \tag{4.13}$$

$$\vec{r}_2 = \vec{u}\left(\vec{x}_{i}^{k} + \frac{1}{2}\Delta t\vec{r}_1\right)$$

$$\vec{r}_3 = \vec{u}\left(\vec{x}_{i}^{k} - \Delta t\vec{r}_1 + 2\Delta t\vec{r}_2\right)$$

$$\vec{x}_{i+1}^{k} = \vec{x}_{i}^{k} + \frac{1}{6}\Delta t[\vec{r}_1 + 4\vec{r}_2 + \vec{r}_3]$$

4th-order Runge-Kutta (RK4)

$$\vec{r}_1 = \vec{u}\left(\vec{x}_{i}^{k}\right) \tag{4.14}$$

$$\vec{r}_2 = \vec{u}\left(\vec{x}_{i}^{k} + \frac{1}{2}\Delta t\vec{r}_1\right)$$

$$\vec{r}_3 = \vec{u}\left(\vec{x}_{i}^{k} + \frac{1}{2}\Delta t\vec{r}_2\right)$$

$$\vec{r}_4 = \vec{u}\left(\vec{x}_i^k + \Delta t \vec{r}_3\right)$$

$$\vec{x}_{i+1}^k = \vec{x}_i^k + \frac{1}{6}\Delta t\left[\vec{r}_1 + 2\vec{r}_2 + 2\vec{r}_3 + \vec{r}_4\right]$$

where k indicates the k^{th} particle and the subscripts i and i+1 denote the particle location at the previous and current time instants, respectively. In the predictor-corrector algorithm $\boldsymbol{f}_o$ and $\boldsymbol{f}_1$ are initial estimates of the velocity vector computed using an Euler-type initializer.

We evaluate the performance of the four particle integration schemes by applying them to calculate a typical, solid body rotation particle trajectory discussed in the previous section. We calculate an "exact" solution numerically by employing the RK4 scheme with a very small time increment ($\Delta t = 10^{-5}$). The computed and "exact" particle positions are then compared by defining an average global error (see Darmofal and Haimes 1996) after N time steps, as follows:

$$\varepsilon_N = \frac{1}{N}\sum_{t=1}^{N}\left|\vec{x}(t^l) - \vec{x}_e(t^l)\right| \tag{4.15}$$

where $\mathbf{x}$ and $\mathbf{x}_e$ are the computed and "exact" position vectors, respectively, $t^l = l\Delta t$, and Δt is the time increment. Figure 4.8 shows the results of the log of the global error of each scheme plotted with respect to the negative log of the time step. This graph indicates both the relative size of the error as well as the order of the scheme. The 1^{st} order Euler scheme yields very large errors for even the smallest time increment. The remaining schemes all show drastic improvement as the time step decreases, although the 4^{th} order

Runge-Kutta is as expected more accurate. As we would expect the slope of the 2nd order Predictor Corrector and 3rd order Runge-Kutta are 2.002 and 2.99 respectively. The fourth order Runge-Kutta has an initial slope of four for small time increments but its rate of convergence diminishes somewhat as the time step is reduced. Its overall rate of convergence, however, is considerably greater than third.

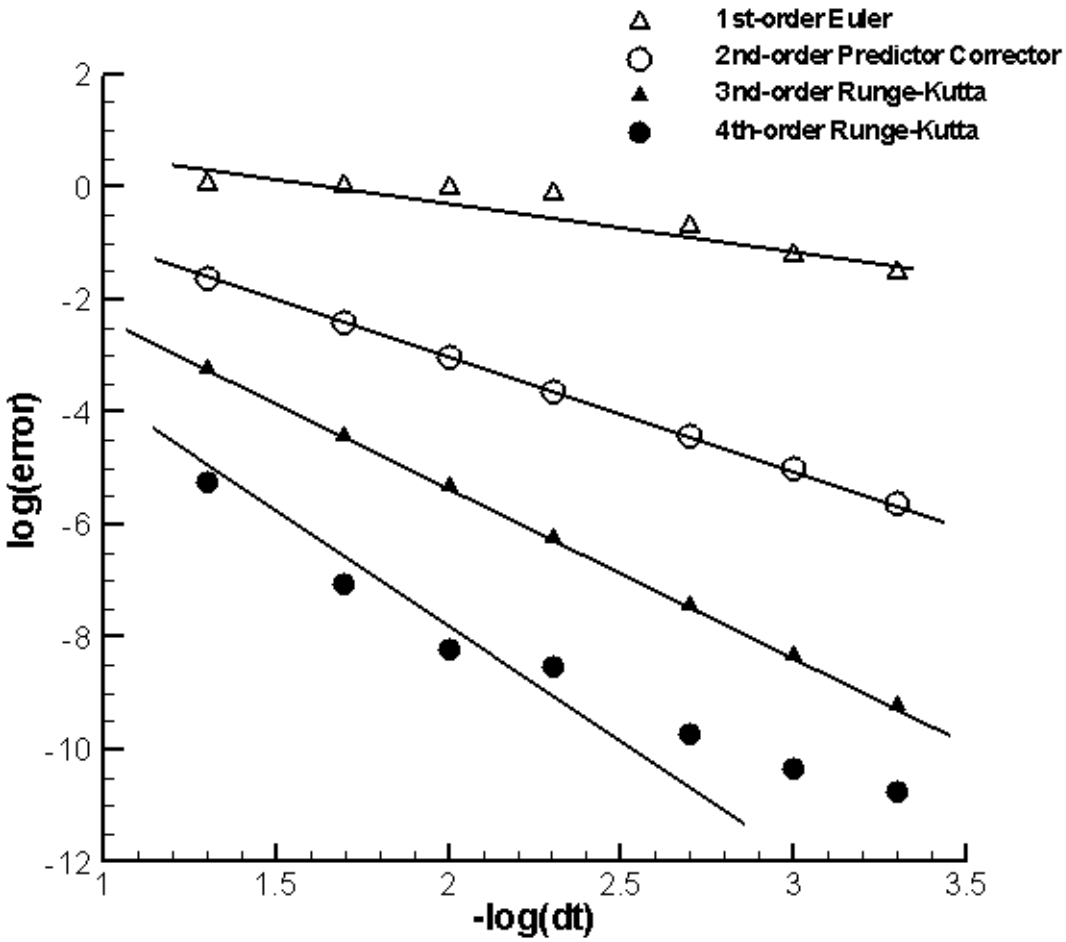

Figure 4.8 Log of global error of each scheme plotted with respect to the negative log of the time step.

4.4 Accuracy Test: Poincaré Map

The accuracy of the numerical scheme can have a significant impact when we calculate Poincaré maps. As mentioned in Chapter 2, Poincaré maps are obtained by calculating a trajectory through the computational space and indicating when it crosses a selected plane within that space. Typically, large integration times are required to illuminate the dynamics of the system and, thus, numerical errors if large could yield even quantitatively different dynamics. Figure 4.9 shows calculated Poincaré maps of a system given by the equations for the analytical model of an axisymmetric vortex breakdown bubble (Wiggins 1990) which will be extensively discussed in a subsequent chapter:

$$\frac{dx}{dt} = 0.04 - r^2 - x^2$$

$$\frac{dr}{dt} = rx \qquad (4.16)$$

$$\frac{d\theta}{dt} = \varpi$$

Since the flow is axisymmetric and steady, the resulting map should consist of a series of pairs of side by side embedded rings which represent the intersection of the toroidal stream-surfaces with the plane of the Poincaré map. The first map (shown in Fig. 4.7a) was created using the 1st-order Euler scheme, 4.9b uses the 2nd-order Predictor-Corrector scheme, 4.7c uses the 3rd-order Runge-Kutta, and 4.9d shows the map obtained using the 4th-order Runge-Kutta algorithm. All maps show the results after 550,000 iterations with

a time step of 0.001. Although the basic form of the Poincaré map remains the same in all cases, the errors in the calculations of the Euler and Predictor-Corrector methods are quite visible in the scattering and broken rings of figure 4.9a and b. In fact the errors in the Euler scheme are so large that regions of numerically-induced chaotic motion appear in the map and one of the particles actually exits the system. As discussed before, however, this is not possible since the advecting velocity field is steady and axisymmetric. This effect of numerically-induced chaos is seen to a somewhat lesser degree in the 2^{nd}-order Predictor-Corrector scheme by the scattering around the outer edges of the map. In stark contrast, the 3^{rd} and 4^{th} order Runge-Kutta algorithms yield maps consistent with a system with integrable dynamics where orbits remain confined on their initial toroidal stream-surfaces for the entire simulated interval. In our work we chose the 4^{th}-order Runge-Kutta to insure the accuracy of our particle tracking algorithm.

In addition it should be noted that similar tests were performed varying the interpolation technique. However it was found that using this system no real difference was perceived between the resulting Poincarè maps. This is most likely due to the fact that the amount of error for all interpolating methods was reasonably low (less than .01 percent). However, as seen in Figure 4.6, the method used in this work is more accurate, and was therefore chosen for calculating particle trajectories in the subsequent complex systems described in this thesis.

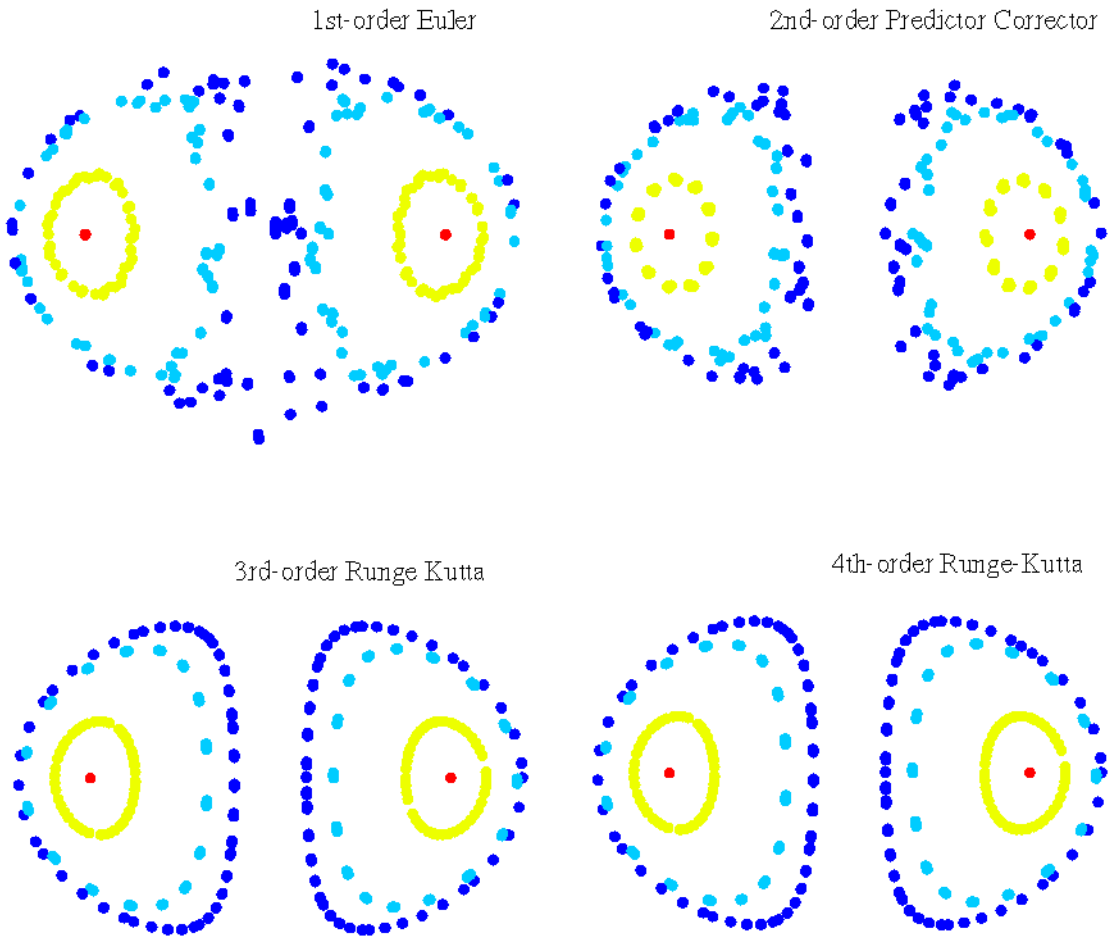

Figure 4.9 Comparison of Poincarè maps calculated with different integration schemes.

CHAPTER 5

CONTAINER WITH ROTATING BOTTOM LID: FLOW WITHIN A VORTEX BREAKDOWN BUBBLE

In the early 1900's Theodore von Karman began what has become a century of exploration in which researchers have sought to describe and understand the multi-faceted aspects of a class of flows bounded by rotating disks. The confined flow of an incompressible fluid in a cylindrical container with rotating bottom lid is perhaps the most widely studied and least understood von Karman flow. Although this flow has been investigated both experimentally and computationally for well over three decades, it is only recently that in depth insights into its extremely rich Eulerian and Lagrangian dynamics have begun to emerge. The first experimental investigations of this flow were reported by Vogel (1968) and Ronnenberg (1977) who explained that Ekman suction and pumping, induced by the Ekman layers on the rotating and stationary disks, drive a meridional flow and lead to the formation of a concentrated vortex core along the axis. Depending on the container aspect ratio (height to radius ratio) and Reynolds number, this vortex core could undergo vortex breakdown, evolving into one or more recirculating bubbles along the centerline axis. Because vortex breakdown occurs, in this case, within a contained, well-defined system, the flow within a cylindrical container with rotating bottom lid has become an important test case to understand various aspects of this

complex fluid mechanics phenomenon, which also occurs, among others, in flows over a delta wing, in swirling combustion chambers, and in some geophysical flows.

In this chapter, we seek to investigate numerically a number of important questions regarding the Lagrangian properties of steady vortex breakdown bubbles using some of the dynamical systems tools and concepts presented in Chapter 2. To accomplish this goal, the problem is approached systematically. First the flow geometry is described and a brief review of previous work regarding this flow is presented. After which, the basic topology of vortex breakdown bubbles is outlined and the potential effect of even very small stationary, three-dimensional perturbations on the Lagrangian dynamics are discussed using dynamical systems theory. Subsequently we analyze the Lagrangian properties of numerically generated flowfields using dynamical systems tools to show that the rich dynamics predicted by the theory indeed occur in the real flow and to reconcile various contradictory views that have been expressed in the literature concerning the axisymmetric character of steady vortex breakdown bubbles. Results are presented for Reynolds numbers ranging from 1492 to 1900 and aspect ratios of 1.75 and 2.0.

5.1 Flow Geometry

We consider flow in a closed cylinder of radius R and height H, which is filled with incompressible fluid of viscosity ν and density ρ. The bottom lid of the cylindrical container rotates with constant angular velocity Ω and the top lid is stationary. The flow is governed by two non-dimensional parameters, the Reynolds number ($Re=\Omega R^2/\nu$) and

the aspect ratio (H/R). Similarly to the unconfined rotating disc flow analyzed by von Karman (1921), the rotation of the bottom lid behaves as an Ekman pump, drawing in fluid vertically downward toward the rotating lid and driving it radially outward in along spiral trajectories. The fluid spirals upward along the sidewall, converges radially inward when it reaches the top lid and is injected vertically downward along the axis to close the loop. The radially inward spiraling motion along the stationary lid results in an initial increase in swirl velocity, due to the conservation of angular momentum, and creates a concentrated vortex core along the container axis with downward (from the stationary to the rotating lid) axial flow. Over a range of governing parameters the ideal (unperturbed) flow is steady and axisymmetric and the flow domain is foliated by a series of embedded invariant toroidal surfaces, the stream-surfaces of the axisymmetric flow—(see figure 5.1)

Vogel (1968, 1975) was the first to discover that depending on Re and H/R the vortex core along the centerline axis undergoes vortex breakdown (see figure 5.2). The streamline topology of vortex breakdown bubbles consists of an upstream stagnation point followed by a closed recirculation zone followed by another stagnation point. Under ideal conditions, a steady vortex breakdown bubble should be axisymmetric. As we will subsequently show, however, this ideal flow structure may be extremely difficult to realize in the laboratory as even small experimental imperfections could have a profound effect on the Lagrangian dynamics of the flow in the interior of vortex breakdown bubbles.

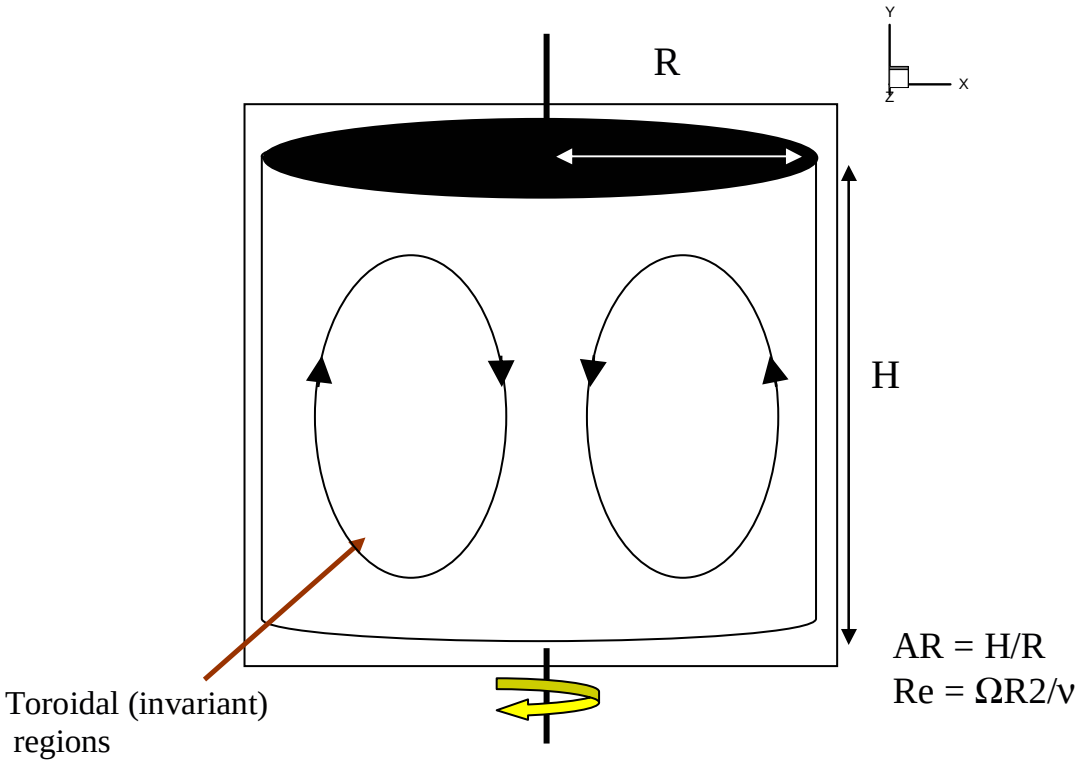

Figure 5.1 Flow geometry for cylindrical container with rotating bottom lid.

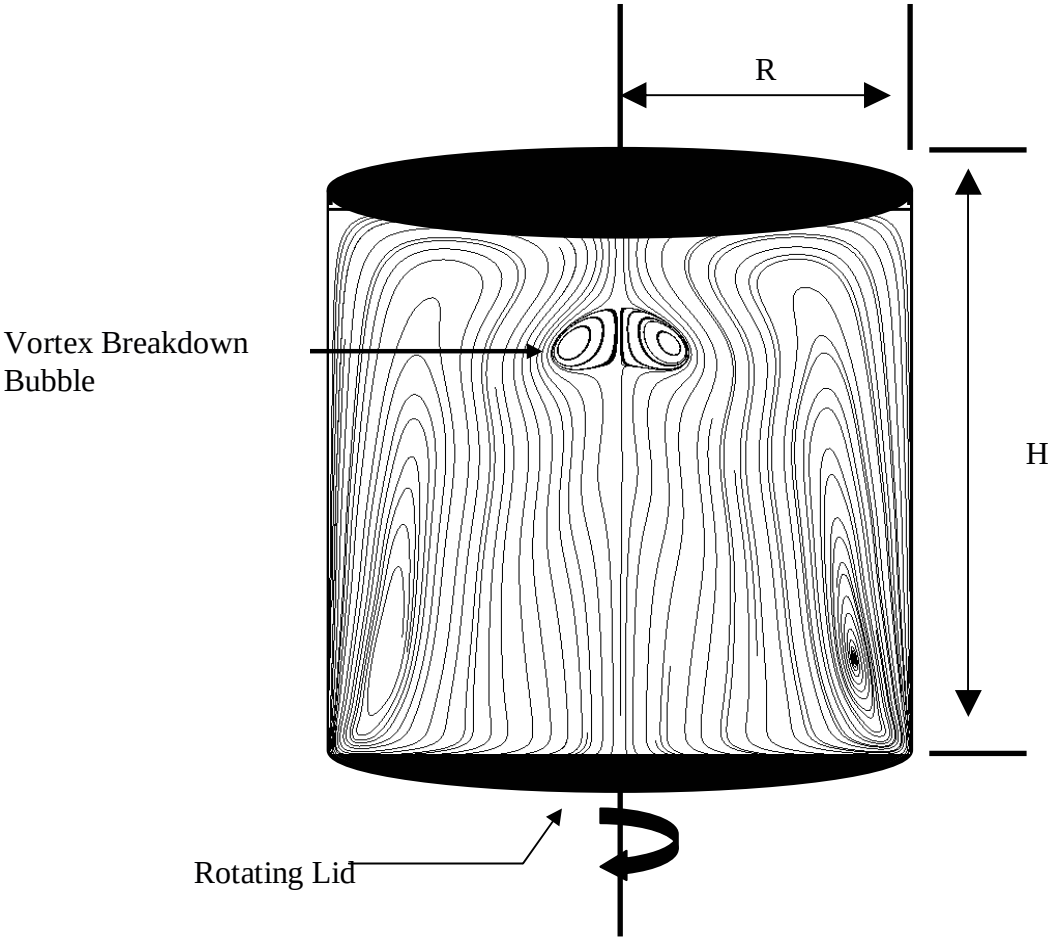

Figure 5.2 Surface streamlines for the vortex breakdown for Re=1850, AR=1.75

5.2 Previous Research

Although the problem has been considered for almost forty years, the first comprehensive flow visualization experiments for the flow within a cylindrical container with rotating bottom lid were performed only twenty years ago by Escudier (1984, 1988). In this extensive study Escudier considers the effect of both aspect ratio and Reynolds number on vortex breakdown bubbles. He develops the thresholds at which different numbers of vortex breakdown bubbles might occur and whether or not they will be in the steady or unsteady regime (see figure 5.3). Later Sorenson (1992) repeated the same experiments over a larger range of rotational speeds. Spohn, Mory, and Hopfinger (1993) considered the case of vortex breakdown bubbles in containers with free surfaces and later go on to (1997) address the confined cylinder case. Recently Liu et al (2000, 2001) performed a series of experiments using LDA (Laser Doppler Anemometer) to obtain quantitative measurements for this flow.

In many of these experiments it was observed that even within the steady flow regime, where the flow was expected to be axisymmetric, there were distinct asymmetries that seemed to persist in all visualization experiments (Escudier 1984; Spohn et al 1993; Hourigan et al 1995; Stevens et al. 1999; Fujimura, Koyama and Kyun 1997). In the Escudier experiment, for instance, dye is clearly seen to have entered into the interior of the vortex breakdown bubbles, which if they were axisymmetric would have been invariant and, thus, inaccessible by the surrounding flow. Another distinct feature that is present in Escudier's and all other visualization experiments is the existence of distinct asymmetric folds at the downstream end of the bubbles. Hourigan et al (1995) attempted

to explain these asymmetries by arguing that they are artifacts of the visualization technique and should be attributed to the inability to inject the dye precisely on the container axis. Supporting the idea of axisymmetric flow were a multitude of numerical investigations over the years, which solved the axisymmetric Navier-Stokes equations (Pao 1970; Lugt and Haussling 1997, 1982; Dijkstra and Heijst 1983; Lugt and Abboud 1987; Lopez 1990; Gelfgat et al 1996; Stevens et al 1999, etc). In these computations, the general flow characteristics (the size, position, and basic shape) of the vortex breakdown bubbles were accurately captured. In addition, these studies were also able to reproduce the variations of the general flow patterns with respect to the Reynolds number and aspect ratio. An example of one such calculation can be seen in figure 5.4 taken from Lopez (1990), which compares an experimental visualization image of vortex breakdown bubbles with the streamlines obtained from their axisymmetric flow computations. The computations capture correctly the shape, size and location of the bubbles but, as one would anticipate, fail to reproduce the distinct asymmetric folds observed in the laboratory images at the downstream end of the first bubble.

Spohn, Mory, and Hopfinger (1998) were the first to attempt to investigate experimentally in a systematic manner the nature of the asymmetries in the flow by examining the flow surrounding the vortex breakdown bubble. Their flow visualizations clearly show the steady, vortex breakdown bubbles to be asymmetric and open at their downstream end, a finding which conflicts with an axisymmetric flow. Spohn et al. (1998) argued that the origin of these flow asymmetries should be traced to asymmetries of the flow inside the wall boundary layers as their flow visualization images showed that above a threshold Reynolds numbers the sidewall boundary layer becomes three-

dimensional and spiral separation lines develop occurs. However the fundamental understanding of the cause of the three-dimensional flow characteristics of vortex breakdown bubbles remained incomplete.

Interestingly the theoretical framework that allows us to reconcile the seemingly conflicting views about this flow were laid out over a decade prior to the Spohn et al (1998) experiments when Holmes (1984), in a not very well known article, suggested that vortex breakdown bubbles could display chaotic Lagrangian dynamics. Holmes raised the intriguing possibility (see section 5.4 for a detailed discussion) that the invariant manifolds connecting the upstream and downstream fixed hyperbolic points of the flow could be sensitive to even extremely small perturbations to the flow. Holmes considered the effect of arbitrarily small time-dependent perturbations to the base axisymmetric flow. At approximately the same time, however, Broer and Vetger (1984) in a separate purely theoretical study considered the effects of arbitrarily small, stationary, three-dimensional perturbations to a dynamical system whose manifold topology is identical to that of a vortex breakdown bubble. Broer and Vetger showed that such perturbations can break the invariance of the bubble surface and lead to the creation of asymmetric folds similar to those observed in laboratory visualization experiments of vortex breakdown bubbles. It is important to note that Broer and Vetger made no connection between their findings and the phenomenon of vortex breakdown. Their findings, however, clearly suggest that even though from an Eulerian viewpoint the flow inside a vortex breakdown bubble could be considered steady and axisymmetric, its Lagrangian dynamics, which is what one visualizes in a laboratory experiment, could be quite different and very rich.

In a recent numerical study Sotiropoulos and Ventikos (2001) solved numerically the three-dimensional Navier-Stokes equations using a curvilinear mesh to discretize the container. They were able to reproduce the three-dimensional characteristics seen in the laboratory experiments of Spohn et al. (1998), including all asymmetric features of the vortex breakdown bubbles and the formation of spiral separation lines along the cylindrical wall of the container (see also Sotiropoulos and Ventikos 1998). Sotiropoulos and Ventikos further showed that the flow in the interior of steady vortex breakdown bubbles exhibit chaotic particle paths, thus, establishing for the first time a firm link between the complexities documented in the laboratory visualization experiments of this flow and the earlier theoretical findings of Holmes and Broer and Vetger. Note that in the numerical simulations of Sotiropoulos and Ventikos the curvilinear mesh they employed introduced a small non-axisymmetric forcing on the flow, which, they argued, emulated collectively the disturbances that are bound to occur in any laboratory set-up (Sotiropoulos and Ventikos 2001). It was this imposed, small, non-axisymmetric forcing that yielded vortex breakdown flowfields essentially axisymmetric from the Eulerian standpoint but resulted in the very rich Lagrangian dynamics observed in the laboratory experiments. In what follows, we develop firm links between the findings of Sotiropoulos and Ventikos (2001) and the theory of dynamical systems and carry out a comprehensive investigation of the rich Lagrangian dynamics of the flow in vortex breakdown bubbles. Much of the work presented below has already been published in two journal papers by Sotiropoulos et al. (2002, 2003).

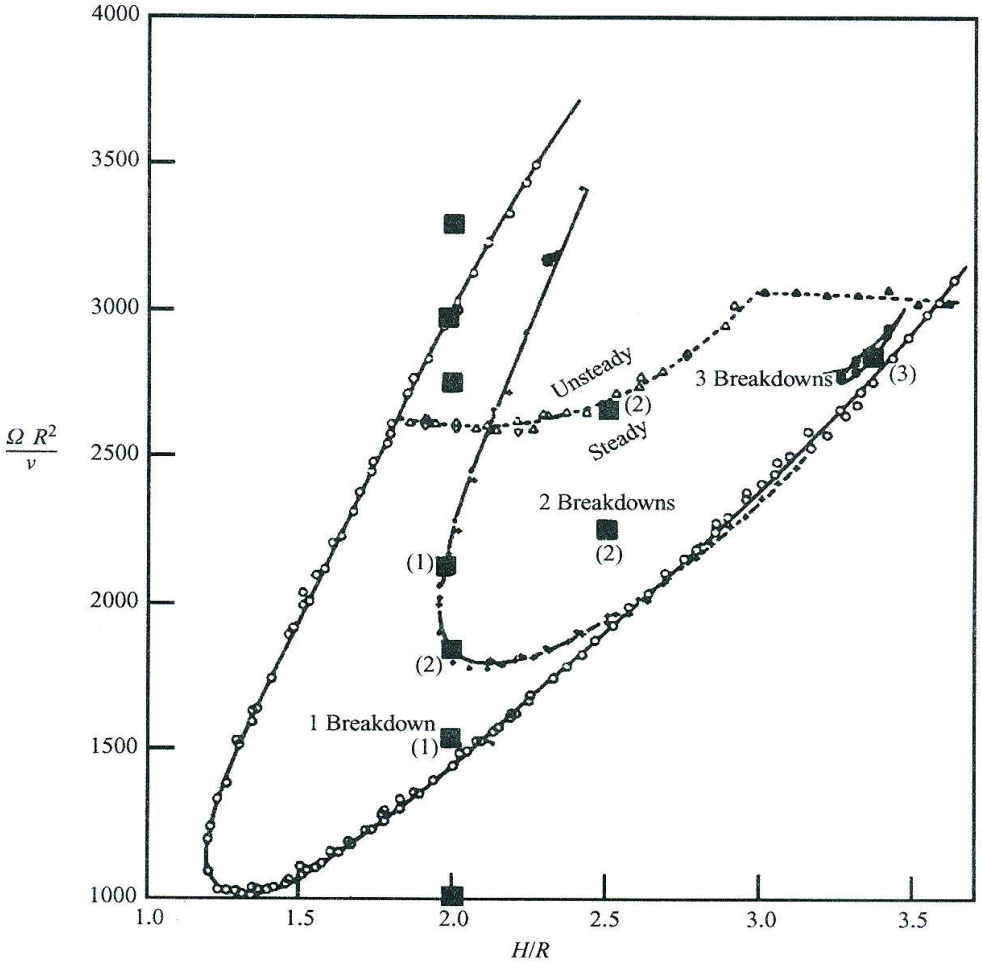

Figure 5.3 Threshold for vortex breakdown bubbles with Re and AR (Escudier 1984).

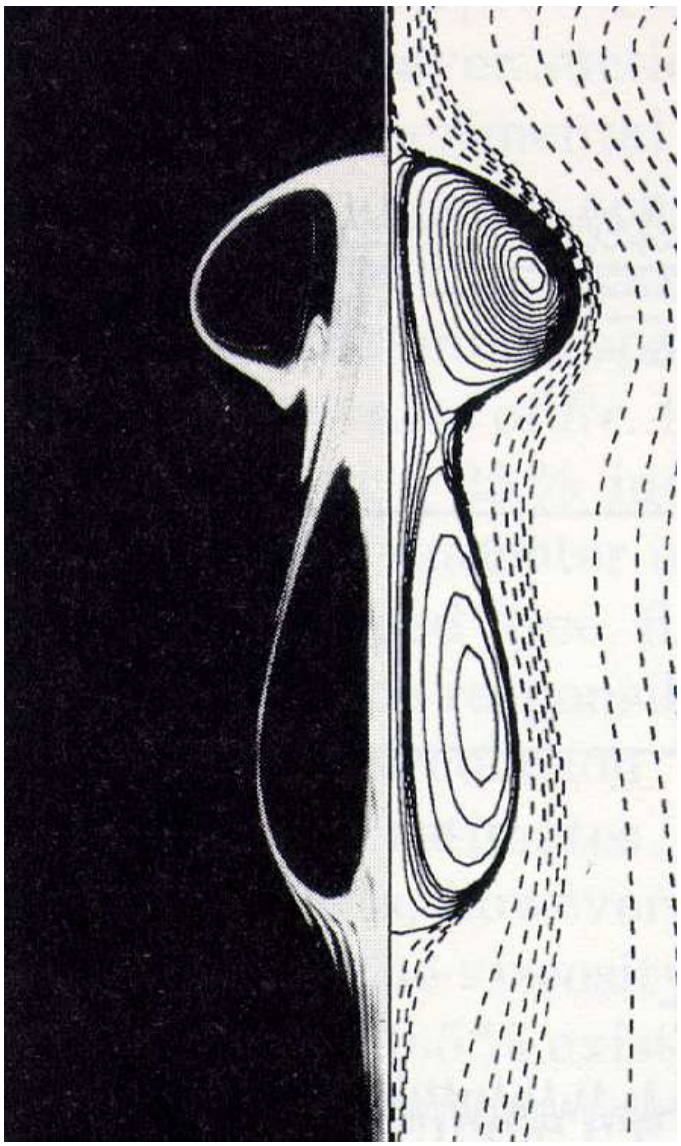

Figure 5.4 Experimental vortex breakdown bubble (left) compared with axisymmetric calculation (right) taken from Lopez (1990).

5.3 Computational Details

The flowfields in the cylindrical container with rotating bottom lid are obtained by solving numerically the fully three-dimensional unsteady Navier-Stokes equations using the method of Sotiropoulos and Ventikos (1998, 2001). The Navier-Stokes equations are formulated in Cartesian coordinates and then transformed to general non-orthogonal curvilinear coordinates. The transformed equations are discretized using a finite volume method and then integrated using a dual (pseudo) time stepping artificial compressibility method. Local time stepping, residual smoothing, and multigrid acceleration are used for convergence acceleration (Lin and Sotiropoulos 1997, Sotiropoulos and Ventikos 1998). The numerical method is second order accurate in both space and time. The results reported were obtained using time-accurate simulations where the steady-state flow fields were reached as the time-asymptotic limits of unsteady computations. The low Reynolds number calculations ($Re < 1500$) were initiated from rest by impulsively spinning up the rotating lid. At higher Reynolds number, the low Reynolds number flow fields were used as initial conditions.

The computational grid for numerical calculations is 150x97x97 (figure 5.5) in the x, y, and z directions respectively. The grid is uniform in the flow direction but is stretched with grid nodes clustered at the walls and at the center of the container in an effort to resolve the complex flow characteristics in boundary layers and in the region of the vortex breakdown bubble. Comprehensive grid sensitivity studies were performed, varying the number of grid nodes from $3x10^5$ to $1.5x10^6$ and the mesh employed herein was found adequate for grid independent solutions.

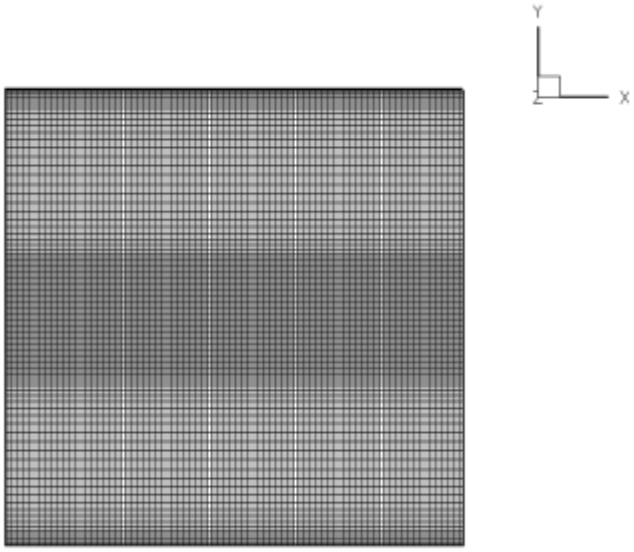

a)

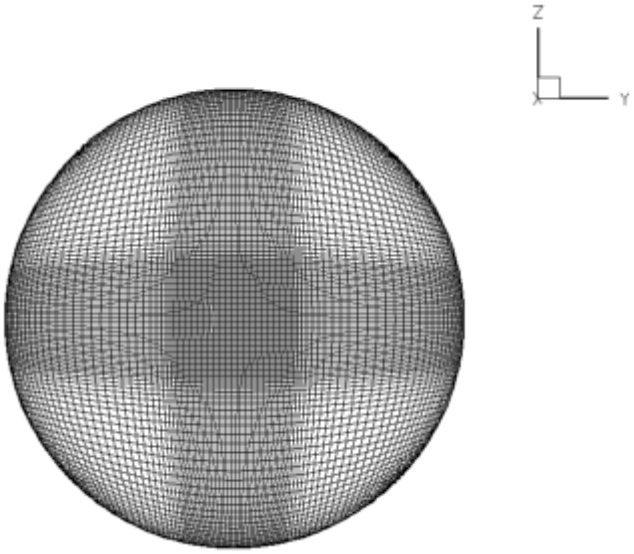

b)

Figure 5.5 Computational grid for cylindrical container with rotating bottom lid.

5.4 Vortex Breakdown Bubble Topology

In this section the streamline topology of the numerically simulated steady vortex breakdown bubbles is described. This is the first step in developing an understanding of the dynamics of the flow within this region. To aid in this process, the behavior of particle trajectories that exist in the bubble is examined. Next the causes behind the variations of trajectories are considered by looking at the structure of the vortex breakdown bubble and the mechanisms that lead to its complex dynamics. It is important to keep in mind that our numerical simulations have been carried out using the curvilinear mesh employed by Sotiropoulos and Ventikos (2001) and, thus, what we investigate herein are the Lagrangian properties of vortex breakdown bubbles under a small albeit finite non-axisymmetric forcing.

The steady-state Eulerian flow field in this work is obtained using a numerical method described in detail in a series of papers (Lin and Sotiropoulos 1997, Sotiropoulos and Ventikos 1998). This method uses a dual time-stepping, artificial compressibility method which has second order accurate differencing spatially and temporally. Using the particle tracking method described in detail in Chapter 4, particle trajectories are calculated by integrating passive particles within the vortex breakdown bubble. At first glance, the simulated vortex breakdown bubble exhibits three basic types of trajectories as shown in figure 5.6. The first type of trajectory (see thick trajectory in figure 5.6) originates upstream of the bubble, spirals around its exterior and continues downstream towards the rotating lid without entering the bubble. The second type of trajectory also originates upstream of the bubble, spirals downstream around the bubble, but when it

approaches the downstream stagnation point it reverses direction, enters the bubble, spirals in its interior several times before it finally escapes and continues downstream. The third trajectory type is confined entirely within the interior of the bubble. Particles circle forever on invariant tori that foliate the interior of the bubble. Such trajectories would be the only type encountered in the interior of a steady, axisymmetric bubble. A more careful consideration of particles paths in the interior of the bubble further reveals that other types of trajectories with very rich dynamics also exist but these intricacies will be discussed in a subsequent section in this chapter. Clearly even this rudimentary examination of the basic types of trajectories suggests that the interior of the simulated vortex breakdown bubbles exhibit very rich dynamics in stark contrast with an axisymmetric structure, which would be closed (and thus not accessible to upstream originating particles) and foliated by invariant toroidal stream-surfaces.

To understand the reasons for the rich dynamics, let us consider the manifold structure of an ideal axisymmetric stationary vortex breakdown bubble (Wiggins 1990) seen in Figure 5.7. Figure 5.7a shows a sketch of both a cross section and the three-dimensional structure of the heteroclinic cycle for the three-dimensional, axisymmetric flow field. Heteroclinic trajectories (also known as saddle connections) are trajectories that join two saddle points. Saddle points are formed by the joining of a stable and unstable manifold. That is, they are points in the phase space of a dynamical system in which trajectories are attracted and repelled from the same position. For a vortex breakdown bubble the saddles are its upstream and downstream stagnation points. The stable manifold is simply represented by the orbits that are attracted to the stagnation point and the unstable manifold is formed by orbits that are repelled by the stagnation

point. In Figure 5.7b the two saddle points are denoted with P_1 and P_2. They connect the two-dimensional unstable manifold $W^U(P_2)$ and one-dimensional stable manifold $W^s(P_2)$ with the two-dimensional stable manifold $W^S(P_1)$ and one-dimensional unstable manifold $W^U(P_1)$. The two-dimensional manifolds cycle around structure and the one dimensional manifolds form the centerline axis of the bubble. The heteroclinic trajectories create an invariant bubble-like surface, which delineates the interior flow from the outer flow as shown in figure 5.7a. The trapped interior flow moves along invariant tori, which are the stream-surfaces of the axisymmetric flow.

The topology seen in figure 5.7 is also the topology of the following autonomous three-dimensional normal form:

$$\begin{aligned} \frac{dr}{dt} &= \mu_1 r + arz + \ldots, \\ \frac{dz}{dt} &= \mu_2 + 2 + br^2 - z^2 + \ldots, \\ \frac{d\theta}{dt} &= \omega + \ldots, \end{aligned} \tag{5.1}$$

where μ_1, μ_2, a, b, and ω are constants, and the dots imply higher-order terms. As shown in Wiggins (1990), for a>0 and b=-1 the stable and unstable manifolds of the hyperbolic fixed points of this system create an invariant sphere. When the higher order terms are ignored, the form is similar to that shown in figure 5.7a, and the periodic orbits become invariant two-tori. Let us now consider the effect of adding higher order terms in the above system in the form of small, non-axisymmetric perturbations. As shown by Broer and Vetger (1984), including such terms, no matter how small they may be, could destroy

the symmetry of the basic form and break the invariant structures of the sphere shown in figure 5.7a. The one-dimensional unstable manifold of P_1 and the one-dimensional stable manifold of P_2 will no longer intersect in three-dimensional space and the two-dimensional manifolds of P_1 and P_2, $W^S(P_1)$ and $W^U(P_2)$ may intersect transversely along heteroclinic orbits. This means that it is possible for the portion of $W^U(P_1)$ and $W^S(P_2)$ inside the bubble to fall into $W^S(P_1)$ $W^U(P_2)$ forming homoclinic (trajectories that start and end at the same fixed point) orbits in three-dimensional space (see Figure 5.7b). That is trajectories that start at a stagnation point, may spiral around the bubble, transect a trajectory coming from the opposite stagnation point and move back to their starting point. It is known from the theory of dynamical systems that homoclinic orbits are structurally unstable and their instability could lead to chaotic dynamics (Arneodo, Coullet & Tresser 1982; Gaspard & Nicolis 1983).

The intertwining of manifolds in figure 5.7b then develops a homoclinic tangle. Whenever a system has a homoclinic tangle (a transverse homoclinic point) there exists a region which is mapped onto itself, providing an area of sufficient stretching and contraction, so that chaotic dynamics are possible. It was first recognized by Sil'nikov (1965) that homoclinic orbits, mapping a saddle focus back onto itself possess a countable infinity of Smale horseshoes (Smale 1963). The Smale horseshoes (see figure 5.8) can be formed by a rectangle that is flattened, stretched, and folded into a horseshoe structure. This process leads to the exponential separation of points that initially reside in close proximity. The existence of a ``horseshoe" as part of a dynamical system is a compelling signature of chaos (Wiggins 1990). Since the structure of the perturbed vortex breakdown bubble contains two saddle foci, it can then be inferred that the

dynamics described by Sil'nikov could exist in this system. The Sil'nikov route to chaos in this situation can be summarized as follows. Material lines entering the bubble through the downstream saddle focus are stretched and folded every time they pass through that saddle and this process ultimately leads nearby orbits to separate exponentially in time.

The Sil'nikov mechanism in the context of the dynamical system given by eqn. (5.1) was studied in detail by Broer & Vegter (1984). By considering the effects of the higher-order terms in these equations, they proved that for the perturbed system a sequence of Sil'nikov's bifurcations will occur, thus, leading to the formation of a countable infinity of Smale horseshoes and non-integrable dynamics. Figure 5.9 shows their interpretation of the three-dimensional structure of the stable and unstable manifolds of the two saddle foci for a perturbed, volume-preserving system of the form of equations 5.1. Interesting to note is the asymmetric folding effect that occurs downstream of the Broer and Vetger "bubble," which is very similar to the folds that appear in essentially all vortex breakdown bubbles visualized in the laboratory (see figure 5.3).

If we apply these concepts to the vortex breakdown bubble trajectories shown previously in figure 5.6, it is possible to understand why each of the sample trajectories exists. The first trajectory in which particles move down the axis, cycle around the bubble and exit, are particles that reach the stagnation point along the stable one-dimensional manifold and then exit along the unstable two-dimensional manifold before approaching the downstream stagnation point along the stable two-dimensional manifold and then exiting the region along the unstable one dimensional manifold. The third type of trajectory is trapped inside the bubble interior and would also be present if the flow

were axisymmetric. However most interesting is the second type of trajectory that enters the bubble interior, stays for an arbitrary amount of time, spiraling in the interior of the bubble before exiting. This type of trajectory could not possibly exist under the axisymmetric assumption and is only possible if trajectories are somehow able to jump from one of orbit to another due to the transverse trajectories.

The higher order terms that need to be added to the dynamical system given by equations (5.1) are exponentially small (Broer and Vetger 1984). In our numerical simulations they have been created numerically because of the curvilinear mesh we have employed. In a laboratory experiment they may arise due to numerous possible experimental imperfections and ambient disturbances no matter how much great care is taken to eliminate them. Thus, the above discussion suggests that even though from the Eulerian standpoint the steady vortex breakdown bubbles are essentially axisymmetric it could be very difficult to visualize them as such in a real-life laboratory experiment because that would require eliminating from the apparatus all disturbances no matter how small.

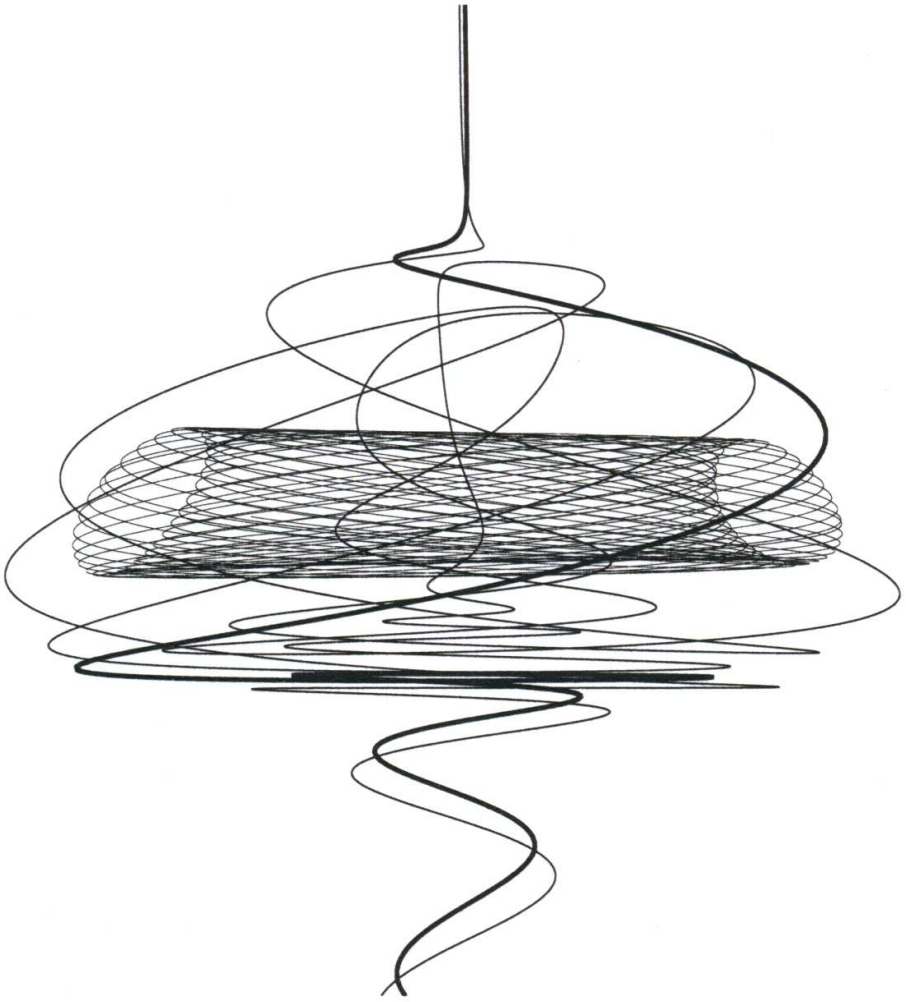

Figure 5.6 Calculated typical three-dimensional particle trajectories in and around the breakdown bubble. (Re = 1850, H/R =1.75). The 'thick' orbit is released from the axis upstream of the breakdown bubble. The 'thin' orbit is released just off the axis also upstream of the bubble. The final orbit remains on a toroidal trajectory.

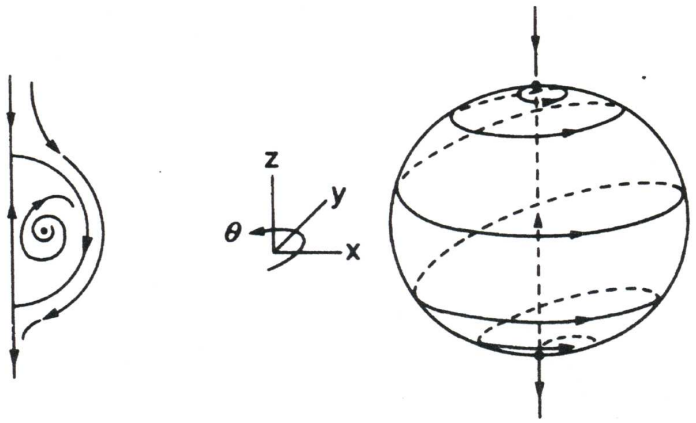

a)

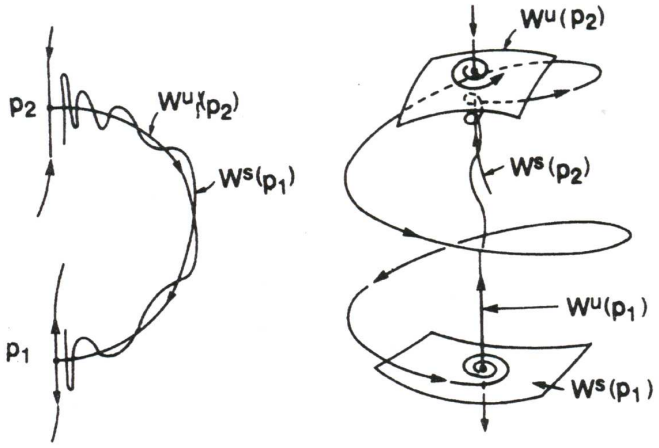

b)

Figure 5.7 (a) Cross-section and three-dimensional structure of the heteroclinic cycle for the truncated normal form, equation (5.1); and (b) cross-section of the perturbed manifolds and homoclinic orbits for the full normal form (including the effect of higher order terms). Wiggins (1990).

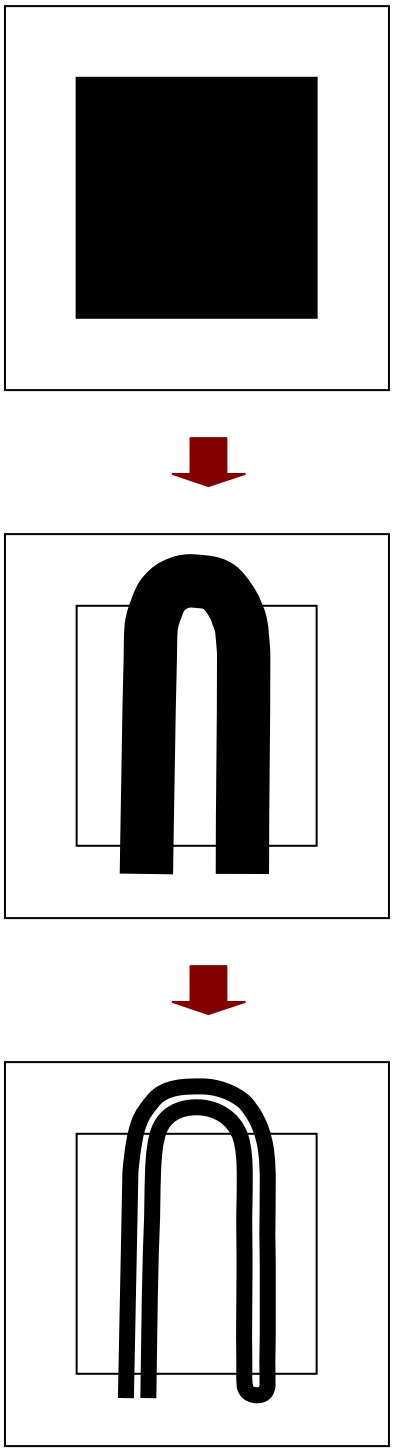

Figure 5.8 Smale horseshoe map.

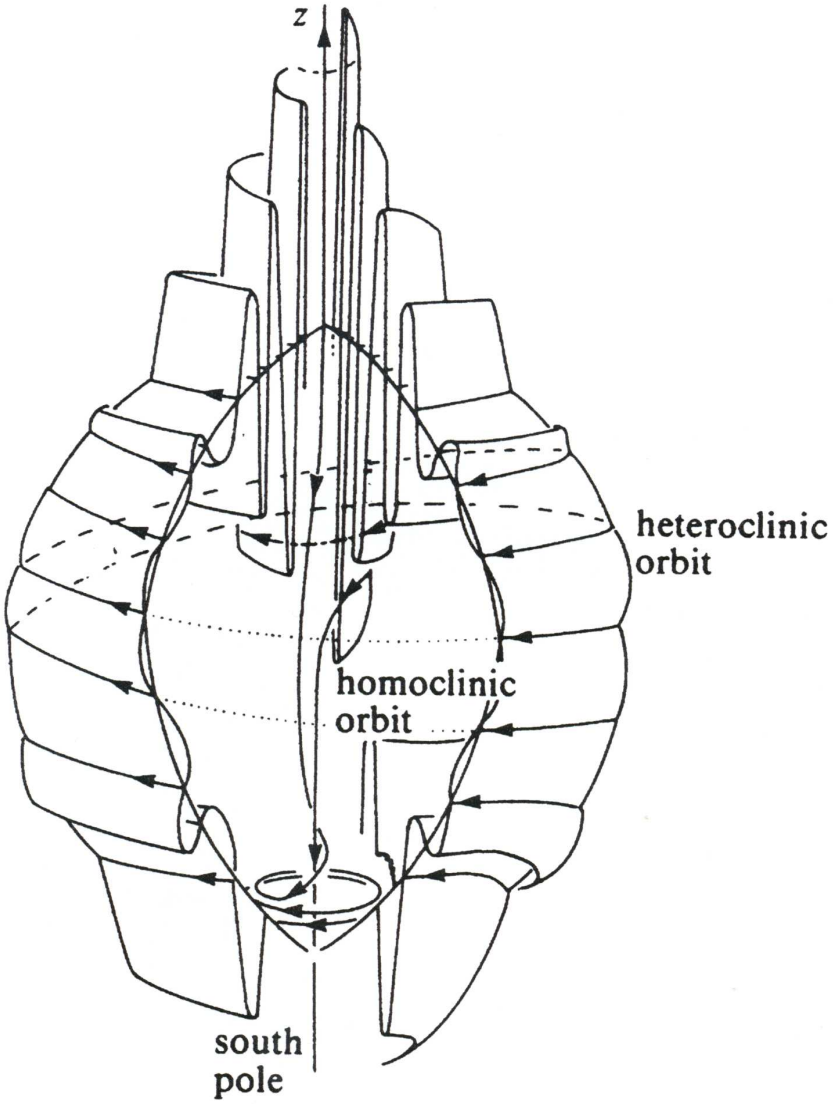

F

Figure 5.9 Cut-open perturbed globe showing a Sil'nikov homoclinic orbit for a volume-preserving system. Taken from Broer and Vegter (1984).

5.5 Stretching, folding and chaotic stirring

The previous section sought to identify the mechanisms (such as the Sil'nikov mechanism) that control the dynamics within the vortex breakdown bubble. It has been theorized that the effect of small perturbations (either numerical or experimental) will have a dramatic effect on these dynamics, causing the axisymmetric representation of the vortex breakdown bubble to instead become a very complex structure that allows for chaotic stirring. To prove these hypotheses analytically would be impossible because of the complexity of the equations. Therefore in this section, we provide evidence that chaos inducing mechanisms are indeed at work within vortex breakdown bubbles by analyzing the Lagrangian dynamics of the numerically simulated velocity fields.

Figure 5.10 shows the evolution of a particle that is initially a straight material line that is recirculating within the vortex breakdown bubble. The filament has 1000 particles spaced 10^{-8}R apart which provides an initial filament length of 10^{-5}R. The filament enters the breakdown bubble region and recirculates several times before all the particles exit the bubble. Position 1 in the figure is the initial release location. Position 2 is just prior to the element passing through the spiral-in saddle for the first time. Positions 3,4, and 5 are snapshots during the second approach of the element toward the spiral-in saddle and position 6 is just before the element enters the breakdown region for the third time. The effects of folding are quite evident in this figure. The filament has now been folded over several times as can be seen in the enlarged snapshot at position 6.

As the filament moves through the central axis of the vortex breakdown bubble and travels through the saddles seen at location 1 and 2, the length of the filament grows

at an exponential rate. This can be seen in figure 5.11, which shows the temporal evolution of the length of the filament. Here we plot the length of the filament, which has been normalized by the initial length of the filament given as L_0, versus time. Each number in parentheses designates one of the stages of growth of the filament depicted in the previous figure. It is observed that the length of the figure does indeed grow exponentially, a feature which is the hallmark of chaotic dynamics.

To illustrate the chaotic stirring of particles in the interior of the bubble we calculate the motion of a series of material circles covering the exterior of the upstream portion of the bubble. Figure 5.12 (a) through (i) shows the progression of these orbits over 484 non-dimensional time units. The particles are color-coded based on their initial distance in the x direction. In figure 5.12b particles have moved around the outside of the bubble and are being drawn into the saddle focal point downstream of the bubble. As particles travel into the bubble by t=25 (figure 5.10c) the stretching and folding characteristics are observed as the material circles begin to twist. The particles continue to move within the bubble, the structure of the surface of particles is folded and stretched more with each movement through the saddle point, becoming more and more disorganized and stirred. Finally, it can be seen by figure 5.12g that particles are eventually observed exiting the bubble in random bursts. The rate of the bursts will be discussed in section 5.6.3. Note that by t=484 in figure 5.12i, the particles are completely disorganized and dispersed chaotically within the bubble.

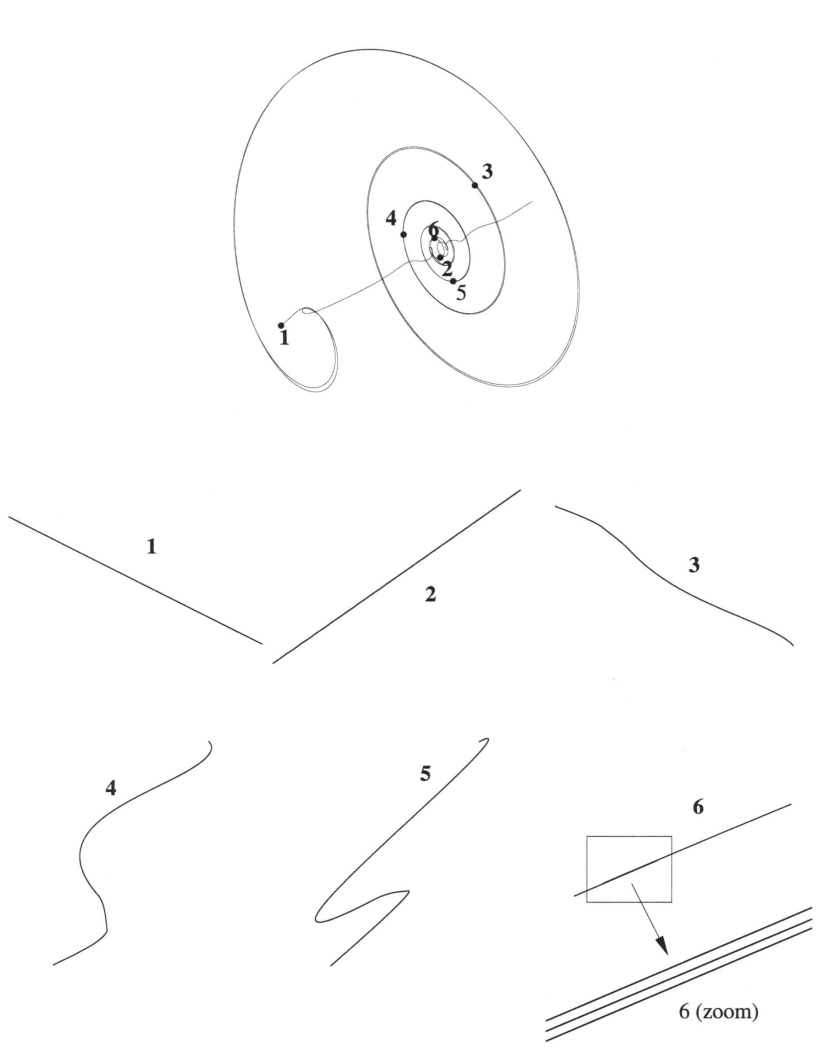

Figure 5.10 Evolution of the shape of an initially straight material line as it recirculates within a stationary vortex breakdown bubble (Re = 1850, H/R=1.75). The material filament consists of 1000 particles spaced uniformly 10^{-5}R apart. The various positions of the filament are marked with numbers along the trajectory of its midpoint.

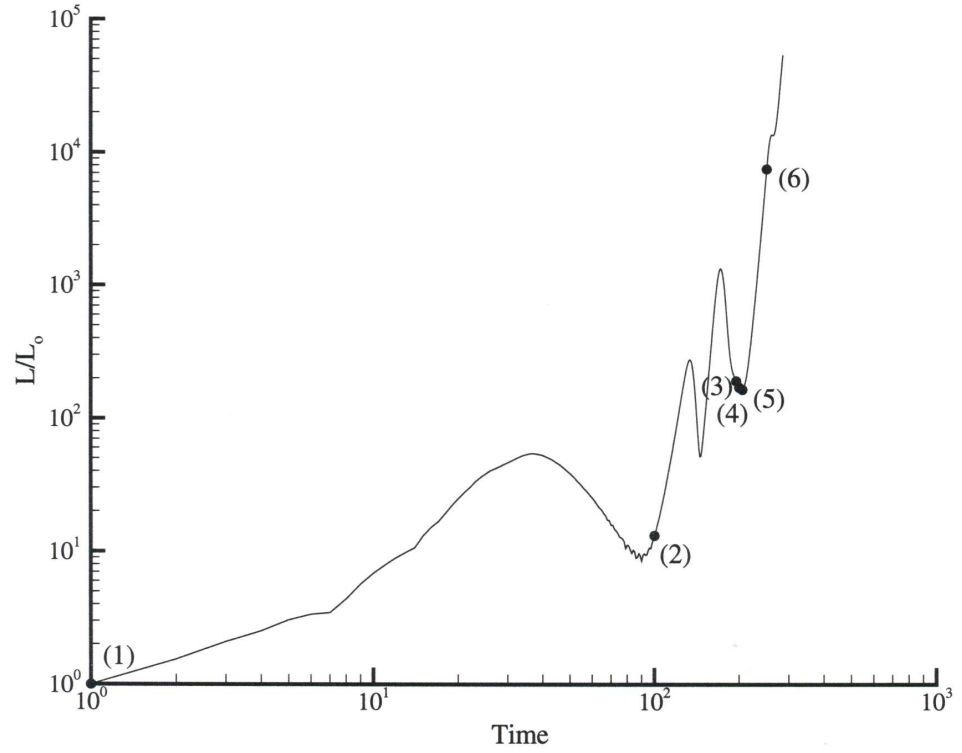

Figure 5.11 Temporal evolution of the length of the filament shown in figure 5.10. The numbers in this figure indicate the various positions of the element defined in that figure. The length (L) has been scaled by the initial length (L_0). The rotating lid completes one revolution in π time units.

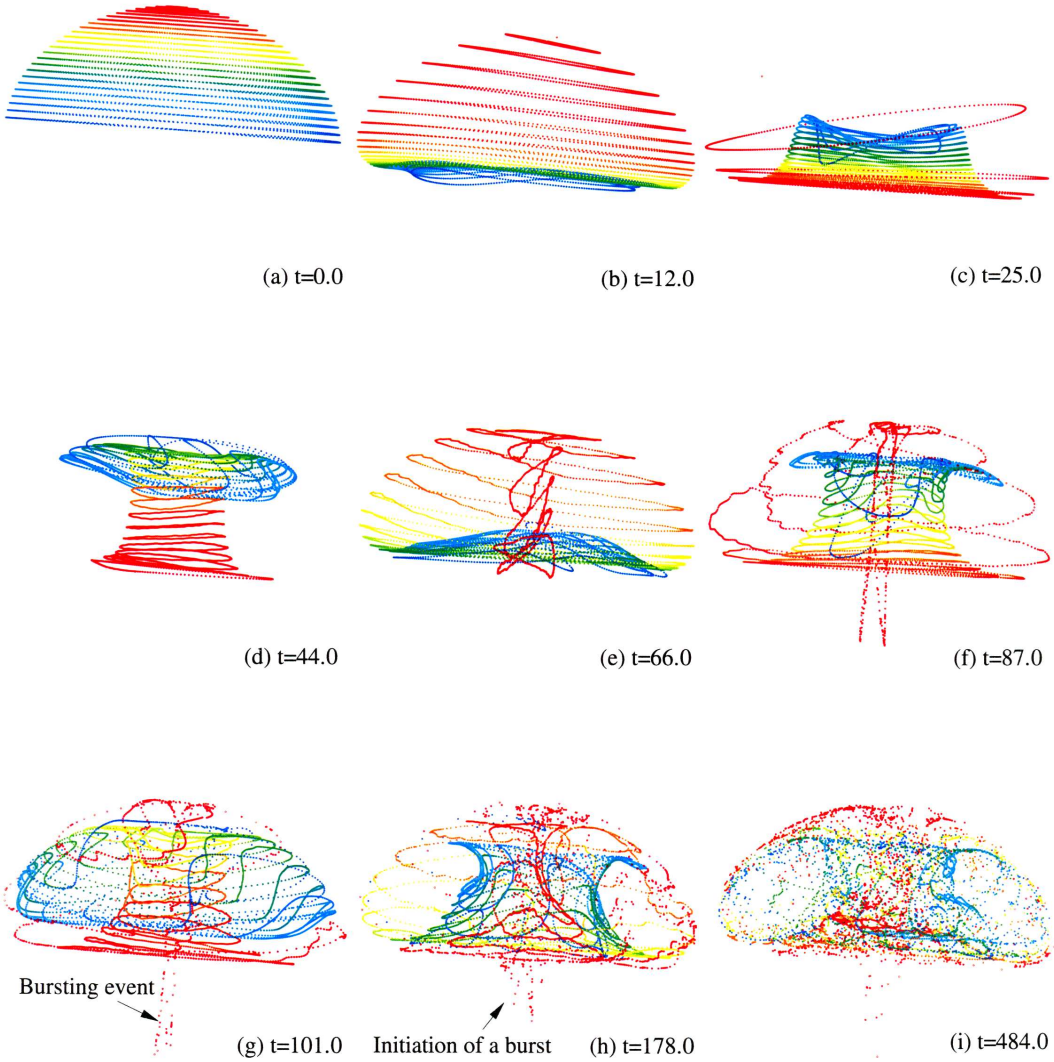

Figure 5.12 Temporal evolution of series of circular material lines, initially placed to span the upstream face of the vortex breakdown bubble (Re = 1850, H/R=1.75). Individual particles are colored based on their axial coordinates at t=0.

5.6 Results and Analysis

In this section we characterize and quantify the Lagrangian dynamics in the interior of the simulated steady vortex breakdown bubble flowfields using Poincaré maps, residence time maps, and tools and concepts from fractal geometry. Finally, the effect of Reynolds number, aspect ratio and the role swirl are addressed.

5.6.1 Poincaré Map

We construct Poincaré maps to characterize and better understand the richness of dynamics in the interior of the bubble. The maps are constructed (see Chapter 2 for detailed description) by allowing particle trajectories placed initially in different flow regions to be advected by the simulated flowfield and marking the position they intersect a given diametral plane, the plane of section of the Poincaré map. Figure 5.13 shows the resulting Poincaré map for the steady vortex breakdown bubble for Reynolds number 1850 in a container with an aspect ratio of 1.75. Particles are colored by their initial conditions, which are marked by the colored "blobs" in the figure. Each blob contains 5 particles, which were released along short straight segments and then iterated for 10^6 time steps. The resulting Poincaré map shows the complex characteristics of the flow within the bubble and reveals a picture that is very similar to the previous descriptions by Helleman (1980) who discussed the effect of three-dimensional perturbations on the dynamics of a volume preserving, dynamical system.

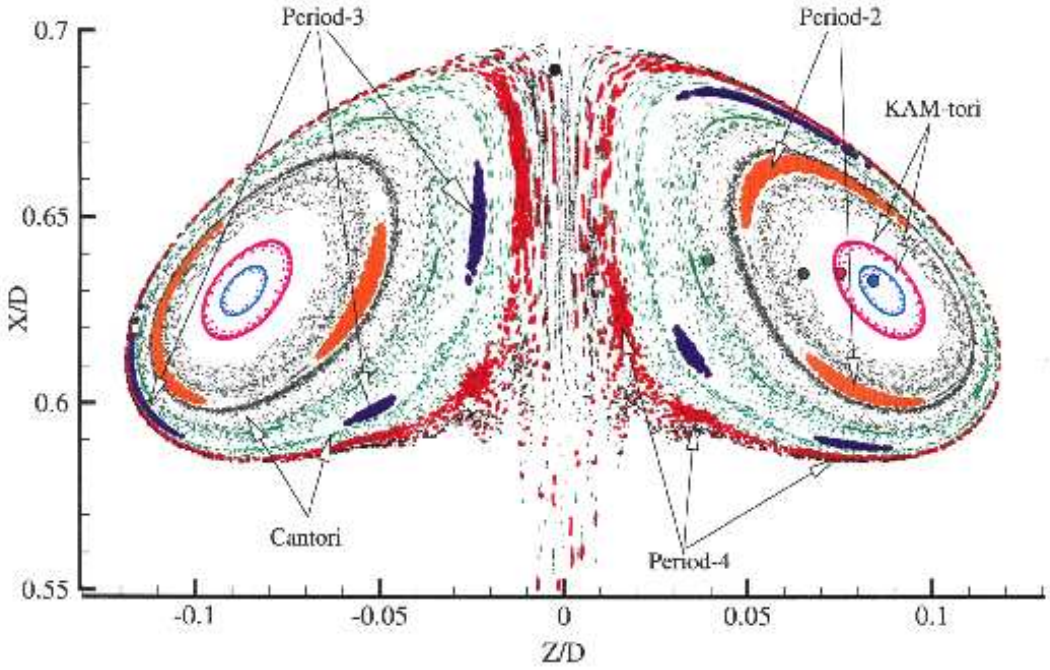

Figure 5.13 Poincarè section of the steady vortex breakdown bubble for (Re = 1850, H/R=1.75). Same-color blobs of markers (5 markers per color) were released along short straight segments, selectively placed within various regions in the interior of the VB bubble. The large dots mark the initial location of the various blobs.

In figure 5.13, the blue and pink points are particles that stay within the toroidal region of the bubble. These areas are KAM-tori, the remnants of the axisymmetric dynamics, and act as impermeable barriers to transport. There existence is consistent with the KAM theorem, which predicts that many of the simple quasi-periodic solutions of the axisymmetric integrable system will, in general, survive mild perturbations.

Moving outward from the two inner KAM-tori shaded in pink and blue, the dynamics become more complex. The gray and green initial points outline cantori. These are leaky barriers to transport on which particles can be trapped or stick for very long times but ultimately escape through fractal "windows" to explore the rest of the flow domain. In the figure, the gray particles outline a rather tight cantorus. Particles seem to be almost confined to that area for a very long time before they start escaping. In contrast, the green region shows a much less structured region. Here particles stick for shorter time and appear to escape more frequently and, thus, many of them have worked their way into other bubble regions.

The gaps between adjacent cantori are populated with both chaotic regions as well as un-mixed island chains of regular motion. The figure shows the Period-2, Period-3, and Period-4 islands in orange and violet and red respectively. These island chains are formed by particles that remain confined on twisted and folded tori of complex topology, whose three-dimensional structure is shown in Figure 5.14. In addition to these low period islands, we have also found higher order period islands in the interior of the bubble. However it is extremely difficult to find and visualize the higher order islands, as space covered by the island diminish in size as the order of the island increases.

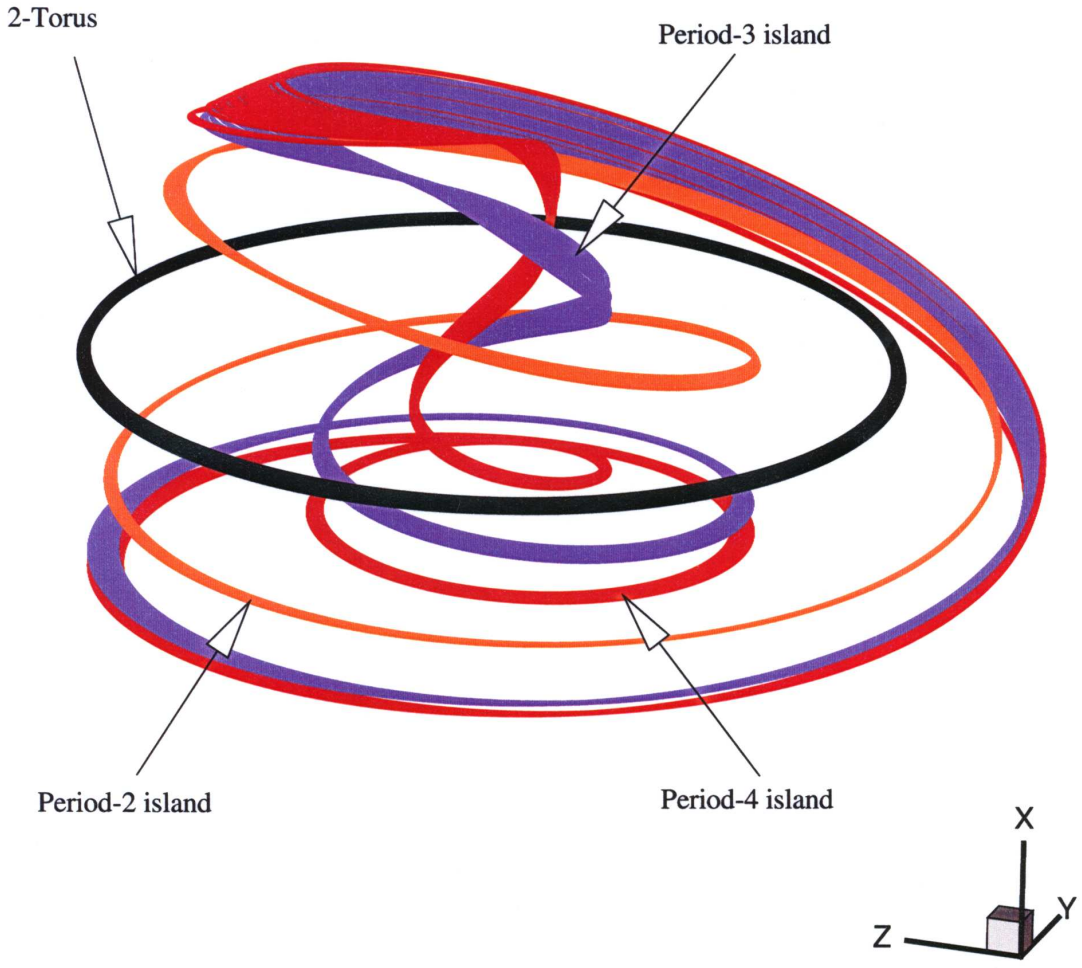

Figure 5.14 Three-dimensional orbits illustrating the intertwining of the period-two, -three, and –four islands in the interior of the bubble shown in figure 5.13.

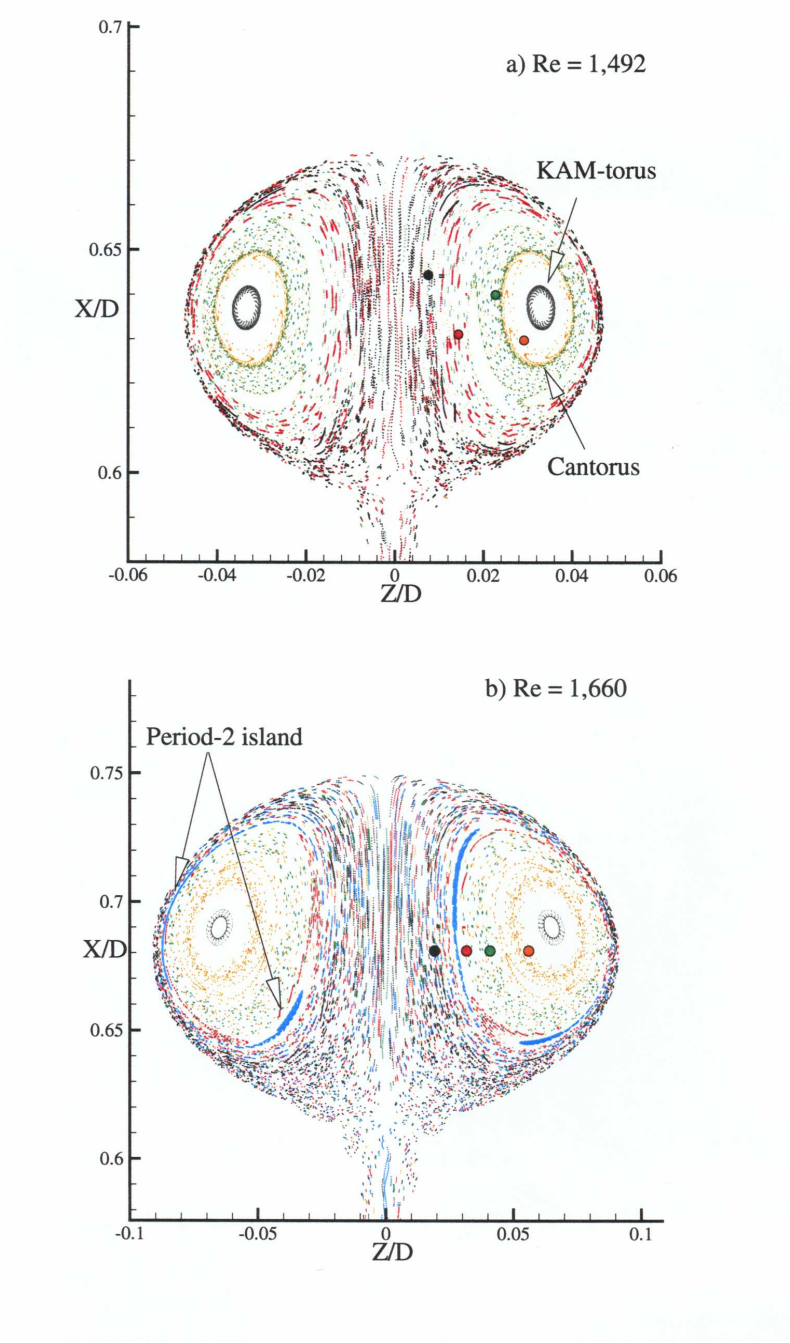

Figure 5.15 Poincarè sections for steady vortex breakdown bubbles in a container with H/R=2. a) Re=1492; (b) Re=1667.

The chaotic regions surrounding the periodic islands, as well as the chaotic area represented by the black "blob" show particles that are extremely sensitive to initial conditions. Particles that originate in these areas become completely mixed. The points of the map colored in black, are representative of orbits that are developed due to the previously introduced Sil'nikov mechanism. The particle trajectories pass through the hyperbolic fixed points and transverse the various heteroclinic orbits of the flow. This mechanism provides the stretching and folding characteristics, which leads to the chaotic behavior of particles within the region and explains why the points show such great scatter across the area of the map.

As shown in the work of Escudier (1984) (see figure 5.3), for various aspect ratio/Reynolds number combinations there exist one-, two-, three- and no-bubble cases. To study the variation in Lagrangian dynamics of the vortex breakdown flowfields, we construct Poincaré maps for calculated vortex breakdown flowfields at various Reynolds numbers and aspect ratios. In figure 5.15, we show representative results for two Reynolds numbers 1492 and 1667 for aspect ratio (AR=H/R) of two. The basic structure of the bubbles remains the same for the maps. There exist chaotic particle trajectories due to the well-stirred Sil'nikov filament that occupies the region in the vicinity of the axis for all Reynolds numbers. There is also the continued presence of the KAM-tori and cantori regions. The first big difference is seen in the Re=1492 case, however, due to the apparent lack of low-period islands existing in the bubble interior. Even with extensive searching, there was no evidence of the low-period islands that were seen in the previous Re=1850 with AR=1.75 case (see figure 5.13). In figure 5.15b, as we increase the Reynolds number to 1667, a Period-2 island appears, although it does not seem to occupy

as large a percentage of the interior as the Period-2 island shown in figure 5.13 for Re=1850.

Other differences in the maps are in the size and structure of the cantori and the chaotic filament along the axis. As the Reynolds number increases from 1492 to 1667, the cantori appear to become “leakier”. There is a noticeably large amount of spreading that occurs in the Re=1667 case as the particles colored in green seem to occupy a larger amount of space than in the Re=1492 case. Also several of the particles in orange have escaped the bubble at the higher Reynolds number. In addition there is a difference in the size of the chaotic filament that resides along the axis. As the Reynolds number increases, the quasi-periodic core has shrunk in size, leaving a much larger portion of the flow filled with the stochastic flow region.

5.6.2 Residence Time

The rate at which particles exit the bubble is explored in this section. Residence time as a means of understanding chaotic advection has been a useful tool in other mixing flows such as the partitioned-pipe mixer (Kusch and Ottino 1992). However in those studies residence times are mapped based on the idea that particles placed in regular or periodic areas will exit the mixer much faster than the chaotic particles, which tend to sample a larger range of velocities and move aimlessly throughout the pipe. Therefore the residence time of particles placed in chaotic areas tends to be much larger than those placed in periodic areas. In the present confined flow that is obviously not the case. Particles trapped in islands and tori will remain in these areas and will not escape the

bubble. In this study we characterize the amount of time upstream originating particles that enter the bubble through the downstream saddle focus spend in its interior. As suggested by figure 5.12, some particles could recirculate within the breakdown region for arbitrarily many times before finally exiting in random bursts. To explore this feature of the flow, we introduce 10,000 particles distributed axisymmetrically along a small disk of radius 0.01R centered around the container axis just upstream of the breakdown bubble. The trajectories of the particles are integrated until every particle exits and their residence time is recorded and mapped back on to the initial particle positions in the contour plot seen in figure 5.16.

The remarkable aspect of the resulting images is their fractal like properties. Here we show the particle positions in the Y and Z direction normalized by the radius R. The initial image (figure 5.16a) shows that the disk contains large regions of comparatively small residence time particles. Within these areas, however, are fractalized swirling bands of initial conditions that lead to much higher residence times. To further explore the apparent fractal-like structure of figure 5.16a, we increase particle resolution at successively smaller spatial scales by distributing all 10,000 particles within smaller and smaller regions, which are shown in figures 5.16b to d. As the resolution is increased, it is apparent that initial conditions that lead to continuously higher residence times are uncovered and fractal-like, self-similar patterns emerge. These bands closely resemble fractal boundaries of basins of attraction for non-attracting chaotic sets and suggest a Cantor-set-like cross-section. Their fractal structure is consistent with the chaotic nature of vortex breakdown flowfields and a direct manifestation of the extreme sensitivity of particle trajectories to arbitrarily small differences in initial conditions.

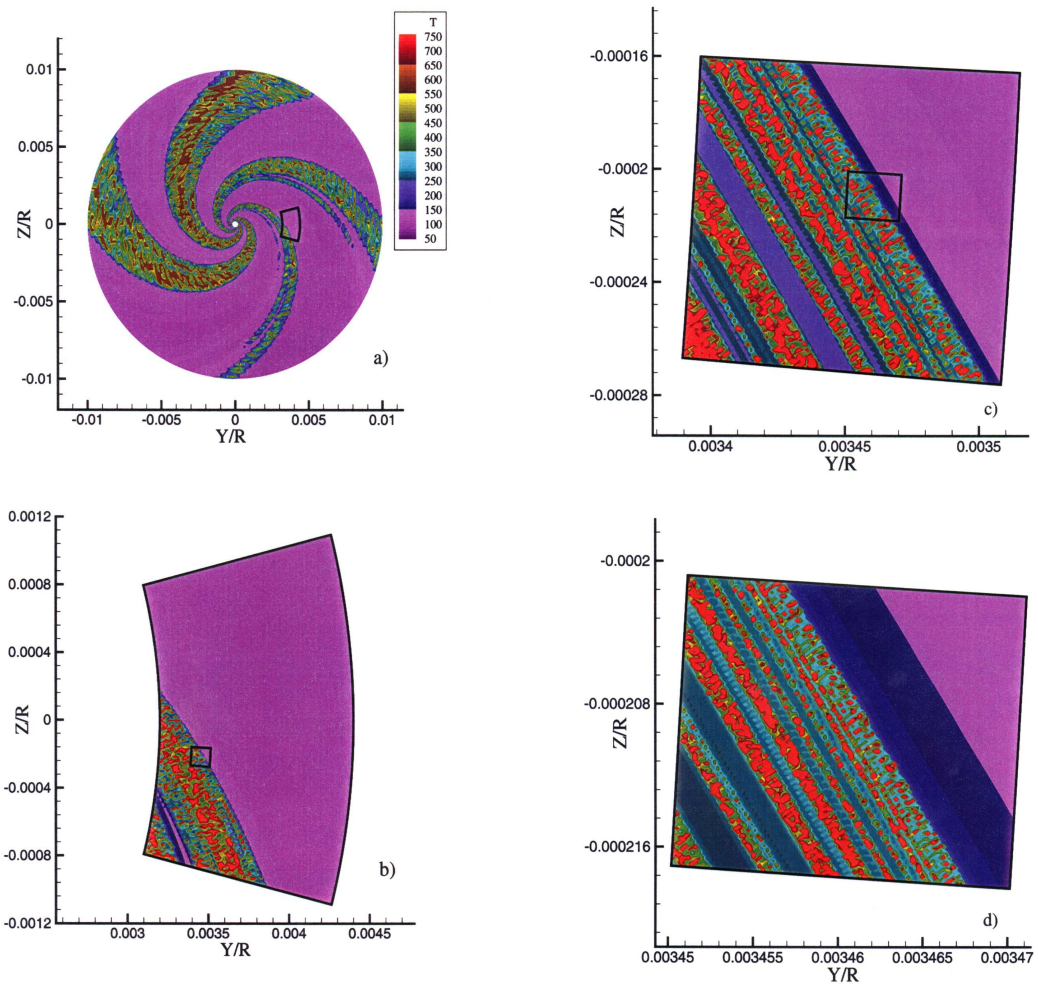

Figure 5.16 Residence time maps for initial conditions with increasing resolution from a)-d).

An important feature of the computed residence time map that is not directly apparent from the figure 5.16, is the fact that as we increase the resolution at smaller scales we uncover release points that lead to continuously increasing residence times. At the resolution of figure 5.16a, the maximum residence time is approximately 700 non-

dimensional units (corresponding to approximately 222 revolutions of the rotating lid), while at the resolution of figure 5.16d, we have picked points which lead to residence times as high as 7000 units (i.e. 2222 revolutions of the rotating lid). To demonstrate this feature, we show in figure 5.17 a plot similar to figure 5.16 but by including, at the two highest resolution levels, only contours that correspond to the very large residence times (the levels included in this plot range from 1000 to 7000). The resulting Cantor-dust-like contour plot strongly suggests that there exists a Cantor set of initial conditions (i.e. a set of measure zero but of finite dimension) that will lead to arbitrarily long residence times within the breakdown region. This conjecture is consistent with the chaotic nature of the flow and, in essence, is identical to the theoretical arguments made by Holmes (1984) that particles will re-circulate within the breakdown region for arbitrarily many times. Moreover, the concept of arbitrarily long residence times associated with a subset of measure zero (i.e. a Cantor set) of the total fluid flux into the bubble has been already introduced by MacKay (1994) in the context of the perturbed spheromak. MacKay (1994) also points out that the distribution of residence times within the bubble is "*likely to be highly non-trivial*," a conjecture that is confirmed by the fractal structure we uncover herein. Finally, the existence of a Cantor set of initial conditions leading to arbitrarily long residence times within non-attracting chaotic sets, such as the volume-preserving vortex breakdown flowfield we study herein, is a well documented phenomenon in studies of chaotic scattering (see Ott (1993) for a detailed review).

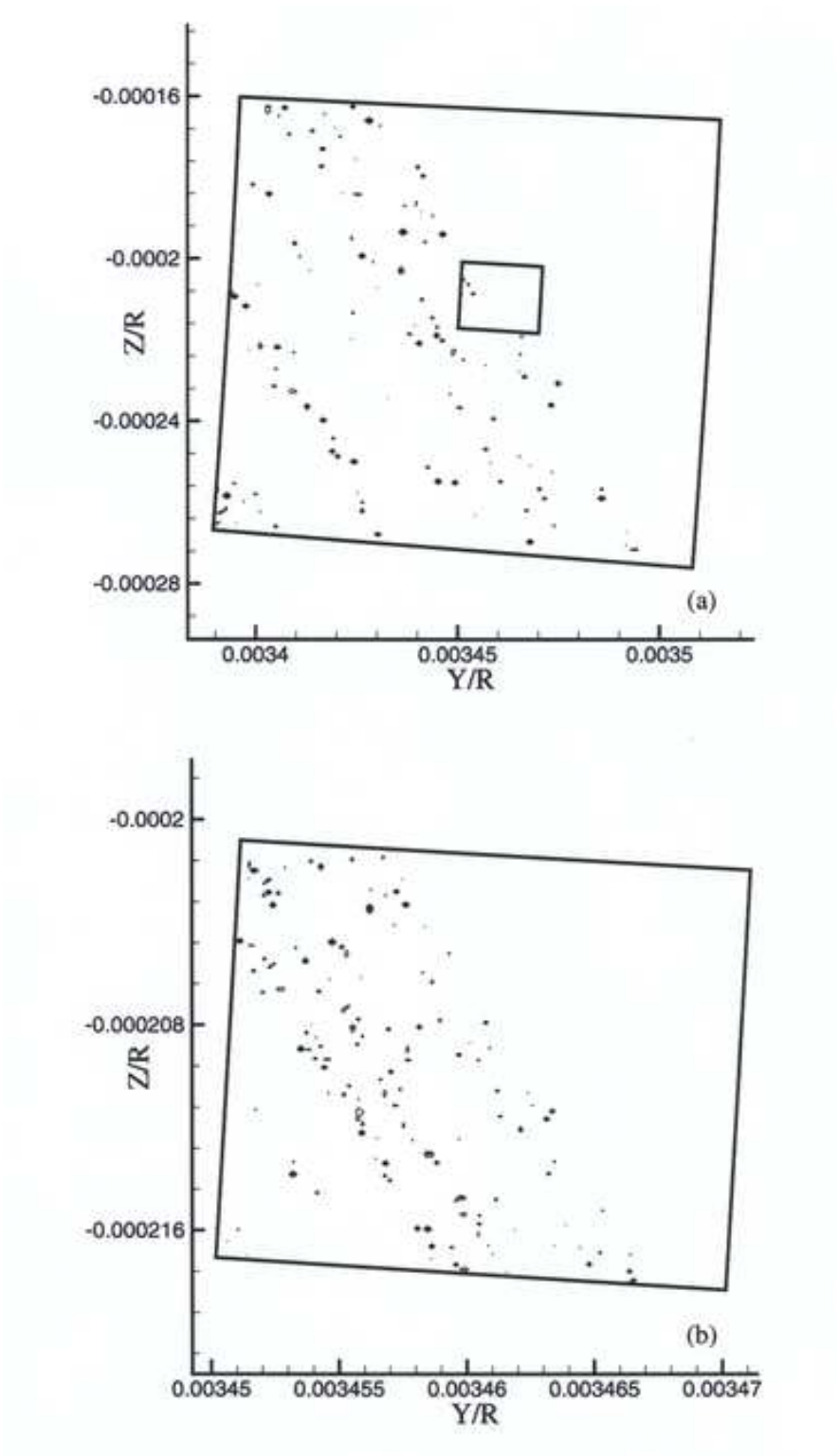

Figure 5.17 Contours of residence time with only large residence times (1000 to 7000); plotted to demonstrate the Cantor-dust-like structure of the resulting map.

5.6.3 Devil's Staircase

In this section we further explore and quantify the curious emptying mechanism discussed in section 5.5, by calculating the rate at which a group of upstream originating particles exits the bubble through the spiral-in saddle. We release the particles from a small disk, similar to that used to study the residence time distributions in the previous section, and record the number of particles that remain inside the bubble at every instant in time until the last particle exits (see below for a clarification of this point). A particle is declared to have exited the bubble when it crosses a certain axial plane just downstream of the spiral-in saddle. Note that for a given set of upstream initial conditions, several particles do not enter the bubble and are, thus, the first to cross the "exit" plane. These particles are omitted from the simulation. To investigate the sensitivity of the results presented herein to the size of the initial particle population, we have varied the particle number from $n = 10^3$ to $3x10^4$ (see figure 5.19 below)—for each simulation, the particles were released from exactly the same small disk upstream of the vortex breakdown bubble. We have also investigated the effect of varying the size of the time increment used in the trajectory integration, by performing, for a fixed number of particles, simulations with successively smaller time steps. The results reported in this section are independent of the size of the time increment.

The computed temporal decay of an initial population of $n = 3x10^4$ particles, for the (Re=1850, H/R=1.75) vortex breakdown bubble, is plotted in figure 5.18. Note that the initial number of particles in the vertical axis is less than $3x10^4$ because, as discussed above, particles that do not enter the bubble are omitted. A remarkable characteristic of

the curve shown in figure 5.18 is that it is a piecewise continuous staircase-like structure, consisting of a series of horizontal plateaus each of seemingly random temporal duration. Furthermore, and as shown in figures 5.18b and c, if part of the curve is magnified, the resulting curve looks very similar to the original one—curves with similar properties have been obtained for all simulated cases. Of course, and as clearly demonstrated in figure 5.18c, magnification continues to reveal similarity at smaller scales up until we reach the resolution of our discrete simulation, which is determined by the total number of particles and the size of the time increment.

The structure of the curve shown in figure 5.18 is strikingly similar to the so-called Devil's staircase (Bak 1986), a fractal curve that has been found to emerge in a number of nonlinear systems, in both physics and engineering, undergoing a mode-locking transition to chaos. In such systems, the staircase has been shown to describe the dynamical behavior as a function of frequency with the characteristic plateaus indicating locking at various rational frequencies (for specific examples see: Bak 1986; Lacis, Barci, Cebers, and Perzynski 1997; Reinchhardt and Nori 1999). Moreover, Lai, Zyczkowski and Grebogi (1999) have recently showed that the devil-staircase characteristic is the universal behavior in the parametric evolution of certain properties of chaotic saddles of non-linear dynamical systems.

The defining characteristic of the staircase, which also led to its name, is that between any two of its plateaus there is an infinite number of steps. Its mathematical construction is closely linked with the Cantor set and this relation is clearly evident in the computed curve shown in figure 5.18. Consider the time axis in this figure and remove all the intervals corresponding to fixed particle populations. What remains is a Cantor

set, that is, a set of points that has measure zero but, as we will subsequently show, finite fractal dimension. Of course a true Cantor set will be obtained in our case only in the limit of infinite number of particles and as the time increment approaches zero.

Most of the physical applications of the staircase described in Bak (1986) involve dissipative systems with two competing frequencies where mode-locking occurs. In the present case, therefore, the Devil's staircase emerges for the first time in an autonomous, three-dimensional, volume-preserving dynamical system that is spatially chaotic. The randomly varying lengths of its plateaus explain the emptying process of the breakdown bubble discussed previously in Section 5.5. The initial particle population decays in time by sampling, as one would expect, all possible states, that is all integer numbers from the initial population to zero, but the temporal interval that the population remains fixed at a particular level varies randomly from level to level. Consequently the long plateaus would appear as pauses in the emptying process while a sequence of several consecutive short plateaus will result in what we previously described as a bursting event. We should emphasize that in the present simulation, with a finite set of discrete particles, the number of steps of the staircase can not be infinite but rather equal to the total number of particles that enter the bubble in a given simulation. Only in the continuum limit we would anticipate that an initial tracer concentration will decay to zero by sampling, for random time intervals, the infinite sequence of all rational numbers between the initial concentration level and zero, thus, yielding a true devil's staircase distribution.

In spite of the finite resolution we employ by specifying a fixed particle population, we can still demonstrate the fractal nature of the computed curve without having to perform simulations for an infinite number of particles. To accomplish this, we

calculate herein the fractal dimension of the Cantor set associated with the staircase shown in figure 5.18. The procedure we employ is that described in Bak (1986). We choose a given time interval *r* and calculate the total width *T(r)* of all plateaus that are larger than *r*. We are interested in the space in between the plateaus, T_{max}-*T(r)*, which eventually shrinks into a Cantor set (T_{max} is the maximum residence time in our discrete simulation). To measure this space we define the total number *N* of "holes" of size *r*, given by:

$$N(r)=\frac{T_{\max}-T(r)}{r}. \tag{5.2}$$

If the variation of *N(r)* versus (*1/r*) on a log-log scale is linear, then:

$$N(r)\approx\left(\frac{1}{r}\right)^{d} \tag{5.3}$$

where *d* is the slope of the resulting straight line. That is, the space between the plateaus vanishes as r^{1-d} at $r \to 0$ and the devil's staircase is complete (Bak 1986). The exponent *d* is the fractal dimension of the Cantor set, which is complimentary to the set of plateaus comprising the devil's staircase.

In figure 5.19, we plot on a log-log scale *N* vs. (*1/r*) for the two staircases obtained from the $n = 10^3$ and $n = 3\text{x}10^4$ simulations, respectively. We include both of these simulations in order to explore the sensitivity of the so computed fractal dimension to the number of initial particles. For both simulations, we find that a straight line with slope $d = 0.4$ fits well all points over a broad range of plateau sizes—approximately 2.3 and 3.0 orders of magnitude variation in *r* for the $n = 10^3$ and $n = 3\text{x}10^4$ cases, respectively. Note, however, that increasing the number of particles results in dramatic

improvements for small values of r and in smoother overall linear variation. We should also note and comment on the apparent departure of the calculated points for the $n = 3x10^4$ case from the linear variation as r approaches large values (see figure 5.19). This trend is an artifact of our incomplete, for this case, numerical simulation. Due to the asymptotic nature of the curve shown in figure 5.18, larger plateaus tend to appear more frequently when relatively few particles remain in the bubble. Since many of these last remaining particles could have arbitrarily long residence times (see previous section), continuation of the time integration long enough for all particles to exit requires excessive computational resources—especially for the large number of particles used in this refined simulation. For that reason we had to terminate the particle integration when approximately 4000 particles were still remaining in the interior of the bubble. Consequently, the so computed staircase does not contain sufficiently many large size plateaus for the linear variation of N to be sustained at larger r sizes. To prove that this is indeed the reason for the observed departure from linearity, we also include in figure 5.19 the curve that resulted when the $n = 10^3$ simulation, which was actually carried out until all particles exited (t=2660), was terminated at a much earlier time (t=128)—only 100 particles were left inside the bubble at t=128 and, thus, more than 2500 secs of additional simulation were required for these few remaining particles to exit. Clearly, reducing the integration time results in the same departure from linear variation at larger values of r as that observed for the $n=3x10^4$ simulation. This small discrepancy not withstanding, figure 5.19 provides conclusive evidence that the curve shown in figure 5.18 is a complete devil's staircase with fractal dimension $d = 0.4$ (see subsequent discussion for the variation of d with Reynolds number and aspect ratio) Interestingly,

this value of the fractal dimension is lower than the *d=0.87* "universal" constant (Bak 1986) that has been previously found in a number of dissipative dynamical systems undergoing mode-locking transition to chaos.

To further explore the statistical properties of the devil's staircase curve, we plot in figure 5.20 the calculated (for the staircase shown in figure 5.18) frequency of occurrence, *S(r)*, of the various plateau sizes (i.e. the waiting times between bursting events) as a function of the plateau size *r*—i.e. the histogram of *r*. Figure 5.20 shows that the frequency of occurrence diminishes monotonically as the plateau size increases. Furthermore, a power law of the form:

$$S(r) \approx \left(\frac{1}{r}\right)^{a} \tag{5.4}$$

with $a = 1.4$ appears to fit well the computed data points. Note that a power-law distribution for *S* is consistent with the nature of the devil staircase, as plateau sizes of zero length correspond to the points of the complimentary Cantor set and should, thus, be infinitely many. It is also important to point out that the apparent relation between the fractal dimension *d* and the exponent *a* ($a = 1 + d$) is not coincidental. Assuming a continuous function $S=S(r)$ of the form given by equation (6) and noting that *T(r)* (the total length of plateaus with size greater than *r*) can be computed from *S* as follows (r_{max} is the size of the largest plateau):

$$T(r) = \int_{r}^{r_{\max}} r' S(r') dr' \tag{5.5}$$

we can easily show that the number of holes *N* of size *r* defined by equation (4) is given by the following equation:

$$N = \frac{1}{r} \int_0^r r' S(r') dr' \approx \left(\frac{1}{r} \right)^{a-1} \tag{5.6}$$

Comparison with equation (5.3) yields the relation implied by the numerical values in figures 5.19 and 5.20, i.e. $d = a\text{-}1$. In other words, the fractal dimension of the complimentary Cantor set can also be calculated from the histogram of plateau sizes.

To investigate whether the fractal dimension of the staircase varies with the governing parameters of this flow (H/R and Re), we carried out computations similar to those described above but for the two bubbles shown in figure 5.15 (Re = 1,492 and 1,667 for H/R=2). Both simulations were carried out using 30000 initial particles. Our computations reveal that the fractal dimension decreases with Reynolds number from 0.69 to 0.55. As we have already discussed above, however, the limited number of cases considered herein do not allow us to establish any meaningful trends. Computations over a much broader range of Reynolds numbers and aspect ratios will be needed before such trends can be extracted.

Finally, it is important to point out that our findings in this and the previous sections, point to the conclusion that the infinite intersections of the stable and unstable manifolds of the spiral-in saddle, through which upstream originating particles enter and exit that bubble, exhibit a fractal spatial structure. Since chaotic Šil'nikov orbits will have to exit through this fractal "window", their exit time will be extremely sensitive to arbitrarily small differences in the particle initial location, and, thus, the resulting fractal structure in the residence time maps and the variations in the sizes of the devil staircase plateaus.

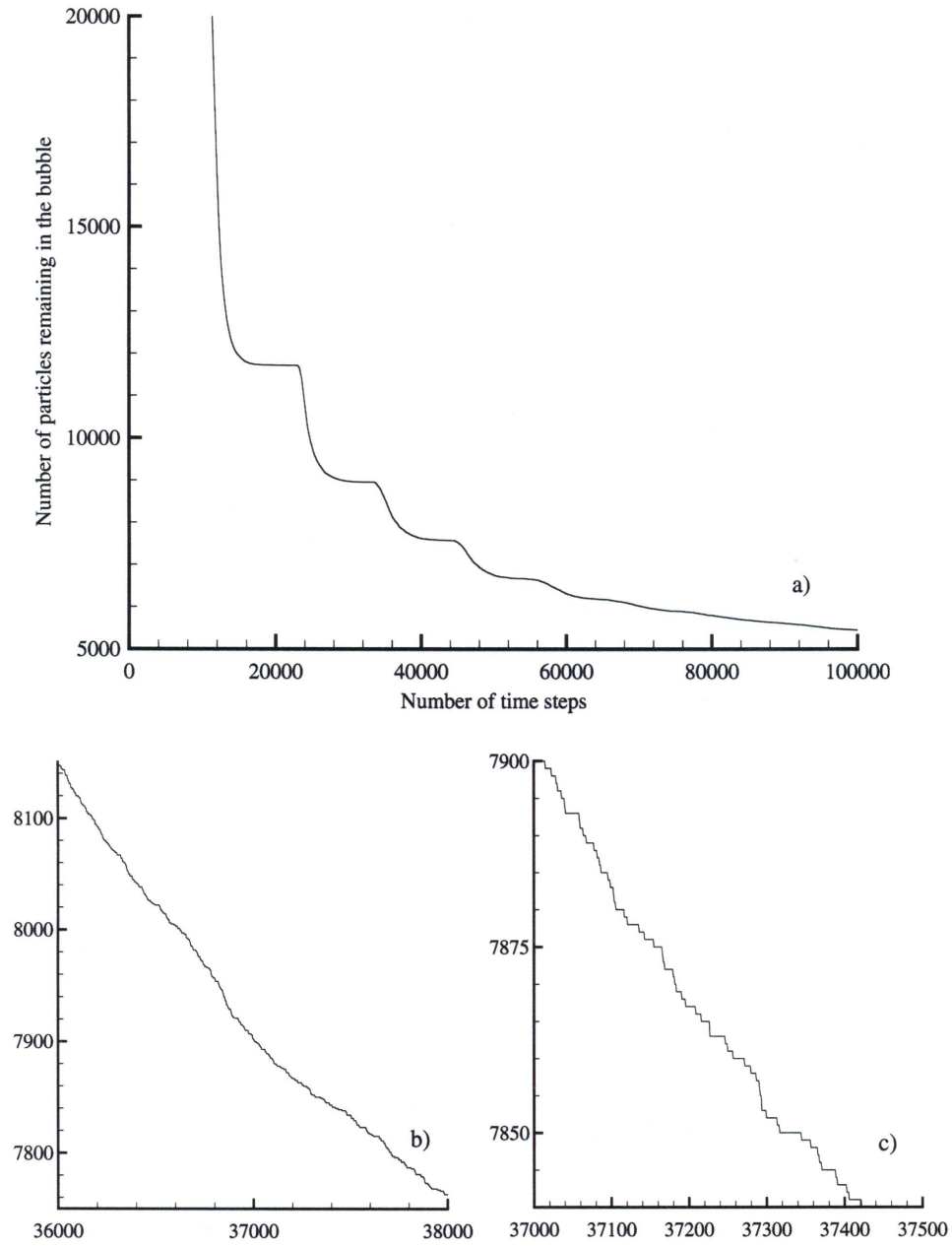

Figure 5.18 Emptying of a calculated stationary vortex breakdown bubble (Re=1850, H/R=1.75). $3x10^4$ particles are distributed along a small disk located just upstream of the bubble. The number of particles remaining in the bubble is plotted as a function of time. Increasing time resolution shown in a)-c).

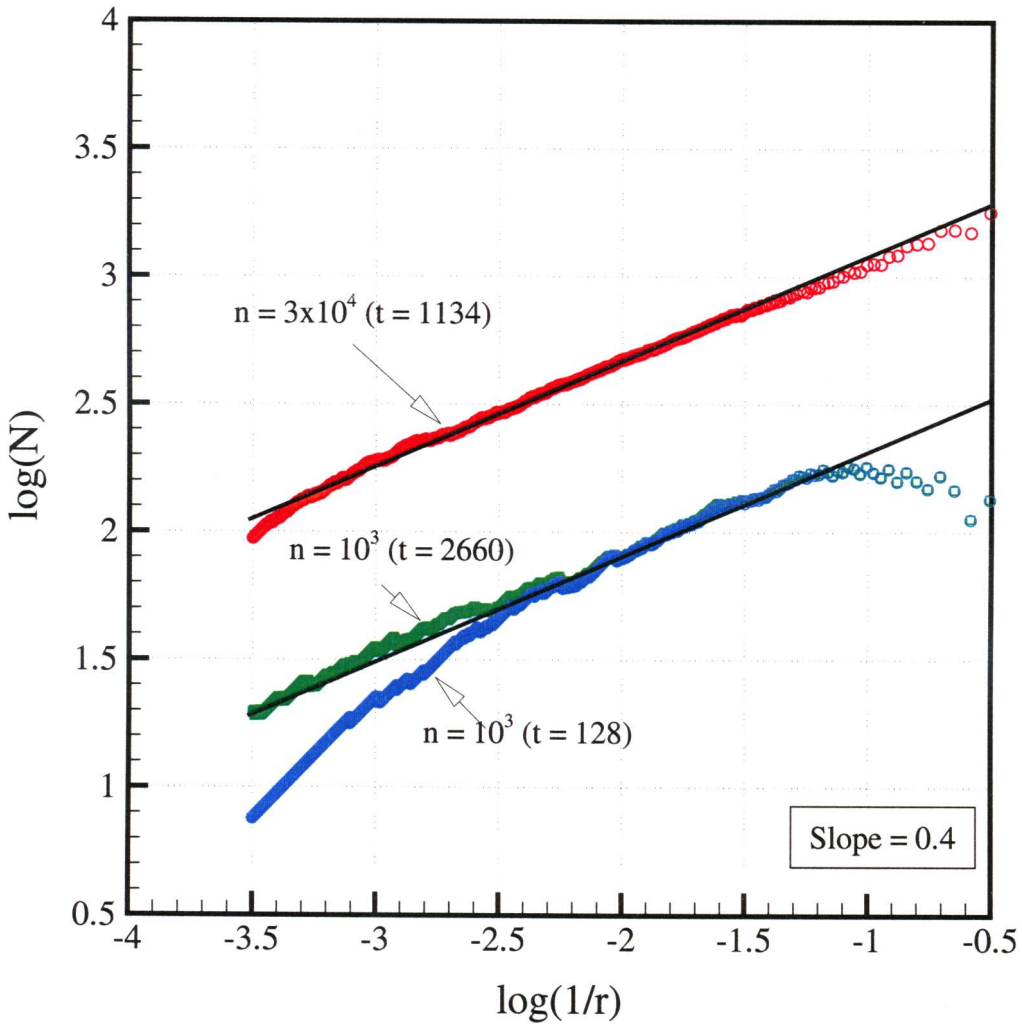

Figure 5.19 Fractal dimension of the Cantor set associated with the devil's staircase shown in figure 5.18. The number of particles used in the simulation is n and the simulated time interval for each case is t.

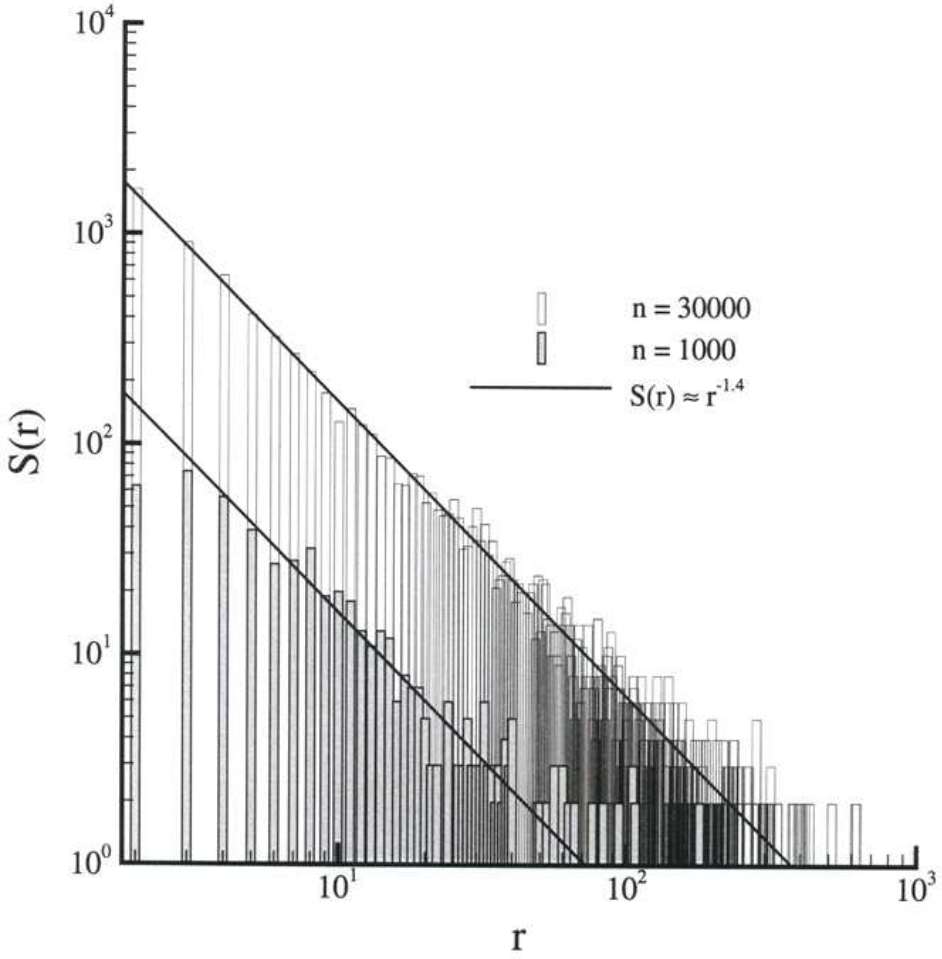

Figure 5.20 Histogram of the staircase plateau sizes for the staircases used to calculate the fractal dimensions in figure 5.19.

5.6.4 Dynamics of the Second Bubble in the Steady Two-Bubble Regime and the Role of Swirl Intensity

As has been stated previously, dependent on the aspect ratio and Reynolds number (see figure 5.3) one, two, three, or no bubbles are possible. In this section the dynamics of the second or bottom bubble formulated in the two-bubble regime is discussed. Figure 5.21 shows to the left a streamline of the two-bubble vortex breakdown case, where the aspect ratio is two and the Reynolds number is 1900. The dynamics of the first bubble are known to be quite similar to the previously seen one bubble Re=1850 (AR=1.75) case (Sotiropoulos et al 2002). From the Poincaré map shown on the right-hand-side of figure 5.21, it is immediately clear however that the dynamics of the second vortex breakdown bubble are quite different than what has been discussed previously.

The second bubble seems to be almost perfectly axisymmetric and is formed by a series of invariant surfaces. This is consistent with previous laboratory experiments (Escudier 1984, Sotiropoulos et al 2002). In Escudier's photographs, the dye used to visualize the flow does not penetrate the interior of the second bubble to the extent that it does the first. Sotiropoulos et al (2002) developed experimental Poincaré maps that agree with the representation, showing the closed invariant tori in the second bubble while displaying the extremely complex dynamics of the first bubble with its various periodic islands chains and KAM-tori.

An explanation of the almost axisymmetric form of the second vortex breakdown bubble in comparison with the first bubble is developed by considering the previously described system (equations 5.1) whose phase space dynamics are similar to the

Lagrangian dynamics of real-life steady vortex breakdown bubbles. The parameters μ_1, μ_2, a, and b of the system are set to 0,-1.96, 1, and -1 respectively, creating the system:

$$\frac{dz}{dt} = 0.04 - r^2 - z^2 + \varepsilon r^3 \sin(2\theta); \qquad \frac{dr}{dt} = rz; \qquad \frac{d\theta}{dt} = \varpi \tag{5.7}$$

In this system ω is the angular velocity and ε controls the magnitude of the term representing the higher order terms that perturb the system and excite the modes of instability. The arbitrarily chosen perturbation field is a mode-2 azimuthal disturbance in the axial velocity component and is designed to ensure that the perturbed system also remains volume preserving. Although the above velocity field does not satisfy the Navier-Stokes equations, it is useful because the qualitative dynamics are similar to the real life vortex breakdown bubble. In particular, this system will provide a further understanding of the effect of adding perturbations to the system than that gained in section 5.4 as well as the effect of swirl parameter.

Figure 5.22 shows numerically constructed Poincaré maps for various ω and ε values. The particle paths were calculated using the same numerical method, time-increment, and a velocity field discretized on the same computational mesh. A Cartesian 51x51x51 box containing the bubble was used as the computational domain. The first set of computations (figures 5.22a to figure 5.22c) maintains a constant swirl (ratio of azimuthal to axial velocity components) but varies the magnitude of the perturbation affecting the flow. The second set of computations (figures 5.22d to figure 5.22f) maintains constant magnitude of perturbation but increases the swirl parameter.

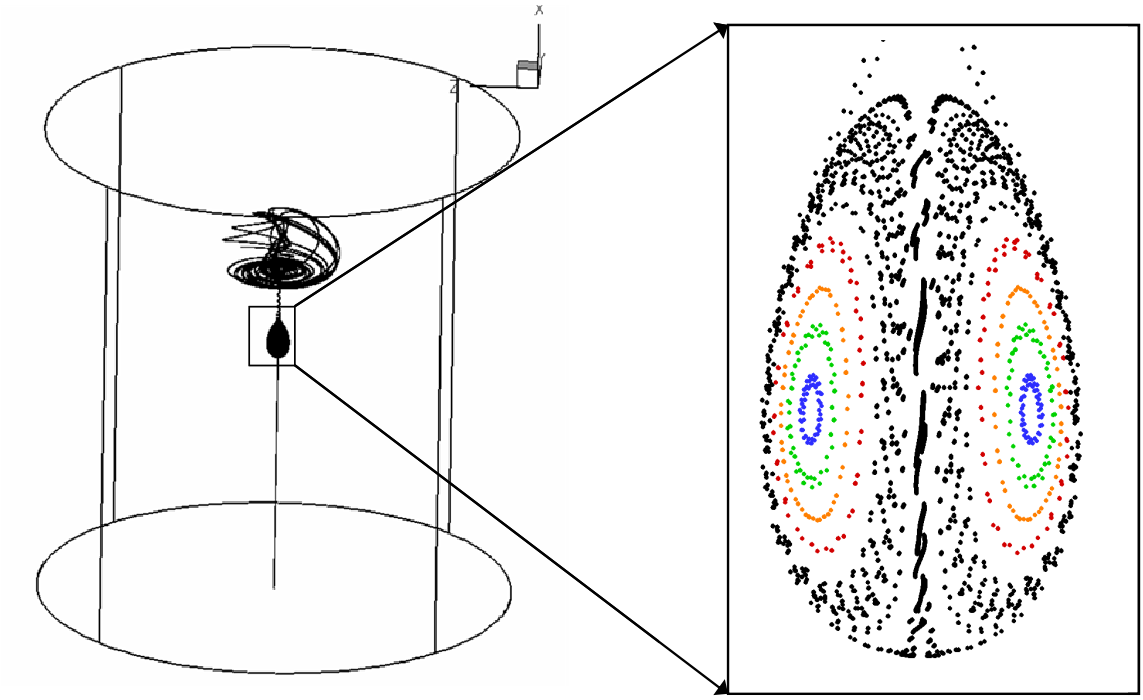

Figure 5.21 Poincare map of lower vortex breakdown bubble in the two bubble regime (Re = 1900, AR=2). To the left are three-dimensional streamlines that show the bubble structure.

Figure 5.22a shows the unperturbed case: ω=0.5 and ε= 0. In this case, the bubble appears to be perfectly axisymmetric. The interior of the bubble contains an uncomplicated series of invariant KAM-tori. A small region along the axis exists that shows chaotic characteristics but can be attributed to numerical chaos due to disturbances introduced by the trajectory integration scheme. It is not possible to eliminate this small region even if the time step is reduced by an order of magnitude. Broer and Vetger (1984) predicted this finding in their theoretical analysis, which showed that exponentially small disturbances could be sufficient to lead to Sil'nikov chaos.

Figures 5.22b and c show the effect of increasing the magnitude of the perturbation for fixed swirl. As ε is increased to 0.1 in (b) the invariant tori begin to break. Periodic islands form and the chaotic region increases. As it is increased even further to 0.5 in (c) the bubble gains similar characteristics to that of experimentally visualized and numerically calculated vortex breakdown bubbles shown previously. Folds form along the bottom of the bubble exterior and the dynamics of the interior become increasingly complex, showing: islands, cantori and KAM-tori.

Figures 5.22 (d) through (f) illustrate the effect of increasing the swirl for the value of ε=0.5. Note that since the asymmetric perturbation is only introduced in the axial velocity field, the axial and radial velocity components are identical for all the maps shown in the figures. This means that from an Eulerian standpoint, the only difference between the three flow fields is the magnitude of the angular velocity. As this value is increased, a dramatic effect is discovered. The chaotic characteristics of the bubble are damped. The folds disappear and the invariant toroidal region increases in size. As the swirl intensity is increased to ω=1.0, the chaotic Sil'nikov column around the axis shrinks

to a very thin region and for all purposes disappears at a value of ω=2.0. This result leads to the conclusion that even though the velocity field can be three-dimensional, at sufficiently high swirl velocities the Lagrangian dynamics are identical to those of the unperturbed, axisymmetric flow. High swirl velocity has a stabilizing effect on the Lagrangian dynamics. This is similar to the effect that strong rotation has on Eulerian turbulence.

Now applying this analysis to the two bubble regime for the computed vortex breakdown case (see figure 5.23), it is possible to infer explanations about the differences in the dynamics of the first and second bubble. The numerical calculations show that the axial velocity component in the downstream region of the first bubble is approximately one order of magnitude smaller than the axial velocity upstream of the bubble. Since the azimuthal velocities do not vary significantly along the axial directions in the vicinity of the two bubbles, the variations of the axial velocity result in swirl ratios that are larger upstream of the second bubble than upstream of the first bubble. Therefore the well-ordered and nearly axisymmetric appearance of the second bubble is in fact due to the larger swirl value.

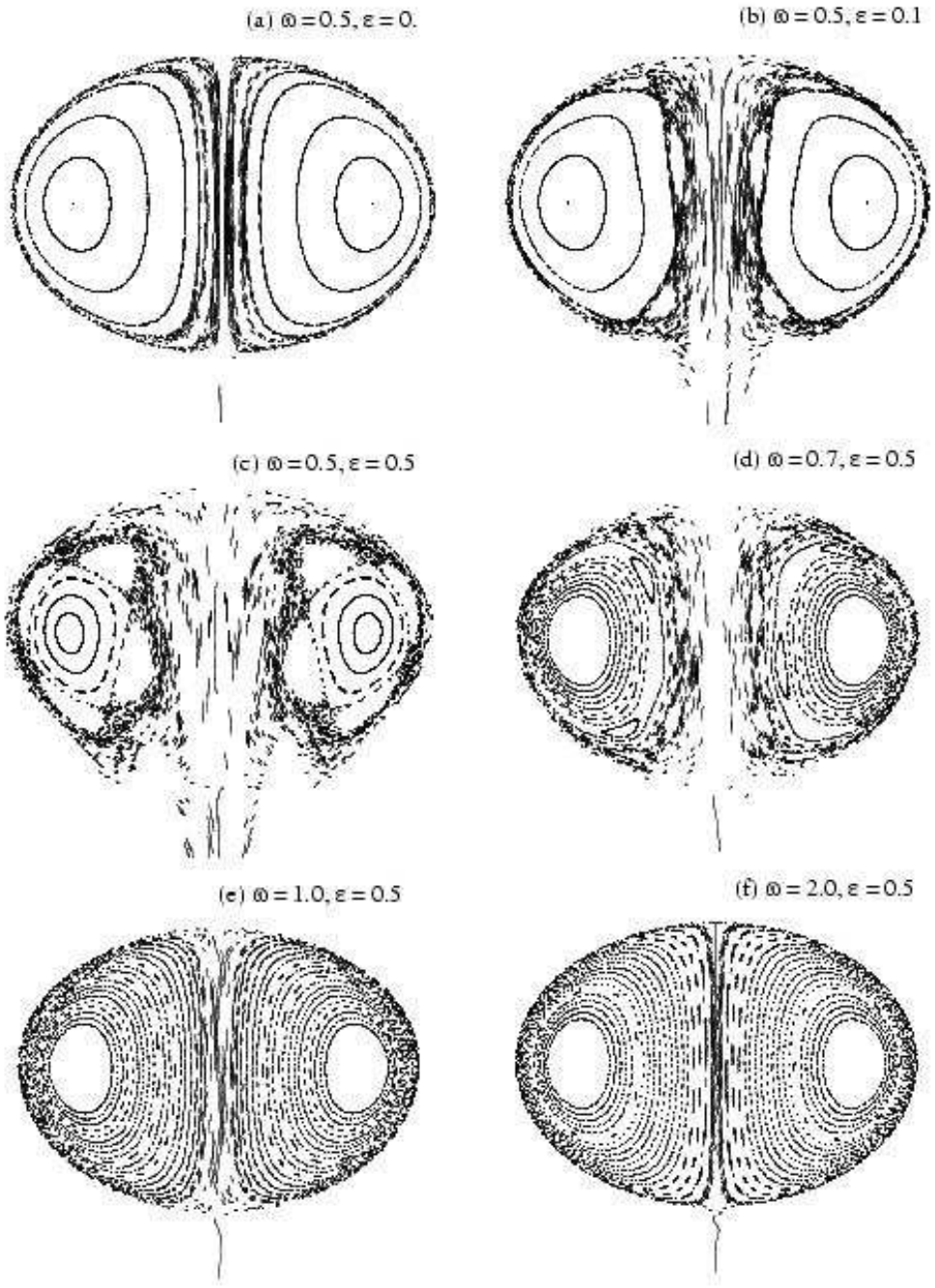

Figure 5.22 Poincare maps for the system given by equation 5.1 for various levels of perturbation strength ε and swirl intensity ω.

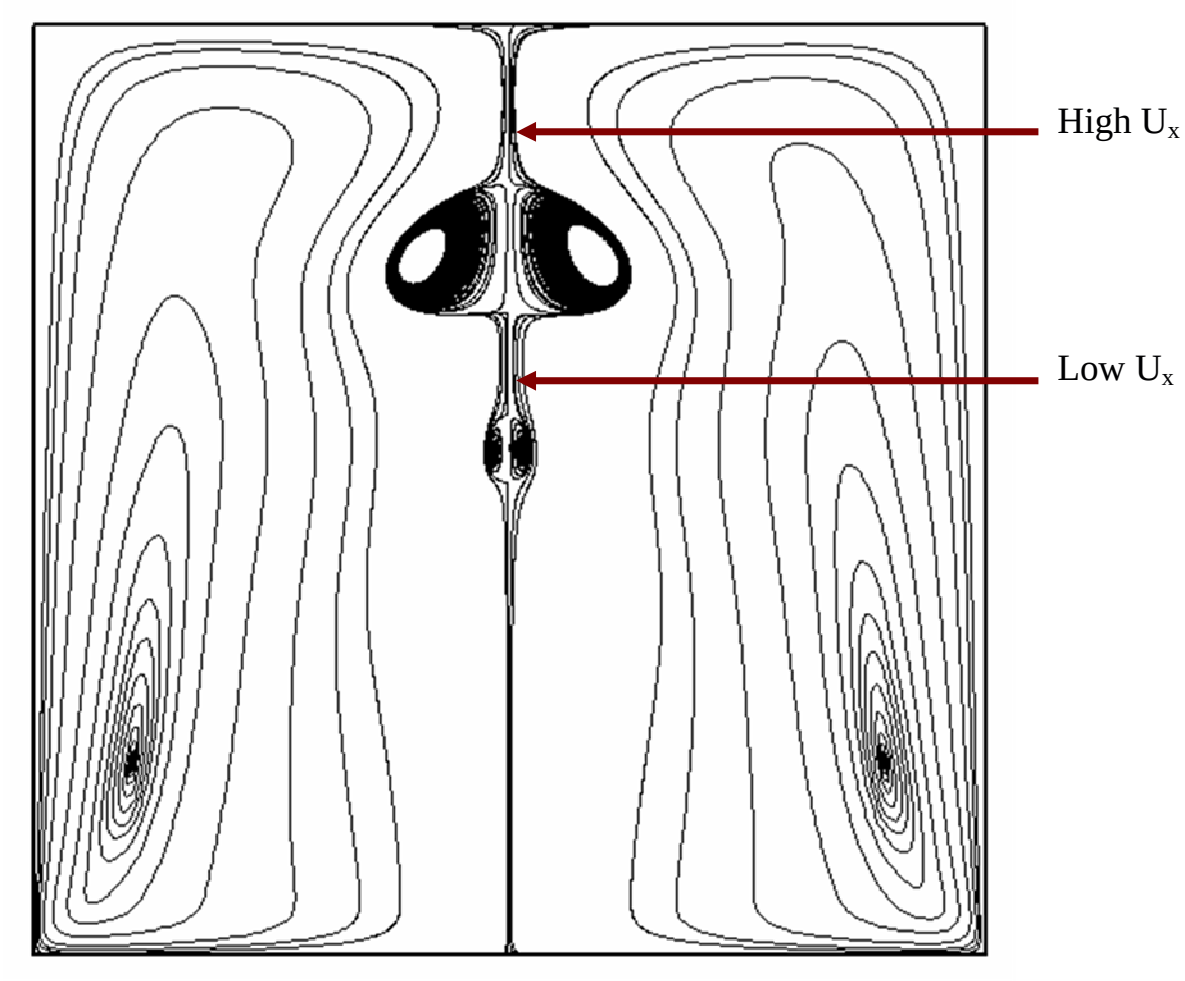

Swirl Ratio=$|U_\theta/U_x|$

Figure 5.23 Axisymmetric streamlines in the two bubble regime depicting positions of high and low swirl ratio.

5.7 Summary

In this chapter we analyzed the Lagrangian properties of steady vortex breakdown bubbles in a closed cylindrical container with rotating bottom lid. The vortex breakdown flowfields were obtained by solving numerically the Navier-Stokes equations. We showed that even though from the Eulerian viewpoint the simulated flowfields are steady and nearly axisymmetric the Lagrangian dynamics could be rich. We developed links with the theory of dynamical systems, which suggested that Silnikov's mechanism plays a critical role in breaking up the invariance of the bubble and giving rise to chaotic dynamics. We also showed that the interior of perturbed vortex breakdown bubbles exhibits Lagrangian richness consistent with what one would anticipate for a mildly perturbed, volume preserving system. Impermeable KAM-tori, leaky cantori, and unmixed island chains are found embedded within chaotically stirred regions. Upstream originating particles enter the bubble from the downstream saddle focus and a Cantor set of initial conditions could stay in the interior of the bubble for arbitrarily long times. Another important feature of the flow is that particles exit the bubble in random bursts and that the rate at which an initial population of particles exits the bubble is a Devil's staircase. By examining the dynamics of a model dynamical system we also reached the striking conclusion that vortex breakdown bubbles, occurring at sufficiently high swirl numbers, exhibit integrable (axisymmetric) dynamics even in the presence of non-axisymmetric perturbation in the advecting velocity field. All our computational findings in this chapter are supported fully by the recent experimental work of Sotiropoulos et al. (2002).

Our findings in this chapter have important implications for understanding the phenomenon of vortex breakdown and the interpretation of the results of laboratory visualization experiments. The finding that for a certain range of swirl numbers very small non-axisymmetric perturbations can have a profound effect on the Lagrangian properties of the bubbles points to the conclusion that it could be very difficult, if not impossible, to visualize perfectly axisymmetric vortex breakdown flowfields in a laboratory experiment. This conclusion explains why axisymmetric computations of the flow can capture correctly most features of vortex breakdown but fail to resolve the asymmetries observed in the laboratory flow visualization experiments. Even though the real-life and ideal (axisymmetric) flowfields are very similar from the Eulerian standpoint, their Lagrangian descriptions are as fundamentally different as order and chaos. The finding concerning the role of swirl intensity on the Lagrangian dynamics further suggests that stirring intensity in the interior of vortex breakdown bubbles could be controlled by varying a simple Eulerian property of the flow, the ratio of the swirl to axial velocity upstream of the bubble. With further work, this finding could lead to a rigorous framework for controlling mixing efficiency and the residence time distribution in vortex breakdown bubbles in flows of technological significance.

CHAPTER 5

CONTAINER WITH ROTATING BOTTOM LID: FLOW WITHIN A VORTEX BREAKDOWN BUBBLE

In the early 1900's Theodore von Karman began what has become a century of exploration in which researchers have sought to describe and understand the multi-faceted aspects of a class of flows bounded by rotating disks. The confined flow of an incompressible fluid in a cylindrical container with rotating bottom lid is perhaps the most widely studied and least understood von Karman flow. Although this flow has been investigated both experimentally and computationally for well over three decades, it is only recently that in depth insights into its extremely rich Eulerian and Lagrangian dynamics have begun to emerge. The first experimental investigations of this flow were reported by Vogel (1968) and Ronnenberg (1977) who explained that Ekman suction and pumping, induced by the Ekman layers on the rotating and stationary disks, drive a meridional flow and lead to the formation of a concentrated vortex core along the axis. Depending on the container aspect ratio (height to radius ratio) and Reynolds number, this vortex core could undergo vortex breakdown, evolving into one or more recirculating bubbles along the centerline axis. Because vortex breakdown occurs, in this case, within a contained, well-defined system, the flow within a cylindrical container with rotating bottom lid has become an important test case to understand various aspects of this

complex fluid mechanics phenomenon, which also occurs, among others, in flows over a delta wing, in swirling combustion chambers, and in some geophysical flows.

In this chapter, we seek to investigate numerically a number of important questions regarding the Lagrangian properties of steady vortex breakdown bubbles using some of the dynamical systems tools and concepts presented in Chapter 2. To accomplish this goal, the problem is approached systematically. First the flow geometry is described and a brief review of previous work regarding this flow is presented. After which, the basic topology of vortex breakdown bubbles is outlined and the potential effect of even very small stationary, three-dimensional perturbations on the Lagrangian dynamics are discussed using dynamical systems theory. Subsequently we analyze the Lagrangian properties of numerically generated flowfields using dynamical systems tools to show that the rich dynamics predicted by the theory indeed occur in the real flow and to reconcile various contradictory views that have been expressed in the literature concerning the axisymmetric character of steady vortex breakdown bubbles. Results are presented for Reynolds numbers ranging from 1492 to 1900 and aspect ratios of 1.75 and 2.0.

5.1 Flow Geometry

We consider flow in a closed cylinder of radius R and height H, which is filled with incompressible fluid of viscosity ν and density ρ. The bottom lid of the cylindrical container rotates with constant angular velocity Ω and the top lid is stationary. The flow is governed by two non-dimensional parameters, the Reynolds number ($Re=\Omega R^2/\nu$) and

the aspect ratio (H/R). Similarly to the unconfined rotating disc flow analyzed by von Karman (1921), the rotation of the bottom lid behaves as an Ekman pump, drawing in fluid vertically downward toward the rotating lid and driving it radially outward in along spiral trajectories. The fluid spirals upward along the sidewall, converges radially inward when it reaches the top lid and is injected vertically downward along the axis to close the loop. The radially inward spiraling motion along the stationary lid results in an initial increase in swirl velocity, due to the conservation of angular momentum, and creates a concentrated vortex core along the container axis with downward (from the stationary to the rotating lid) axial flow. Over a range of governing parameters the ideal (unperturbed) flow is steady and axisymmetric and the flow domain is foliated by a series of embedded invariant toroidal surfaces, the stream-surfaces of the axisymmetric flow—(see figure 5.1)

Vogel (1968, 1975) was the first to discover that depending on Re and H/R the vortex core along the centerline axis undergoes vortex breakdown (see figure 5.2). The streamline topology of vortex breakdown bubbles consists of an upstream stagnation point followed by a closed recirculation zone followed by another stagnation point. Under ideal conditions, a steady vortex breakdown bubble should be axisymmetric. As we will subsequently show, however, this ideal flow structure may be extremely difficult to realize in the laboratory as even small experimental imperfections could have a profound effect on the Lagrangian dynamics of the flow in the interior of vortex breakdown bubbles.

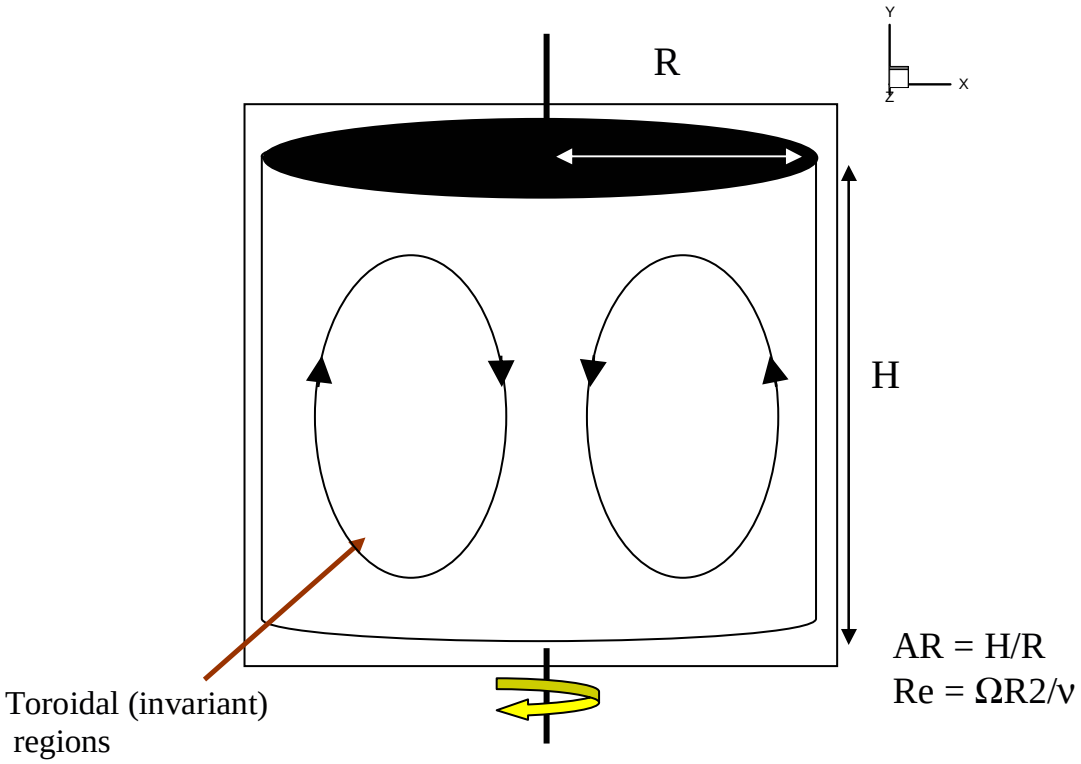

Figure 5.1 Flow geometry for cylindrical container with rotating bottom lid.

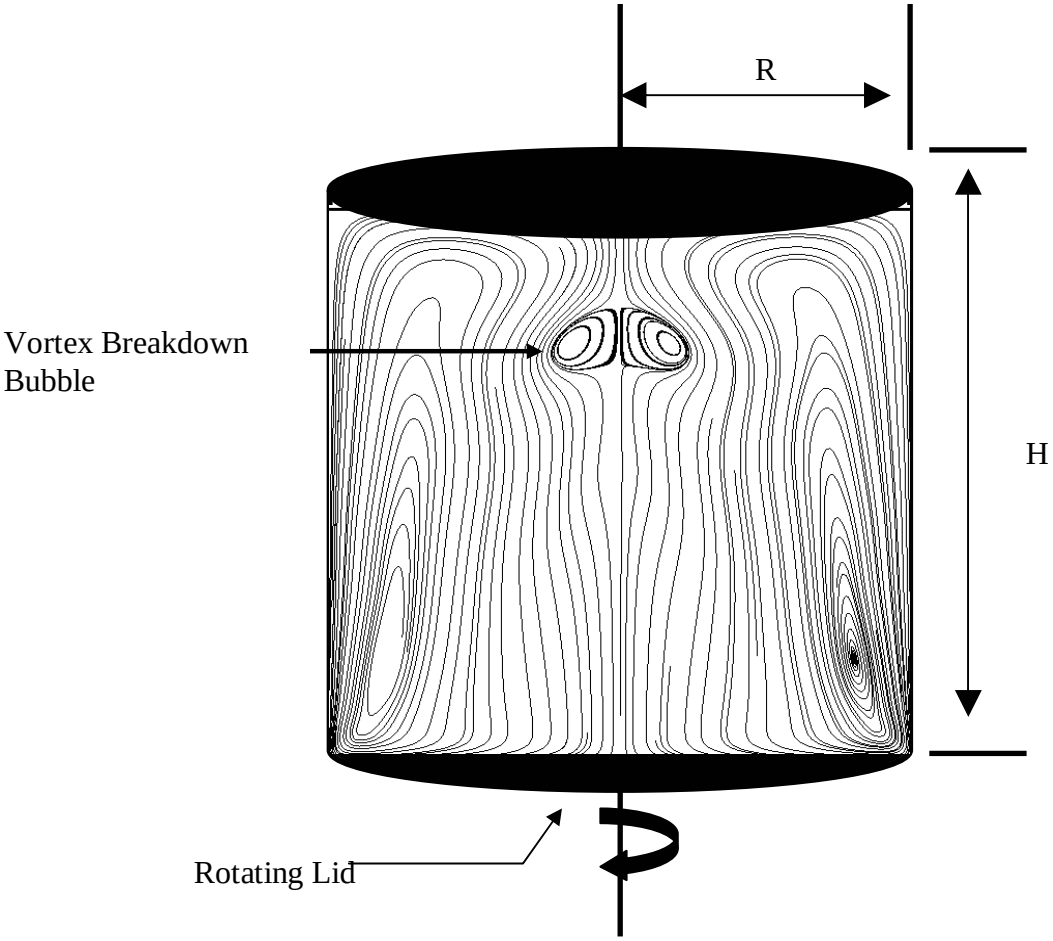

Figure 5.2 Surface streamlines for the vortex breakdown for Re=1850, AR=1.75

5.2 Previous Research

Although the problem has been considered for almost forty years, the first comprehensive flow visualization experiments for the flow within a cylindrical container with rotating bottom lid were performed only twenty years ago by Escudier (1984, 1988). In this extensive study Escudier considers the effect of both aspect ratio and Reynolds number on vortex breakdown bubbles. He develops the thresholds at which different numbers of vortex breakdown bubbles might occur and whether or not they will be in the steady or unsteady regime (see figure 5.3). Later Sorenson (1992) repeated the same experiments over a larger range of rotational speeds. Spohn, Mory, and Hopfinger (1993) considered the case of vortex breakdown bubbles in containers with free surfaces and later go on to (1997) address the confined cylinder case. Recently Liu et al (2000, 2001) performed a series of experiments using LDA (Laser Doppler Anemometer) to obtain quantitative measurements for this flow.

In many of these experiments it was observed that even within the steady flow regime, where the flow was expected to be axisymmetric, there were distinct asymmetries that seemed to persist in all visualization experiments (Escudier 1984; Spohn et al 1993; Hourigan et al 1995; Stevens et al. 1999; Fujimura, Koyama and Kyun 1997). In the Escudier experiment, for instance, dye is clearly seen to have entered into the interior of the vortex breakdown bubbles, which if they were axisymmetric would have been invariant and, thus, inaccessible by the surrounding flow. Another distinct feature that is present in Escudier's and all other visualization experiments is the existence of distinct asymmetric folds at the downstream end of the bubbles. Hourigan et al (1995) attempted

to explain these asymmetries by arguing that they are artifacts of the visualization technique and should be attributed to the inability to inject the dye precisely on the container axis. Supporting the idea of axisymmetric flow were a multitude of numerical investigations over the years, which solved the axisymmetric Navier-Stokes equations (Pao 1970; Lugt and Haussling 1997, 1982; Dijkstra and Heijst 1983; Lugt and Abboud 1987; Lopez 1990; Gelfgat et al 1996; Stevens et al 1999, etc). In these computations, the general flow characteristics (the size, position, and basic shape) of the vortex breakdown bubbles were accurately captured. In addition, these studies were also able to reproduce the variations of the general flow patterns with respect to the Reynolds number and aspect ratio. An example of one such calculation can be seen in figure 5.4 taken from Lopez (1990), which compares an experimental visualization image of vortex breakdown bubbles with the streamlines obtained from their axisymmetric flow computations. The computations capture correctly the shape, size and location of the bubbles but, as one would anticipate, fail to reproduce the distinct asymmetric folds observed in the laboratory images at the downstream end of the first bubble.

Spohn, Mory, and Hopfinger (1998) were the first to attempt to investigate experimentally in a systematic manner the nature of the asymmetries in the flow by examining the flow surrounding the vortex breakdown bubble. Their flow visualizations clearly show the steady, vortex breakdown bubbles to be asymmetric and open at their downstream end, a finding which conflicts with an axisymmetric flow. Spohn et al. (1998) argued that the origin of these flow asymmetries should be traced to asymmetries of the flow inside the wall boundary layers as their flow visualization images showed that above a threshold Reynolds numbers the sidewall boundary layer becomes three-

dimensional and spiral separation lines develop occurs. However the fundamental understanding of the cause of the three-dimensional flow characteristics of vortex breakdown bubbles remained incomplete.

Interestingly the theoretical framework that allows us to reconcile the seemingly conflicting views about this flow were laid out over a decade prior to the Spohn et al (1998) experiments when Holmes (1984), in a not very well known article, suggested that vortex breakdown bubbles could display chaotic Lagrangian dynamics. Holmes raised the intriguing possibility (see section 5.4 for a detailed discussion) that the invariant manifolds connecting the upstream and downstream fixed hyperbolic points of the flow could be sensitive to even extremely small perturbations to the flow. Holmes considered the effect of arbitrarily small time-dependent perturbations to the base axisymmetric flow. At approximately the same time, however, Broer and Vetger (1984) in a separate purely theoretical study considered the effects of arbitrarily small, stationary, three-dimensional perturbations to a dynamical system whose manifold topology is identical to that of a vortex breakdown bubble. Broer and Vetger showed that such perturbations can break the invariance of the bubble surface and lead to the creation of asymmetric folds similar to those observed in laboratory visualization experiments of vortex breakdown bubbles. It is important to note that Broer and Vetger made no connection between their findings and the phenomenon of vortex breakdown. Their findings, however, clearly suggest that even though from an Eulerian viewpoint the flow inside a vortex breakdown bubble could be considered steady and axisymmetric, its Lagrangian dynamics, which is what one visualizes in a laboratory experiment, could be quite different and very rich.

In a recent numerical study Sotiropoulos and Ventikos (2001) solved numerically the three-dimensional Navier-Stokes equations using a curvilinear mesh to discretize the container. They were able to reproduce the three-dimensional characteristics seen in the laboratory experiments of Spohn et al. (1998), including all asymmetric features of the vortex breakdown bubbles and the formation of spiral separation lines along the cylindrical wall of the container (see also Sotiropoulos and Ventikos 1998). Sotiropoulos and Ventikos further showed that the flow in the interior of steady vortex breakdown bubbles exhibit chaotic particle paths, thus, establishing for the first time a firm link between the complexities documented in the laboratory visualization experiments of this flow and the earlier theoretical findings of Holmes and Broer and Vetger. Note that in the numerical simulations of Sotiropoulos and Ventikos the curvilinear mesh they employed introduced a small non-axisymmetric forcing on the flow, which, they argued, emulated collectively the disturbances that are bound to occur in any laboratory set-up (Sotiropoulos and Ventikos 2001). It was this imposed, small, non-axisymmetric forcing that yielded vortex breakdown flowfields essentially axisymmetric from the Eulerian standpoint but resulted in the very rich Lagrangian dynamics observed in the laboratory experiments. In what follows, we develop firm links between the findings of Sotiropoulos and Ventikos (2001) and the theory of dynamical systems and carry out a comprehensive investigation of the rich Lagrangian dynamics of the flow in vortex breakdown bubbles. Much of the work presented below has already been published in two journal papers by Sotiropoulos et al. (2002, 2003).

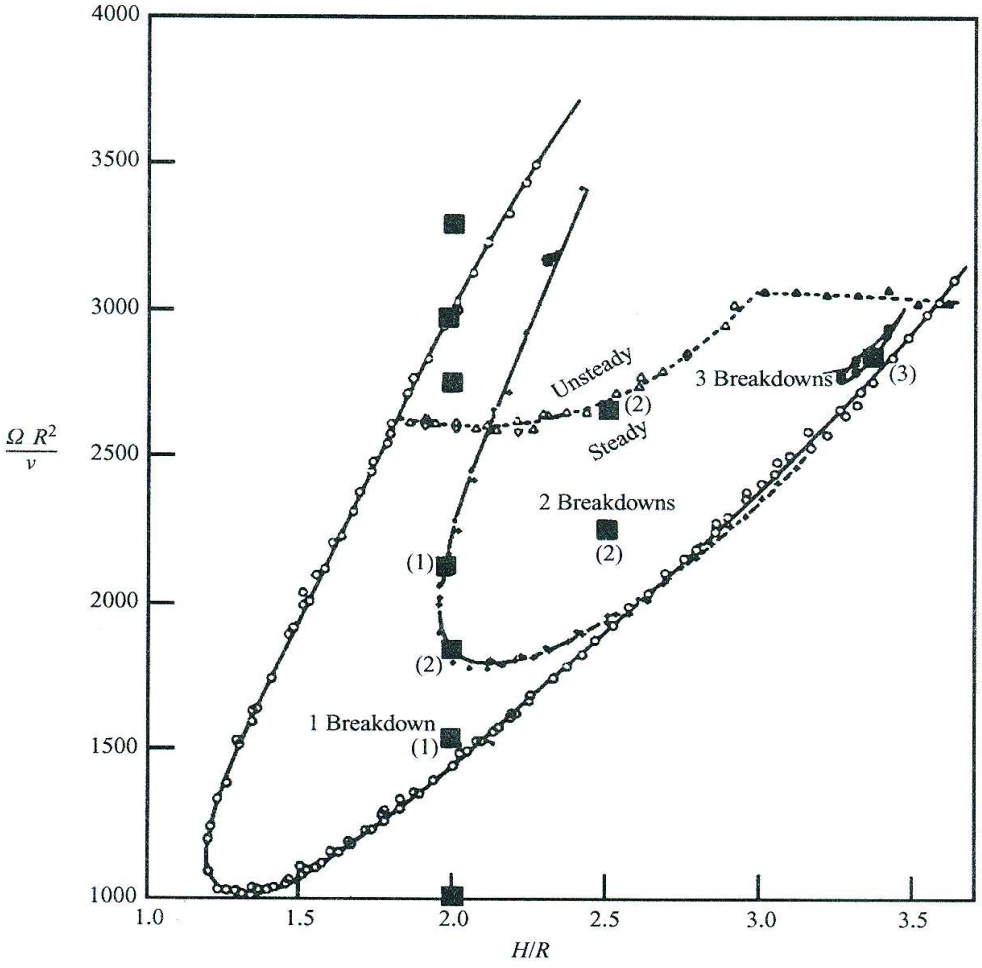

Figure 5.3 Threshold for vortex breakdown bubbles with Re and AR (Escudier 1984).

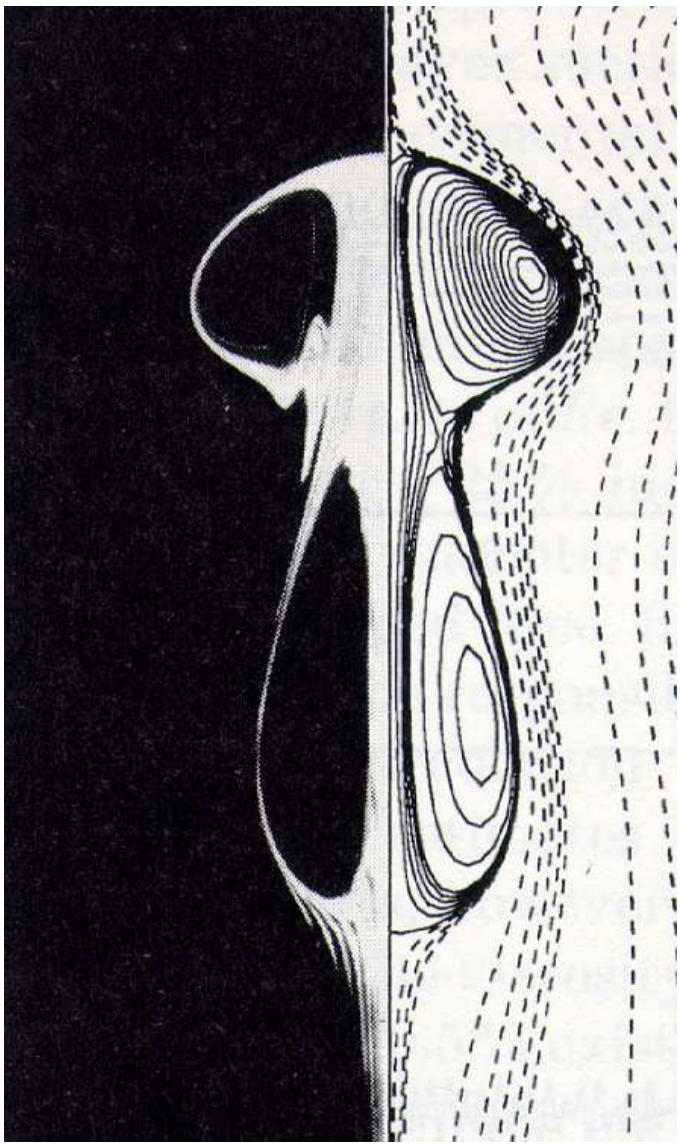

Figure 5.4 Experimental vortex breakdown bubble (left) compared with axisymmetric calculation (right) taken from Lopez (1990).

5.3 Computational Details

The flowfields in the cylindrical container with rotating bottom lid are obtained by solving numerically the fully three-dimensional unsteady Navier-Stokes equations using the method of Sotiropoulos and Ventikos (1998, 2001). The Navier-Stokes equations are formulated in Cartesian coordinates and then transformed to general non-orthogonal curvilinear coordinates. The transformed equations are discretized using a finite volume method and then integrated using a dual (pseudo) time stepping artificial compressibility method. Local time stepping, residual smoothing, and multigrid acceleration are used for convergence acceleration (Lin and Sotiropoulos 1997, Sotiropoulos and Ventikos 1998). The numerical method is second order accurate in both space and time. The results reported were obtained using time-accurate simulations where the steady-state flow fields were reached as the time-asymptotic limits of unsteady computations. The low Reynolds number calculations ($Re < 1500$) were initiated from rest by impulsively spinning up the rotating lid. At higher Reynolds number, the low Reynolds number flow fields were used as initial conditions.

The computational grid for numerical calculations is 150x97x97 (figure 5.5) in the x, y, and z directions respectively. The grid is uniform in the flow direction but is stretched with grid nodes clustered at the walls and at the center of the container in an effort to resolve the complex flow characteristics in boundary layers and in the region of the vortex breakdown bubble. Comprehensive grid sensitivity studies were performed, varying the number of grid nodes from $3x10^5$ to $1.5x10^6$ and the mesh employed herein was found adequate for grid independent solutions.

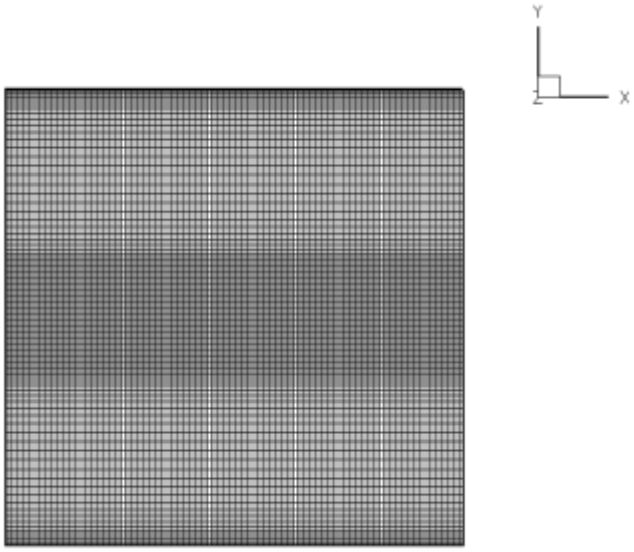

a)

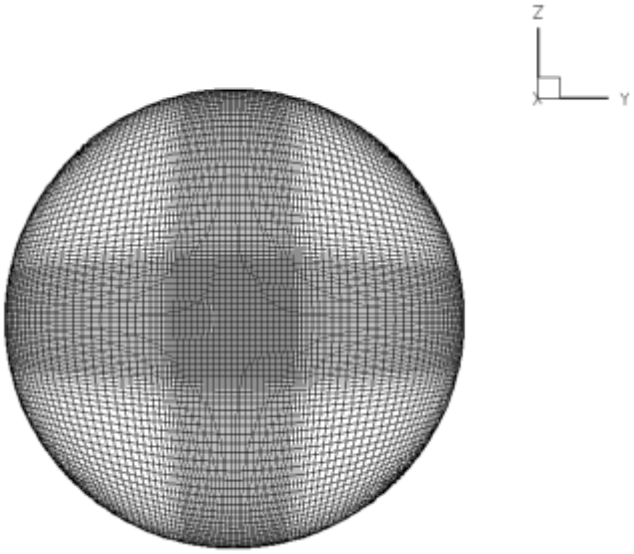

b)

Figure 5.5 Computational grid for cylindrical container with rotating bottom lid.

5.4 Vortex Breakdown Bubble Topology

In this section the streamline topology of the numerically simulated steady vortex breakdown bubbles is described. This is the first step in developing an understanding of the dynamics of the flow within this region. To aid in this process, the behavior of particle trajectories that exist in the bubble is examined. Next the causes behind the variations of trajectories are considered by looking at the structure of the vortex breakdown bubble and the mechanisms that lead to its complex dynamics. It is important to keep in mind that our numerical simulations have been carried out using the curvilinear mesh employed by Sotiropoulos and Ventikos (2001) and, thus, what we investigate herein are the Lagrangian properties of vortex breakdown bubbles under a small albeit finite non-axisymmetric forcing.

The steady-state Eulerian flow field in this work is obtained using a numerical method described in detail in a series of papers (Lin and Sotiropoulos 1997, Sotiropoulos and Ventikos 1998). This method uses a dual time-stepping, artificial compressibility method which has second order accurate differencing spatially and temporally. Using the particle tracking method described in detail in Chapter 4, particle trajectories are calculated by integrating passive particles within the vortex breakdown bubble. At first glance, the simulated vortex breakdown bubble exhibits three basic types of trajectories as shown in figure 5.6. The first type of trajectory (see thick trajectory in figure 5.6) originates upstream of the bubble, spirals around its exterior and continues downstream towards the rotating lid without entering the bubble. The second type of trajectory also originates upstream of the bubble, spirals downstream around the bubble, but when it

approaches the downstream stagnation point it reverses direction, enters the bubble, spirals in its interior several times before it finally escapes and continues downstream. The third trajectory type is confined entirely within the interior of the bubble. Particles circle forever on invariant tori that foliate the interior of the bubble. Such trajectories would be the only type encountered in the interior of a steady, axisymmetric bubble. A more careful consideration of particles paths in the interior of the bubble further reveals that other types of trajectories with very rich dynamics also exist but these intricacies will be discussed in a subsequent section in this chapter. Clearly even this rudimentary examination of the basic types of trajectories suggests that the interior of the simulated vortex breakdown bubbles exhibit very rich dynamics in stark contrast with an axisymmetric structure, which would be closed (and thus not accessible to upstream originating particles) and foliated by invariant toroidal stream-surfaces.

To understand the reasons for the rich dynamics, let us consider the manifold structure of an ideal axisymmetric stationary vortex breakdown bubble (Wiggins 1990) seen in Figure 5.7. Figure 5.7a shows a sketch of both a cross section and the three-dimensional structure of the heteroclinic cycle for the three-dimensional, axisymmetric flow field. Heteroclinic trajectories (also known as saddle connections) are trajectories that join two saddle points. Saddle points are formed by the joining of a stable and unstable manifold. That is, they are points in the phase space of a dynamical system in which trajectories are attracted and repelled from the same position. For a vortex breakdown bubble the saddles are its upstream and downstream stagnation points. The stable manifold is simply represented by the orbits that are attracted to the stagnation point and the unstable manifold is formed by orbits that are repelled by the stagnation

point. In Figure 5.7b the two saddle points are denoted with P_1 and P_2. They connect the two-dimensional unstable manifold $W^U(P_2)$ and one-dimensional stable manifold $W^s(P_2)$ with the two-dimensional stable manifold $W^S(P_1)$ and one-dimensional unstable manifold $W^U(P_1)$. The two-dimensional manifolds cycle around structure and the one dimensional manifolds form the centerline axis of the bubble. The heteroclinic trajectories create an invariant bubble-like surface, which delineates the interior flow from the outer flow as shown in figure 5.7a. The trapped interior flow moves along invariant tori, which are the stream-surfaces of the axisymmetric flow.

The topology seen in figure 5.7 is also the topology of the following autonomous three-dimensional normal form:

$$\begin{aligned} \frac{dr}{dt} &= \mu_1 r + arz + \ldots, \\ \frac{dz}{dt} &= \mu_2 + 2 + br^2 - z^2 + \ldots, \\ \frac{d\theta}{dt} &= \omega + \ldots, \end{aligned} \tag{5.1}$$

where μ_1, μ_2, a, b, and ω are constants, and the dots imply higher-order terms. As shown in Wiggins (1990), for a>0 and b=-1 the stable and unstable manifolds of the hyperbolic fixed points of this system create an invariant sphere. When the higher order terms are ignored, the form is similar to that shown in figure 5.7a, and the periodic orbits become invariant two-tori. Let us now consider the effect of adding higher order terms in the above system in the form of small, non-axisymmetric perturbations. As shown by Broer and Vetger (1984), including such terms, no matter how small they may be, could destroy

the symmetry of the basic form and break the invariant structures of the sphere shown in figure 5.7a. The one-dimensional unstable manifold of P_1 and the one-dimensional stable manifold of P_2 will no longer intersect in three-dimensional space and the two-dimensional manifolds of P_1 and P_2, $W^S(P_1)$ and $W^U(P_2)$ may intersect transversely along heteroclinic orbits. This means that it is possible for the portion of $W^U(P_1)$ and $W^S(P_2)$ inside the bubble to fall into $W^S(P_1)$ $W^U(P_2)$ forming homoclinic (trajectories that start and end at the same fixed point) orbits in three-dimensional space (see Figure 5.7b). That is trajectories that start at a stagnation point, may spiral around the bubble, transect a trajectory coming from the opposite stagnation point and move back to their starting point. It is known from the theory of dynamical systems that homoclinic orbits are structurally unstable and their instability could lead to chaotic dynamics (Arneodo, Coullet & Tresser 1982; Gaspard & Nicolis 1983).

The intertwining of manifolds in figure 5.7b then develops a homoclinic tangle. Whenever a system has a homoclinic tangle (a transverse homoclinic point) there exists a region which is mapped onto itself, providing an area of sufficient stretching and contraction, so that chaotic dynamics are possible. It was first recognized by Sil'nikov (1965) that homoclinic orbits, mapping a saddle focus back onto itself possess a countable infinity of Smale horseshoes (Smale 1963). The Smale horseshoes (see figure 5.8) can be formed by a rectangle that is flattened, stretched, and folded into a horseshoe structure. This process leads to the exponential separation of points that initially reside in close proximity. The existence of a ``horseshoe" as part of a dynamical system is a compelling signature of chaos (Wiggins 1990). Since the structure of the perturbed vortex breakdown bubble contains two saddle foci, it can then be inferred that the

dynamics described by Sil'nikov could exist in this system. The Sil'nikov route to chaos in this situation can be summarized as follows. Material lines entering the bubble through the downstream saddle focus are stretched and folded every time they pass through that saddle and this process ultimately leads nearby orbits to separate exponentially in time.

The Sil'nikov mechanism in the context of the dynamical system given by eqn. (5.1) was studied in detail by Broer & Vegter (1984). By considering the effects of the higher-order terms in these equations, they proved that for the perturbed system a sequence of Sil'nikov's bifurcations will occur, thus, leading to the formation of a countable infinity of Smale horseshoes and non-integrable dynamics. Figure 5.9 shows their interpretation of the three-dimensional structure of the stable and unstable manifolds of the two saddle foci for a perturbed, volume-preserving system of the form of equations 5.1. Interesting to note is the asymmetric folding effect that occurs downstream of the Broer and Vetger "bubble," which is very similar to the folds that appear in essentially all vortex breakdown bubbles visualized in the laboratory (see figure 5.3).

If we apply these concepts to the vortex breakdown bubble trajectories shown previously in figure 5.6, it is possible to understand why each of the sample trajectories exists. The first trajectory in which particles move down the axis, cycle around the bubble and exit, are particles that reach the stagnation point along the stable one-dimensional manifold and then exit along the unstable two-dimensional manifold before approaching the downstream stagnation point along the stable two-dimensional manifold and then exiting the region along the unstable one dimensional manifold. The third type of trajectory is trapped inside the bubble interior and would also be present if the flow

were axisymmetric. However most interesting is the second type of trajectory that enters the bubble interior, stays for an arbitrary amount of time, spiraling in the interior of the bubble before exiting. This type of trajectory could not possibly exist under the axisymmetric assumption and is only possible if trajectories are somehow able to jump from one of orbit to another due to the transverse trajectories.

The higher order terms that need to be added to the dynamical system given by equations (5.1) are exponentially small (Broer and Vetger 1984). In our numerical simulations they have been created numerically because of the curvilinear mesh we have employed. In a laboratory experiment they may arise due to numerous possible experimental imperfections and ambient disturbances no matter how much great care is taken to eliminate them. Thus, the above discussion suggests that even though from the Eulerian standpoint the steady vortex breakdown bubbles are essentially axisymmetric it could be very difficult to visualize them as such in a real-life laboratory experiment because that would require eliminating from the apparatus all disturbances no matter how small.

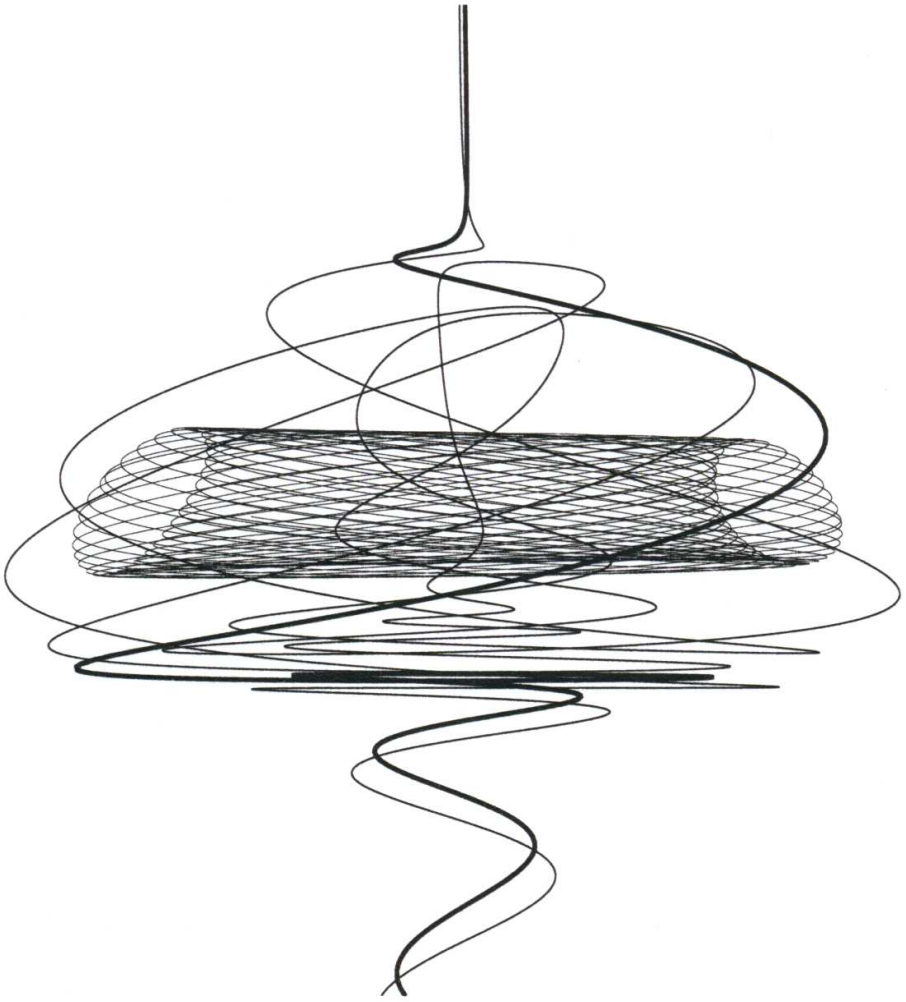

Figure 5.6 Calculated typical three-dimensional particle trajectories in and around the breakdown bubble. (Re = 1850, H/R =1.75). The 'thick' orbit is released from the axis upstream of the breakdown bubble. The 'thin' orbit is released just off the axis also upstream of the bubble. The final orbit remains on a toroidal trajectory.

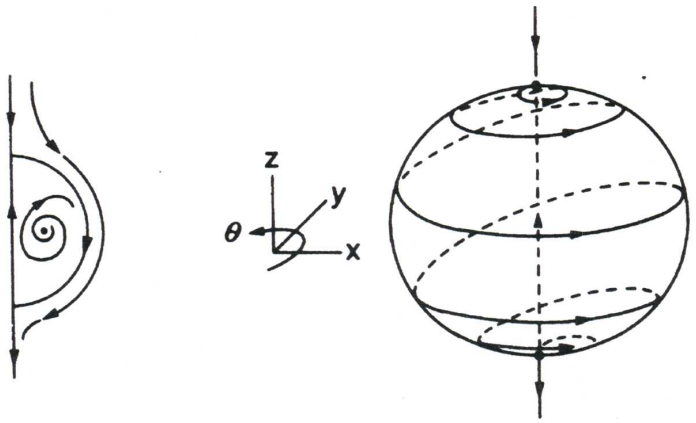

a)

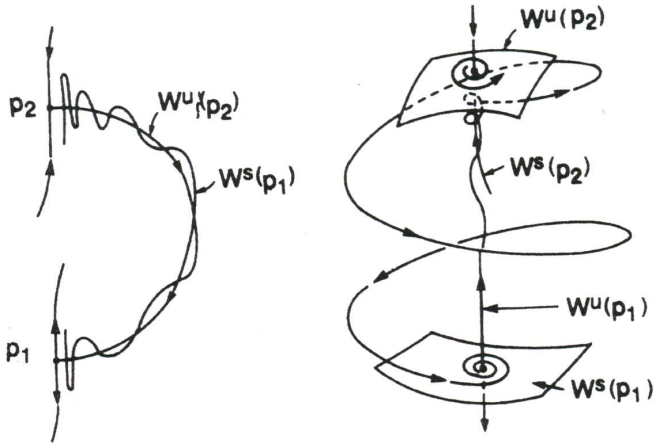

b)

Figure 5.7 (a) Cross-section and three-dimensional structure of the heteroclinic cycle for the truncated normal form, equation (5.1); and (b) cross-section of the perturbed manifolds and homoclinic orbits for the full normal form (including the effect of higher order terms). Wiggins (1990).

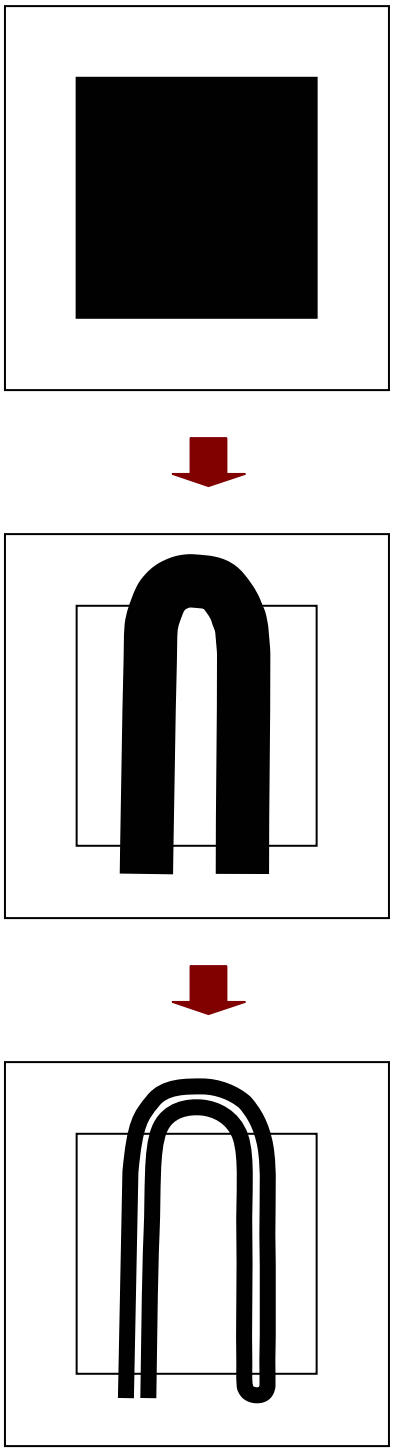

Figure 5.8 Smale horseshoe map.

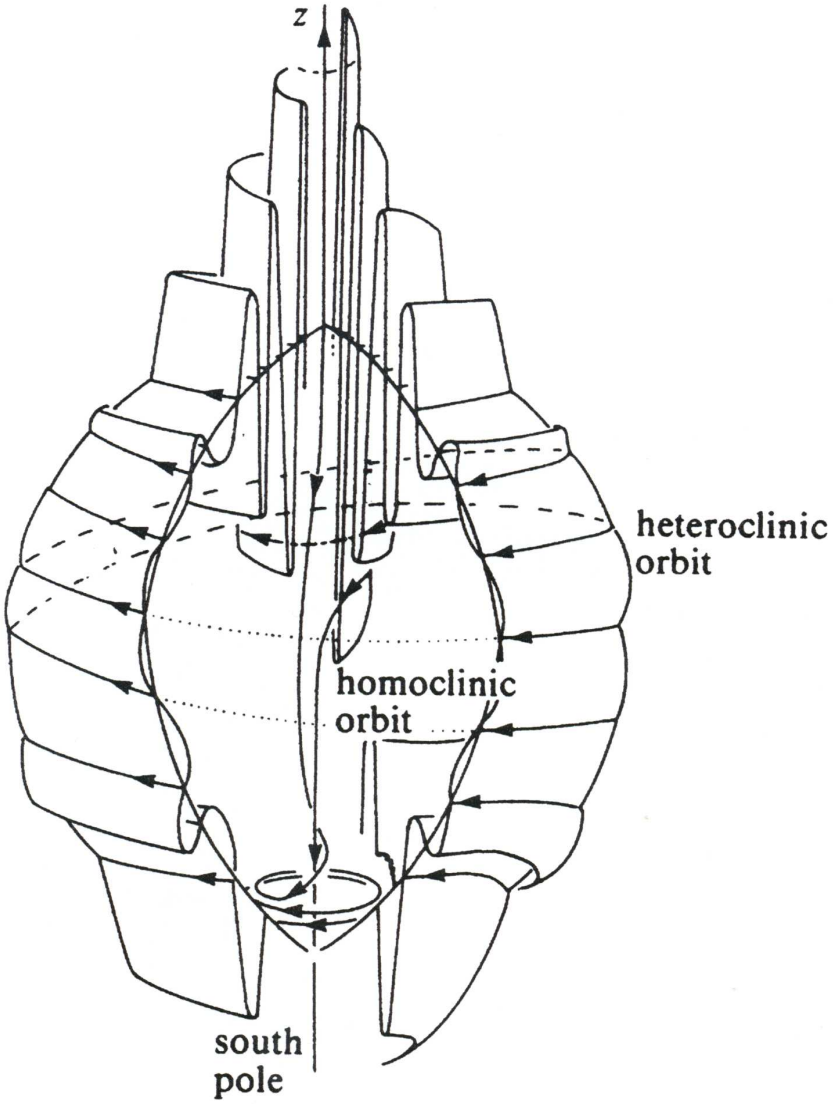

F

Figure 5.9 Cut-open perturbed globe showing a Sil'nikov homoclinic orbit for a volume-preserving system. Taken from Broer and Vegter (1984).

5.5 Stretching, folding and chaotic stirring

The previous section sought to identify the mechanisms (such as the Sil'nikov mechanism) that control the dynamics within the vortex breakdown bubble. It has been theorized that the effect of small perturbations (either numerical or experimental) will have a dramatic effect on these dynamics, causing the axisymmetric representation of the vortex breakdown bubble to instead become a very complex structure that allows for chaotic stirring. To prove these hypotheses analytically would be impossible because of the complexity of the equations. Therefore in this section, we provide evidence that chaos inducing mechanisms are indeed at work within vortex breakdown bubbles by analyzing the Lagrangian dynamics of the numerically simulated velocity fields.

Figure 5.10 shows the evolution of a particle that is initially a straight material line that is recirculating within the vortex breakdown bubble. The filament has 1000 particles spaced 10^{-8}R apart which provides an initial filament length of 10^{-5}R. The filament enters the breakdown bubble region and recirculates several times before all the particles exit the bubble. Position 1 in the figure is the initial release location. Position 2 is just prior to the element passing through the spiral-in saddle for the first time. Positions 3,4, and 5 are snapshots during the second approach of the element toward the spiral-in saddle and position 6 is just before the element enters the breakdown region for the third time. The effects of folding are quite evident in this figure. The filament has now been folded over several times as can be seen in the enlarged snapshot at position 6.

As the filament moves through the central axis of the vortex breakdown bubble and travels through the saddles seen at location 1 and 2, the length of the filament grows

at an exponential rate. This can be seen in figure 5.11, which shows the temporal evolution of the length of the filament. Here we plot the length of the filament, which has been normalized by the initial length of the filament given as L_0, versus time. Each number in parentheses designates one of the stages of growth of the filament depicted in the previous figure. It is observed that the length of the figure does indeed grow exponentially, a feature which is the hallmark of chaotic dynamics.

To illustrate the chaotic stirring of particles in the interior of the bubble we calculate the motion of a series of material circles covering the exterior of the upstream portion of the bubble. Figure 5.12 (a) through (i) shows the progression of these orbits over 484 non-dimensional time units. The particles are color-coded based on their initial distance in the x direction. In figure 5.12b particles have moved around the outside of the bubble and are being drawn into the saddle focal point downstream of the bubble. As particles travel into the bubble by t=25 (figure 5.10c) the stretching and folding characteristics are observed as the material circles begin to twist. The particles continue to move within the bubble, the structure of the surface of particles is folded and stretched more with each movement through the saddle point, becoming more and more disorganized and stirred. Finally, it can be seen by figure 5.12g that particles are eventually observed exiting the bubble in random bursts. The rate of the bursts will be discussed in section 5.6.3. Note that by t=484 in figure 5.12i, the particles are completely disorganized and dispersed chaotically within the bubble.

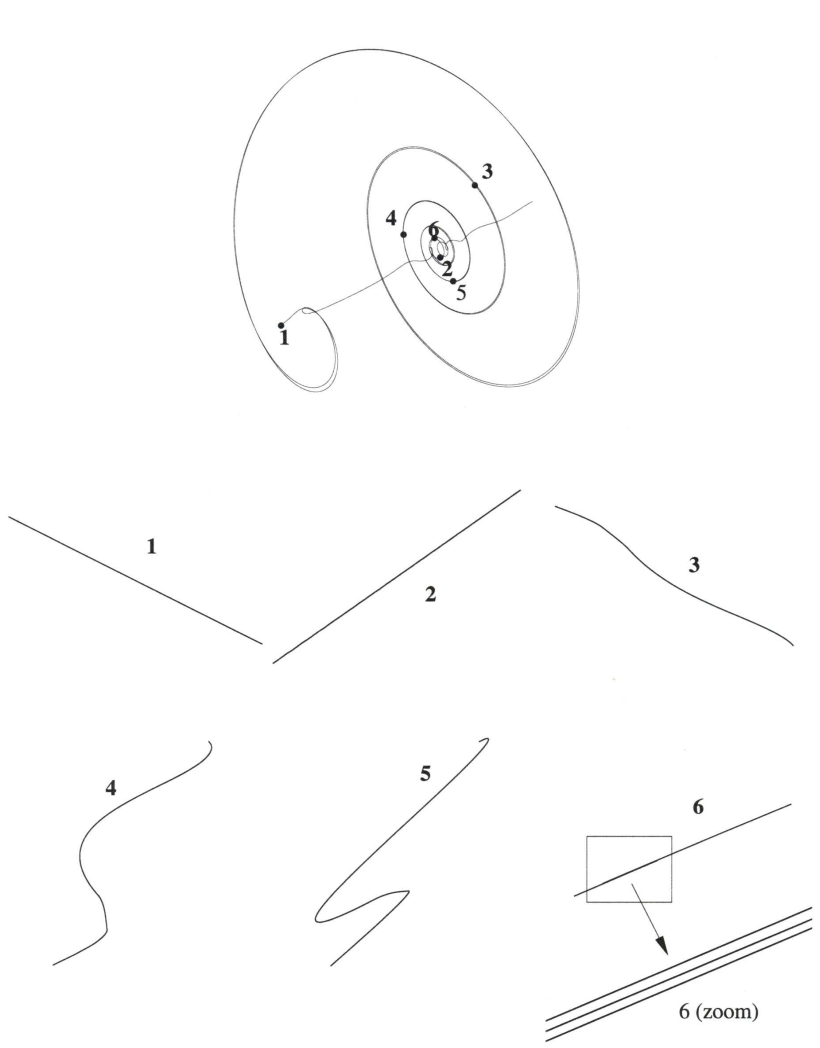

Figure 5.10 Evolution of the shape of an initially straight material line as it recirculates within a stationary vortex breakdown bubble (Re = 1850, H/R=1.75). The material filament consists of 1000 particles spaced uniformly 10^{-5}R apart. The various positions of the filament are marked with numbers along the trajectory of its midpoint.

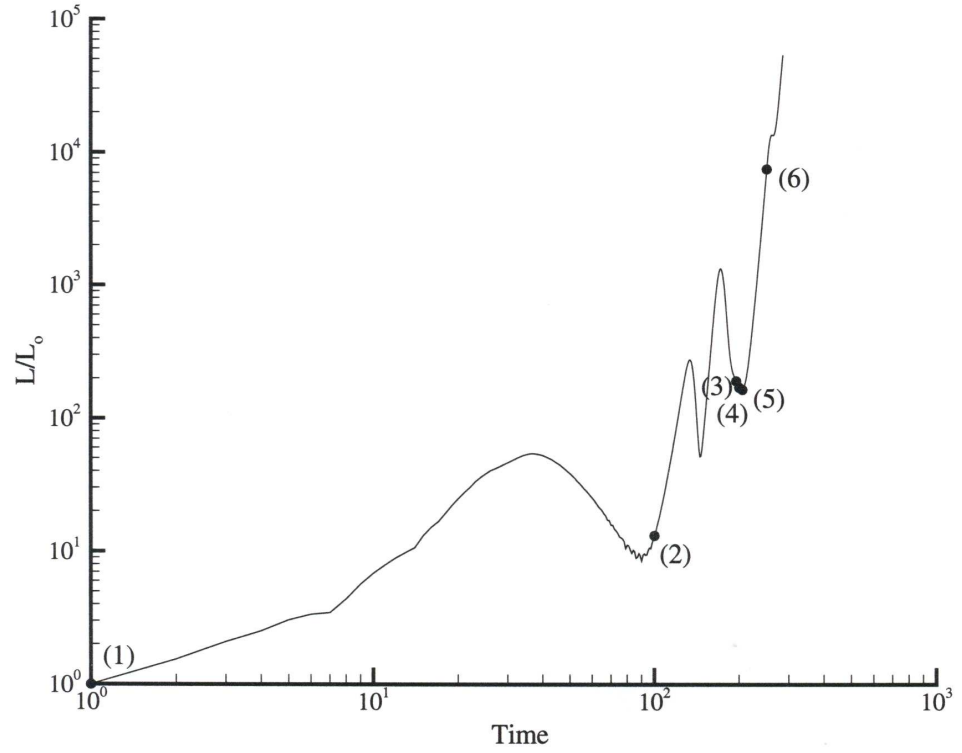

Figure 5.11 Temporal evolution of the length of the filament shown in figure 5.10. The numbers in this figure indicate the various positions of the element defined in that figure. The length (L) has been scaled by the initial length (L_0). The rotating lid completes one revolution in π time units.

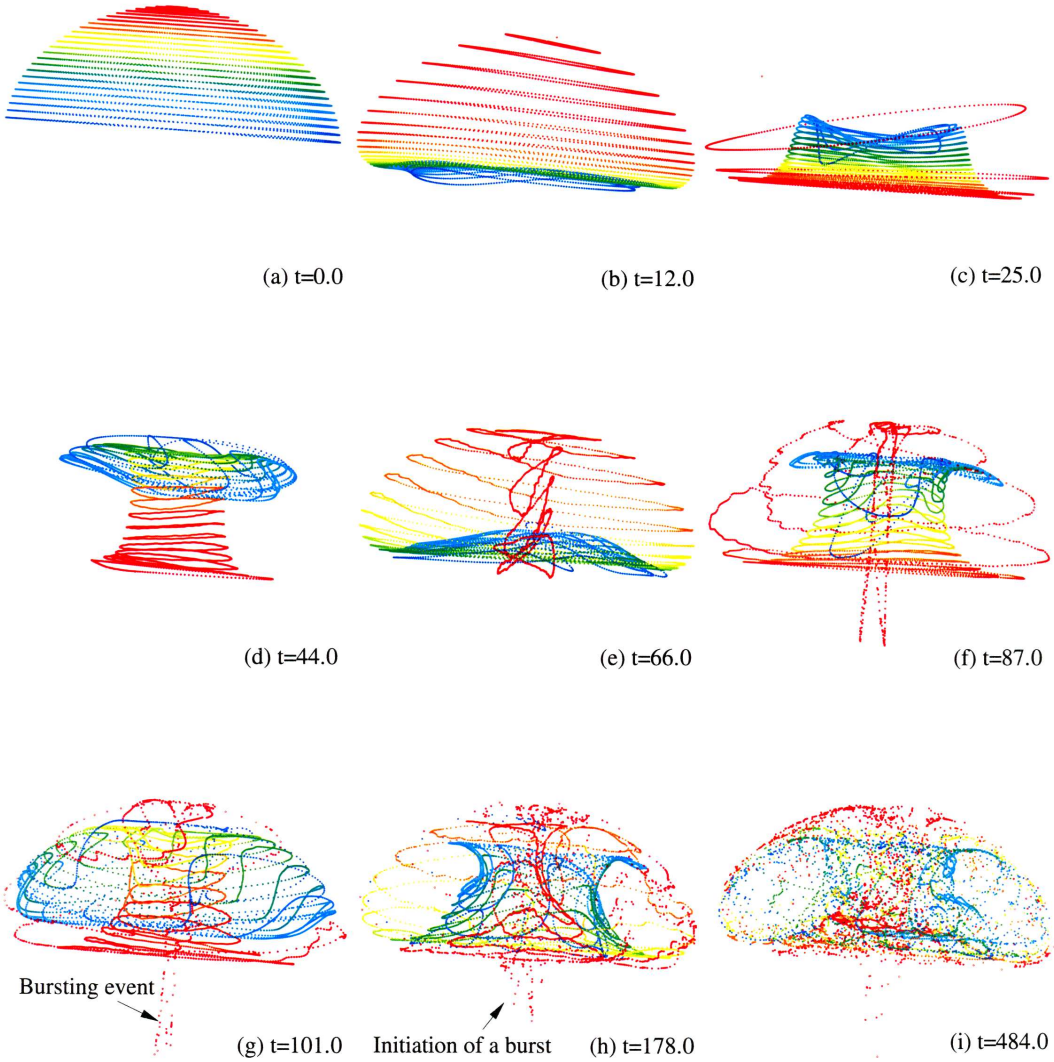

Figure 5.12 Temporal evolution of series of circular material lines, initially placed to span the upstream face of the vortex breakdown bubble (Re = 1850, H/R=1.75). Individual particles are colored based on their axial coordinates at t=0.

5.6 Results and Analysis

In this section we characterize and quantify the Lagrangian dynamics in the interior of the simulated steady vortex breakdown bubble flowfields using Poincaré maps, residence time maps, and tools and concepts from fractal geometry. Finally, the effect of Reynolds number, aspect ratio and the role swirl are addressed.

5.6.1 Poincaré Map

We construct Poincaré maps to characterize and better understand the richness of dynamics in the interior of the bubble. The maps are constructed (see Chapter 2 for detailed description) by allowing particle trajectories placed initially in different flow regions to be advected by the simulated flowfield and marking the position they intersect a given diametral plane, the plane of section of the Poincaré map. Figure 5.13 shows the resulting Poincaré map for the steady vortex breakdown bubble for Reynolds number 1850 in a container with an aspect ratio of 1.75. Particles are colored by their initial conditions, which are marked by the colored "blobs" in the figure. Each blob contains 5 particles, which were released along short straight segments and then iterated for 10^6 time steps. The resulting Poincaré map shows the complex characteristics of the flow within the bubble and reveals a picture that is very similar to the previous descriptions by Helleman (1980) who discussed the effect of three-dimensional perturbations on the dynamics of a volume preserving, dynamical system.

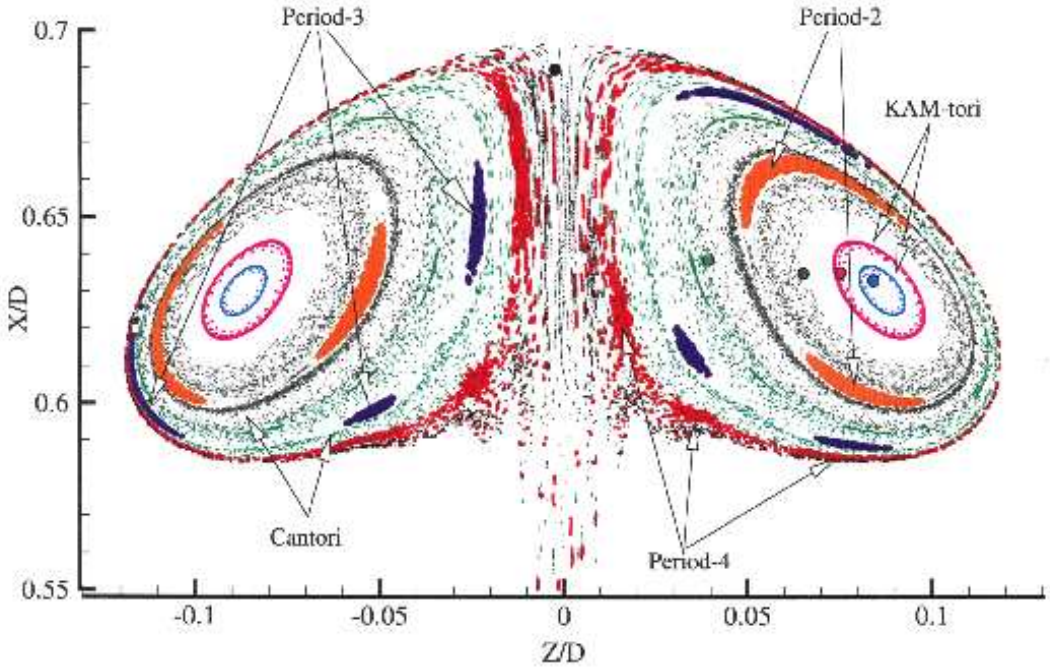

Figure 5.13 Poincarè section of the steady vortex breakdown bubble for (Re = 1850, H/R=1.75). Same-color blobs of markers (5 markers per color) were released along short straight segments, selectively placed within various regions in the interior of the VB bubble. The large dots mark the initial location of the various blobs.

In figure 5.13, the blue and pink points are particles that stay within the toroidal region of the bubble. These areas are KAM-tori, the remnants of the axisymmetric dynamics, and act as impermeable barriers to transport. There existence is consistent with the KAM theorem, which predicts that many of the simple quasi-periodic solutions of the axisymmetric integrable system will, in general, survive mild perturbations.

Moving outward from the two inner KAM-tori shaded in pink and blue, the dynamics become more complex. The gray and green initial points outline cantori. These are leaky barriers to transport on which particles can be trapped or stick for very long times but ultimately escape through fractal "windows" to explore the rest of the flow domain. In the figure, the gray particles outline a rather tight cantorus. Particles seem to be almost confined to that area for a very long time before they start escaping. In contrast, the green region shows a much less structured region. Here particles stick for shorter time and appear to escape more frequently and, thus, many of them have worked their way into other bubble regions.

The gaps between adjacent cantori are populated with both chaotic regions as well as un-mixed island chains of regular motion. The figure shows the Period-2, Period-3, and Period-4 islands in orange and violet and red respectively. These island chains are formed by particles that remain confined on twisted and folded tori of complex topology, whose three-dimensional structure is shown in Figure 5.14. In addition to these low period islands, we have also found higher order period islands in the interior of the bubble. However it is extremely difficult to find and visualize the higher order islands, as space covered by the island diminish in size as the order of the island increases.

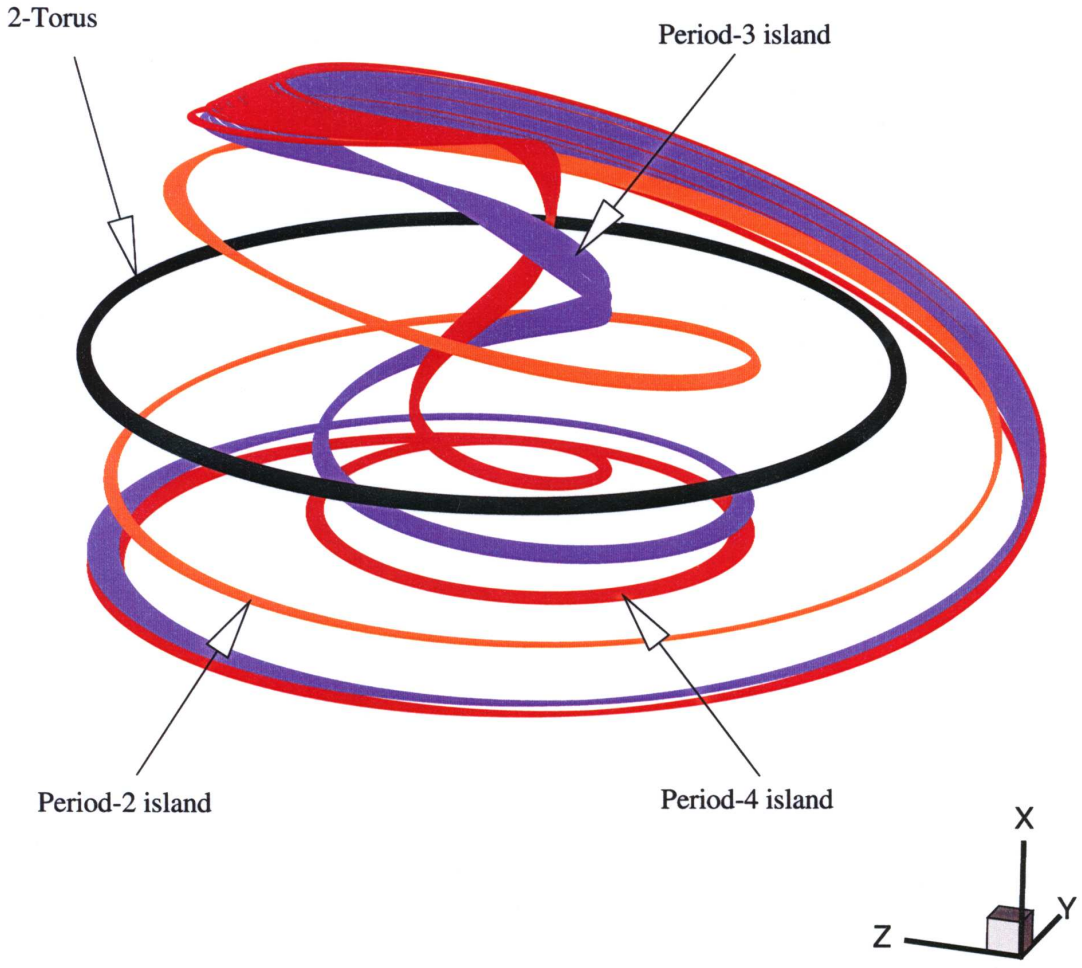

Figure 5.14 Three-dimensional orbits illustrating the intertwining of the period-two, -three, and –four islands in the interior of the bubble shown in figure 5.13.

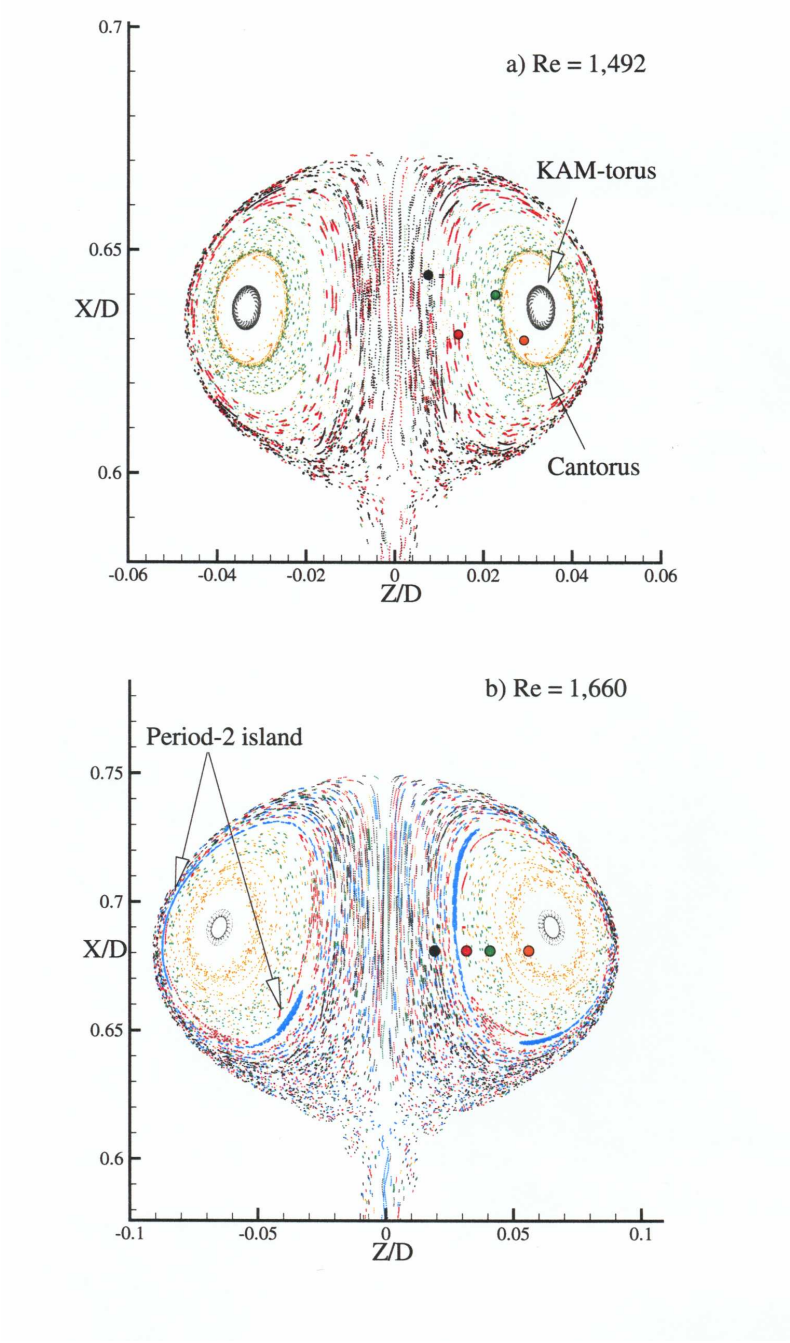

Figure 5.15 Poincarè sections for steady vortex breakdown bubbles in a container with H/R=2. a) Re=1492; (b) Re=1667.

The chaotic regions surrounding the periodic islands, as well as the chaotic area represented by the black "blob" show particles that are extremely sensitive to initial conditions. Particles that originate in these areas become completely mixed. The points of the map colored in black, are representative of orbits that are developed due to the previously introduced Sil'nikov mechanism. The particle trajectories pass through the hyperbolic fixed points and transverse the various heteroclinic orbits of the flow. This mechanism provides the stretching and folding characteristics, which leads to the chaotic behavior of particles within the region and explains why the points show such great scatter across the area of the map.

As shown in the work of Escudier (1984) (see figure 5.3), for various aspect ratio/Reynolds number combinations there exist one-, two-, three- and no-bubble cases. To study the variation in Lagrangian dynamics of the vortex breakdown flowfields, we construct Poincaré maps for calculated vortex breakdown flowfields at various Reynolds numbers and aspect ratios. In figure 5.15, we show representative results for two Reynolds numbers 1492 and 1667 for aspect ratio (AR=H/R) of two. The basic structure of the bubbles remains the same for the maps. There exist chaotic particle trajectories due to the well-stirred Sil'nikov filament that occupies the region in the vicinity of the axis for all Reynolds numbers. There is also the continued presence of the KAM-tori and cantori regions. The first big difference is seen in the Re=1492 case, however, due to the apparent lack of low-period islands existing in the bubble interior. Even with extensive searching, there was no evidence of the low-period islands that were seen in the previous Re=1850 with AR=1.75 case (see figure 5.13). In figure 5.15b, as we increase the Reynolds number to 1667, a Period-2 island appears, although it does not seem to occupy

as large a percentage of the interior as the Period-2 island shown in figure 5.13 for Re=1850.

Other differences in the maps are in the size and structure of the cantori and the chaotic filament along the axis. As the Reynolds number increases from 1492 to 1667, the cantori appear to become “leakier”. There is a noticeably large amount of spreading that occurs in the Re=1667 case as the particles colored in green seem to occupy a larger amount of space than in the Re=1492 case. Also several of the particles in orange have escaped the bubble at the higher Reynolds number. In addition there is a difference in the size of the chaotic filament that resides along the axis. As the Reynolds number increases, the quasi-periodic core has shrunk in size, leaving a much larger portion of the flow filled with the stochastic flow region.

5.6.2 Residence Time

The rate at which particles exit the bubble is explored in this section. Residence time as a means of understanding chaotic advection has been a useful tool in other mixing flows such as the partitioned-pipe mixer (Kusch and Ottino 1992). However in those studies residence times are mapped based on the idea that particles placed in regular or periodic areas will exit the mixer much faster than the chaotic particles, which tend to sample a larger range of velocities and move aimlessly throughout the pipe. Therefore the residence time of particles placed in chaotic areas tends to be much larger than those placed in periodic areas. In the present confined flow that is obviously not the case. Particles trapped in islands and tori will remain in these areas and will not escape the

bubble. In this study we characterize the amount of time upstream originating particles that enter the bubble through the downstream saddle focus spend in its interior. As suggested by figure 5.12, some particles could recirculate within the breakdown region for arbitrarily many times before finally exiting in random bursts. To explore this feature of the flow, we introduce 10,000 particles distributed axisymmetrically along a small disk of radius 0.01R centered around the container axis just upstream of the breakdown bubble. The trajectories of the particles are integrated until every particle exits and their residence time is recorded and mapped back on to the initial particle positions in the contour plot seen in figure 5.16.

The remarkable aspect of the resulting images is their fractal like properties. Here we show the particle positions in the Y and Z direction normalized by the radius R. The initial image (figure 5.16a) shows that the disk contains large regions of comparatively small residence time particles. Within these areas, however, are fractalized swirling bands of initial conditions that lead to much higher residence times. To further explore the apparent fractal-like structure of figure 5.16a, we increase particle resolution at successively smaller spatial scales by distributing all 10,000 particles within smaller and smaller regions, which are shown in figures 5.16b to d. As the resolution is increased, it is apparent that initial conditions that lead to continuously higher residence times are uncovered and fractal-like, self-similar patterns emerge. These bands closely resemble fractal boundaries of basins of attraction for non-attracting chaotic sets and suggest a Cantor-set-like cross-section. Their fractal structure is consistent with the chaotic nature of vortex breakdown flowfields and a direct manifestation of the extreme sensitivity of particle trajectories to arbitrarily small differences in initial conditions.

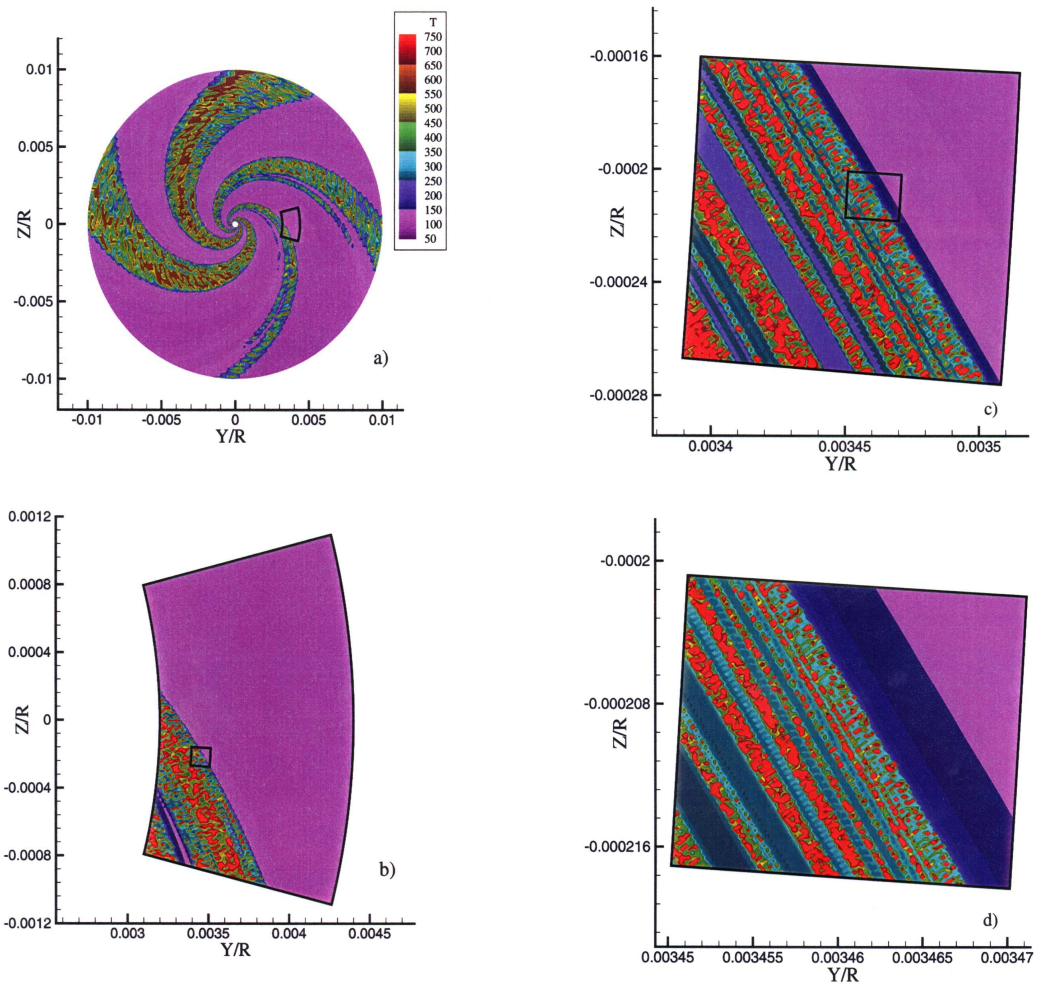

Figure 5.16 Residence time maps for initial conditions with increasing resolution from a)-d).

An important feature of the computed residence time map that is not directly apparent from the figure 5.16, is the fact that as we increase the resolution at smaller scales we uncover release points that lead to continuously increasing residence times. At the resolution of figure 5.16a, the maximum residence time is approximately 700 non-

dimensional units (corresponding to approximately 222 revolutions of the rotating lid), while at the resolution of figure 5.16d, we have picked points which lead to residence times as high as 7000 units (i.e. 2222 revolutions of the rotating lid). To demonstrate this feature, we show in figure 5.17 a plot similar to figure 5.16 but by including, at the two highest resolution levels, only contours that correspond to the very large residence times (the levels included in this plot range from 1000 to 7000). The resulting Cantor-dust-like contour plot strongly suggests that there exists a Cantor set of initial conditions (i.e. a set of measure zero but of finite dimension) that will lead to arbitrarily long residence times within the breakdown region. This conjecture is consistent with the chaotic nature of the flow and, in essence, is identical to the theoretical arguments made by Holmes (1984) that particles will re-circulate within the breakdown region for arbitrarily many times. Moreover, the concept of arbitrarily long residence times associated with a subset of measure zero (i.e. a Cantor set) of the total fluid flux into the bubble has been already introduced by MacKay (1994) in the context of the perturbed spheromak. MacKay (1994) also points out that the distribution of residence times within the bubble is "*likely to be highly non-trivial*," a conjecture that is confirmed by the fractal structure we uncover herein. Finally, the existence of a Cantor set of initial conditions leading to arbitrarily long residence times within non-attracting chaotic sets, such as the volume-preserving vortex breakdown flowfield we study herein, is a well documented phenomenon in studies of chaotic scattering (see Ott (1993) for a detailed review).

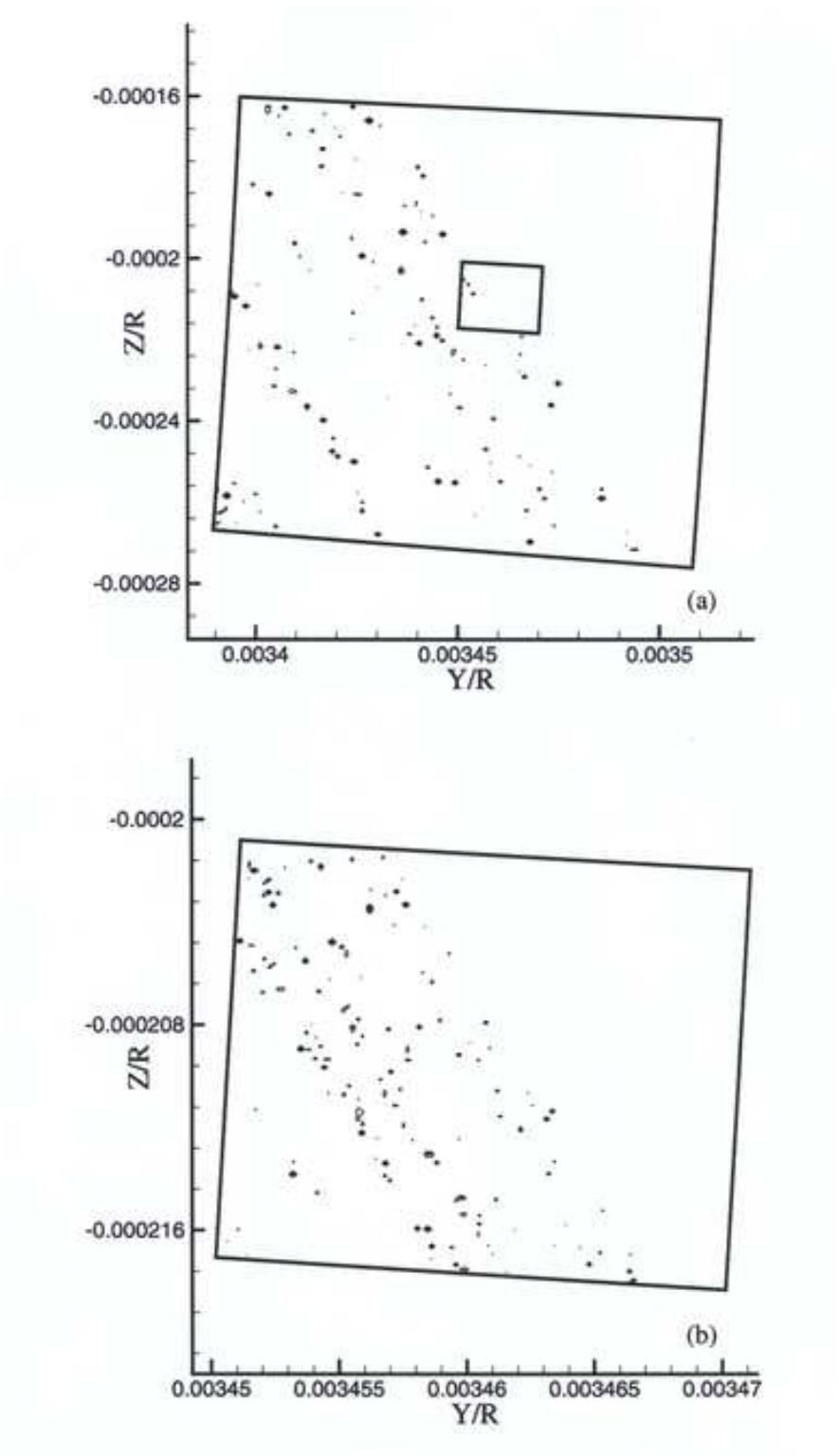

Figure 5.17 Contours of residence time with only large residence times (1000 to 7000); plotted to demonstrate the Cantor-dust-like structure of the resulting map.

5.6.3 Devil's Staircase

In this section we further explore and quantify the curious emptying mechanism discussed in section 5.5, by calculating the rate at which a group of upstream originating particles exits the bubble through the spiral-in saddle. We release the particles from a small disk, similar to that used to study the residence time distributions in the previous section, and record the number of particles that remain inside the bubble at every instant in time until the last particle exits (see below for a clarification of this point). A particle is declared to have exited the bubble when it crosses a certain axial plane just downstream of the spiral-in saddle. Note that for a given set of upstream initial conditions, several particles do not enter the bubble and are, thus, the first to cross the "exit" plane. These particles are omitted from the simulation. To investigate the sensitivity of the results presented herein to the size of the initial particle population, we have varied the particle number from $n = 10^3$ to $3x10^4$ (see figure 5.19 below)—for each simulation, the particles were released from exactly the same small disk upstream of the vortex breakdown bubble. We have also investigated the effect of varying the size of the time increment used in the trajectory integration, by performing, for a fixed number of particles, simulations with successively smaller time steps. The results reported in this section are independent of the size of the time increment.

The computed temporal decay of an initial population of $n = 3x10^4$ particles, for the (Re=1850, H/R=1.75) vortex breakdown bubble, is plotted in figure 5.18. Note that the initial number of particles in the vertical axis is less than $3x10^4$ because, as discussed above, particles that do not enter the bubble are omitted. A remarkable characteristic of

the curve shown in figure 5.18 is that it is a piecewise continuous staircase-like structure, consisting of a series of horizontal plateaus each of seemingly random temporal duration. Furthermore, and as shown in figures 5.18b and c, if part of the curve is magnified, the resulting curve looks very similar to the original one—curves with similar properties have been obtained for all simulated cases. Of course, and as clearly demonstrated in figure 5.18c, magnification continues to reveal similarity at smaller scales up until we reach the resolution of our discrete simulation, which is determined by the total number of particles and the size of the time increment.

The structure of the curve shown in figure 5.18 is strikingly similar to the so-called Devil's staircase (Bak 1986), a fractal curve that has been found to emerge in a number of nonlinear systems, in both physics and engineering, undergoing a mode-locking transition to chaos. In such systems, the staircase has been shown to describe the dynamical behavior as a function of frequency with the characteristic plateaus indicating locking at various rational frequencies (for specific examples see: Bak 1986; Lacis, Barci, Cebers, and Perzynski 1997; Reinchhardt and Nori 1999). Moreover, Lai, Zyczkowski and Grebogi (1999) have recently showed that the devil-staircase characteristic is the universal behavior in the parametric evolution of certain properties of chaotic saddles of non-linear dynamical systems.

The defining characteristic of the staircase, which also led to its name, is that between any two of its plateaus there is an infinite number of steps. Its mathematical construction is closely linked with the Cantor set and this relation is clearly evident in the computed curve shown in figure 5.18. Consider the time axis in this figure and remove all the intervals corresponding to fixed particle populations. What remains is a Cantor

set, that is, a set of points that has measure zero but, as we will subsequently show, finite fractal dimension. Of course a true Cantor set will be obtained in our case only in the limit of infinite number of particles and as the time increment approaches zero.

Most of the physical applications of the staircase described in Bak (1986) involve dissipative systems with two competing frequencies where mode-locking occurs. In the present case, therefore, the Devil's staircase emerges for the first time in an autonomous, three-dimensional, volume-preserving dynamical system that is spatially chaotic. The randomly varying lengths of its plateaus explain the emptying process of the breakdown bubble discussed previously in Section 5.5. The initial particle population decays in time by sampling, as one would expect, all possible states, that is all integer numbers from the initial population to zero, but the temporal interval that the population remains fixed at a particular level varies randomly from level to level. Consequently the long plateaus would appear as pauses in the emptying process while a sequence of several consecutive short plateaus will result in what we previously described as a bursting event. We should emphasize that in the present simulation, with a finite set of discrete particles, the number of steps of the staircase can not be infinite but rather equal to the total number of particles that enter the bubble in a given simulation. Only in the continuum limit we would anticipate that an initial tracer concentration will decay to zero by sampling, for random time intervals, the infinite sequence of all rational numbers between the initial concentration level and zero, thus, yielding a true devil's staircase distribution.

In spite of the finite resolution we employ by specifying a fixed particle population, we can still demonstrate the fractal nature of the computed curve without having to perform simulations for an infinite number of particles. To accomplish this, we

calculate herein the fractal dimension of the Cantor set associated with the staircase shown in figure 5.18. The procedure we employ is that described in Bak (1986). We choose a given time interval *r* and calculate the total width *T(r)* of all plateaus that are larger than *r*. We are interested in the space in between the plateaus, T_{max}-*T(r)*, which eventually shrinks into a Cantor set (T_{max} is the maximum residence time in our discrete simulation). To measure this space we define the total number *N* of "holes" of size *r*, given by:

$$N(r)=\frac{T_{\max}-T(r)}{r}. \tag{5.2}$$

If the variation of *N(r)* versus (*1/r*) on a log-log scale is linear, then:

$$N(r)\approx\left(\frac{1}{r}\right)^{d} \tag{5.3}$$

where *d* is the slope of the resulting straight line. That is, the space between the plateaus vanishes as r^{1-d} at $r \to 0$ and the devil's staircase is complete (Bak 1986). The exponent *d* is the fractal dimension of the Cantor set, which is complimentary to the set of plateaus comprising the devil's staircase.

In figure 5.19, we plot on a log-log scale *N* vs. (*1/r*) for the two staircases obtained from the $n = 10^3$ and $n = 3\text{x}10^4$ simulations, respectively. We include both of these simulations in order to explore the sensitivity of the so computed fractal dimension to the number of initial particles. For both simulations, we find that a straight line with slope $d = 0.4$ fits well all points over a broad range of plateau sizes—approximately 2.3 and 3.0 orders of magnitude variation in *r* for the $n = 10^3$ and $n = 3\text{x}10^4$ cases, respectively. Note, however, that increasing the number of particles results in dramatic

improvements for small values of r and in smoother overall linear variation. We should also note and comment on the apparent departure of the calculated points for the $n = 3x10^4$ case from the linear variation as r approaches large values (see figure 5.19). This trend is an artifact of our incomplete, for this case, numerical simulation. Due to the asymptotic nature of the curve shown in figure 5.18, larger plateaus tend to appear more frequently when relatively few particles remain in the bubble. Since many of these last remaining particles could have arbitrarily long residence times (see previous section), continuation of the time integration long enough for all particles to exit requires excessive computational resources—especially for the large number of particles used in this refined simulation. For that reason we had to terminate the particle integration when approximately 4000 particles were still remaining in the interior of the bubble. Consequently, the so computed staircase does not contain sufficiently many large size plateaus for the linear variation of N to be sustained at larger r sizes. To prove that this is indeed the reason for the observed departure from linearity, we also include in figure 5.19 the curve that resulted when the $n = 10^3$ simulation, which was actually carried out until all particles exited (t=2660), was terminated at a much earlier time (t=128)—only 100 particles were left inside the bubble at t=128 and, thus, more than 2500 secs of additional simulation were required for these few remaining particles to exit. Clearly, reducing the integration time results in the same departure from linear variation at larger values of r as that observed for the $n=3x10^4$ simulation. This small discrepancy not withstanding, figure 5.19 provides conclusive evidence that the curve shown in figure 5.18 is a complete devil's staircase with fractal dimension $d = 0.4$ (see subsequent discussion for the variation of d with Reynolds number and aspect ratio) Interestingly,

this value of the fractal dimension is lower than the *d=0.87* "universal" constant (Bak 1986) that has been previously found in a number of dissipative dynamical systems undergoing mode-locking transition to chaos.

To further explore the statistical properties of the devil's staircase curve, we plot in figure 5.20 the calculated (for the staircase shown in figure 5.18) frequency of occurrence, *S(r)*, of the various plateau sizes (i.e. the waiting times between bursting events) as a function of the plateau size *r*—i.e. the histogram of *r*. Figure 5.20 shows that the frequency of occurrence diminishes monotonically as the plateau size increases. Furthermore, a power law of the form:

$$S(r) \approx \left(\frac{1}{r}\right)^{a} \tag{5.4}$$

with $a = 1.4$ appears to fit well the computed data points. Note that a power-law distribution for *S* is consistent with the nature of the devil staircase, as plateau sizes of zero length correspond to the points of the complimentary Cantor set and should, thus, be infinitely many. It is also important to point out that the apparent relation between the fractal dimension *d* and the exponent *a* ($a = 1 + d$) is not coincidental. Assuming a continuous function $S=S(r)$ of the form given by equation (6) and noting that *T(r)* (the total length of plateaus with size greater than *r*) can be computed from *S* as follows (r_{max} is the size of the largest plateau):

$$T(r) = \int_{r}^{r_{\max}} r' S(r') dr' \tag{5.5}$$

we can easily show that the number of holes *N* of size *r* defined by equation (4) is given by the following equation:

$$N = \frac{1}{r} \int_0^r r' S(r') dr' \approx \left(\frac{1}{r} \right)^{a-1} \tag{5.6}$$

Comparison with equation (5.3) yields the relation implied by the numerical values in figures 5.19 and 5.20, i.e. $d = a\text{-}1$. In other words, the fractal dimension of the complimentary Cantor set can also be calculated from the histogram of plateau sizes.

To investigate whether the fractal dimension of the staircase varies with the governing parameters of this flow (H/R and Re), we carried out computations similar to those described above but for the two bubbles shown in figure 5.15 (Re = 1,492 and 1,667 for H/R=2). Both simulations were carried out using 30000 initial particles. Our computations reveal that the fractal dimension decreases with Reynolds number from 0.69 to 0.55. As we have already discussed above, however, the limited number of cases considered herein do not allow us to establish any meaningful trends. Computations over a much broader range of Reynolds numbers and aspect ratios will be needed before such trends can be extracted.

Finally, it is important to point out that our findings in this and the previous sections, point to the conclusion that the infinite intersections of the stable and unstable manifolds of the spiral-in saddle, through which upstream originating particles enter and exit that bubble, exhibit a fractal spatial structure. Since chaotic Šil'nikov orbits will have to exit through this fractal "window", their exit time will be extremely sensitive to arbitrarily small differences in the particle initial location, and, thus, the resulting fractal structure in the residence time maps and the variations in the sizes of the devil staircase plateaus.

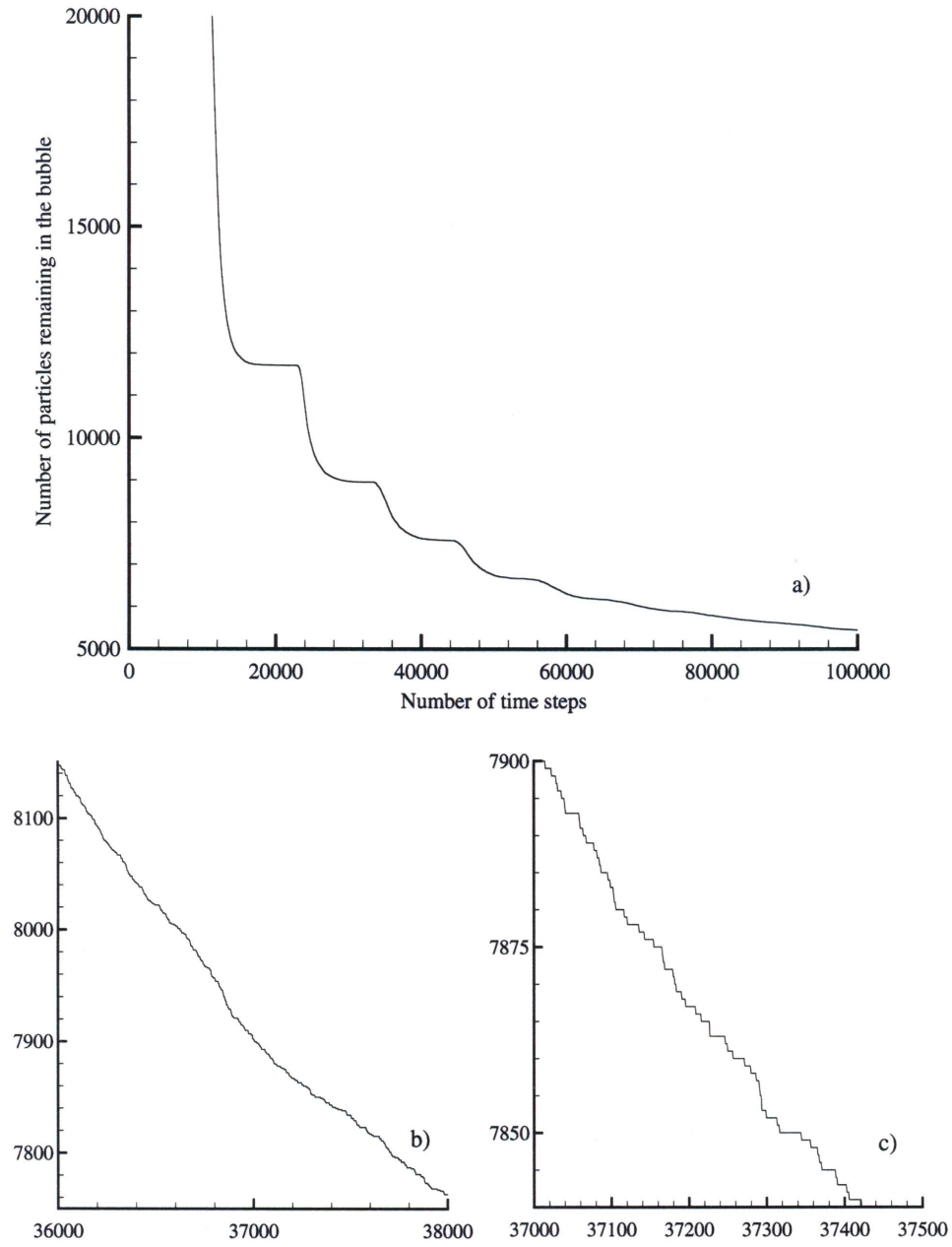

Figure 5.18 Emptying of a calculated stationary vortex breakdown bubble (Re=1850, H/R=1.75). $3x10^4$ particles are distributed along a small disk located just upstream of the bubble. The number of particles remaining in the bubble is plotted as a function of time. Increasing time resolution shown in a)-c).

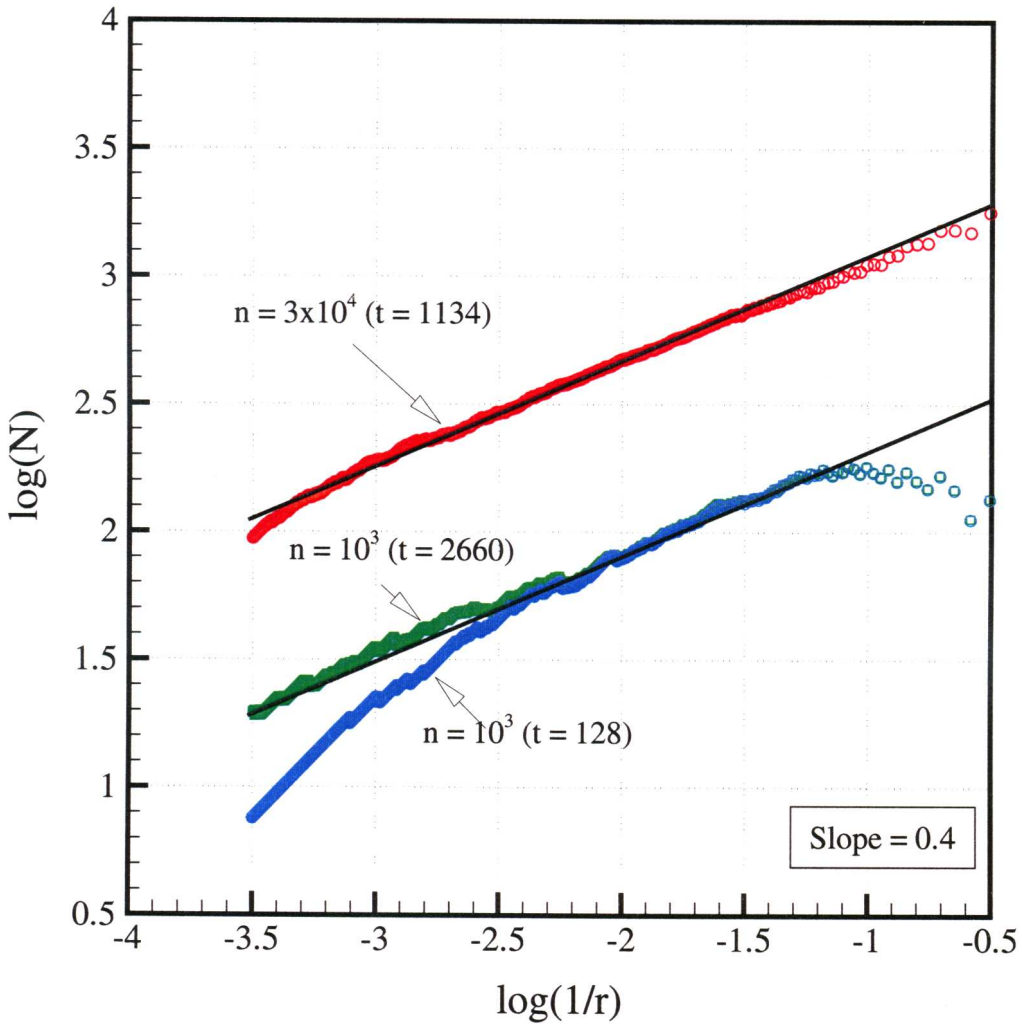

Figure 5.19 Fractal dimension of the Cantor set associated with the devil's staircase shown in figure 5.18. The number of particles used in the simulation is n and the simulated time interval for each case is t.

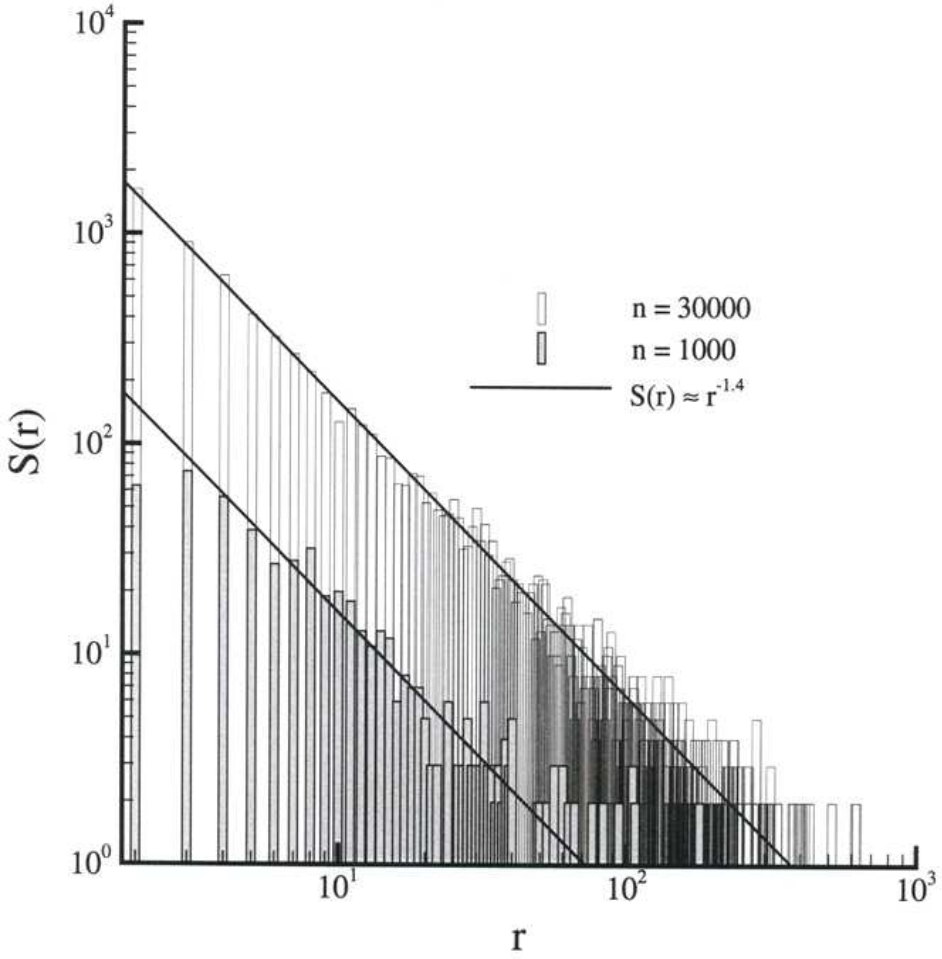

Figure 5.20 Histogram of the staircase plateau sizes for the staircases used to calculate the fractal dimensions in figure 5.19.

5.6.4 Dynamics of the Second Bubble in the Steady Two-Bubble Regime and the Role of Swirl Intensity

As has been stated previously, dependent on the aspect ratio and Reynolds number (see figure 5.3) one, two, three, or no bubbles are possible. In this section the dynamics of the second or bottom bubble formulated in the two-bubble regime is discussed. Figure 5.21 shows to the left a streamline of the two-bubble vortex breakdown case, where the aspect ratio is two and the Reynolds number is 1900. The dynamics of the first bubble are known to be quite similar to the previously seen one bubble Re=1850 (AR=1.75) case (Sotiropoulos et al 2002). From the Poincaré map shown on the right-hand-side of figure 5.21, it is immediately clear however that the dynamics of the second vortex breakdown bubble are quite different than what has been discussed previously.

The second bubble seems to be almost perfectly axisymmetric and is formed by a series of invariant surfaces. This is consistent with previous laboratory experiments (Escudier 1984, Sotiropoulos et al 2002). In Escudier's photographs, the dye used to visualize the flow does not penetrate the interior of the second bubble to the extent that it does the first. Sotiropoulos et al (2002) developed experimental Poincaré maps that agree with the representation, showing the closed invariant tori in the second bubble while displaying the extremely complex dynamics of the first bubble with its various periodic islands chains and KAM-tori.

An explanation of the almost axisymmetric form of the second vortex breakdown bubble in comparison with the first bubble is developed by considering the previously described system (equations 5.1) whose phase space dynamics are similar to the

Lagrangian dynamics of real-life steady vortex breakdown bubbles. The parameters μ_1, μ_2, a, and b of the system are set to 0,-1.96, 1, and -1 respectively, creating the system:

$$\frac{dz}{dt} = 0.04 - r^2 - z^2 + \varepsilon r^3 \sin(2\theta); \qquad \frac{dr}{dt} = rz; \qquad \frac{d\theta}{dt} = \varpi \tag{5.7}$$

In this system ω is the angular velocity and ε controls the magnitude of the term representing the higher order terms that perturb the system and excite the modes of instability. The arbitrarily chosen perturbation field is a mode-2 azimuthal disturbance in the axial velocity component and is designed to ensure that the perturbed system also remains volume preserving. Although the above velocity field does not satisfy the Navier-Stokes equations, it is useful because the qualitative dynamics are similar to the real life vortex breakdown bubble. In particular, this system will provide a further understanding of the effect of adding perturbations to the system than that gained in section 5.4 as well as the effect of swirl parameter.

Figure 5.22 shows numerically constructed Poincaré maps for various ω and ε values. The particle paths were calculated using the same numerical method, time-increment, and a velocity field discretized on the same computational mesh. A Cartesian 51x51x51 box containing the bubble was used as the computational domain. The first set of computations (figures 5.22a to figure 5.22c) maintains a constant swirl (ratio of azimuthal to axial velocity components) but varies the magnitude of the perturbation affecting the flow. The second set of computations (figures 5.22d to figure 5.22f) maintains constant magnitude of perturbation but increases the swirl parameter.

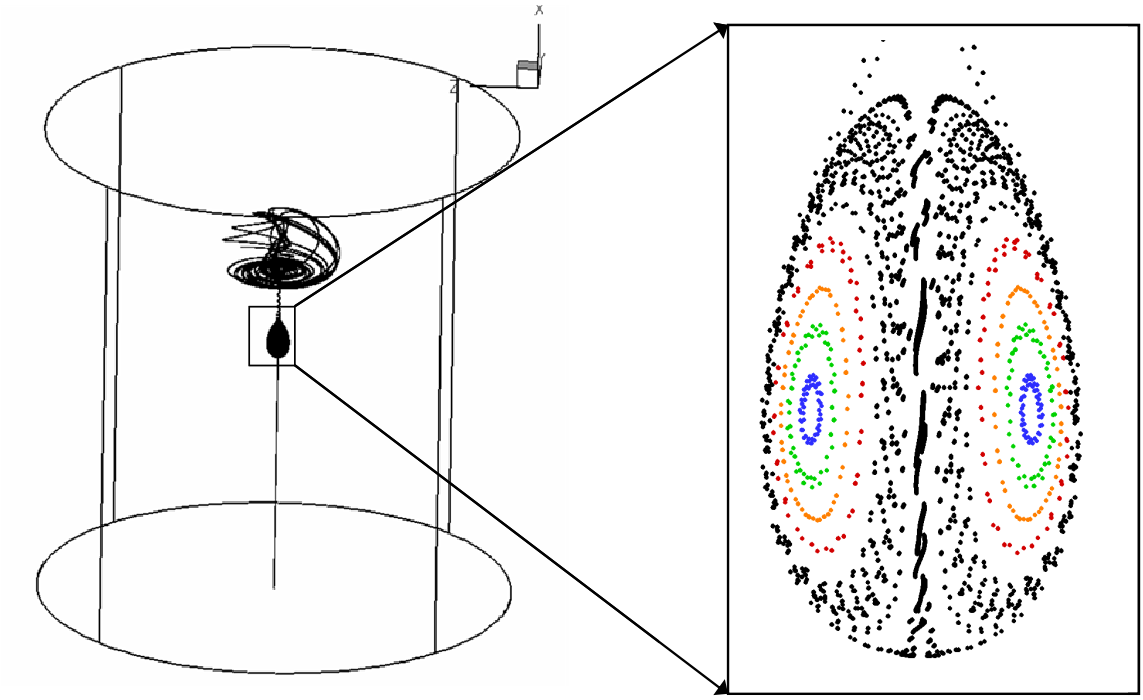

Figure 5.21 Poincare map of lower vortex breakdown bubble in the two bubble regime (Re = 1900, AR=2). To the left are three-dimensional streamlines that show the bubble structure.

Figure 5.22a shows the unperturbed case: ω=0.5 and ε= 0. In this case, the bubble appears to be perfectly axisymmetric. The interior of the bubble contains an uncomplicated series of invariant KAM-tori. A small region along the axis exists that shows chaotic characteristics but can be attributed to numerical chaos due to disturbances introduced by the trajectory integration scheme. It is not possible to eliminate this small region even if the time step is reduced by an order of magnitude. Broer and Vetger (1984) predicted this finding in their theoretical analysis, which showed that exponentially small disturbances could be sufficient to lead to Sil'nikov chaos.

Figures 5.22b and c show the effect of increasing the magnitude of the perturbation for fixed swirl. As ε is increased to 0.1 in (b) the invariant tori begin to break. Periodic islands form and the chaotic region increases. As it is increased even further to 0.5 in (c) the bubble gains similar characteristics to that of experimentally visualized and numerically calculated vortex breakdown bubbles shown previously. Folds form along the bottom of the bubble exterior and the dynamics of the interior become increasingly complex, showing: islands, cantori and KAM-tori.

Figures 5.22 (d) through (f) illustrate the effect of increasing the swirl for the value of ε=0.5. Note that since the asymmetric perturbation is only introduced in the axial velocity field, the axial and radial velocity components are identical for all the maps shown in the figures. This means that from an Eulerian standpoint, the only difference between the three flow fields is the magnitude of the angular velocity. As this value is increased, a dramatic effect is discovered. The chaotic characteristics of the bubble are damped. The folds disappear and the invariant toroidal region increases in size. As the swirl intensity is increased to ω=1.0, the chaotic Sil'nikov column around the axis shrinks

to a very thin region and for all purposes disappears at a value of ω=2.0. This result leads to the conclusion that even though the velocity field can be three-dimensional, at sufficiently high swirl velocities the Lagrangian dynamics are identical to those of the unperturbed, axisymmetric flow. High swirl velocity has a stabilizing effect on the Lagrangian dynamics. This is similar to the effect that strong rotation has on Eulerian turbulence.

Now applying this analysis to the two bubble regime for the computed vortex breakdown case (see figure 5.23), it is possible to infer explanations about the differences in the dynamics of the first and second bubble. The numerical calculations show that the axial velocity component in the downstream region of the first bubble is approximately one order of magnitude smaller than the axial velocity upstream of the bubble. Since the azimuthal velocities do not vary significantly along the axial directions in the vicinity of the two bubbles, the variations of the axial velocity result in swirl ratios that are larger upstream of the second bubble than upstream of the first bubble. Therefore the well-ordered and nearly axisymmetric appearance of the second bubble is in fact due to the larger swirl value.

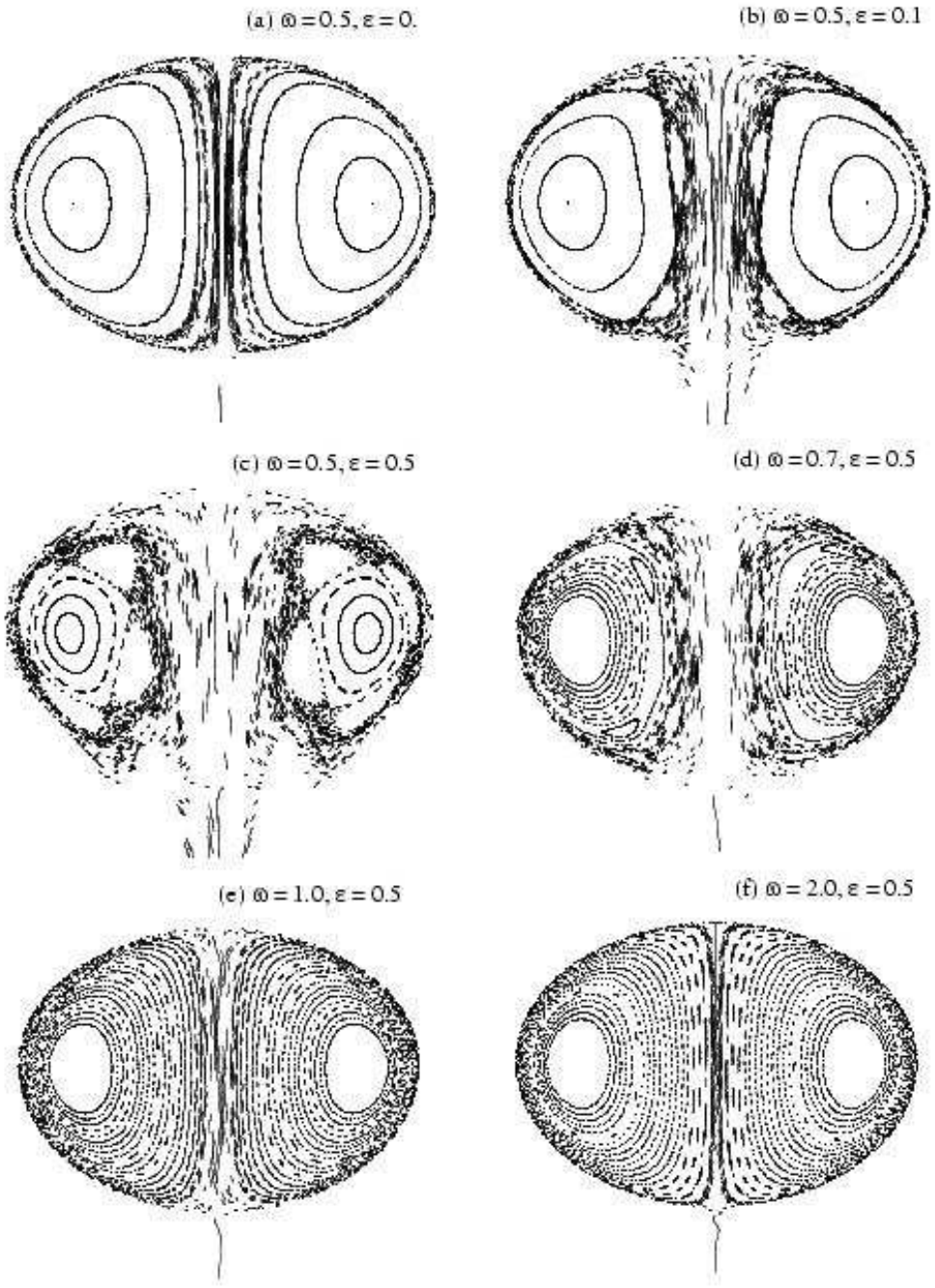

Figure 5.22 Poincare maps for the system given by equation 5.1 for various levels of perturbation strength ε and swirl intensity ω.

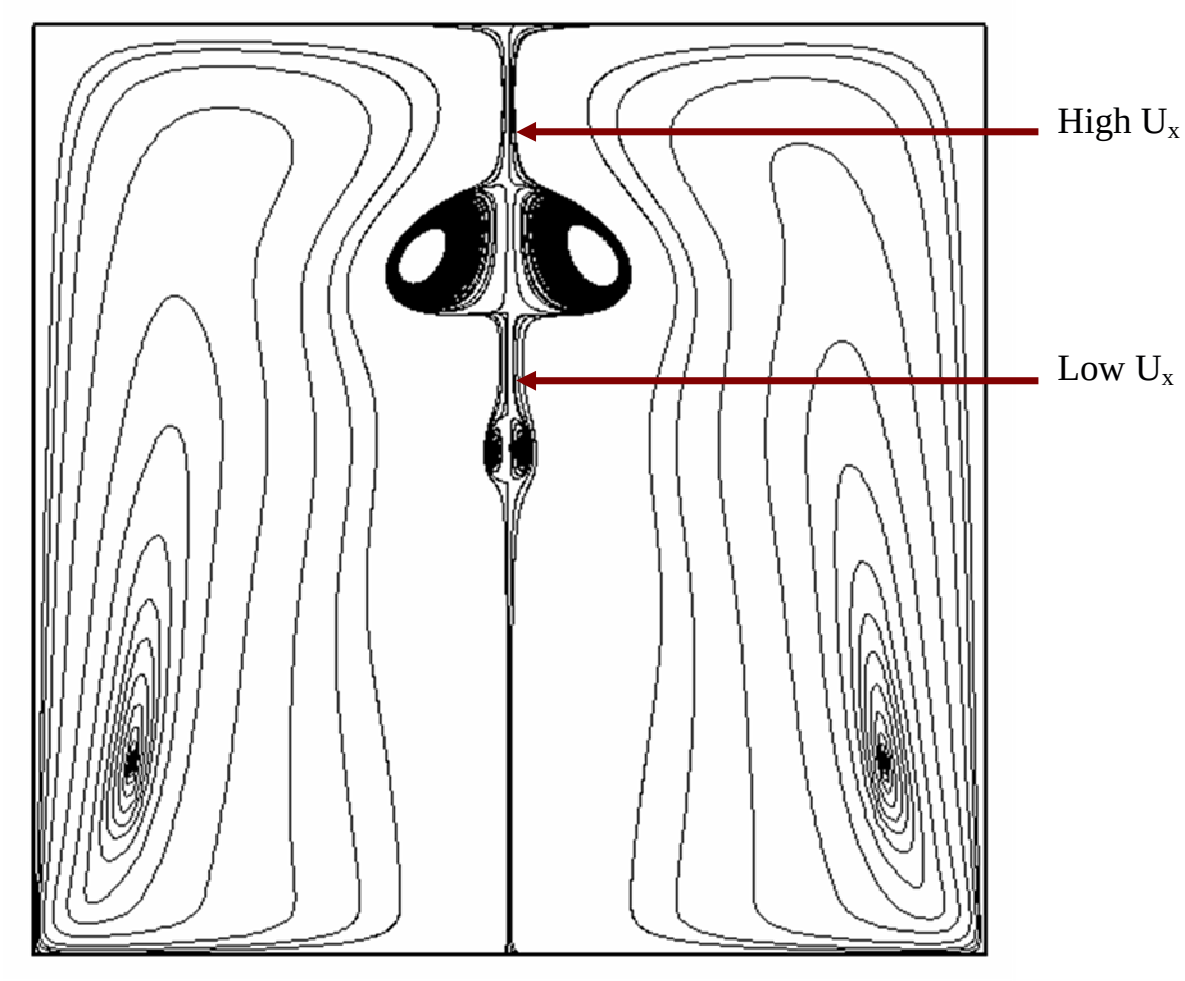

Swirl Ratio=$|U_\theta/U_x|$

Figure 5.23 Axisymmetric streamlines in the two bubble regime depicting positions of high and low swirl ratio.

5.7 Summary

In this chapter we analyzed the Lagrangian properties of steady vortex breakdown bubbles in a closed cylindrical container with rotating bottom lid. The vortex breakdown flowfields were obtained by solving numerically the Navier-Stokes equations. We showed that even though from the Eulerian viewpoint the simulated flowfields are steady and nearly axisymmetric the Lagrangian dynamics could be rich. We developed links with the theory of dynamical systems, which suggested that Silnikov's mechanism plays a critical role in breaking up the invariance of the bubble and giving rise to chaotic dynamics. We also showed that the interior of perturbed vortex breakdown bubbles exhibits Lagrangian richness consistent with what one would anticipate for a mildly perturbed, volume preserving system. Impermeable KAM-tori, leaky cantori, and unmixed island chains are found embedded within chaotically stirred regions. Upstream originating particles enter the bubble from the downstream saddle focus and a Cantor set of initial conditions could stay in the interior of the bubble for arbitrarily long times. Another important feature of the flow is that particles exit the bubble in random bursts and that the rate at which an initial population of particles exits the bubble is a Devil's staircase. By examining the dynamics of a model dynamical system we also reached the striking conclusion that vortex breakdown bubbles, occurring at sufficiently high swirl numbers, exhibit integrable (axisymmetric) dynamics even in the presence of non-axisymmetric perturbation in the advecting velocity field. All our computational findings in this chapter are supported fully by the recent experimental work of Sotiropoulos et al. (2002).

Our findings in this chapter have important implications for understanding the phenomenon of vortex breakdown and the interpretation of the results of laboratory visualization experiments. The finding that for a certain range of swirl numbers very small non-axisymmetric perturbations can have a profound effect on the Lagrangian properties of the bubbles points to the conclusion that it could be very difficult, if not impossible, to visualize perfectly axisymmetric vortex breakdown flowfields in a laboratory experiment. This conclusion explains why axisymmetric computations of the flow can capture correctly most features of vortex breakdown but fail to resolve the asymmetries observed in the laboratory flow visualization experiments. Even though the real-life and ideal (axisymmetric) flowfields are very similar from the Eulerian standpoint, their Lagrangian descriptions are as fundamentally different as order and chaos. The finding concerning the role of swirl intensity on the Lagrangian dynamics further suggests that stirring intensity in the interior of vortex breakdown bubbles could be controlled by varying a simple Eulerian property of the flow, the ratio of the swirl to axial velocity upstream of the bubble. With further work, this finding could lead to a rigorous framework for controlling mixing efficiency and the residence time distribution in vortex breakdown bubbles in flows of technological significance.

CHAPTER 6

Container with Exactly Counter-Rotating Lids

The flow in a cylindrical container with exactly counter rotating lids is among the least studied of the von Karman type flows. Yet the dynamics of this flow are extremely complex. The counter-rotation of the lids gives rise to an azimuthal shear layer at the container mid-plane, which has been shown to lose stability in the form of radial vortices even at rather low Reynolds number when the flow is steady (see Nore et al 2003 for a recent review). Therefore, unlike the previously studied container flow with rotating lid where in the absence of asymmetric forcing the base flow is steady and axisymmetric, the present flow loses symmetry naturally as a result of an azimuthal Kelvin-Helmholtz instability. The various instability modes, bifurcations and flow regimes as a function of container aspect ratio and flows Reynolds number for the counter-rotating case have been studied extensively in a number of recent stability studies by Gauthier et al 2002, Lopez 2002 , and Nore et al 2003. However, neither the nature of the symmetry-breaking vortical structures in this flow nor the Lagrangian dynamics of the flow have been previously explored. Yet this flow can serve as an excellent test case for exploring fundamental questions of chaotic advection in a steady, three-dimensional flow for two main reasons. First the fact that the base flow is naturally unstable to three-dimensional modes eliminates the need for introducing arbitrary three-dimensional perturbations to instigate the break of axial symmetry. Secondly, the flow remains steady over a rather

broad range of Reynolds numbers greater than the threshold Reynolds number for the onset of the shear layer instability. Thus, this flow can be used to explore the fundamental relationship between mixing intensity and Reynolds number in a steady, three-dimensional flow and test the validity of a recently proposed related theory by Mezić (2001).

In this chapter we report the results of three-dimensional Navier-Stokes computations for this flow and carry out a comprehensive investigation of its Lagrangian properties. Furthermore, we explore and quantify for the first time the effect of Reynolds number on intensity of chaotic stirring. The chapter is organized as follows. First we describe the flow geometry and review previous related research. Next we discuss the numerical method we employ to solve the Navier-Stokes equations and various computational details. This is followed by a discussion of the Eulerian aspects of the flow and a detailed analysis of its Lagrangian properties.

6.1 Flow Geometry

We consider steady flow of an incompressible fluid within a closed cylindrical container of radius R and height H with two exactly counter rotating lids. That is, the magnitude of the angular velocity $|\Omega|$ of the lids is the same but they rotate in opposite directions ($\Omega_{bottom}=-\Omega_{top}$). Due to Ekman pumping, meridional recirculation zones are formed in the upper and lower half on the container. As shown in the sketch in figure 6.1, fluid particles near each lid spiral outward from the centerline toward the sidewall. Upon reaching there the fluid starts moving vertically along the sidewalls spiraling towards the vertical midplane of the container. Fluid particles from the upper and lower

halves of the container meet at the mid-plane where they are forced inward towards the center of the container forming a radial jet that ends at the stagnation point at the center of the container. The fluid very near the stagnation point is either pushed upwards or downwards along the vertical axis, thereby forming a saddle point in the flow. Because of the opposite direction of rotation of fluid in the upper and lower halves of the container an azimuthal shear layer forms at the mid-plane where the two flows collide.

For the base axisymmetric flow, the so resulting recirculating motion consists of two sets of invariant tori in the upper and lower halves of the container, respectively, with the flow in each set of tori rotating in opposite direction. Particle trajectories remain trapped on their respective invariant surfaces and chaotic advection is not possible. The azimuthal shear layer at the mid-plane, however, can become unstable leading to a complex, three-dimensional flow (Lopez et al 2002). The flow is governed by two parameters: the Reynolds number ($Re = \Omega R^2/\nu$ based on the angular velocity Ω, the radius of the container R, and υ the viscosity of the fluid) and the aspect ratio (AR=H/R where H is the height of the container). As established in Nore et al (2004), the relationship between these two parameters determines thresholds in which one can witness either axisymmetric or three-dimensional flow characteristics.

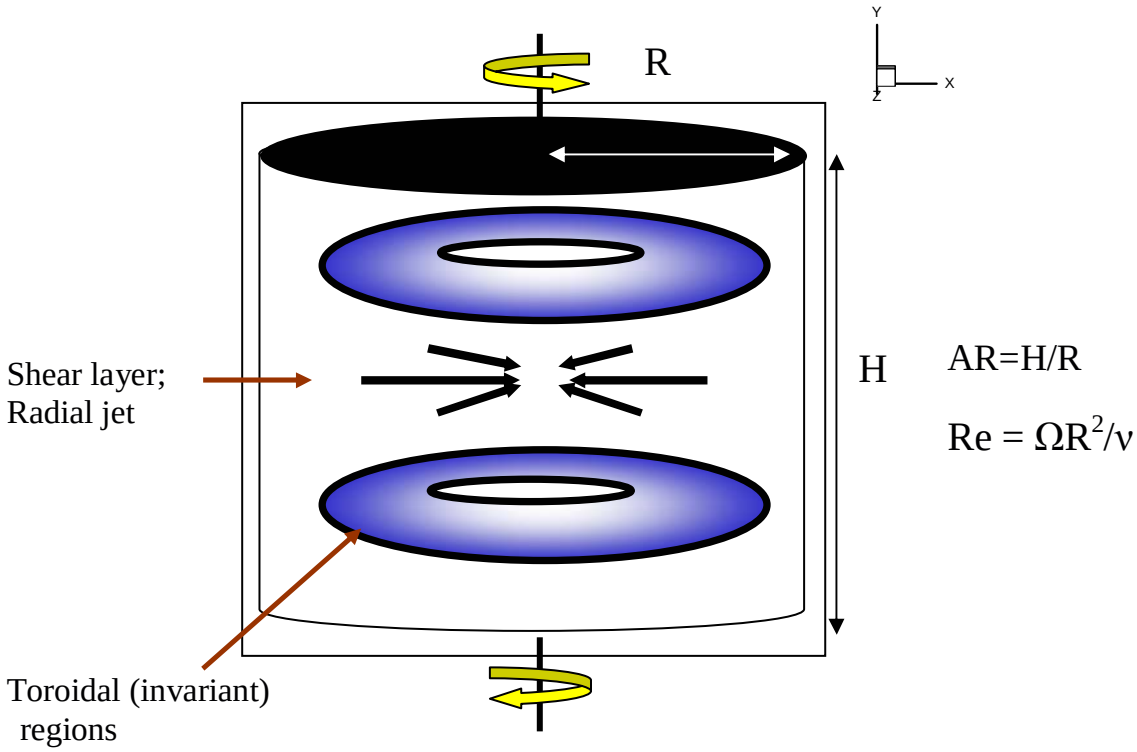

Figure 6.1 Flow geometry for cylindrical container with exactly counter-rotating lids.

6.2 Previous Research

Batchelor (1951), extending the work of von Karman (1921) was the first to study flow between two rotating disks. Batchelor argued that for high Reynolds number the bulk of the flow rotates with constant angular velocity while thin boundary layers develop at both disks. He further suggested that for exactly counter-rotating disks the flow will be separated into two parts rotating in opposite directions and separated by a transition (or shear) layer. Stewartson (1951) in his investigation of the same flow disagreed arguing that the bulk flow would not rotate at all. Throughout the next twenty years a series of studies were performed (Mellor et al (1968), Ngyen et al(1975), Holodniok et al(1977)), which confirmed that both the Batchelor type flow as well as the Stewartson flow were indeed possible. Depending on the parameter $s = \Omega_T/\Omega_B$, which is the ratio of the angular velocities of the top (Ω_T) and bottom (Ω_B) lid, and the Reynolds number many branches of solutions are possible. These results were eventually extended to confined, rotating flows in cylindrical containers.

The counter-rotating case ($s < 0$) has recently received considerable attention due to the very rich three-dimensional instabilities that emerge as a result of the shear layer instability. Lopez et al. (2002) considered the flow for AR = 0.5 and Re=1000 and varied s between 0 and -0.8. They reported unsteady flows with very rich dynamics dominated by rotating funnel-like vortices of azimuthal wave numbers 4 and 5. Gauthier et al (2002) studied the flow in a container with AR = 0.05 and observed a new kind of "negative" spiral structures, which roll up toward the centre in the direction of the opposite to that of the faster disk. They attributed the origins of this spiral instability to the same free shear layer instability mechanism proposed by Lopez et al. (2002).

Moisy et al. (2003) carried out experiments for various aspect ratios and s in the range -1 < s < -0.135 and found flow patterns consisting of vertical vortices and negative spirals. They found that for moderate AR and/or large Re the flow is dominated by vertical vortices while for small AR and/or small Re the negative spiral dominate.

Nore et al. (2003) carried out linear stability analysis of the flow for s = -1 and AR = 2. They showed that when the disk rotation rate is increased, axial symmetry breaks as a result of a Kelvin-Helmholtz instability of the azimuthal shear layer. They reported both steady states, with one or two radially oriented vortices, and unsteady flows dominated by traveling waves, modulated traveling waves and near heteroclinic cycles. In a more recent study, Nore et al. (2004) reported the most comprehensive to-date stability analysis of the exactly counter-rotating case (s = -1) by varying both the Reynolds number and the aspect ratio AR (0.5<AR<3).

6.3 Computational Details and Numerical Sensitivity Studies

We study numerically the flow in a closed cylinder of aspect ratio AR = 1 driven by two exactly counter-rotating lids for a range of Reynolds numbers within which the flow remains steady but transitions from axisymmetric to three-dimensional (295 < Re < 850). Since the base flow is unstable to three-dimensional disturbances there is no need to introduce an explicit forcing to the flow by adopting a curvilinear mesh topology as was done for the vortex breakdown flow studied in the previous chapter. We, thus, solve the incompressible, Navier-Stokes equations in a cylindrical polar mesh, which is shown in figure 6.2. The numerical method is second-order accurate and is described in detail in Appendix A.

Grid sensitivity studies are carried out for Re = 350 and Re=700 by performing simulations on three successively finer meshes (total number of grid nodes ranging from approximately 0.5 to 1.8 million): Grid A with 61×141×61 nodes; Grid B with 61×141×161 nodes; and Grid C with 81×211×161 nodes in the radial, vertical, and azimuthal directions respectively to guarantee grid independence. In Grids A and B the grid nodes were distributed uniformly in all three directions. In Grid C the grid nodes were stretched near the container walls using a hyperbolic stretching function. Computed solutions on various grids for Re = 350 are compared with each other in figure 6.3 and 6.4, in terms of axial, radial, and azimuthal velocity components. Comparisons are shown at the horizontal mid-plane and a diametral plane. It can seen that the computed solutions on all three meshes are very close to each other and only small quantitative discrepancies are observed between the predictions on the coarsest and finest mesh. This conclusion is also been verified at Reynolds number 700 (figures 6.5 and 6.6) where the flow is expected to be more complex. Once again the solutions are in good agreement with each other. Based on the results shown in figures 6.3 through 6.6, we consider the 61x141x161 uniform grid to be sufficient for obtaining mesh independent solutions and we employ this grid resolution in all subsequently presented computations.

According to the stability analysis results of Nore et al. (2004), for the aspect ratio considered herein (AR = 1) the critical Reynolds number for the onset of the shear-layer instability and the break of axisymmetry is $Re_c \cong 300$. As we will discuss in the following section, our computations for Re = 295 yielded in agreement with the stability results steady and axisymmetric (see subsequent discussion) solutions. To obtain three-dimensional solutions at Re> Re_c we attempted to spin-up the steady solution obtained at Re=295 to the desired Reynolds number and then iterate this initial guess until

convergence is reached. This approach was adopted for Re = 350 but the numerical algorithm converged to a steady and axisymmetric solution. Presumably the transient perturbation imposed on the flow by the relatively weak spin-up from Re = 295 to 350 was not sufficiently strong to trigger the onset of the three-dimensional instability and the algorithm converged to the axisymmetric solution, which is also solution to the Navier-Stokes equations at this Reynolds number. To excite the three-dimensional instability we adopted the following transient perturbation approach. Starting form the Re = 295 flowfield we spin-up the flow to a much higher Reynolds number, say Re = 700. After few hundred time steps at this Reynolds number, the flowfield is spun-down to the desired Re > Re_c and the iterative algorithm is applied until a converged steady state solution is obtained. This procedure was found adequate to trigger the shear layer instability. When applied for the Re = 350 case, for example, this procedure yielded a steady and three-dimensional solution at convergence. The same transient perturbation approach was also adopted for simulations at higher Reynolds numbers.

6.4 Eulerian Aspects of the Flow

In this section we analyze the calculated flowfields with emphasis on the Eulerian characteristics of the flow. Our main objective here is to understand the three-dimensional features of the flow and characterize the nature and structure of the three-dimensional vortices that emerge as a result of the shear-layer instability. The results presented herein are novel as no such in-depth analysis of the steady, three-dimensional flowfields for the counter-rotating case has ever been reported before in the literature.

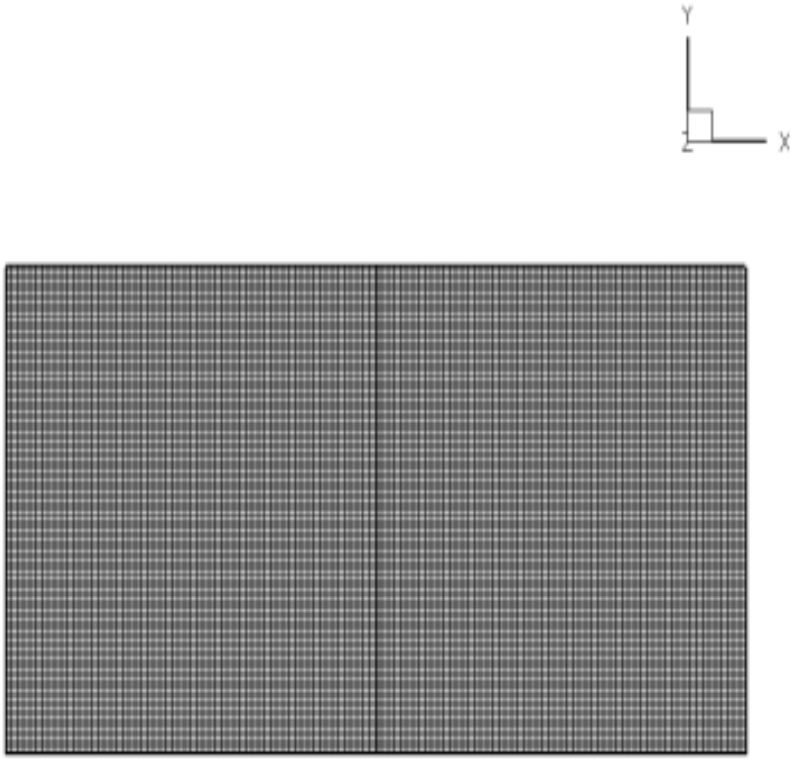

a)

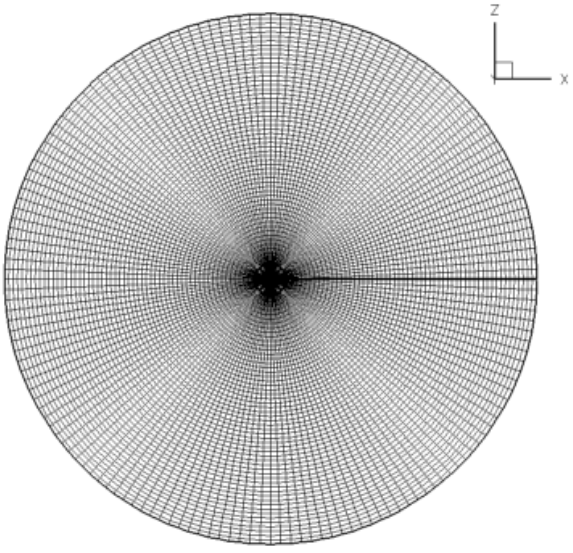

b)

Figure 6.2 Computational grid for cylindrical container with exactly counter-rotating lids

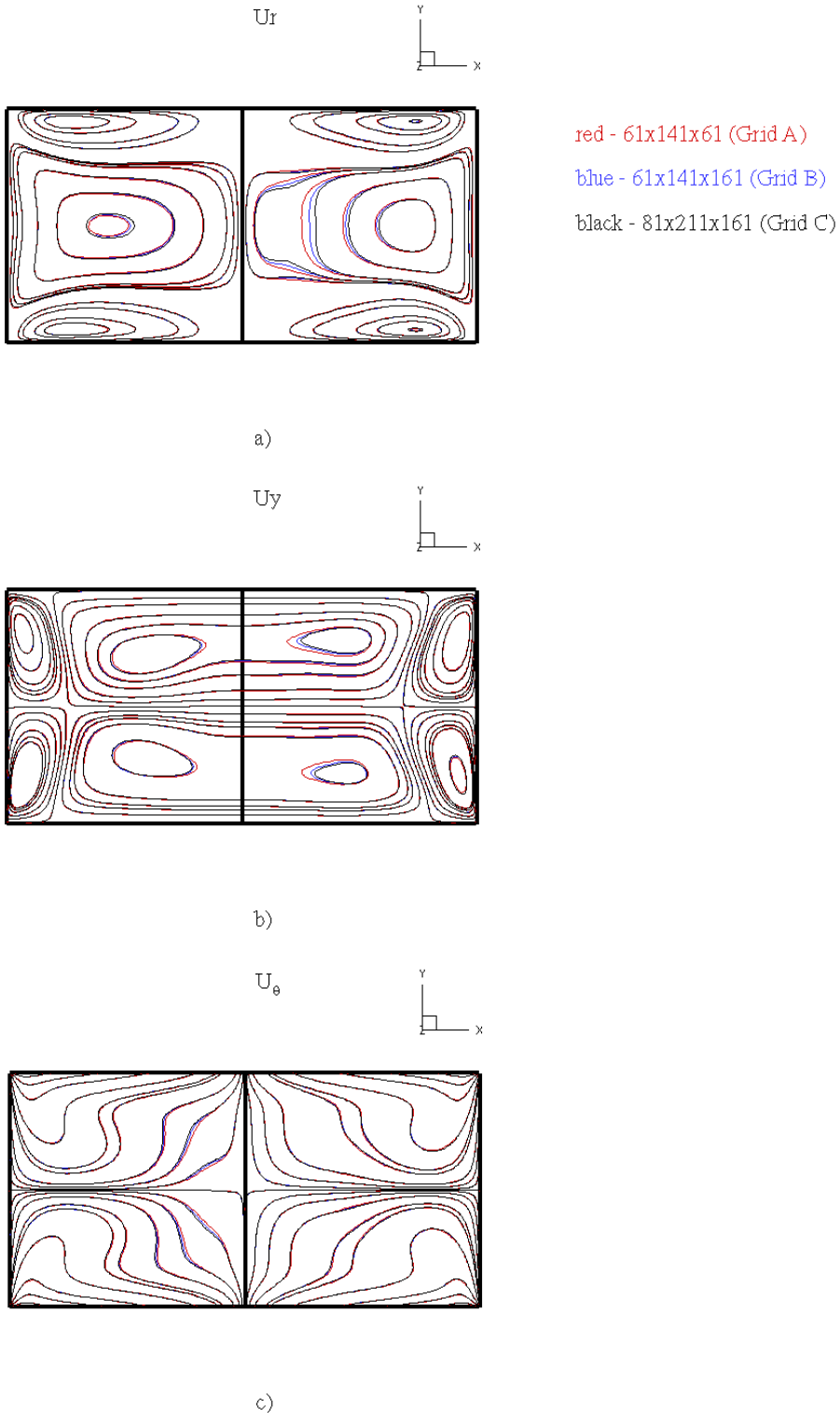

Figure 6.3 Comparison of Re = 350 velocity components with grid resolution for constant azimuthal planes. θ = 0 and 180 degrees.

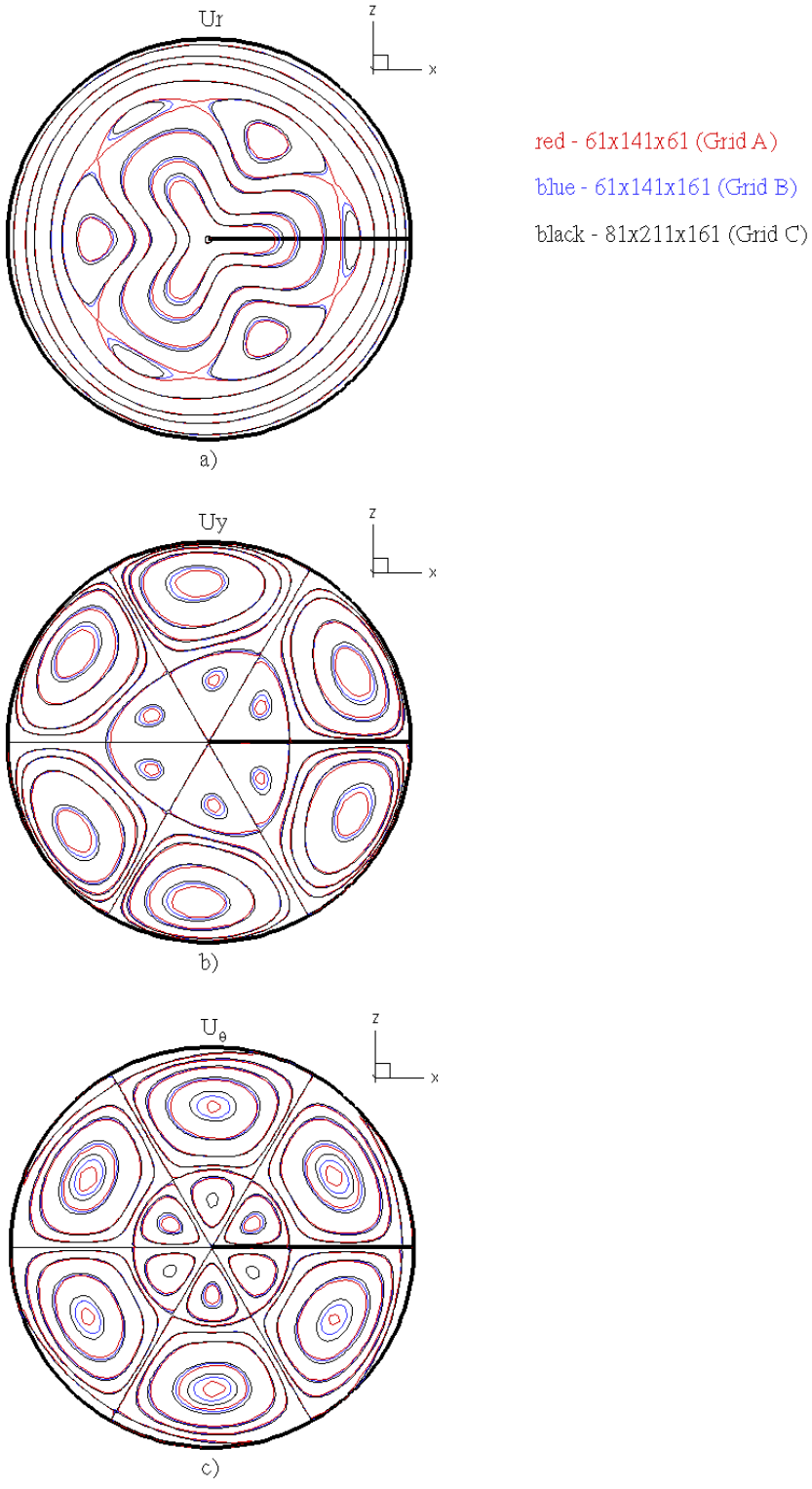

Figure 6.4 Comparison of Re = 350 velocity components with grid resolution at the equatorial plan

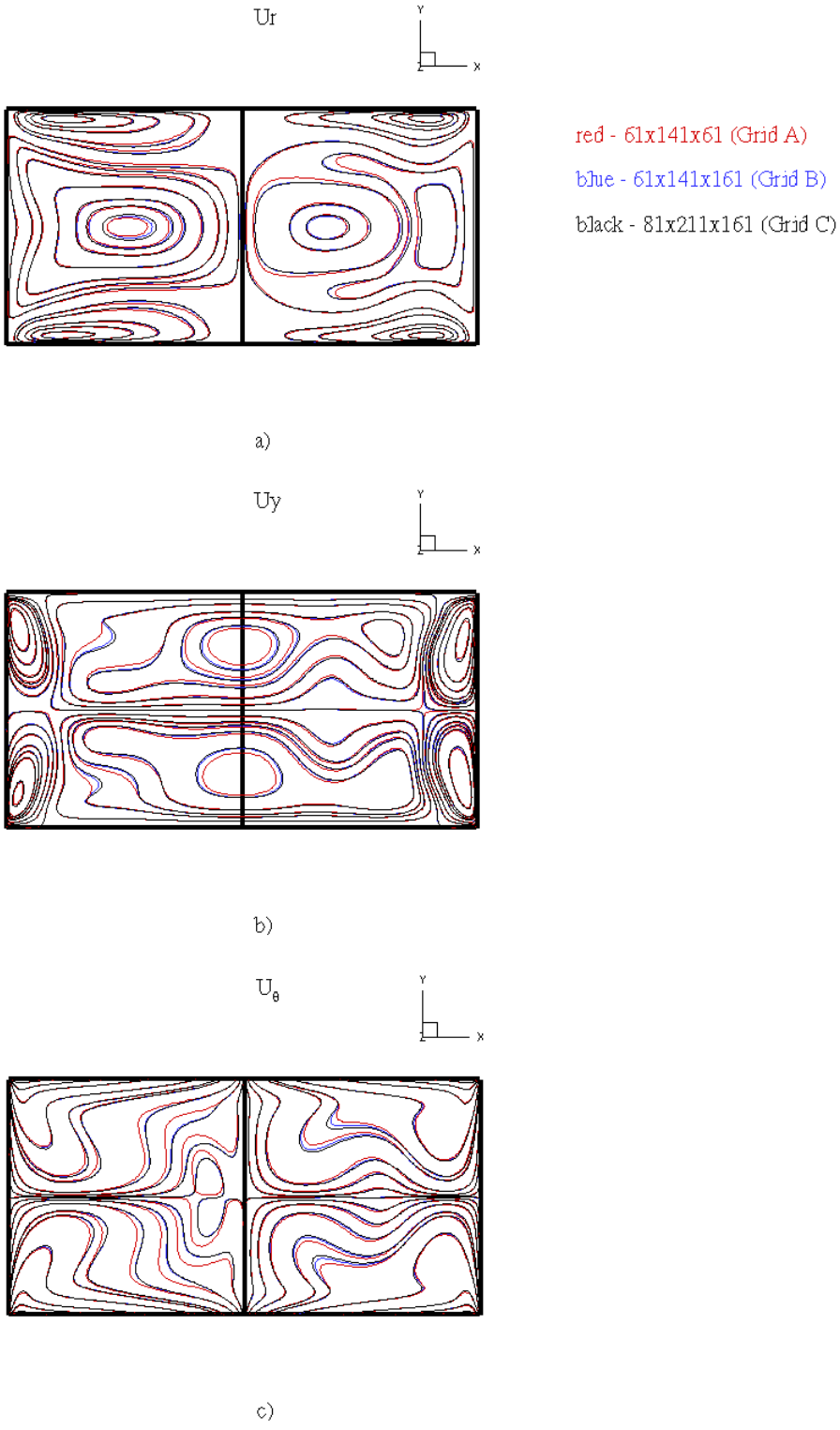

Figure 6.5 Comparison of Re = 700 velocity components with grid resolution for constant azimuthal planes. θ = 0 and 180 degrees.

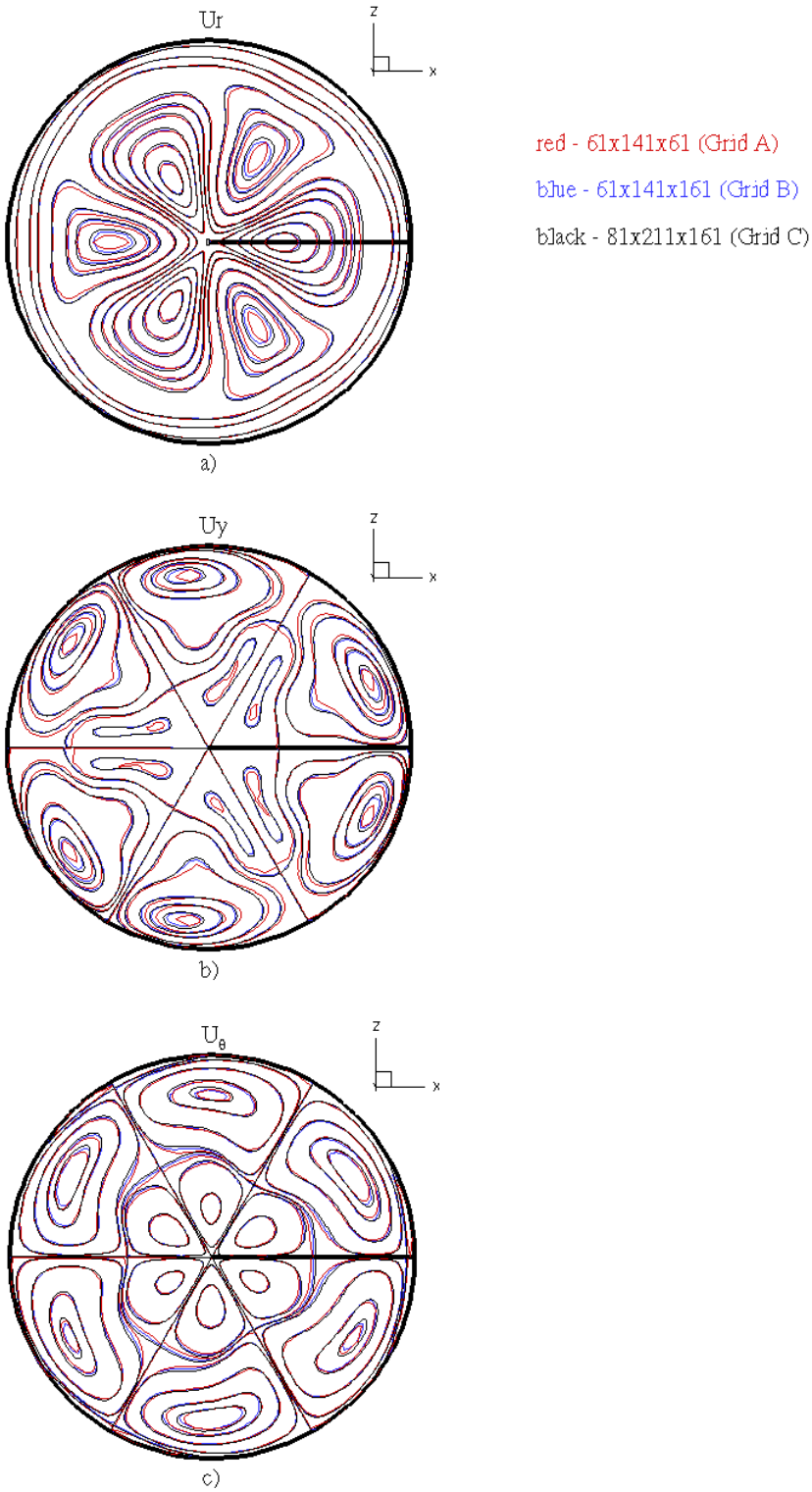

Figure 6.6 Comparison of Re = 700 velocity components with grid resolution at the equatorial plane.

6.4.1 Shear Layer Instability

As has been documented in the stability studies of Nore et al (2001, 2004), the flow is dominated by the instability of the equatorial shear layer. The instability mechanism is essentially the azimuthal equivalent of the classical Kelvin-Helmholtz instability, which is encountered in linear shear layers. Lord Kelvin and Hermann von Helmholtz proposed this instability mechanism at the end of the 19th century to explain the formation of sea waves due to the wind stress on the sea surface (Guyon et al. 2001). In a linear shear layer the instability manifests itself in the form of co-rotating, cat's eye vortices whose axes are perpendicular to the plane of the flow (see figure 6.7). In the rotating flow, as fluid from the upper and lower halves of the container is swirling in opposite directions along the equatorial plane towards the center axis of the container an azimuthal shear layer is established. At a threshold Reynolds number, the shear layer rolls up to form a series of radial cat's eye vortices and the flow becomes fully three-dimensional. Nore et al (2003, 2004), further explain that the radial position of the shear layer disturbance evolves with the aspect ratio, where large values of the aspect ratio show the maximum disturbance located near the vertical axis while, for small values (within the range of this work where the aspect ratio is held constant at 1.0), the largest gradients are concentrated at the periphery. This feature of the flow becomes evident as we further explore the three-dimensional flow characteristics in the next section.

According to the results of Nore et al. (2004) the radial cat's eye vortices are stationary and their number—the most unstable azimuthal wave number of the flow—depends critically on the container aspect ratio. Based on the findings of Nore et al. (2004), the AR = 1 case we study herein lies exactly at the interface between the

emergence of the m = 2 and m = 3 azimuthal modes (the former dominates for AR>1) and the stability results appear inconclusive. Nore et al. (2004) have in fact reported that for AR =0.95 a co-dimension two bifurcation occurs with the m = 2 and m = 3 modes competing with each other.

Our results, which are the first to be obtained by solving the full non-linear equations of motion, show that for AR = 1 the m = 3 azimuthal mode is excited. Figure 6.8 depicts the onset of three-dimensional instability in terms of axial velocity contours at the container mid-plane for all simulated Reynolds numbers. For axisymmetric, exactly counter-rotating flow U_x at the mid-plane should be zero and its value is indeed very close to zero (of order 10^{-5}) for the Re = 295 case—see also figure 6.9, which shows the variation of the maximum magnitude of U_x, V_{max}, at the mid-plane with Reynolds number. At higher Reynolds numbers, however, the flow across the mid-plane increases rapidly and the computed velocity contours show clearly the excited m = 3 azimuthal mode. The general structure of the contours remains the same at all simulated Reynolds numbers, consisting of an inner and an outer layer of adjacent pockets of up (U_x >0) and down (U_x <0) flow across the mid-plane. As the Reynolds number increases the vertical flow through the outer layer pockets (closer to the container wall) increases significantly. These outer pockets grow in size and tend to stretch the inner pockets in the radial direction. Overall the trend of increasing V_{max} with Reynolds number implies that increasing Re will lead to much more complicated Lagrangian dynamics. As more particles are able to cross that plane and explore the entire container, more intricate particle paths (as opposed to simple toroidal trajectories) become possible and the possibility of efficient global stirring increases. As we will show in subsequent sections,

however, the Lagrangian dynamics of the flow are far too complex and could lead to surprising conclusions.

To further ensure the accuracy of our simulations, we have also carried out one computation for a set of parameters (AR = 0.7 and Re = 340), which, according to the stability results, is well within the parameter space region where the m = 3 mode is excited. The computed results for this case are shown in figure 6.10 in terms of velocity vectors and axial velocity contours at the $\theta = 0^o$ plane and axial velocity contours at the mid-plane. It is clearly evident from figure 6.10b that the m = 3 mode is excited for this aspect ratio, which is in agreement with the findings of Nore et al. (2004).

To illustrate the cat's eye vortical structures that develop in the flow as the Reynolds number increases, we plot in figure 6.9, contours of radial vorticity and surface streamlines at the azimuthal plane $r = 0.75R$. The azimuthal plane has been unfolded and plotted in two dimensions (θ, r). At Reynolds number of 295, for which in agreement with the stability findings of Nore et al. (2004) the flow is steady and axisymmetric, trajectories originating at the top of the container, advance towards the equatorial plane. At this point the flow is then driven inward in the form of a radial jet, which is marked by the azimuthal line of convergence at the vertical mid-plane. As the Reynolds number increases to 350, which is above Re_c for this aspect ratio, the streamlines near the two lids become wavy and the shear layer rolls up to form the characteristic, co-rotating cat's eye vortical structures. For Re = 350 and 400 the vortex cores are stable saddle foci with the streamlines spiraling inward toward the cores. At higher Reynolds numbers, however, the cores are unstable foci with the trajectories spiraling outward from the cores. It should be noted that this difference underscores the highly three-dimensional nature of the flow as the radial vortical structures tend to move

away from the center line as the Reynolds number increases and in figure 6.11 all the results for all Reynolds numbers are show at the same r = const. plane. To illustrate the changing topology of the streamlines with r, we plot in figure 6.12 two-dimensional streamlines at various r = const. planes for the Re = 350 case. The figure also includes the contour of zero axial velocity ($U_x = 0$) as the sign of the axial flow readily explains the changing streamline topology. Near the center of the container $U_x > 0$ in the upper half and $U_x < 0$ in the lower half with this trend reversing as the container wall is approach. Since the sign of the azimuthal velocity component does not change with radius, the fixed points at the cores of the vortices will transition from spiral-in foci to spiral-out foci as we move from the center to the outer wall and this is shown clearly in figure 6.12. As one would expect at some distance from the center the streamline topology resembles that of limit cycles around fixed hyperbolic points at the core (see plot at $r = 0.73$ in figure 6.12).

The two-dimensional plots shown in the figures in this section yield only an over-simplified glimpse into the very complex and highly 3D flow patterns that develop as the Reynolds number increases. These patterns are elucidated in the subsequent section, which focuses on the three-dimensional nature of the vortical structures in the flow.

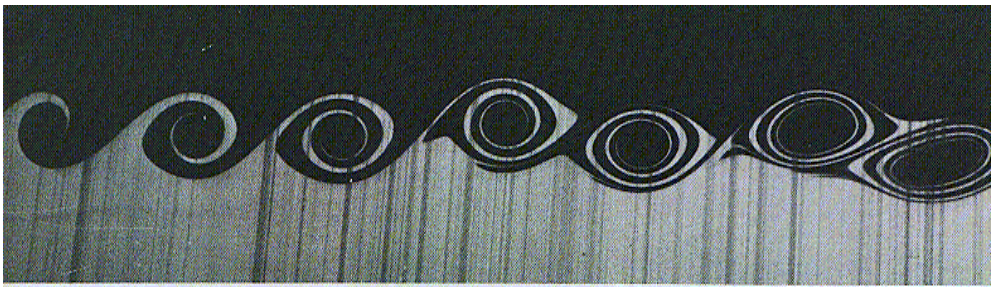

Figure 6.7 Kelvin-Helmholtz cat's eye (photo taken from An Album of Fluid Motion)

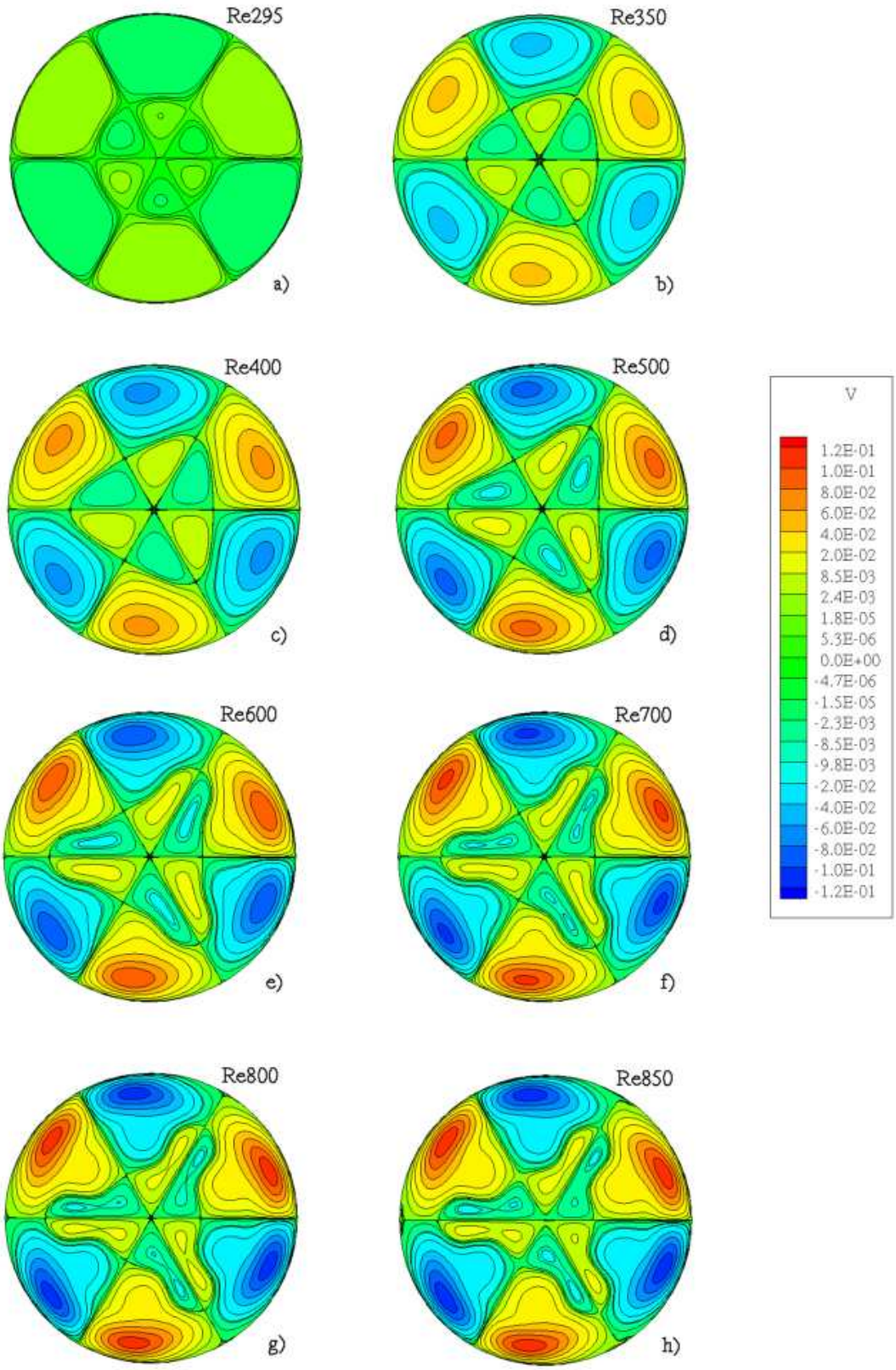

Figure 6.8 Axial velocity contours at the container mid-plane for all Reynolds numbers.

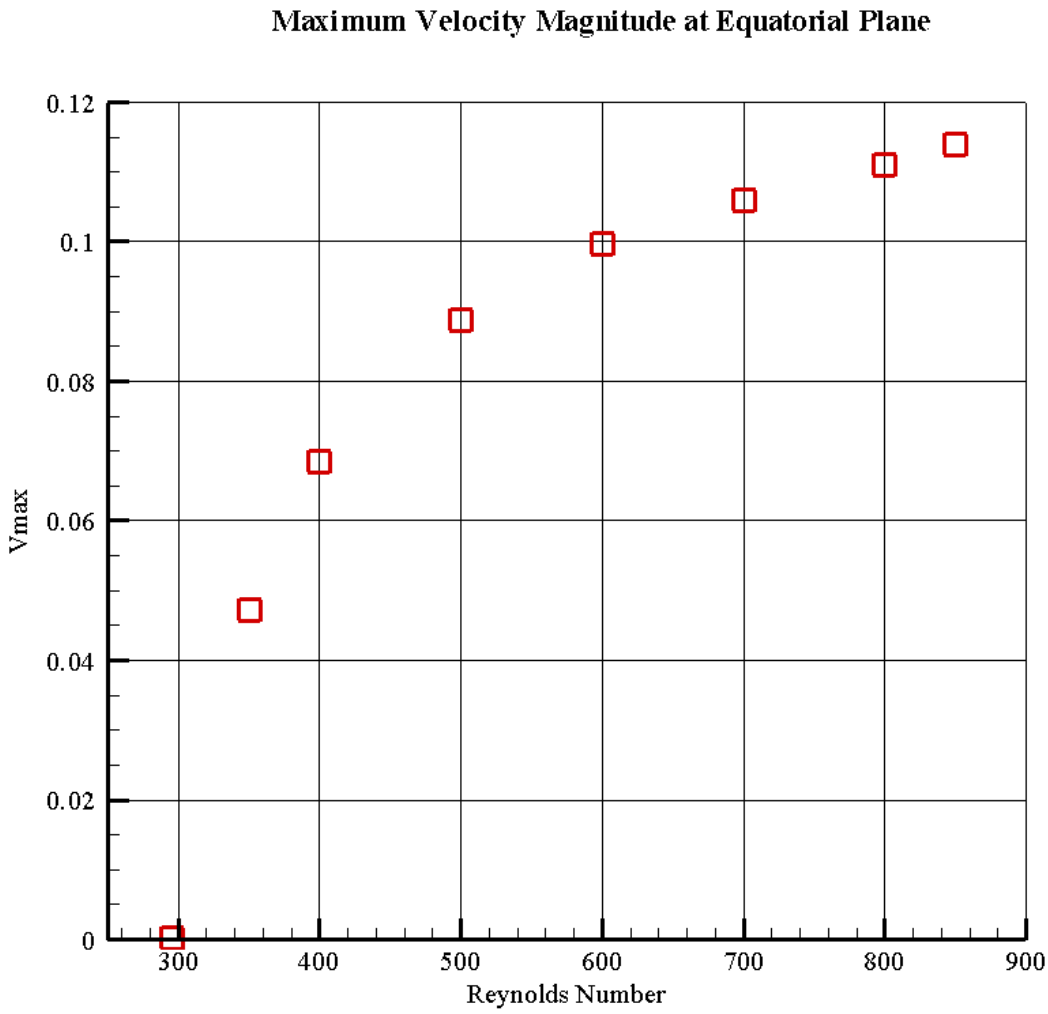

Figure 6.9 Variation of maximum magnitude of axial velocity at the mid-plane with Reynolds number.

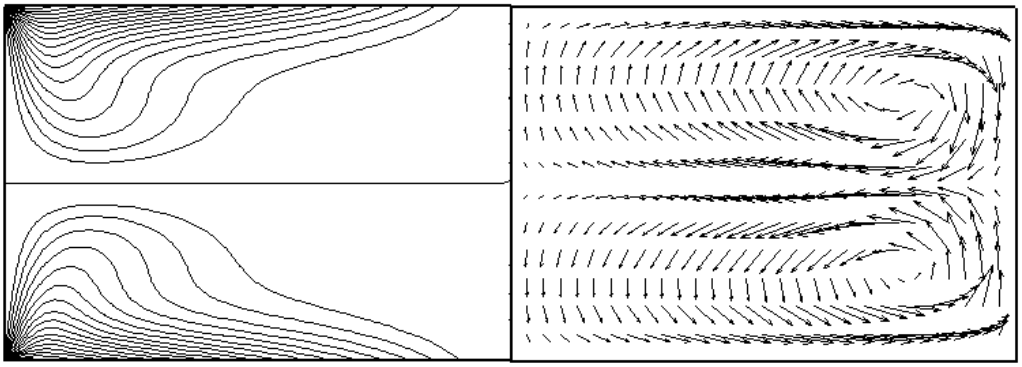

a)

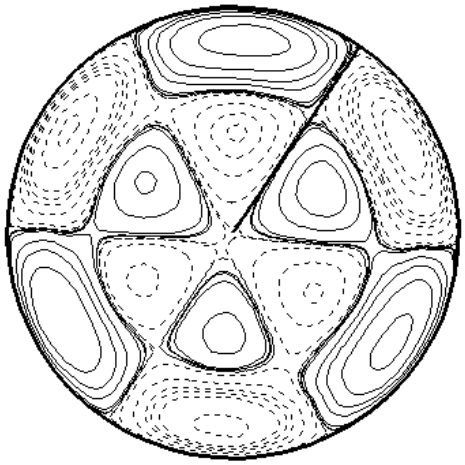

b)

Figure 6.10 a) Velocity vectors and axial velocity contours at the $\theta=0^o$ plane b) axial velocity contours at axial mid-plane (dotted lines indicate negative velocity).

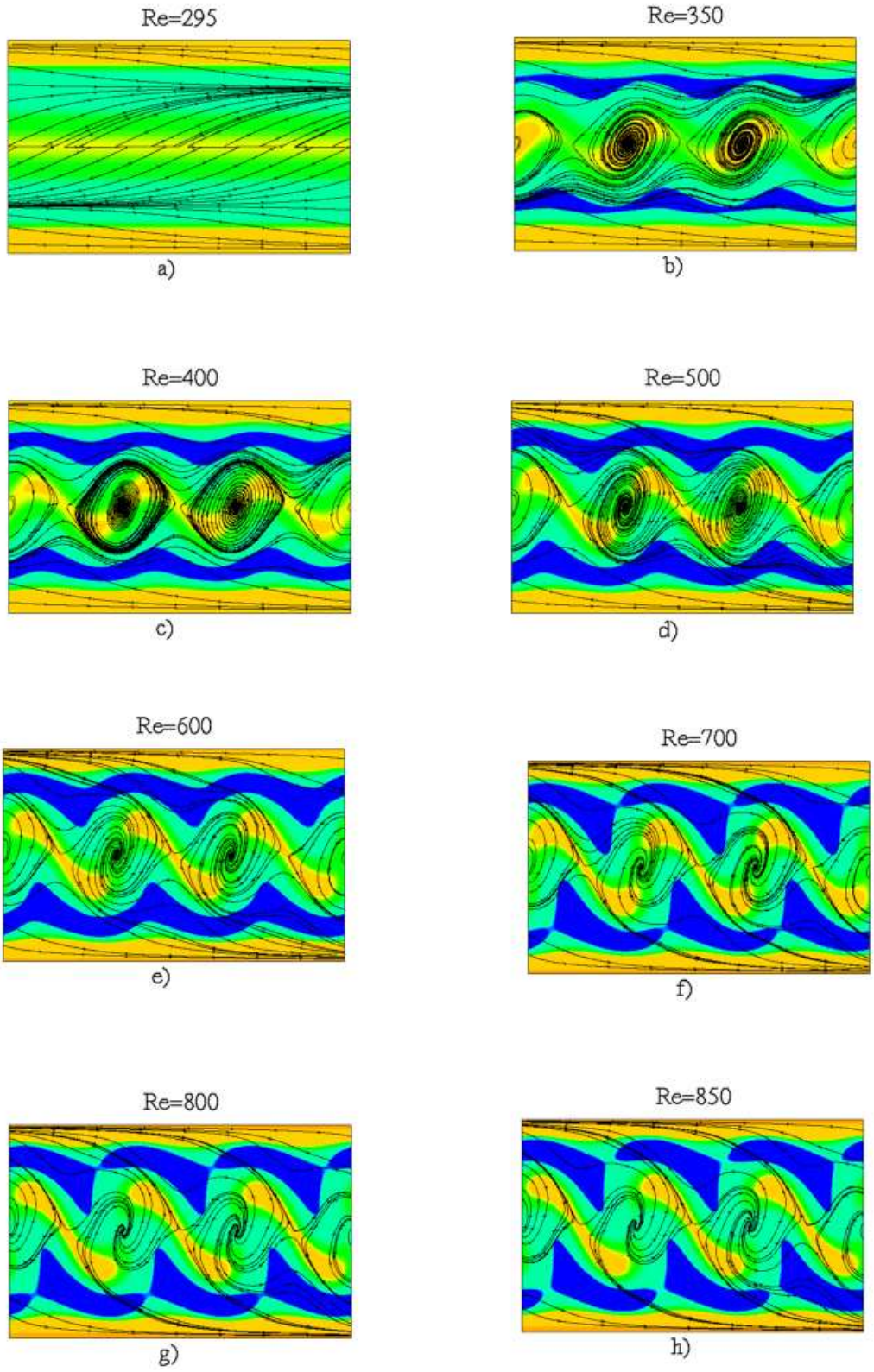

Figure 6.11 Contours of radial vorticity and surface streamlines at the azimuthal plane r=0.75R. The azimuthal plane has been unfolded and plotted in two dimensions (θ,r).

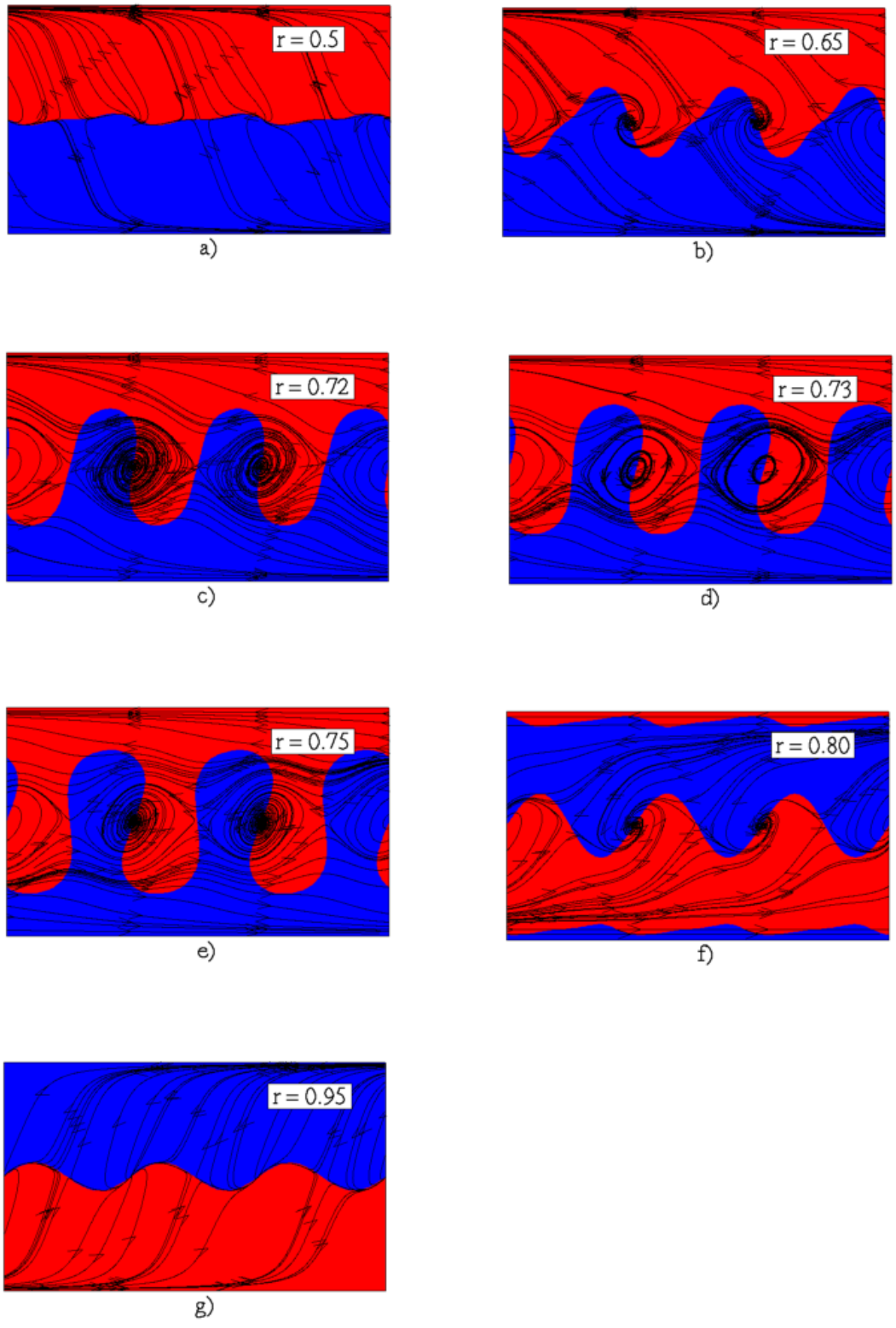

Figure 6.12 Positive and negative contours of axial velocity plotted with two-dimensional streamlines at various r=constant planes for Re=350.

6.4.2 Three-Dimensional Flow Characteristics

In this section we seek to elucidate the three-dimensional structure of the flow using iso-surfaces of velocity components, vorticity magnitude, and normalized helicity, as well as three-dimensional particle trajectories.

In figure 6.13 we plot two iso-surfaces of radial velocity U_r component for all simulated Reynolds numbers. The positive (red) and negative (blue) iso-surfaces shown are U_r = -0.1 and 0.065, respectively. For Re = 295 the axisymmetric flow structure is consistent with what we expect for the flow between counter-rotating disks. The two tori of positive U_r near the two lids are due to Ekman pumping that pushes fluid radially outward along the two disks while the torus of negative U_r at the mid-plane marks the location of the radial jet that drives the flow toward the container center. The onset of the shear layer instability is clearly evident for the Re=350 case where the negative iso-surface at the mid-plane develops a m = 3 azimuthal disturbance. The disturbance manifests itself in the form of an azimuthal waviness of the iso-surface and the formation of three pockets of increased negative U_r, presumably due to the development of the radial vortices. At higher Re, the iso-surface of negative U_r breaks up in three pieces and regions of positive U_r appear at the mid-plane. Even though in figure 6.13 this feature of the flow becomes evident only for Re = 700, where inclined columnar regions of positive U_r appear connecting the two tori near the top and bottom lids, the regions of positive U_r at the mid-plane actually appear first for the Re = 400 when the torus of negative U_r breaks up. To elucidate this rather striking feature of the flow, we plot in figure 6.14 two-dimensional streamlines and the contour of U_r=0.0 at the equatorial plane for Re = 350, 400, and 800. As seen in this figure, for Re=350 the streamlines develop regions of

azimuthal convergence, which marks the appearance of the radial, Kelvin-Helmholtz vortices. At Re=400, the radial streamlines in between the three regions of convergence develop stagnation points as three small pockets of regions of positive negative velocity emerge. At higher Re, these pockets grow in size and three pairs of spiral-in foci develop. Streamlines originating from the cylinder wall in the regions of azimuthal convergence approach the center where they turn backward and are directed toward the cylinder wall again before they are captured into the spiral-in foci. This feature of the flow is clearly evident for all Reynolds numbers Re>400 we have simulated and is depicted in figure 6.12c for the Re=800 case. Since the flow is three-dimensional, flow should be ejected out of the mid-plane, upward or downward, through the saddle foci, which must be the footprints on the mid-plane of vortical structures oriented in the axial direction. This complex feature of the flow is illustrated in figure 6.15, which shows three-dimensional particle paths that were introduced inside one of the pairs of saddle foci and their trajectories were integrated backward and forward in time. As seen, particles from a wide range of initial conditions are captured by the foci and organized in two coherent streaks. The appearance of pairs of saddle foci in the flow has important implications vis-à-vis the Lagrangian dynamics of the flow as saddle-foci tend to promote stretching and folding and lead to efficient stirring. This feature of the flow will be discussed further in a subsequent section.

Before we further clarify the three-dimensional structure of the flow it is important to point out that the development of the pairs of foci is the direct consequence of the emergence of radial and azimuthal pressure gradients in the flow. Figure 6.16 shows pressure contours at the mid-plane along with the same streamlines shown in figure 6.14 before for clarity. For the Re=295 case the pressure is decreasing with radius

so that the flow can be driven toward the container center against the action of the centrifugal force. After the onset of the three-dimensional instability, however, the azimuthal region of high pressure along the outer wall breaks up into three pockets of high pressure as a result of the shear layer instability and strong circumferential gradients develop in the pressure field. In addition a region of high pressure develops at the container center. Consequently particles originating from the outer wall in between the pockets of high pressure, encounter as they move toward the center and adverse pressure gradient in the radial direction. That is the pressure is now acting to enhance the destabilizing effect of the centrifugal force. Above a threshold Re the combined destabilizing effect of pressure gradient and centrifugal force, cause stagnation and flow reversal in the radial region. As seen in the figure, this first occurs for Re = 400.

The results presented so far suggest that upon the onset of the shear layer three-dimensional instability, very complex vortical structures emerge in the flow. The two-dimensional streamline plots and the three-dimensional particle paths discussed in figures 6.11 to 6.16 before suggest that both radial and axial vortical structures develop. To illustrate these structures we employ iso-surfaces of normalized helicity and of vorticity magnitude. Normalized helicity is the cosine of the angle between the velocity and vorticity vectors and is defined as follows:

$$h = \frac{\vec{\omega} \cdot \vec{u}}{|\vec{\omega}||\vec{u}|} \tag{6.1}$$

By definition, $h = 1$ occurs in regions of the flow where the vorticity and velocity vectors are aligned. Therefore, a helicity iso-surface close to one should visualize vortical structures for which there is a strong alignment between velocity and vorticity. Figure

6.17, shows the h = 0.97 iso-surface for Re = 295 and 350. For Re = 295 the flow is axisymmetric and a toroidal region of helicity occupies the mid-plane, which marks the azimuthal shear layer. For Re=350, however, a strikingly complex, multi-connected iso-surface develops, which clearly demonstrates the instability of the shear layer and the formation of cat's eye radial vortices. These are the flattened, pancake-like features of the iso-surface that exist at the mid-plane. As seen in the figure, these radial structures coincide exactly with the cores of the cat's eye vortices shown in the superimposed, two-dimensional streamlines. In the interior of the flow the iso-surface becomes too complex to interpret but it appears to suggest the emergence of axial, inclined vortical structures. These are the structures, which at higher Re, strengthen and lead to the formation of the foci pairs at the mid-plane. The helicity iso-surface could not reveal these structures clearly because of its complexity but a properly selected iso-surface of vorticity magnitude was able to visualize them. This is shown in figure 6.18, which depicts an iso-surface of vorticity magnitude for Re = 800. For clarity, the two-dimensional streamlines at the mid-plane have also been superimposed to this figure. It is clearly evident from this figure, that the pairs of foci are indeed the footprints of highly three-dimensional, vortical structures that are axial oriented but also are inclined in the azimuthal direction.

The results presented in this section show that the azimuthal shear layer instability gives rise to a very complex, three-dimensional flow dominated by an intricate web of radial and axially oriented structures. The pairs of saddle-foci at the mid-plane raise intriguing possibilities concerning the Lagrangian dynamics of the flow as they provide a mechanism for global transport. The Lagrangian dynamics of the flow are investigated in detail in the next section.

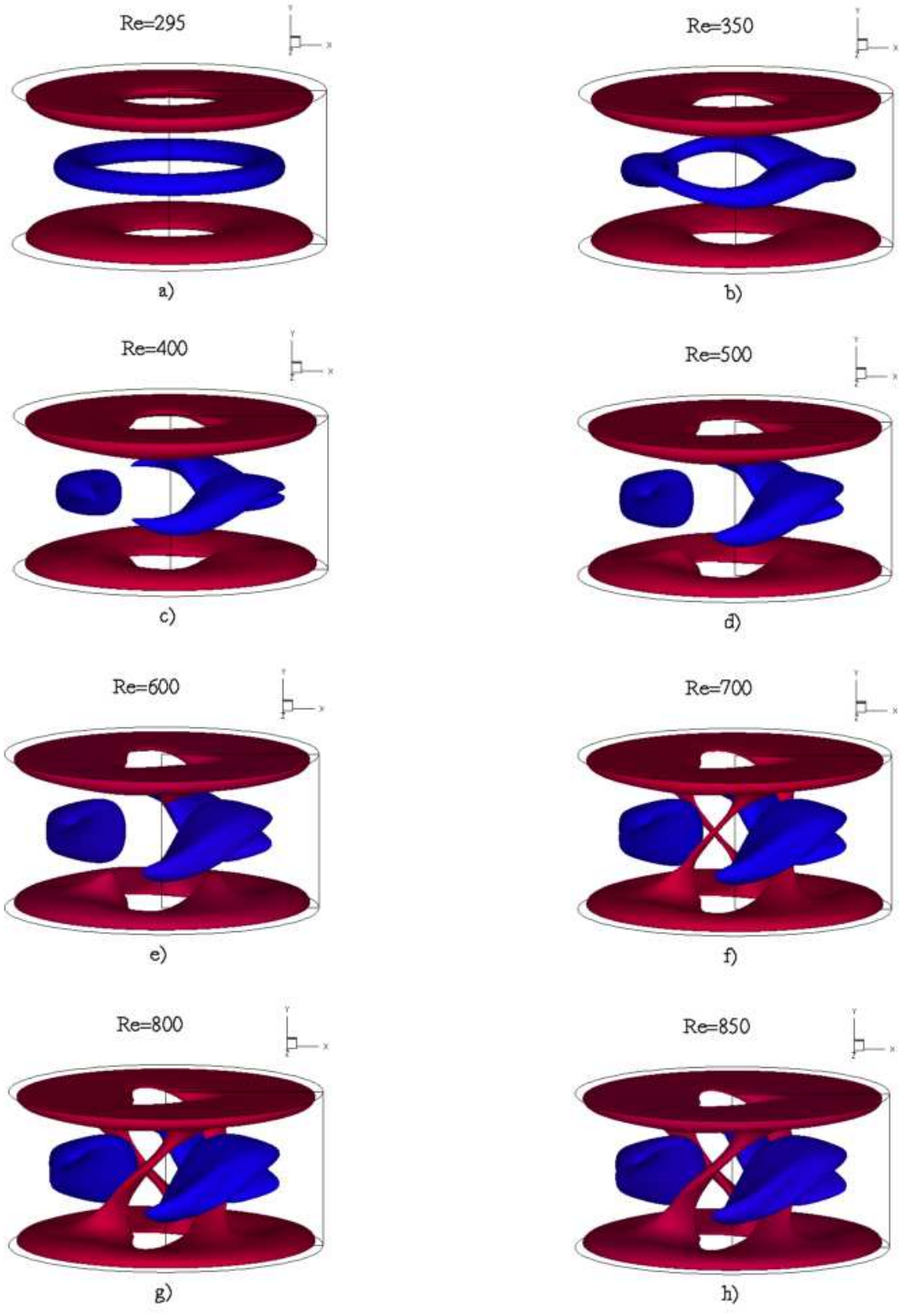

Figure 6.13 Iso-surfaces of the radial velocity component for all simulated Reynolds numbers. Positive (red) and negative (blue) iso-surfaces shown at U_r=-0.1 and 0.065 respectively.

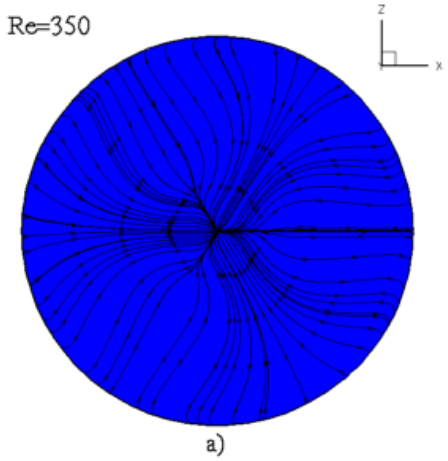

a)

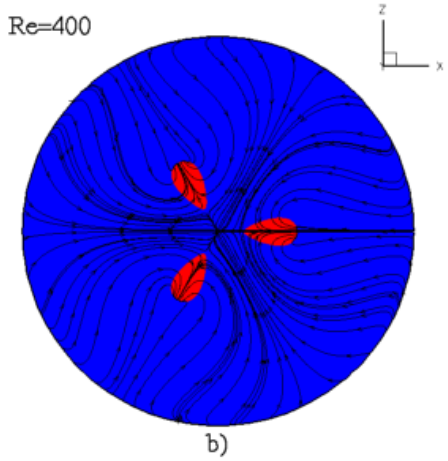

b)

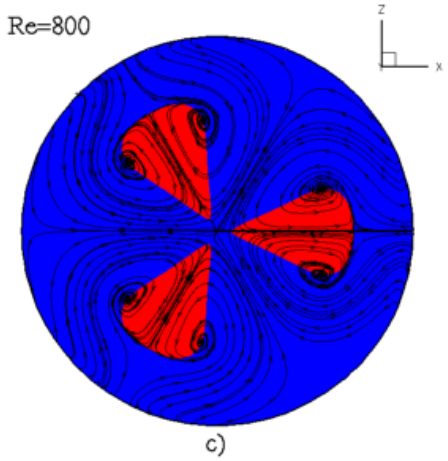

c)

Figure 6.14 Two-dimensional streamlines and radial velocity contours of U_r=0 at the equatorial plane for Re=350,400, and 800.

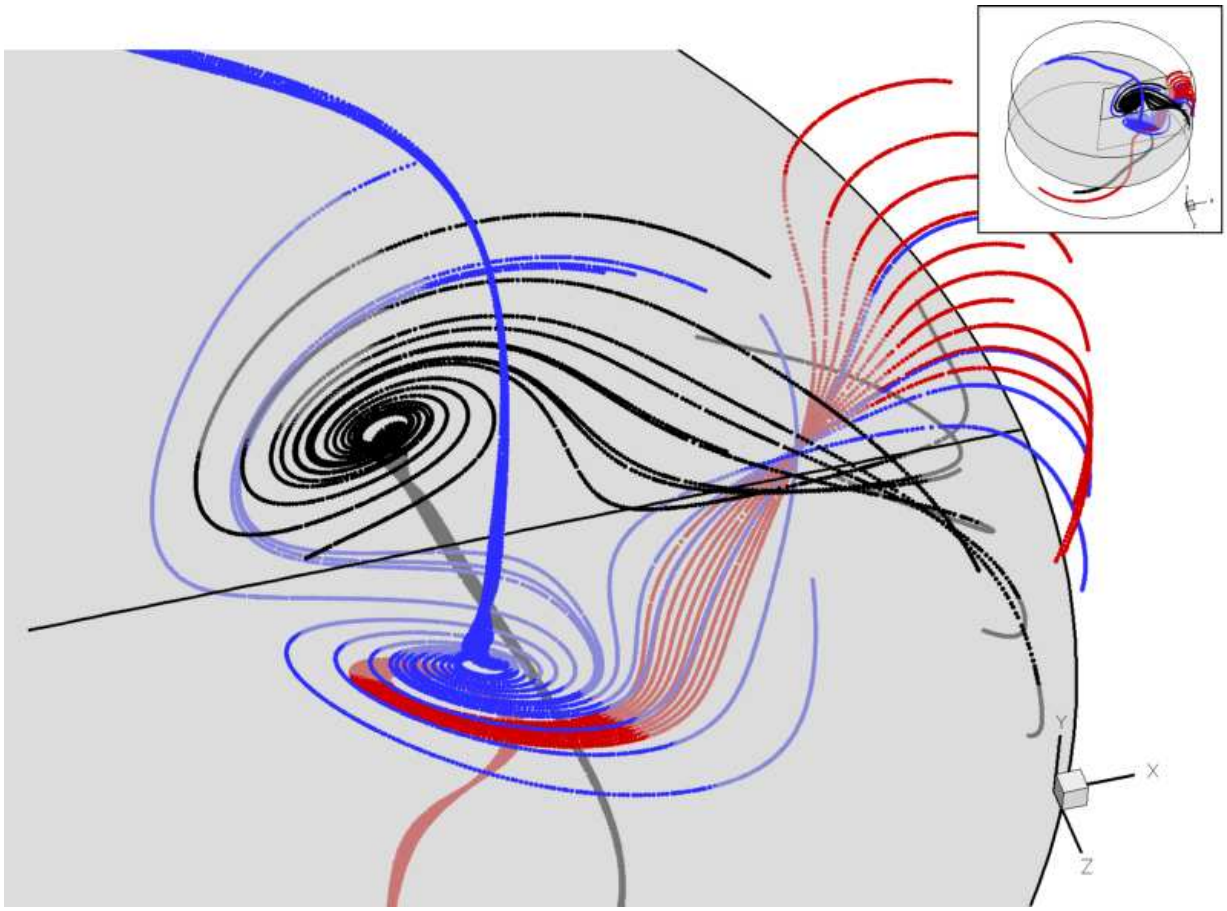

Figure 6.15 Three-dimensional particle paths inside the spiral vortices (Re=500).

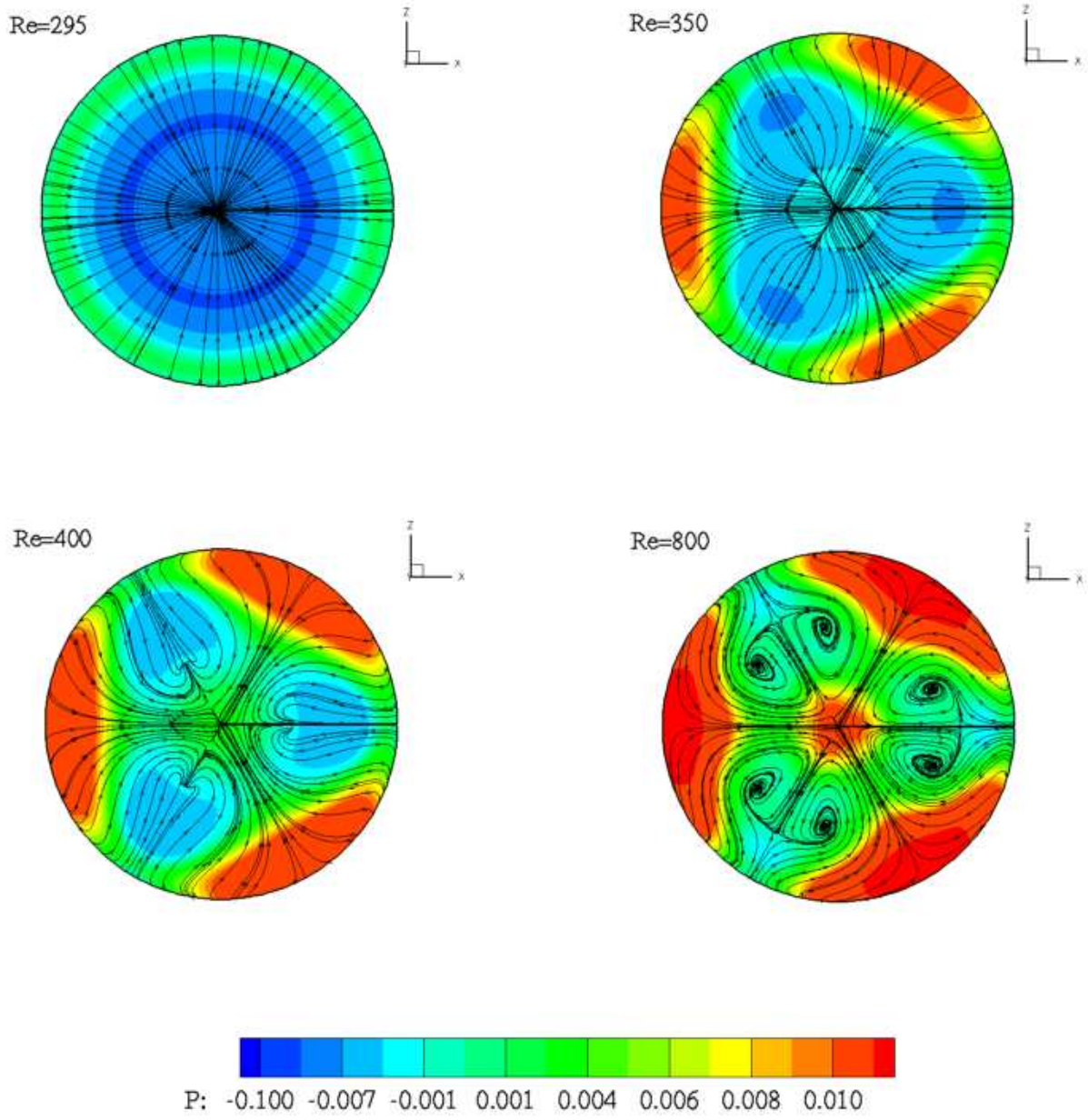

Figure 6.16 Pressure contours at the axial mid-plane with two-dimensional streamlines.

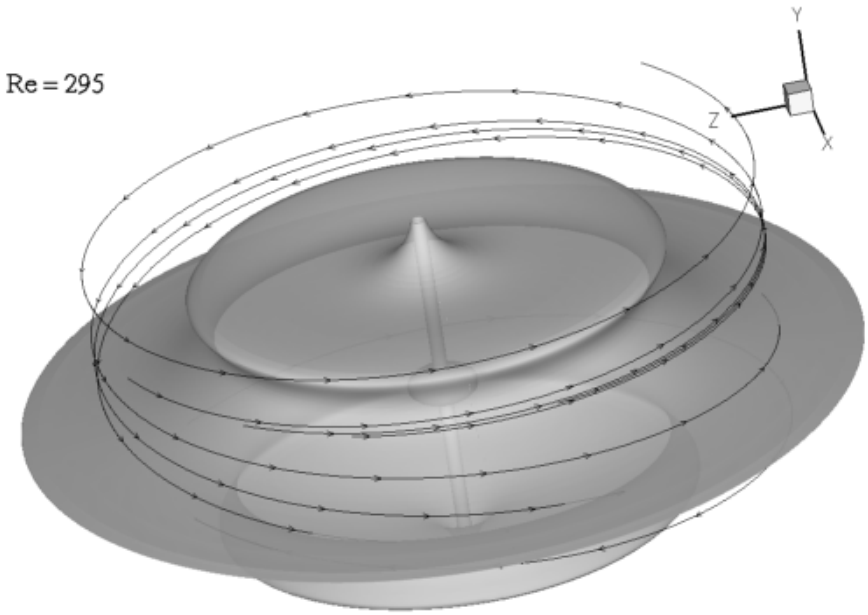

a)

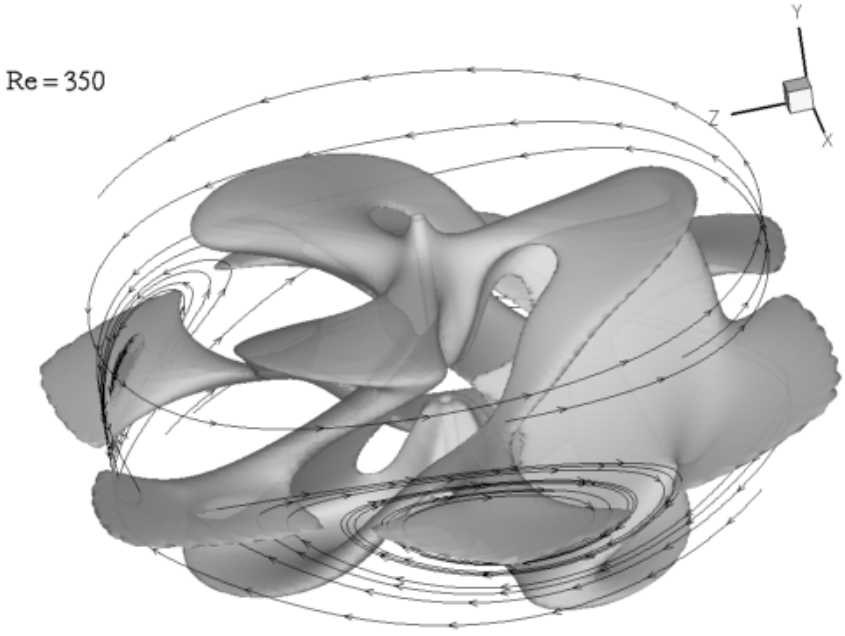

b)

Figure 6.17 Helicity iso-surfaces for Re = 295 and 350 (h=0.97) plotted with surface streamlines at r=0.75.

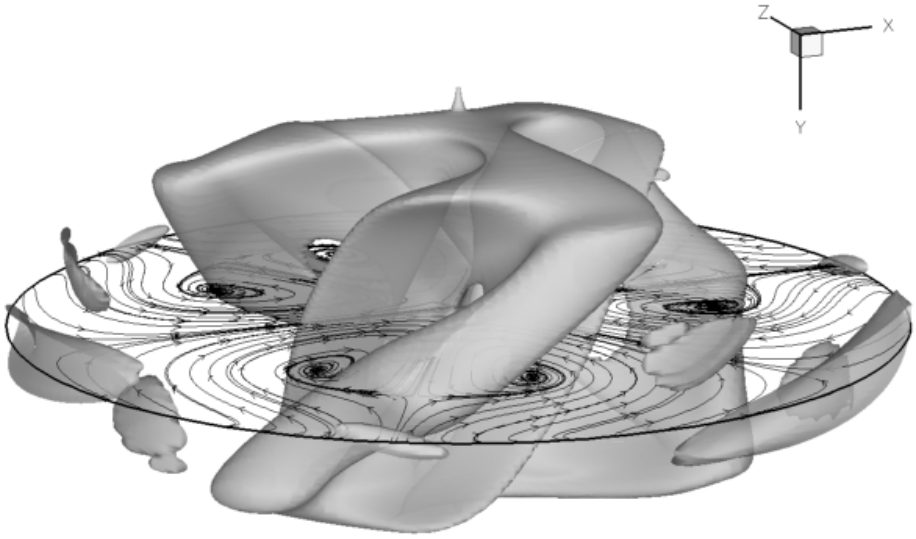

a)

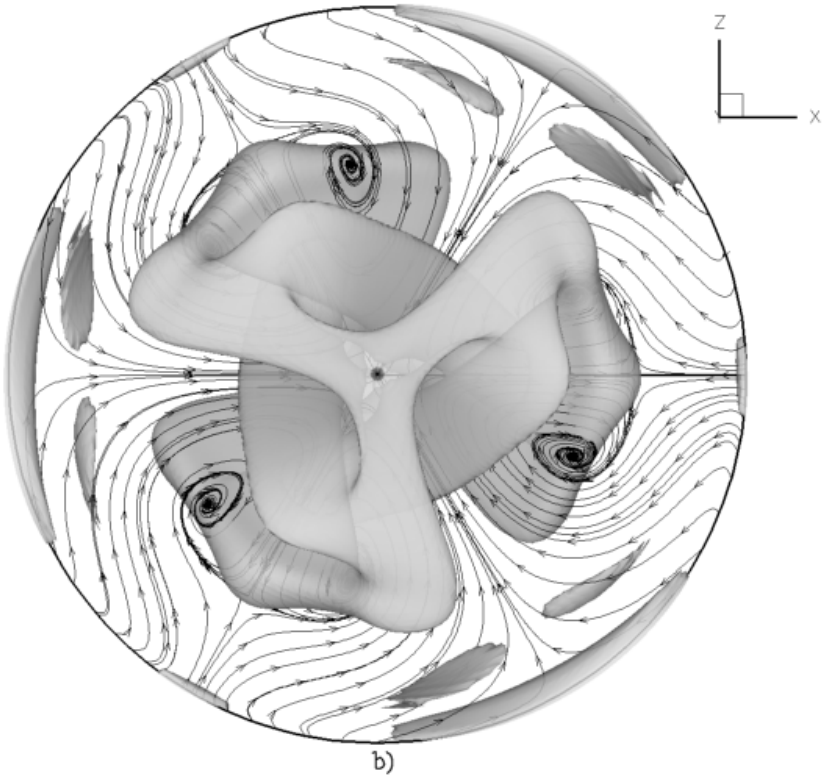

b)

Figure 6.18 Vorticity iso-surfaces for Re =800 plotted with surface streamlines at equatorial plane; a) side view and b) top view.

6.5 Lagrangian Dynamics

In this section we report the results of a comprehensive investigation of the Lagrangian properties of the flow over the range of simulated Reynolds numbers. Our objective is twofold. First we seek to visualize the richness of dynamics that emerge following the onset of the shear layer instability. Secondly we seek to quantify the effect of Reynolds number on mixing intensity. We begin our discussion by constructing Lagrangian averaging and stretching maps. Using these maps we uncover and discuss various types of particle paths and identify unmixed islands in the flow. Subsequently we calculate mixing rates as a function of Reynolds number and show that mixing intensity is not a monotonic function of Reynolds number. A link between our findings and a recently proposed theory of chaotic advection is also established.

6.5.1 Visualization of unmixed islands

As we have discussed in Chapter 2, Poincaré maps are usually employed to visualize the richness of dynamics and identify unmixed regions in the flow. The success of a Poincaré map relies critically on the choice of initial conditions, which should be selected to lie within areas where interesting dynamics occur. For that reason, Poincaré maps have been developed and work well for mildly perturbed systems for which many of the periodic orbits and invariant surfaces of the base axisymmetric flow remain intact (see for example the case of the vortex breakdown bubble discussed in the previous chapter). In our case, however, a highly complex, three-dimensional flow, fundamentally different than the base axisymmetric flow emerges shortly after the onset

of the three-dimensional instability. In such a case, Poincaré maps are not very helpful because the dynamics is very rich and drastically different than those of the base flow. Thus, our initial attempt to identify by trial-and-error initial conditions which elucidate the richness in dynamics was proven futile and can be likened to searching for a needle in a haystack. For that reason, we chose to visualize the dynamics of the calculated flowfields by constructing Lagrangian time average maps, an approach which allows us to systematically identify unmixed regions in the flow without trial-and-error searching for a proper set of initial conditions.

We construct Lagrangian time-average maps for Reynolds numbers ranging from 295 to 850. The Lagrangian time-average map is constructed by averaging the velocity magnitude along the trajectories of 10,000 particles initially distributed on a 100^2 grid of equally spaced initial conditions located at the $\theta = 0$ plane. The grid of initial conditions covers only the lower part of the container and is shown in figure 6.19. In figure 6.20 we show representative such maps for Re = 295, 350, 500, and 700. The calculated Lagrangian averages at each initial release point are plotted as fractional differences from the mean velocity magnitude of the entire flow. That is, the following variable is plotted:

$$\tilde{V}_{i,j}^{L} = \frac{V_{i,j}^{L} - \overline{V}}{\overline{V}} \tag{6.2}$$

where $V_{i,j}^{L}$ is the Lagrangian average along the trajectory originating at the *(I,j)* initial node and $\overline{V}$ is the average velocity magnitude over the entire container. Presenting the Lagrangian average maps in terms of $\tilde{V}_{i,j}^{L}$ provides a consistent scaling of the results for all Reynolds numbers. Also note that the above scaling will yield $\tilde{V}_{i,j}^{L}$=0 at all points if the flow is globally chaotic since all particles will cover ergodically the entire flow

domain and sample all possible velocities in the flow. Thus, in a flow for which most of the domain is occupied by chaotic trajectories values of the average near zero will be obtained for most points while values significantly greater than zero will be obtained for points in invariant regions.

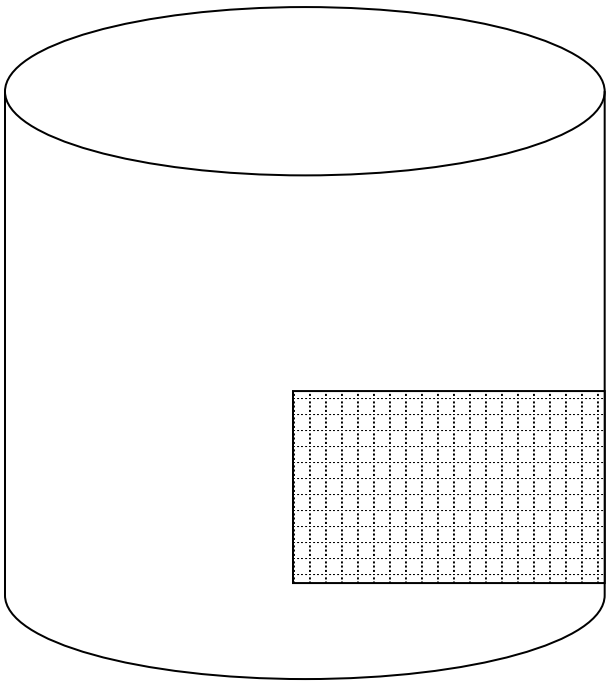

Figure 6.19 Grid of initial conditions for Lagrangian time-average maps.

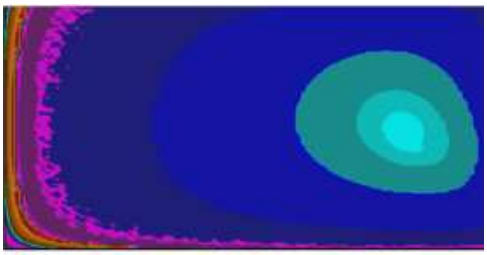

Re = 295

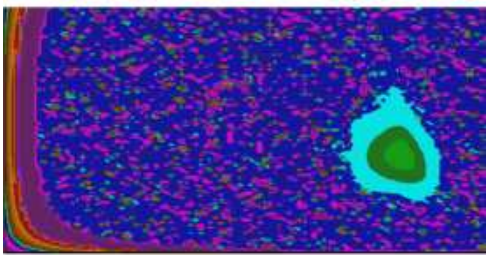

Re = 350

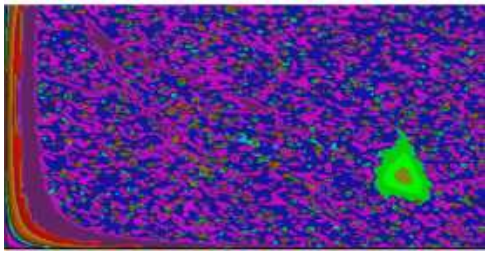

Re = 500

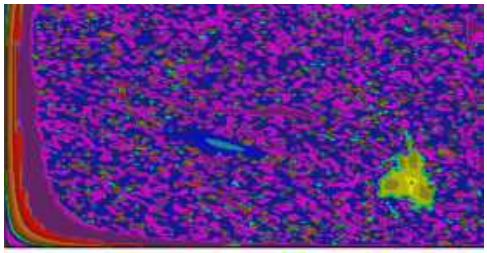

Re = 700

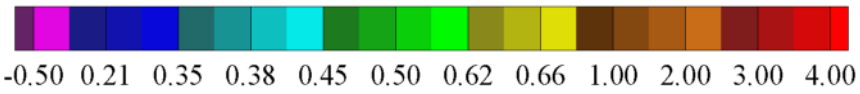

Figure 6.20 Lagrangian time-average maps for Re=295,350,500, and 700

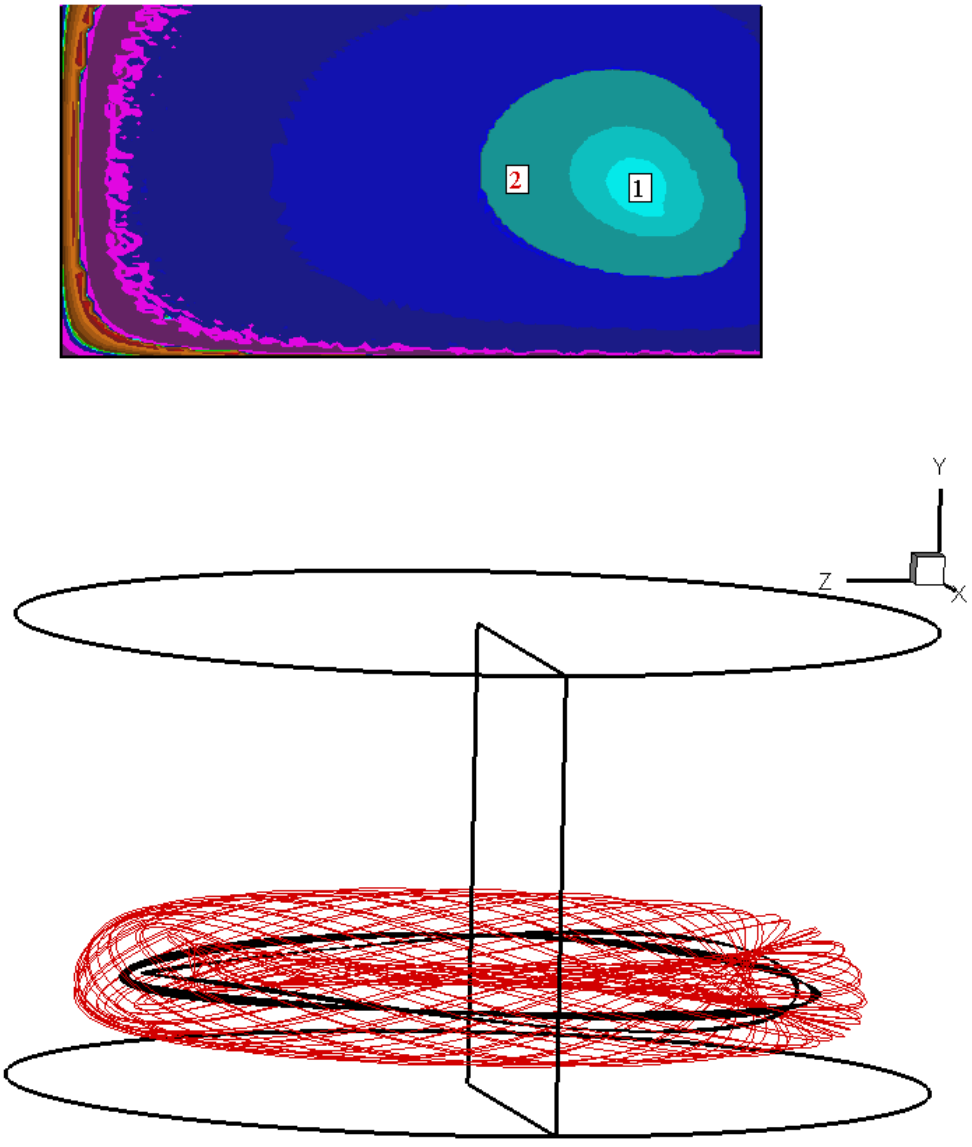

Figure 6.21 Lagrangian time-average map and particle paths for Re = 295 (axisymmetric flow)

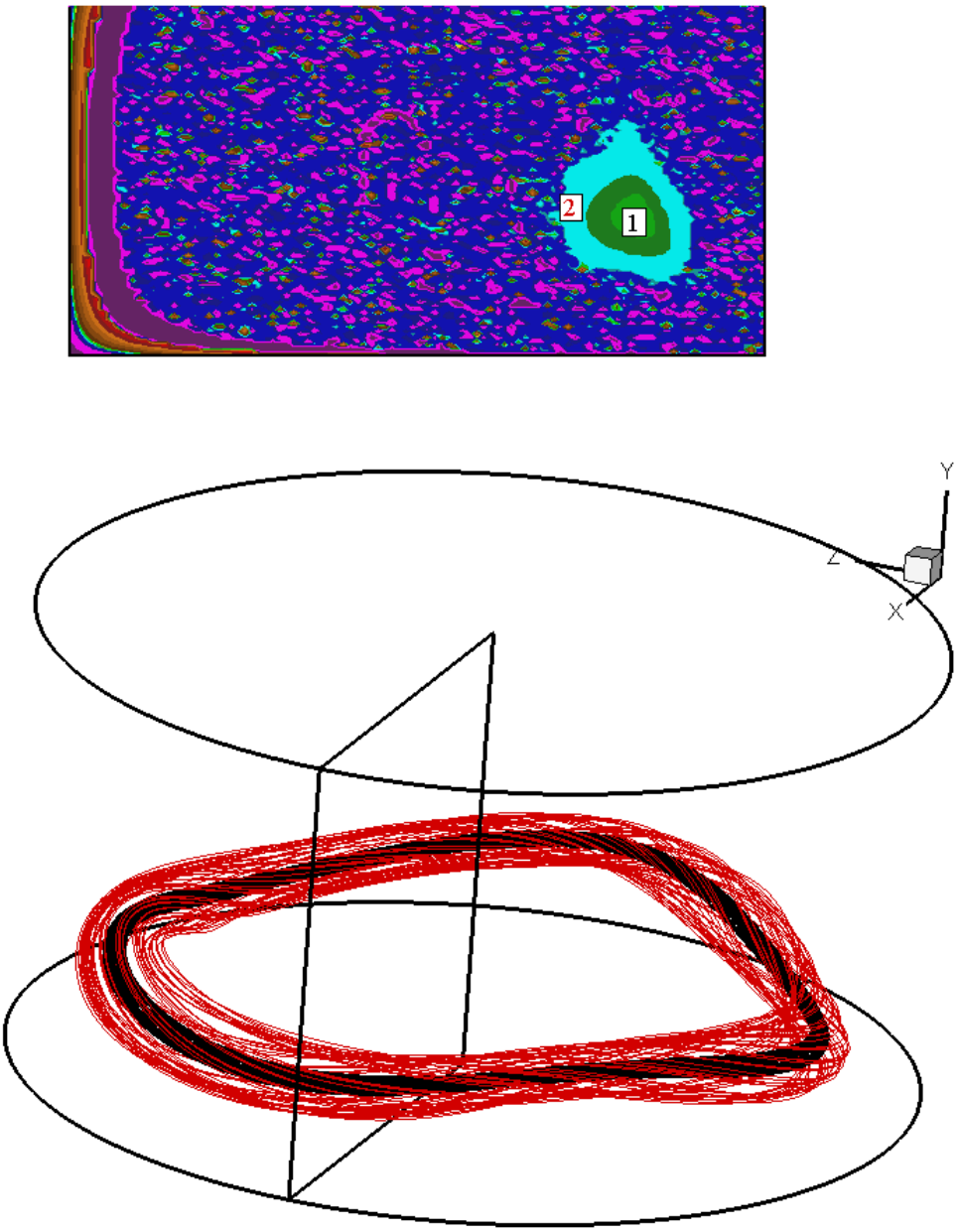

Figure 6.22 Lagrangian time-average map and particle paths for invariant sets of Re = 350 flow.

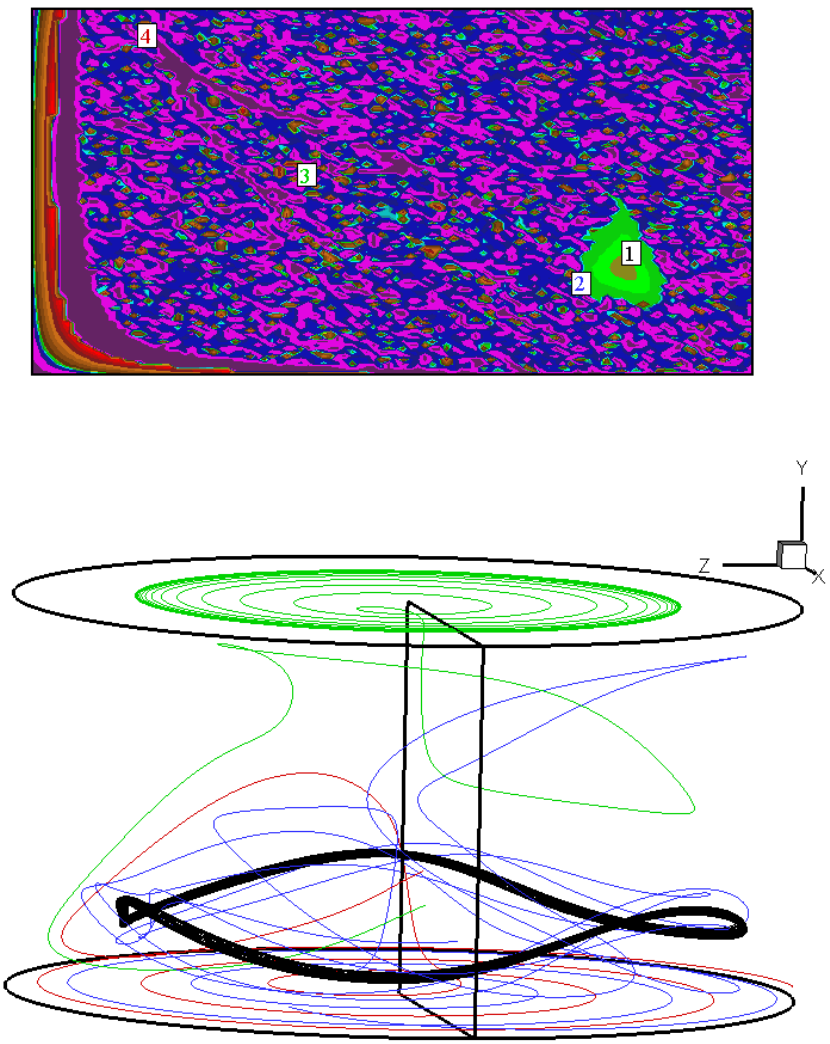

Figure 6.23 Lagrangian time-average map and sample particle paths for Re = 500 flow.

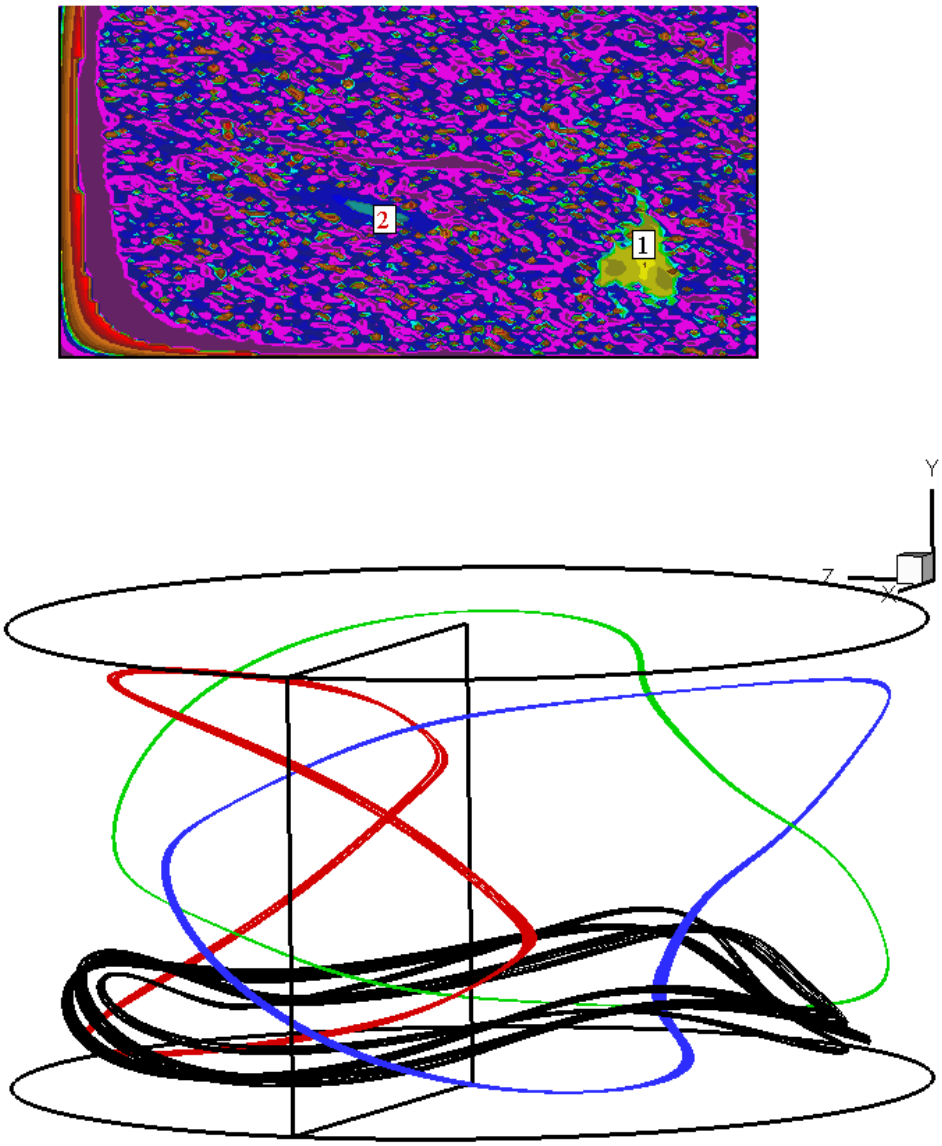

Figure 6.24 Lagrangian time-average map and particle paths for invariant sets of Re = 700 flow. Black tori are particle paths initiated in region 1. Red, green, and blue particles are originated in region 2 or similar areas.

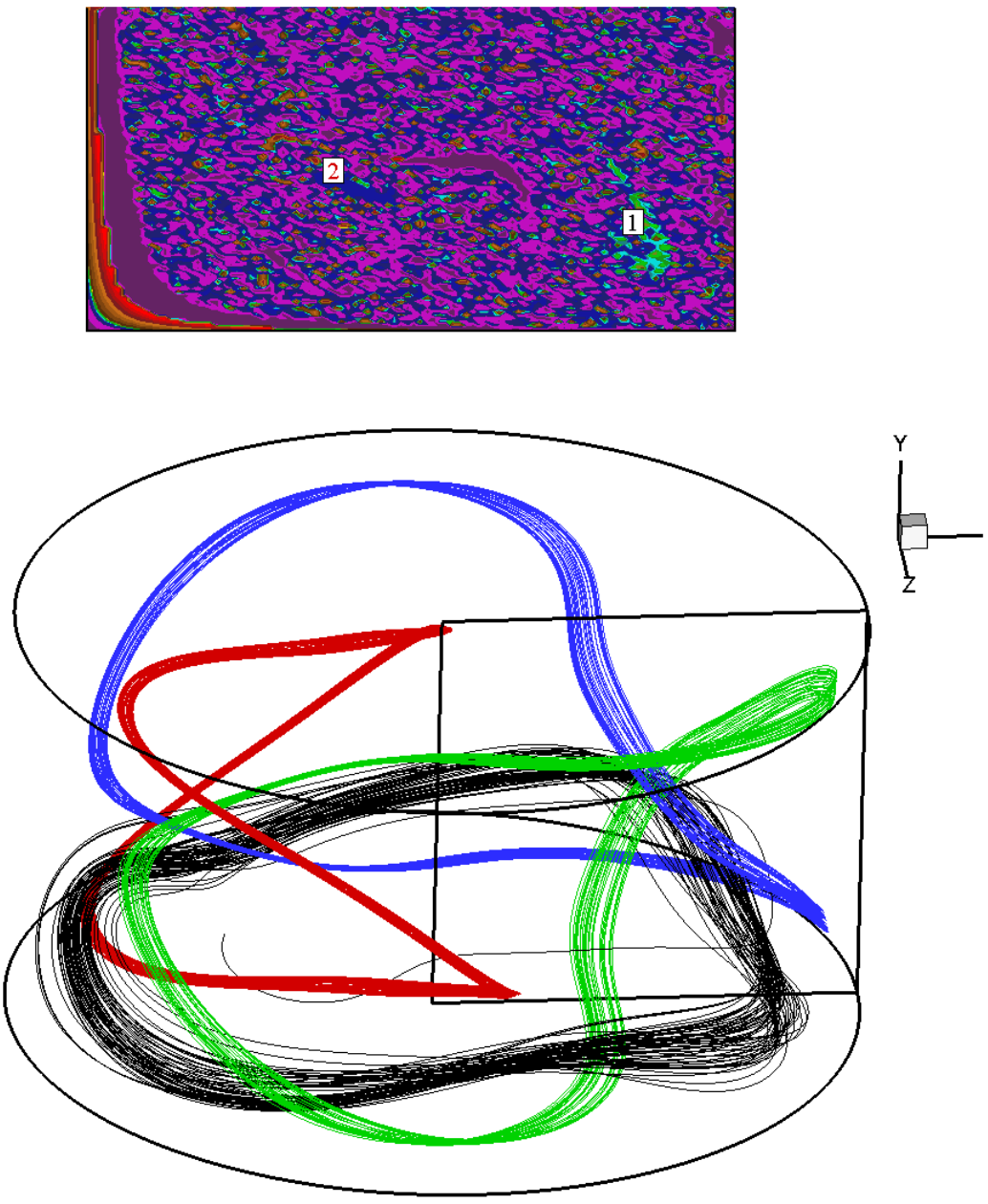

Figure 6.25 Lagrangian time-average map and particle paths for invariant sets of Re = 800 flow.

For the *Re* = 295 case the Lagrangian time-average map reveals, as expected for an axisymmetric flow, integrable dynamics. The iso-contours of the averages are embedded tori, which mark the invariant stream-surfaces of the axisymmetric flow. The outer layer of these tori shows fractalized characteristics, which would suggest that periodic orbits in this region have begun to break up. Recall, however, that this Reynolds number is just below the critical *Re* for the onset of the three-dimensional instability and the apparent break-up of the near-axis stream-surfaces is due to very small three-dimensional disturbances that are present in the calculated flowfield. Such disturbances are also evident in the previously discussed figure 6.9, which showed the contours of axial velocity at the mid-plane. For the Re=295 case the maximum of axial velocity is indeed very small (of order 10^{-5}) but there is clearly a very weak m = 3 azimuthal mode, which is presumably responsible from the small departures from integrability observed in Lagrangian average map.

For the Re = 350 case a dramatically different map emerges. The flow has become fully three-dimensional and most invariant surfaces have disappeared. The map exhibits fractalized features almost everywhere with only exception the toroidal region near the lower right corner, which marks the integrable core that has survived the onset of three-dimensionality. A very similar picture emerges also for the Re = 500 case but here the integrable core appears to have shrunk even further and a nearly globally chaotic flow has emerged. As the Reynolds number is increased to 700, however, new and rather striking features emerge. First, the toroidal invariant region that has persisted at all lower Reynolds numbers has broken down into three smaller areas. Perhaps the most striking feature at this Re is the new invariant region that has emerged in the previously chaotic area of the flow. This region is marked by the large “blue” area at the center of

the plane, which marks initial conditions that sample ergodically the same subset of the flow and, thus, yield the same value for the Lagrangian time average. Similar unmixed regions first appeared for Re = 600 and persist at all higher Reynolds numbers we have simulated.

The Lagrangian averaging maps can be used to identify and explore various types of particle trajectories in the flow and in particular those in invariant regions. By examining these maps we identify initial conditions in invariant regions and calculate their particle paths to elucidate the three-dimensional structures of unmixed areas and other types of trajectories. Typical results from such and investigation are shown in figures 6.21 to 6.26. In all these figures, we include the corresponding Lagrangian average map with the location of the initial conditions for which particle trajectories are computed marked with numbers on the map. In figure 6.21, we show few typical invariant toroidal regions for the Re = 295 axisymmetric flow case. As one would expect, trajectories cover ergodically toroidal invariant regions. The previously discussed effect of very small perturbations for this Re is also evident in the innermost toroidal region shown in figure 6.21, which has broken into two, intertwined tori. Overall, however, almost the entire flow domain for this Re is foliated by invariant tori similar to the 'red' torus in the figure.

For the Re = 350 case, the invariant toroidal core has shrunk dramatically and undergone a mode 3 azimuthal modulation, evidenced by the waviness and three-dimensional distortion of the 'red' torus in figure 6.21. For this case, all other invariant regions have broken up and most of the flow domain is covered by chaotically advected trajectories. The same is also true for the Re = 500 case. Trajectories for this case are shown in figure 6.22. Only one invariant region has survived at this Re, the 'black'

azimuthally twisted torus in the figure. The 'green' and 'red' trajectories shown in this figure are typical to a class of trajectories that emerge at these higher Reynolds numbers. These trajectories are captured by either the top or bottom lid Ekman layers and spend a very large time in them before they finally escape to explore the remaining flow domain. The 'blue' trajectory is that of a chaotically advected particle path, which at certain times moves appears to be trapped along a boomerang-type structure. At this Reynolds number, such particles do not stick on this organized structure but the emergence of this feature is interesting because at higher Reynolds numbers this boomerang-like structure evolves into an unmixed region of the same shape. The emergence of these topologically complex unmixed regions is clearly shown in figure 6.24, which shows the invariant trajectories for the Re = 700 case. As seen in the figure several such unmixed areas have emerged for this Reynolds number in regions which at lower *Re* used to be occupied by chaotic trajectories. As previously mentioned, this is very striking feature of the flow as it appears to suggest that even though the complexity of the flow from the Eulerian standpoint increases with increasing Re, above a threshold Re the flow starts becoming more organized and the extent of the chaotic regions in the flow is reduced. This feature is further clarified in figure 6.25, which shows the unmixed regions for Re = 850. They have the same general structure as for the Re = 700 case but now they seem to have expanded and occupy a larger portion of the flow domain.

Finally in figure 6.26 the unmixed islands for the Re = 700 case are linked with an important Eulerian feature of the flow. The contours of vertical velocity at the mid-plane superimposed in this figure to the particle trajectories reveal that the unmixed islands actually coincide with the previously discussed pockets of increased axial flow across the mid-plane located neat the periphery of the container. That is, even though

vertical transport across the mid-plane increases with Re, figure 6.26 suggests this increased transport does not necessarily imply enhanced mixing efficiency. Particles in these regions are actually trapped in unmixed islands and keep on continuously crossing the mid-plane through their respective pockets of increased axial flow without mixing with the surrounding flow

The results presented in this section suggest a complex and non-monotonic relationship between stirring intensity and the Reynolds number of the flow. Based on the unexpected appearance of unmixed islands above a threshold Re, it would appear that a Reynolds number exists for which stirring is optimal for this flow and further increase in Re actually cause chaotic stirring to decline. This very significant finding is further re-enforced and discussed extensively in the subsequent section.

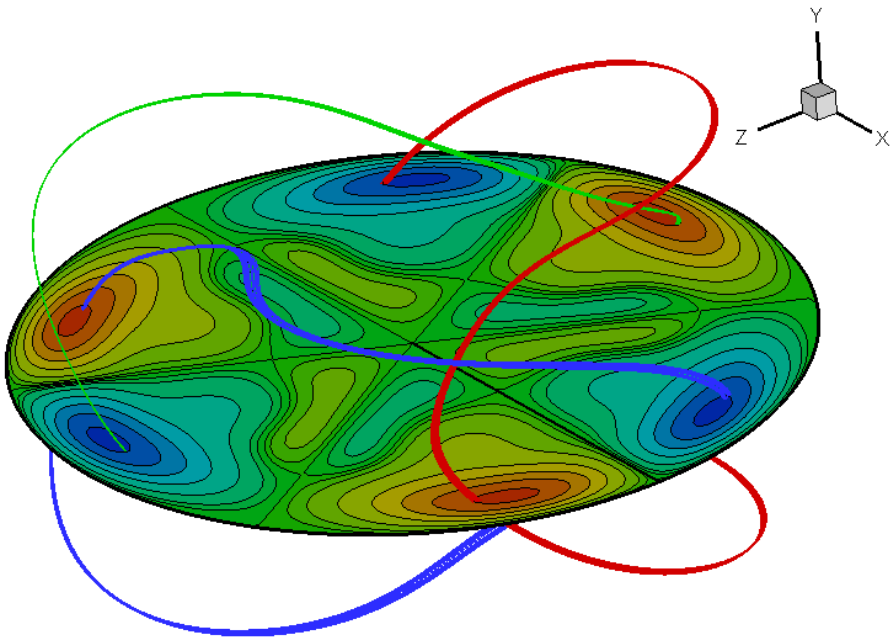

Figure 6.26 Contours of vertical velocity at the mid-plane superimposed with unmixed islands for Re=700.

6.5.2 Quantification of Stirring Intensity: Variance of Concentration

6.5.2.1 The Concept of Variance of Concentration

To quantify stirring intensity we develop the method of variance of concentration, which allows us to calculate the stirring rate as a function of the Reynolds number of the flow. Our technique is inspired by and closely mimics numerically similar approaches used in laser-induced fluorescence (LIF) based experimental techniques, which quantify mixing efficiency in terms of the variance of concentration of a scalar tracer with time (Voth et al 2003). In such experimental studies, instantaneous LIF images are post-processed to extract a local value of concentration in terms of the intensity of scattered light at each pixel of the plane illuminated by the laser sheet. The instantaneous variance of the so obtained concentration field can then been calculated and its temporal evolution can be recorded. The rate at which the so computed variance approaches zero can be used to define the mixing rate for the flow (see Voth et al 2003). The numerical equivalent of the concentration variance is calculated as follows.

A closely packed set of N initial conditions—the equivalent of a blob of dye in an experiment—is introduced at some point in the flow. The particles are then advected by the flowfield for approximately fifty lid revolutions. Assuming that the initial conditions are prescribed in a location that is not inside an invariant region, fifty lid revolutions were found adequate to completely stir the particles for all simulated Reynolds numbers but the axisymmetric Re = 295 case for which stirring is very slow. Several representative snapshots depicting the stirring of two blobs of particles (red and blue blobs) for the Re=350 case are shown in figure 6.27. The red blob is placed in an invariant toroidal region and remains intact and unmixed for the entire time integration

interval. The blue blob is placed in a chaotic area and as time progress it undergoes intense stretching and folding and is ultimately stirred completely by the flow.

Every point of every trajectory of the specified blob of particles can be uniquely described in terms of four variables: r, z, θ and time t. To better illustrate the approach we have developed to calculate the variance of concentration, we should note that when we construct a Poincaré map, and assuming that the flow is steady, we in essence visualize a two-dimensional slice of this four-dimensional space. This is accomplished by eliminating one spatial dimension—by specifying the plane of section of the map, say by fixing θ to a constant value—and collapsing the time dimension by marking the position particles cross the plane of section of the map regardless of when the particular crossing took place. In other words, a Poincaré map contains information that is not time accurate. To design a method that allows us to calculate the time evolution of the variance of concentration, however, we obviously need to utilize time-accurate information.

For that reason, instead of collapsing time, we collapse one of the three spatial dimensions as illustrated in figure 6.28. In the figure 6.28a, the initial blob of particles (a material sphere of small radius) is centered at a given grid node. At any given instant in time t the calculated, instantaneous three-dimensional particle positions (6.28b) are collapsed in the θ-direction and mapped onto a single θ = constant plane. The resulting two-dimensional plot contains the time-accurate (synchronized) positions of all particles in the r-z plane but obviously information about the exact three-dimensional position of particles has been lost. We associate each (i, j) grid node of the r-z plane with a two-dimensional control volume such that all control volumes cover the entire plane without any overlapping. We then count the number of particles $n_{ij}(t)$ that are contained at this

instant in time within the (*i*, *j*) control volume. The discrete, instantaneous value of concentration at every grid node is then calculated as follows:

$$C_{i,j}(t) = n_{ij}(t) \tag{6.3}$$

Contours of $C_{i,j}(t)$ can then be plotted to illustrate how the stirring of the discrete blob of particles proceeds in time. Representative images of the application of this technique for the Re = 350 case and for N = 20,000 are shown in figure 6.29. As seen the initial blob is stretched and folded by the flow and the concentration gradients diminish with time as the particles are stirred by the flow. After sufficiently long time, the blob has been dispersed in the entire plane except the region occupied by invariant toroidal regions (see figure 6.29f).

At every instant in time, the statistical variance σ_c of the discrete concentration field can be calculated as follows:

$$\sigma_c^{\,2}(t) = \frac{1}{I \times J} \sum_{i}^{I} \sum_{j}^{J} \left(C_{ij}(t) - \overline{C}(t) \right)^2 \tag{6.4}$$

where I and J are the maximum number of grid nodes in the r, and z-directions, respectively, and $\overline{C}$ is the mean concentration at time t, which is calculated as follows:

$$\overline{C}(t) = \frac{1}{I \times J} \sum_{i}^{I} \sum_{j}^{J} C_{ij}(t) \tag{6.5}$$

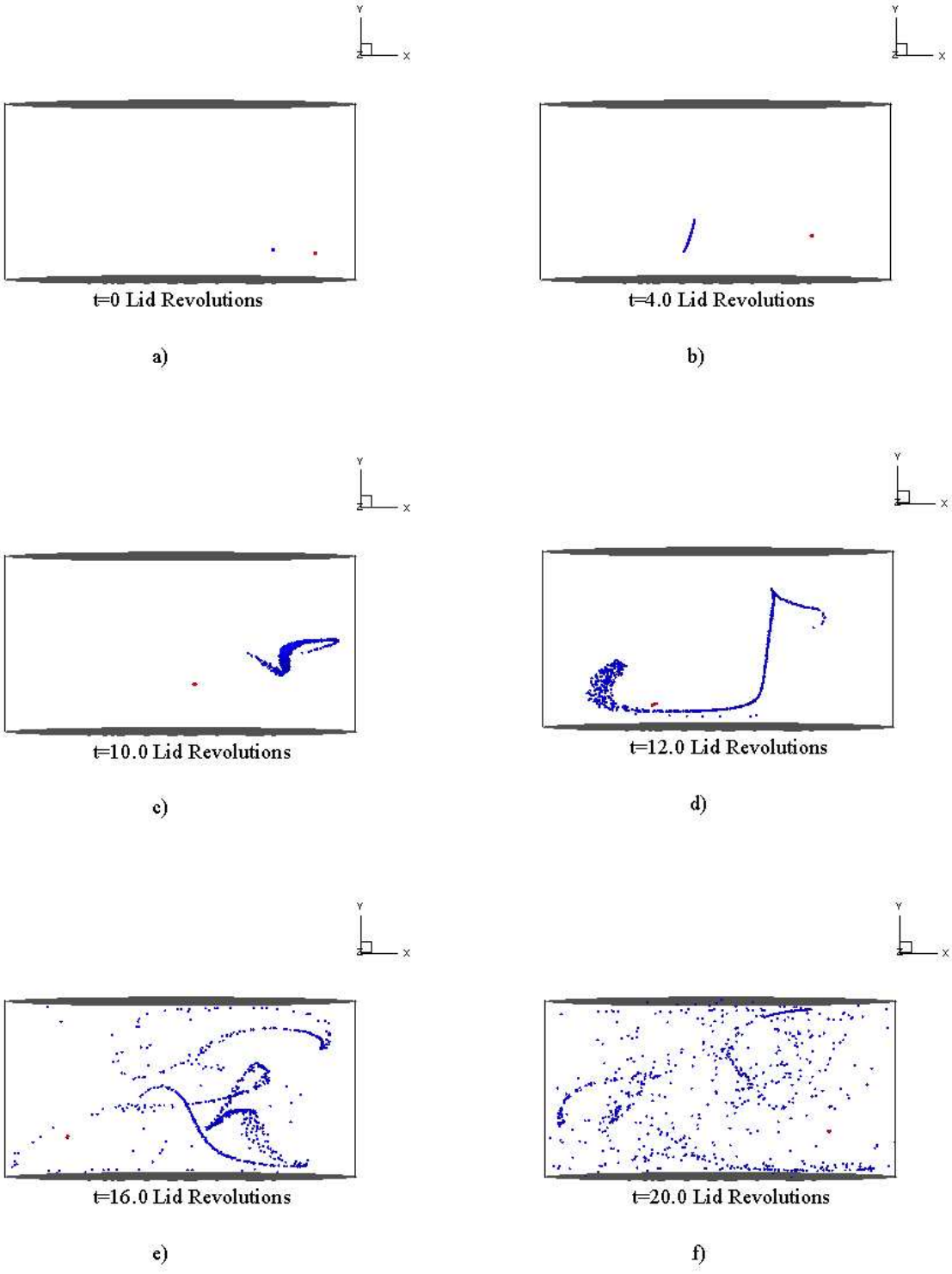

Figure 6.27 Mixing snapshot of particle "blobs" introduced into Re=350 flow. Red particles are introduced into the invariant flow region. Blue particles are placed in a chaotically advected flow area.

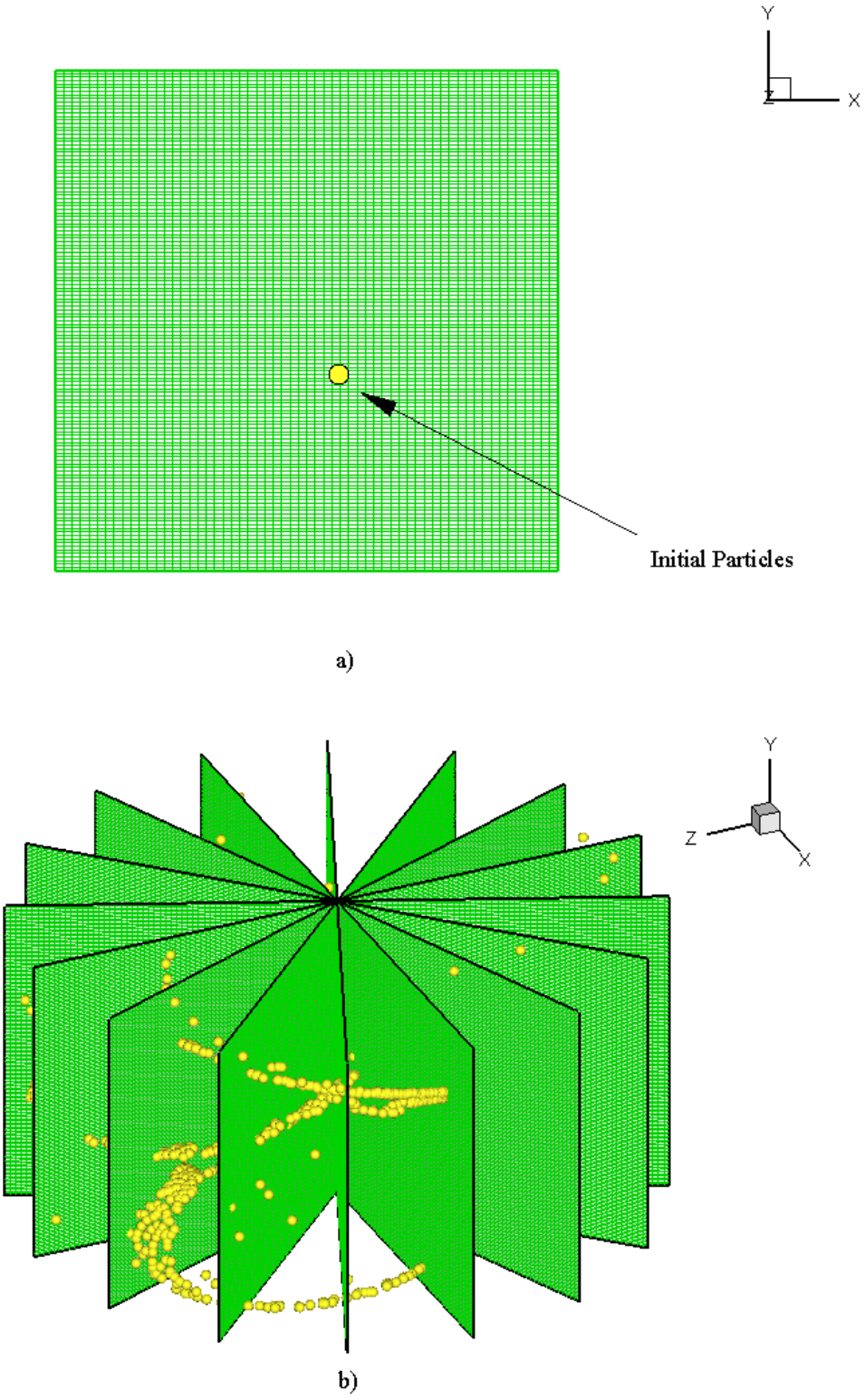

Figure 6.28 a) Initial blob of particles.b) Instantaneous three-dimensional snapshot of particle positions.

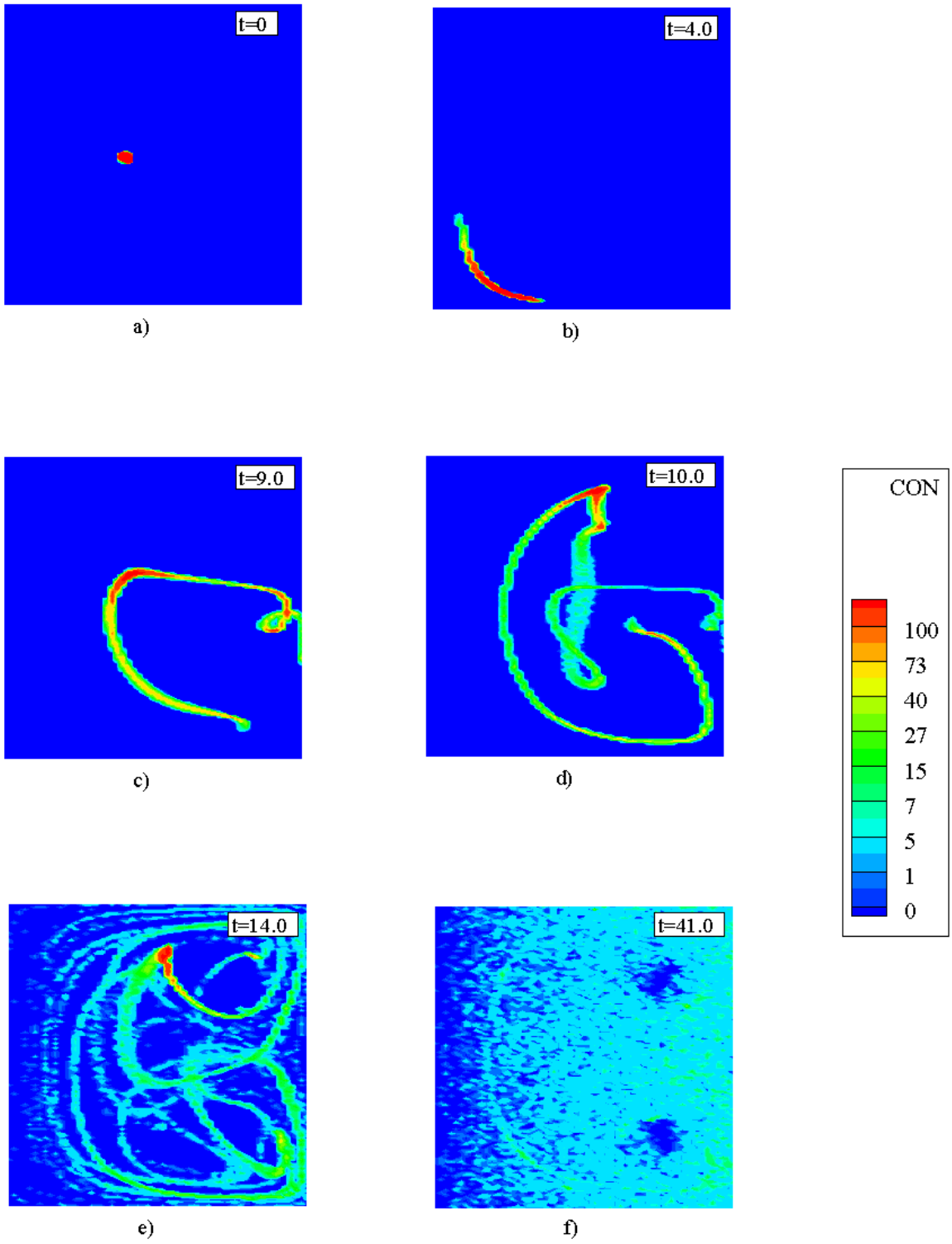

Figure 6.29 Concentration maps for Re=350 flow at different times t (t is measured in lid revolutions).

For a chaotically stirred flow, the variance of concentration will approach zero and the rate at which it approaches zero can be used to define the stirring rate of the flow as explained below.

Few comments regarding this technique are in order before we present results from its application. First, the above procedure can be also applied in a fully three-dimensional manner without collapsing one spatial dimension. Instead of two dimensional control volumes one simply has to define three-dimensional control volumes at each grid node and count the number of particles within each such volume. This procedure will yield the discrete equivalent of the three-dimensional concentration field, $C_{i,j,k}(t)$, and the instantaneous variance can be calculated in exactly the same manner as described above. Numerical experiments, however, showed that the full 3-D approach requires many more particles to yield accurate and smooth results. Furthermore, the 3-D technique takes considerably more computational time per particle because it obviously necessitates a full three-dimensional search to find the control volume where each particle is located as compared to the two-dimensional search required by its 2-D equivalent. To ensure that the 2-D technique indeed yields the correct concentration variance we have also carried out calculations with the three-dimensional technique for few Reynolds numbers and as we will show in the following section the results of the two calculations compare well with each other.

In the 2D technique described above we have chosen arbitrarily to collapse the azimuthal coordinate. It is obvious, however, that the same approach can be used in conjunction with any one of the three spatial directions. To explore whether the stirring of particles exhibits any spatial anisotropies, we further conducted calculations by collapsing the particle locations in the axial direction. These results are also included in

the subsequent section and have yielded identical trends and mixing rates that are very close to those obtained with the azimuthal approach.

6.5.2.2 Stirring Rate as Function of the Reynolds Number

Using the above technique we calculate the stirring rate for all simulated Reynolds numbers. In figure 6.30 we plot on a semi-log scale the time evolution of the variance of concentration calculated using the 2D technique with azimuthal collapse for various Re. Similar time series are also obtained when we employ the 2D technique with axial collapse and the full 3D technique. Each time series starts from a large value of concentration variance, which is gradually diminishing with time. This initial high value is to be expected because, as seen in figure 6.29, all particles are initially tightly packed together and, thus, the variance would have to be at its highest value at the initial time. The subsequent decay of the variance for all cases suggests a linear trend, which implies an exponential decay law:

$$\sigma_c^{\,2}(t) = C_0 \exp(-R_m t) + C_1 \tag{6.6}$$

where R_m is a positive constant equal to the slope of the line, and C_o and C_1 are constants. The larger R_m is, the more rapidly the flow can stir the initial blob of particles. Therefore, R_m is defined as the stirring rate of the flow (see Voth et al 2003). For all Reynolds number we calculate R_m by fitting, via least square fitting, a straight line to the log of the variance decay curve and then taking the negative of the slope. Hence, the equation for R_m becomes:

$$R_m = -\left[\frac{n\sum_1^n[\phi * t] - \sum_1^n \phi \sum_1^n t}{n\sum_1^n (t^2) - \left(\sum_1^n t\right)^2}\right] \tag{6.7}$$

where n is the total number of data points considered within the time interval, ϕ is the log of the variance of concentration σ_c^2, and t is the time in lid revolutions. This calculation was performed with the assistance of EXCEL software. The curve fitting time interval for all cases starts and ends at 3 and 20 lid revolutions, respectively, after the initial time.

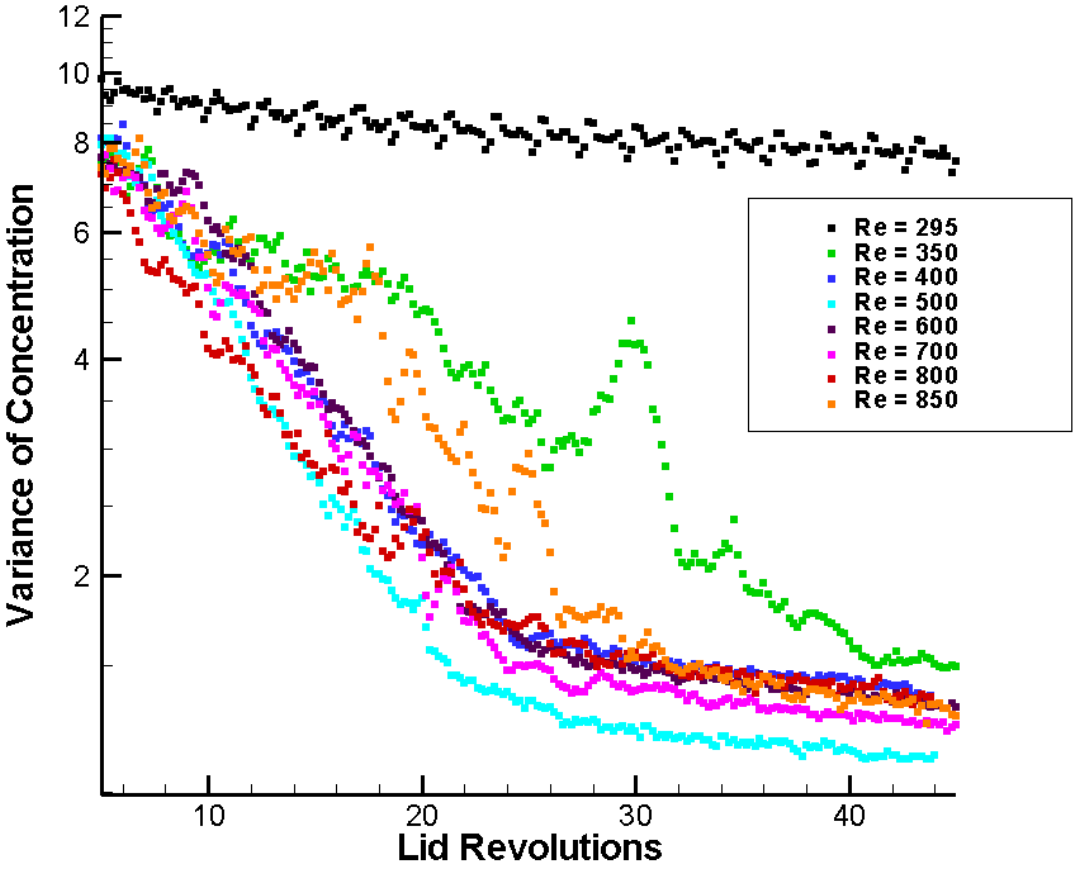

Figure 6.30 Variance of Concentration with time (in lid revolutions) for the azimuthal collapse technique, for various Reynolds numbers.

The so calculated stirring rates for all Reynolds numbers and from all three techniques (2D with azimuthal and axial collapse and full 3D) are plotted in figure 6.31. The calculated results with all three methods are in good agreement with each other and show that the stirring rate initially increases with Re but reaches a maximum for Re ~ 500. Beyond that point, further increase in Reynolds number causes the stirring rate to decline. This trend is sustained for the highest simulated Re, Re = 850. Note that obtaining steady solutions for Re > 800 was found to be extremely difficult and Re = 850 is the largest Re for which the iterative algorithm reached a fully converged steady state.

The existence of a Reynolds number at which stirring rate is maximized, counter-intuitive as it may first appear, is entirely consistent and coincides with the previously discussed appearance of unmixed regions in the flow as the Reynolds number is increased beyond Re = 500. The emergence of unmixed islands reduces the volume of the flowfield that is occupied by chaotically advected trajectories and, thus, material elements will, on average, experience less stretching and folding leading to less efficient and slower stirring. The question that needs to answered, therefore, in order to understand this striking and potentially very significant phenomenon is: Why do unmixed islands begin to appear in the flow above a threshold *Re*?

The answer to this question follows from a recently proposed theory by Mezić (2001) who argued that mixing rate in bounded, three-dimensional chaotically advected flows will indeed decline with Reynolds number assuming that the flow remains steady and no instabilities are present. According to Mezić this follows from the fact that a viscous flow can be split into two parts: an inviscid, Euler part and a viscous contribution. With only exception the very special case of the ABC (Arnold-Beltrami-Childress) flow—a flow in which the velocity and vorticity vectors are proportional to

each other—inviscid flows are integrable and the Bernoulli function serves as the integral of motion (Mezić 2001). Thus, Mezić argues that the cause of chaotic motion must lie in the viscous forces. Consequently for any bounded, three-dimensional flow at very small Reynolds numbers, where viscous forces dominate the inertial forces, chaotic mixing should increase with Re but the chaotic regions in the flow should diminish as $Re \rightarrow \infty$—assuming, of course, that the flow remains steady and stable. Using classical boundary layer scaling arguments in conjunction with Melnikov theory, Mezić (2001) was able to show that the chaotic mixing will diminish as $Re^{-1/2}$. Mezić's arguments clearly suggest that an optimal Reynolds number must exist at which mixing rate is maximized and this is indeed the type of trend we find in the present flow. In fact based on our previous discussion of the particle paths as a function of Reynolds number, our simulations clearly show that the integrable part of the flow—i.e. that occupied by unmixed islands—begins to increase above a threshold Re, Re>500.

To explore whether our stirring rate data follow the scaling proposed by Mezić (2001), we plot in figure 6.32 the variation of mixing rate with Reynolds number in log-log scale. The $Re^{-1/2}$ trend line is also included in the figure. It is seen that our data for Re>500 exhibit indeed a nearly linear decay trend and follow with reasonable accuracy Mezić's scaling. The only deviation from the trend appears at the highest Re, Re = 850, where our simulations imply a faster decay rate—note, however, that Mezić's (2001) scaling provides only an upper bound limit to the rate of decay of chaotic stirring.

Mezić (2001) provided some evidence for the validity of his theory using the experimental results of Wereley and Lueptow (1998) and Desmet et al. (1996) and the numerical results of Rudman (1997) for wavy vortex flow in the Taylor-Couette apparatus. The results presented in this thesis provide yet another significant piece of

evidence of this striking theory, which obviously can have significant implications for designing and optimizing low Reynolds number mixing devices. Unfortunately, the flow we studied appears to transition to the unsteady regime for Re >850 and, thus, we could not obtain steady solutions at even higher Reynolds numbers to firmly establish the existence of the $Re^{-1/2}$ trend.

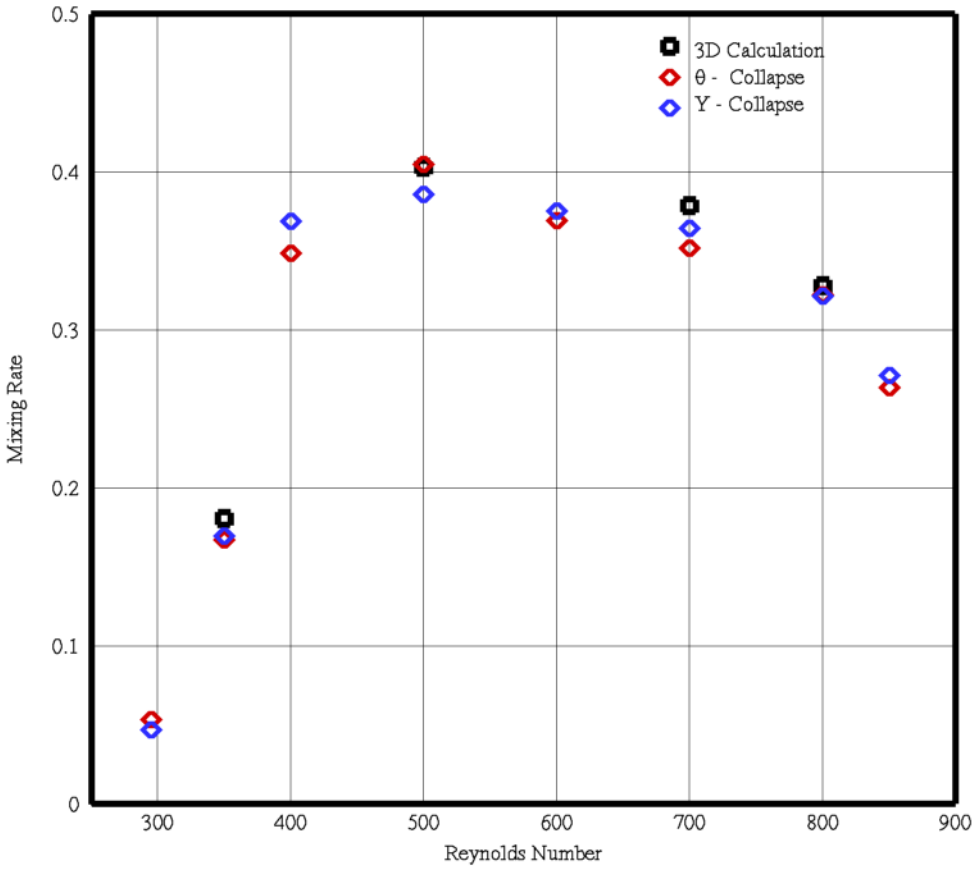

Figure 6.31 Mixing rates plotted with Reynolds numbers for 2D azimuthal and axial collapse as well as full 3D technique.

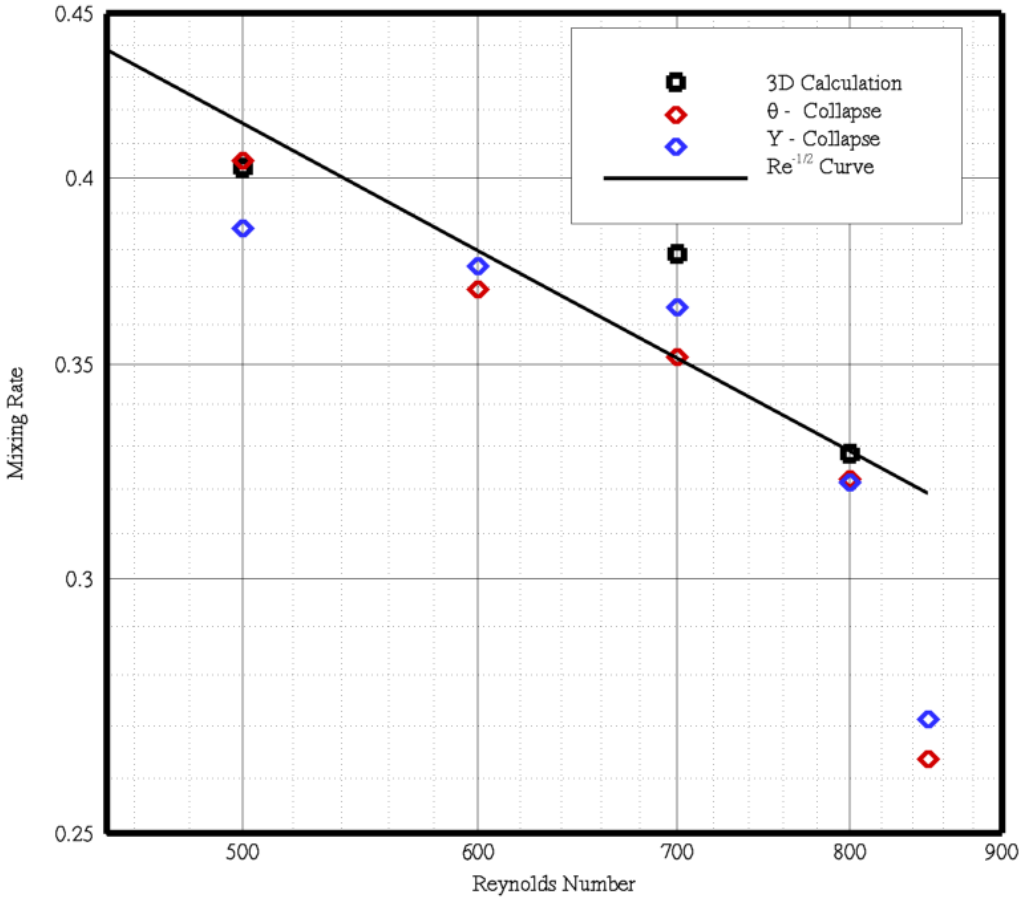

Figure 6.32 Variation of mixing rate with Reynolds number in log-log scale. Theoretical trend line of $Re^{-1/2}$ included.

6.6 Summary

In this chapter we have studied numerically the Eulerian and Lagrangian properties of the steady flow in a cylindrical container with two exactly counter-rotating lids. Our computations have elucidated for the first time the complex vortical structures in this flow, which are dominated by an intricate web of cat's eyes radial vortices at the unstable equatorial shear layer and axial vortices inclined in the azimuthal direction. We have also shown numerically that the shear-layer instability that gives rise to a complex three-dimensional flow enhances transport and stirring via chaotic advection. A striking finding of our work is that there is an optimal Reynolds number at which stirring rate is maximized. Above this Reynolds number the integrable (unmixed) part of the flow begins to grow and stirring rate declines. Our findings have been explained in terms of a recently proposed theory of chaotic advection. The calculated rate of decay of stirring rate with Reynolds numbers appears to be in good agreement with the rate of decay predicted by the theory.

CHAPTER 7

STIRRED TANK FLOW WITH COUNTER-ROTATING DISKS

It has been estimated (Harnby et al. 1992, Alvarez et al. 2002) that the lack of fundamental knowledge of the physics of mixing in industrial systems, which naturally results in inefficient mixing devices, costs the industry in North America alone nearly ten billion dollars per year. In this chapter we seek to demonstrate that fundamental studies of mixing in simple model systems, such as that reported in the previous chapter, are not important only from an academic standpoint. The fundamental understanding gained from such studies can lead to specific improvements and design modifications of standard mixing devices, which can drastically enhance mixing performance. More specifically, we seek to demonstrate that the shear-layer instability between two counter-rotating disks can be exploited to modify and enhance the performance of a widely used industrial mixing device, that of a stirred tank.

Stirred tanks are employed to mix just about everything: from household items when preparing a cake, to pharmaceutical products, such as insulin and penicillin, to nuclear waste products during treatment. A stirred tank consists of a container filled with fluid and one or more agitators that take the form of rotating impellers or disks. The simplest example of such an agitator is the hand-mixer used to blend cake materials in the

kitchen. More sophisticated agitators are used in industrial mixers, which consist of multiple impellers of disks mounted along a rotating shaft. As the agitators rotate, they set up a three-dimensional flow, which could exhibit chaotic particle paths and lead to efficient mixing. Quite often baffles are also used in stirred tanks to enhance its mixing performance. These are obstacles that are positioned parallel to the agitator arm at the edge of the tank to enhance the three-dimensionality of the flow and promote chaotic stirring and mixing.

Although mixing in stirred tanks has been studied since the 1950's, starting with the early work of Rushton (Rushton et al 1950) on the so-called Rushton Turbine, many of these early studies were performed under the assumption that the flow could be thoroughly mixed only by increasing mechanical energy, i.e. direct agitation and turbulence. However in many industrial applications, such as in the pharmaceutical and food industries, it is necessary to achieve good mixing under laminar flow conditions. Examples range from the mixing of highly viscous fluids in the food processing industries (pastes, dough, yogurt, etc.) to low velocity mixing in bio-reactors where low levels of shearing stresses are required to avoid harming living cells. Under such conditions, efficient mixing can only be achieved via chaotic advection (Harvey et al 2000, Alvarez et al 2001, Zalc et al 2001, etc…).

A typical stirred tank configuration consists of an impeller shaft, located along the central axis of the container, with one or more co-rotating disks or impellers (see figure 7.1). When disks are used the flow remains axisymmetric and mixing efficiency is very poor. Figure 7.1 shows some experimental results of scalar mixing in a co-rotating disk stirred tank performed by Alvarez et al (2002). The top half of the container shows the

lack of mixing either between or within the nested tori by the unmixed different colored dye streaks that were injected with needles into the container. The bottom half of the figure shows a slice through the tank axis, displaying the perfectly axisymmetric invariant tori. Many attempts to break the symmetry of this configuration and thereby promote chaotic mixing have been reported in the literature. These efforts have included among others attempts to displace the shaft away from the axis and/or add additional shafts with disks (Ascanio et al 2002). A different approach for breaking the symmetry is to replace the disk with bladed impellers (Recknagle and Shekarriz 1998, Zalc et al 1999, Alvarez et al 2002a & 2002b, Zalc et al 2002,etc…). While these approaches have succeeded in inducing chaotic mixing, they require more complex machinery and are thus more susceptible to wear.

In this work we look specifically at the flow geometry within a cylindrical container with three rotating disks. The co-rotating disk version of this flow has been studied both numerically and experimentally by Zalc et al (2001, 2002) who utilized this as a base flow for their investigation of mixing using three Rushton turbines. The resulting flows in this device are steady and axisymmetric and, thus, mixing is very slow as it can only be affected by molecular diffusion. In this chapter we apply the concepts of innate flow instabilities developed due to counter rotation of the disks. We seek to show that by simply reversing the rotation of the central disk, the Lagrangian properties of the flow are drastically altered—due to the effect of the shearing instabilities discussed in detail in the last chapter—and mixing is dramatically enhanced.

This chapter will proceed as follows. First we review previous research on mixing in stirring tanks. Subsequently we describe the geometry of the co-rotating and

counter-rotating stirred tank configurations and the various computational details of our simulations. This is followed by the discussion of the computed results for the co-rotating and counter-rotating cases from the Eulerian standpoint. Finally we analyze and compare the Lagrangian characteristics of the various flowfields.

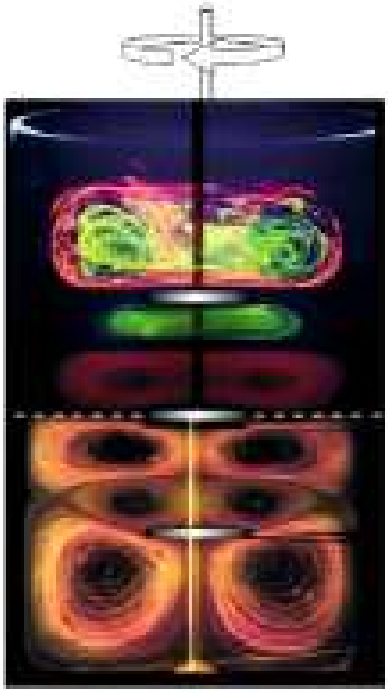

Figure 7.1 Experimental results of scalar mixing in a stirred tank with three co-rotating disks. Top) Unmixed different colored dye streaks injected with needles. Bottom) Slice through tank axis, displaying invariant tori. (Alvarez 2002).

7.1 Previous Research

The stirred tank mixer is perhaps the most commonly used industrial mixer. Early experiments on this device focused primarily on performance and mixing times (O'Connell and Mack 1950, Rushton et al 1950a, 1950b) and were performed under the assumption that mixing performance is proportional to the mechanical energy of the impeller. For the most part, these works were oriented towards creating power curves for different impeller configurations under various operating conditions and did not delve deeply into the dynamics of the flow and the physical mechanisms, which enhanced mixing. In subsequent years various methods for quantifying mixing in stirred tanks were developed. Norwood and Metzer (1960) carried out a series of neutralization experiments to visually determine mixing times. Other methods for measuring mixing times were based on the variance of pH or using conductivity equipment (Sano and Usui 1985).

In recent years the advancement of non-intrusive experimental techniques, such as PIV and LIF, has allowed for the first time detailed and simultaneous measurements of velocity profiles and scalar concentration in mixing devices. Furthermore, the ability to generate numerical solutions to the complex flowfields using CFD has provided an additional method for determining the Lagrangian and Eulerian aspects of such flows. Ranada (1997) computed laminar flowfields in a baffled stirred tank with a single Rushton turbine. However in this work, they do not solve the full time-dependent flow equations. Instead they compute a quasi-steady flowfield for any momentary impeller position by taking an instantaneous "snapshot" of the time-dependent three-dimensional

flow. The resulting averaged velocity fields were compared with experimental data and found in general to have good agreement. However this type of investigation would be insufficient for in-depth mixing studies. Bakker et al (1996) computed the laminar flow field in a stirred tank with a single pitched blade turbine. In this study also, the results they obtained using CFD agreed in general with experimental results, but these first CFD studies were not centered on understanding mixing mechanisms.

Much of the research in mixing in stirred tanks over the years involved turbulent flows (Norwood and Metzner 1960, Bakker et al 2000, Compolo et al 2003) where the focus is primarily on the method of capturing the various scales of flow structures. As the importance of such devices for mixing in the laminar regime has become evident, however, many studies in the last decade have considered low Reynolds number flows (i.e. Re<500) and employed the theory of chaotic advection to understand and enhance mixing rates. Lamberto et al (1996) proposed to enhance mixer performance by introducing periodic fluctuations to their agitation, thus, making their flow time dependent. They studied both baffled and un-baffled systems and concluded that the size and location of unmixed areas in the flow are dependent on the Reynolds number. This work was continued (Lamberto et al 1999, 2000) in their experimental and numerical investigation of this one impeller system. However, using their numerical technique, they only calculated one-sixth of the flow geometry due to the inherent symmetry of the tank. They characterized mixing in the flow using Poincare maps and by developing stretching distributions and were able to visualize the two ring unmixed structures that appear above and below the blades. Tanguy et al (1997) proposed to enhance mixing using a combination of Rushton impeller and helical ribbon turbine mounted on the same shaft.

They found that by rotating these two different impeller types at different speeds, they were able to out perform either one of the impellers alone. A ribbon impeller was also studied by de la Villeon et al (1998) who performed a numerical investigation of that geometry and calculated stretching lengths and Lyapunov exponents. This type of study was continued by Harvey III et al 1997 who used four different impellers of varying sizes on the same shaft, obtaining velocity profiles and streamline plots to characterize mixing. Recknagle and Shekarrize (1998) investigated the effect of the pitch blade impeller system. They showed that laminar mixing correlates with rotational speed for both Newtonian and Non-Newtonian fluids. Additional unconventional configurations were adopted by Ascanio et al (2002) who studied varying combinations of Rushton impellers and hydrofoil impellers. In addition they also considered time dependent perturbations to the flow and off-center placement of the impeller shaft. They found that creating dynamic perturbations was sufficient to enhance mixing in small size tanks. For larger mixing tanks, however, it would be extremely challenging to implement unsteady forcing as that would require the installation of a variable direction control for the motor and also perhaps magnetic breaks.

Harvey III et al (2000) performed a milestone experiment when they began to rigorously look at flow visualization of the unmixed regions of the flow in a stirring tank with multiple impellers. Using CFD, they also constructed Poincaré maps to visualize the unmixed regions of the flow. This work was the first to simulate numerically the full laminar flow fields in an unbaffled stirring tank with multiple impellers and paved the way for a series of other experiments—Zalc et al 2001, Shrinbrot et al 2001, Alvarez et al 2002a, Alvarez et al 2002b, Zalc et al 2002. In these works, the investigators report on

the use of Rushton impellers to improve mixing in stirred tanks. They show a series of results in which they describe the mixing that occurs in the base flow (flow with co-rotating disks) becoming greatly improved as small perturbations to the integrable flow are introduced which lead to the emergence of 3D horseshoes. Poincaré maps as well as stretching maps are computed numerically and compared to experimental visualization techniques that are used to differentiate between the mixed and unmixed regions of the flow.

In all the previously discussed stirred tank configurations, co-rotating disks/impellers have been used. The primary emphasis of these studies has been on approaches for perturbing the base axisymmetric flow and inducing chaotic advection either by breaking the symmetry of the flow (using impellers and various unconventional configurations) or by introducing time dependent perturbations. In this work, we instead, consider the effect of counter-rotation of the disks to exploit innate flow instabilities in the system and instigate chaotic mixing.

7.2 Flow Geometry and Computational Details

We study flow in a closed cylindrical container of diameter D and height H driven by three, co-axial rotating disks of diameter d. The centers of all disks are located on the container centerline as shown in the schematic of figure 7.2. We consider two cases: 1) co-rotating disks, where all three disks rotate in the same direction with constant angular velocity Ω; and 2) counter-rotating disks, where all three disks rotate with constant angular velocity Ω but the middle disk rotates in the opposite direction from the top and

bottom disks. For both cases the diameter of the container is three times the size of the disks ($D = 3\times d$). The container aspect ratio ($AR = R/H$, where R=D/2) is set equal to 1/3 and the three disks are spaced .25H apart. This specific configuration is selected because it is identical to the co-rotating case studied extensively by Zalc et al. (2002), whose work will serve to validate our computations for the co-rotating case. The Reynolds number for both cases is based on the disk diameter and is defined as follows:

$$Re = \frac{\rho N d^2}{\mu} \qquad 7.1$$

where N is the disk speed expressed in rotations per sec (RPS), ρ is the density, and μ is the fluid viscosity.

For all cases the flow fields are generated by solving numerically the three-dimensional Navier-Stokes equations using the numerical method described in Appendix A. A polar/cylindrical grid with approximately 1.4 million nodes is used for all computations—61×161×141 nodes in the radial, axial, and circumferential directions, respectively (Figure 7.3). The grid is stretched, using the hyperbolic tangent function to cluster nodes at the three rotating disks and the stationary container lids. For all cases the disks are assumed to have zero thickness. Solutions for both co- and counter- rotation are calculated for *Re = 40* and *80*. For the counter-rotating case a solution at *Re = 100* has also been obtained.

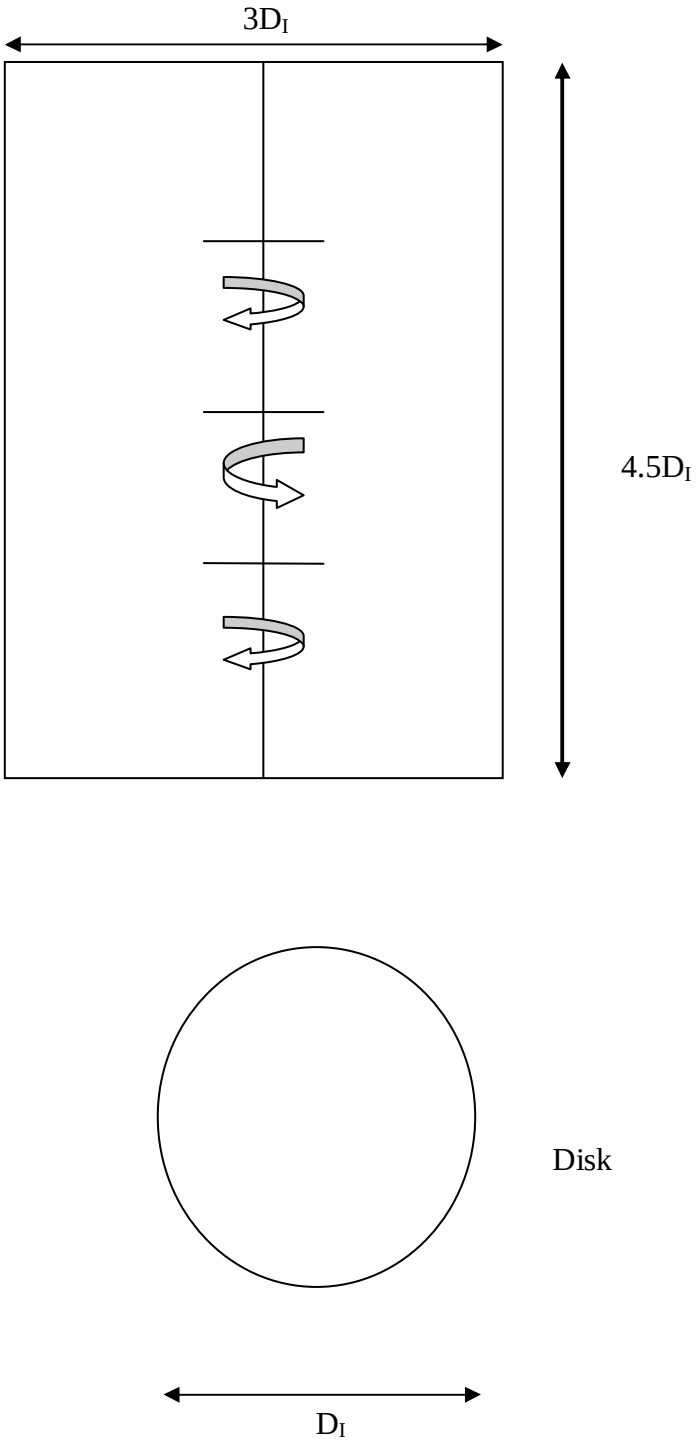

Figure 7.2 Schematic of counter-rotating disk system.

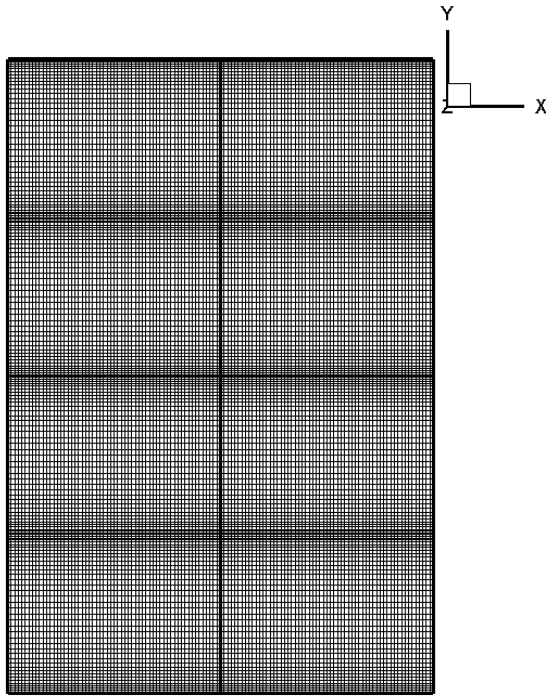

a)

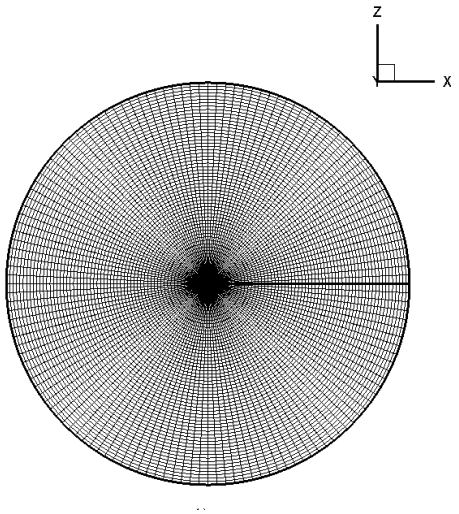

b)

Figure 7.3 Computational grid for flow with co- and counter-rotating disks.

7.3 Eulerian Flow Characteristics

In this section we investigate the Eulerian aspects of the co-rotating and counter-rotating flowfields in order to illustrate that the same shear-layer instability that was discussed in the previous chapter does occur for the latter case. We compare numerical solutions for the two configurations at Re = 40 and 80 and we also show results for the counter-rotating case for Re = 100. For the co-rotating case the flow is steady and axisymmetric for Re = 40 and 80. For the counter-rotating case, axisymmetric flow is obtained for Re = 40 but steady three-dimensional flows emerge at the two higher Reynolds numbers.

To aid the discussion of the flow, the following conventions are developed to refer to different flow regions. The upper most disk in the stirred tank is Disk 1. The middle disk is Disk 2 and the bottom disk is Disk 3. The equatorial plane between disks 1 and 2 is called Shear Layer 1 (SL1) and the equatorial plane between disks 2 and 3 is called Shear Layer 2 (SL2).

As the disks rotate, Ekman suction and pumping drives meridional recirculating regions in the flow. Fluid particles spiral outward in the vertical plane of the disks, are forced along the side walls of the container and then pushed back inwards towards the central axis of the container where the finally close the trajectories by moving up or down the axis back towards their origin. This creates a series of toroidal stream-surfaces in the co-rotating case and in the axisymmetric regime of the counter rotating case. In figure 7.4, the structure of these toroidal vortices for both systems are shown by plotting two-dimensional streamlines at a diametral plane for *Re = 40*.

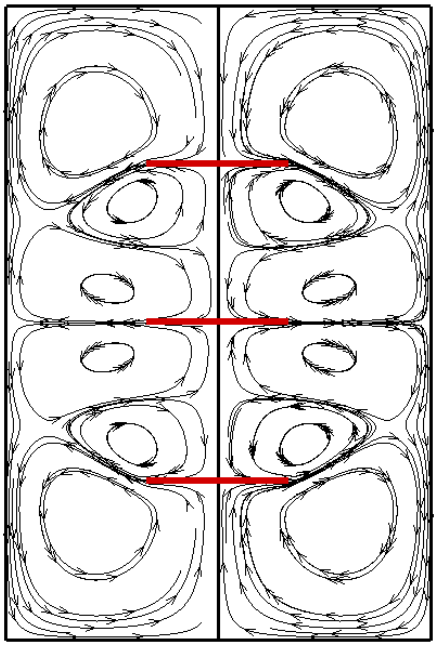

Co-rotating

a)

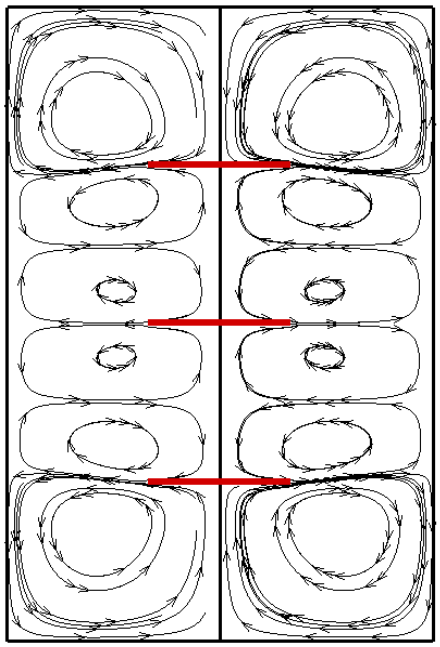

Counter-rotating

b)

Figure 7.4 Structure of toroidal surfaces for a) co-rotating and b) counter-rotating disk systems.

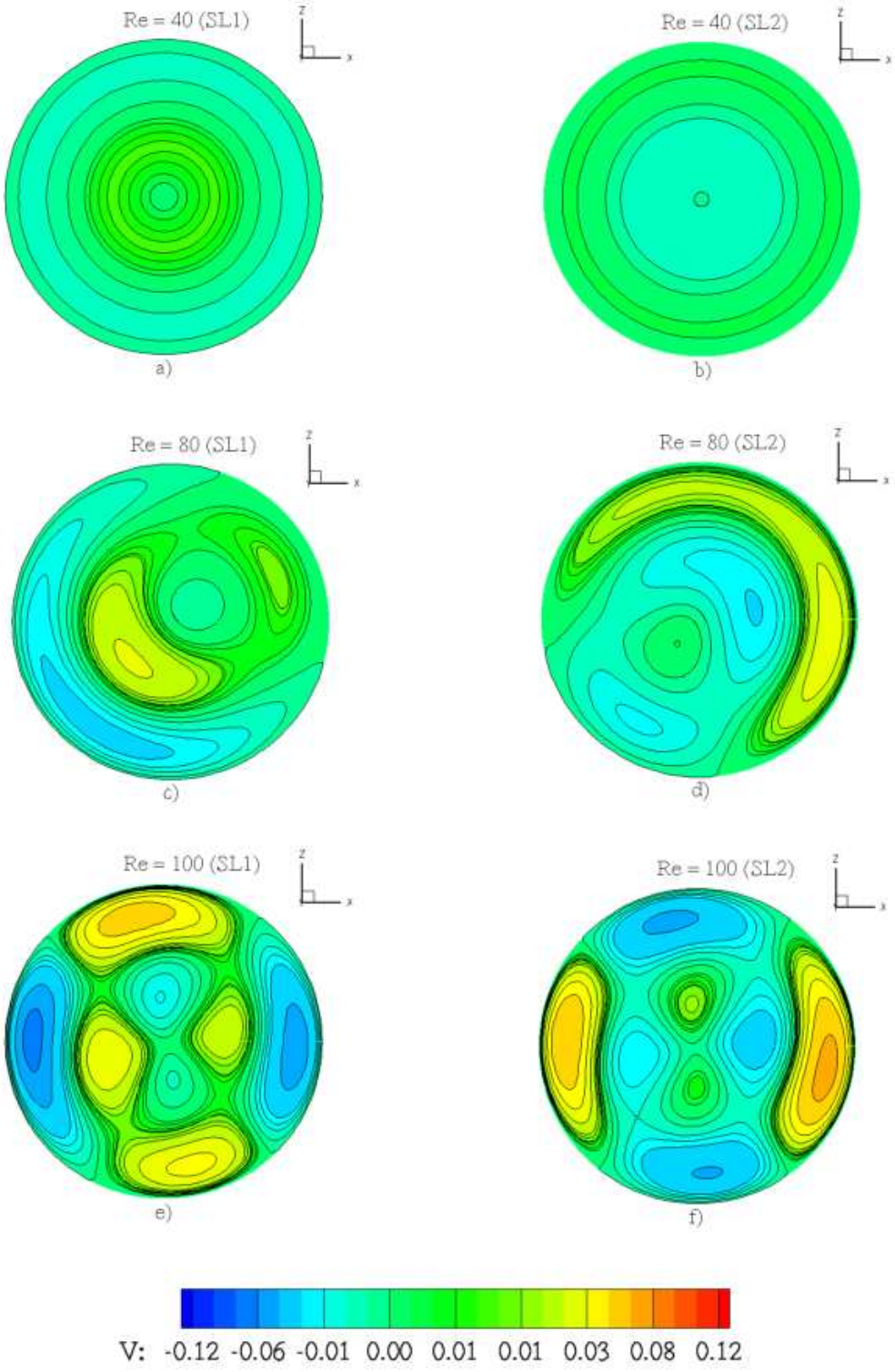

Figure 7.5 Vertical velocity contours at the shear layer planes for Re=40, 80, and 100 counter-rotating flows.

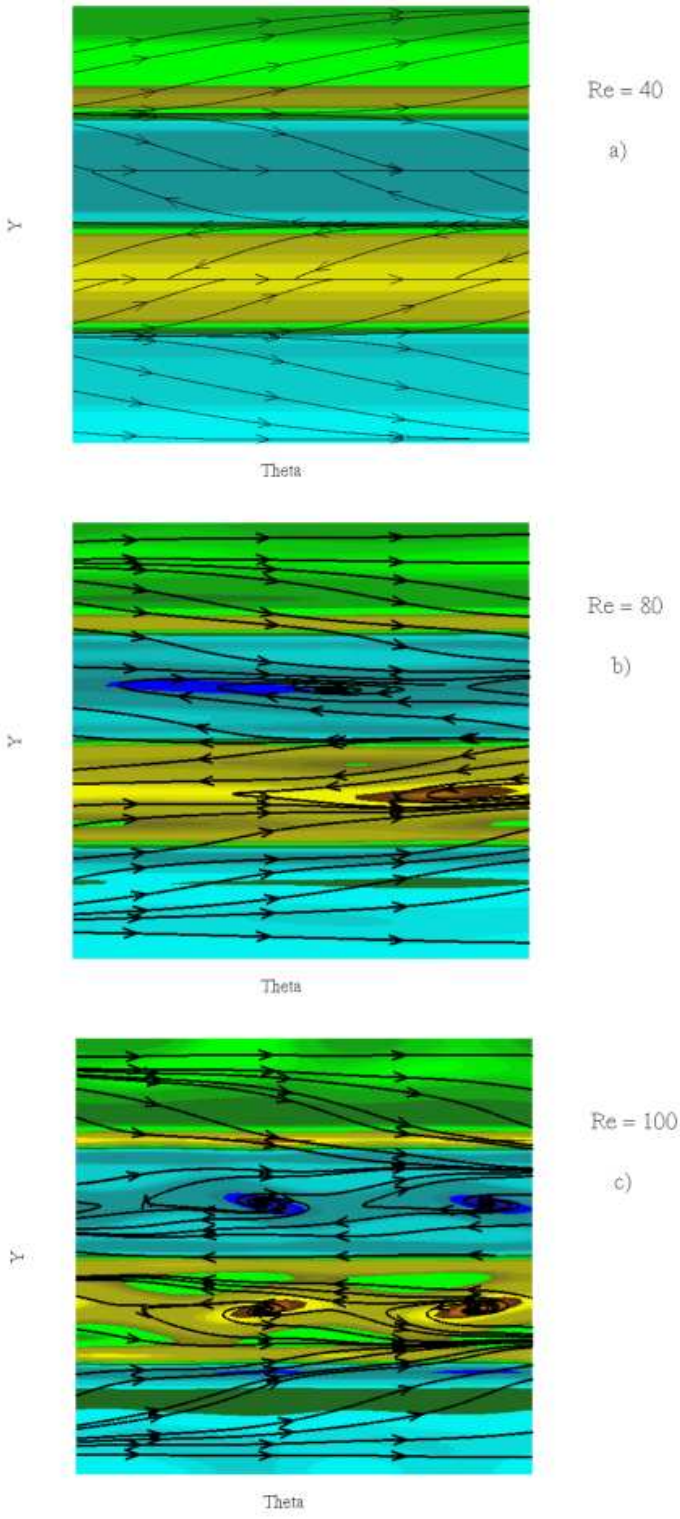

Figure 7.6 Surface streamlines and radial vorticity contours of unfolded radial plane.

The vertical velocity contours in figure 7.5 compare the flow at planes SL1 and SL2 for Re = 40, 80, and 100 for the counter rotating flow—as mentioned before the numerically simulated flowfields for the co-rotating case remain perfectly axisymmetry and are not shown here. Similar to the flow described in the previous chapter (container with exactly counter rotating lids), regions of alternating positive and negative vertical velocity appear at the mid-planes between the disks for Re = 80 and 100, marking the onset of the shear-layer instability. There are, however, some notable differences. Firstly, the figure shows the m = 1 and m=2 modes emerging for Re = 80 and 100, respectively, as opposed to the m = 3 mode that appeared in the simulations reported in the previous chapter. This discrepancy should not come as a surprise, however, as the stability work of Nore et al. (2004) clearly showed that the most critical azimuthal mode is a strong function of aspect ratio. In addition to differences in aspect ratio between the stirred tank configuration and the container flow, the fact that the disks do not extend all the way to the wall in the former case should also be expected to have a significant effect on the dynamics and stability characteristics of the flow.

Another important feature in the flowfields shown in Figure 7.5 is the fact that the mirror-image symmetry of the flow along the vertical direction also appears to break. For the Re=40 case (figure 7.5a), where the flow is axisymmetric, the vertical velocity contours at the SL1 and SL2 planes are essentially zero but even the very small contour levels retain the mirror-image symmetry that would be expected from the symmetry of the configuration. For the two higher *Re*, however, this mirror-image symmetry breaks as can be seen by comparing the contours at the SL1 and SL2 planes. The break of mirror-image symmetry in the streamwise direction should also be attributed to the presence of

the large gaps between the disks and the container wall ($d < D$) and should be expected to enhance transport in the entire container.

We argue that the symmetry break in the vertical direction is the result of a secondary instability, which is excited by the primary instability for this configuration: the formation of radial, cat's-eye vortices at SL1 and SL2. This is shown in figure 7.6, which depicts streamlines and radial vorticity contours on an unfolded plane of constant radius (similar format as that of figure 6.x in the previous chapter). For Re = 40 the flow is axisymmetric and SL1 and SL2 are marked by perfectly straight lines of convergence. The emergence of the m = 1 and m = 2 modes for the Re = 80 and 100 cases, respectively, is illustrated clearly in these figures by the appearance of radial vortices centered on each shear layer.

In figure 7.7 we show an iso-surface of vorticity magnitude for all three *Re* to further highlight the three-dimensional feature of the flow. For Re = 40, the flow is axisymmetric and a notable feature of the flow are the two small vorticity pockets centered around each saddle point at SL1 and SL2 planes, respectively. Near the container wall there are annular bands of vorticity, which mark areas where the fluid is pushed radially inward toward the centerline. For the Re=80 case shown in figure 7.7b, the bands along the outer wall of the container shrink in size and become azimuthally wavy and distorted as the m = 1 mode emerges. The distortion and three-dimensionality of the vorticity contours is even more pronounced for the Re = 100 case. It is worth noting in this case the increase in size and distortion of the pockets of vorticity around the two saddles at Sl1 and SL2. The patterns developing in these regions suggest the growth

of vertically inclined structures similar to those observed in the container case in the previous chapter.

Figure 7.8 show a positive and a negative iso-surface of normalized helicity (see eqn 6.1) for all three Reynolds numbers. Once again the effect of the shear layer instabilities become visible as the shape of the iso-surfaces evolves from the simple disk-like shapes in the Re=40 case to the topologically rich, three-dimensional structures seen in figures 7.8b and c. A pair of vortical structures resides along the axial plane on either side of each shearing plane. The shear layers are tilted upwards and downwards at the edges. These features are similar to those observed in similar plots for the container with counter-rotating lids.

7.4 Lagrangian Dynamics

In this section we analyze the Lagrangian characteristics of the co- and counter-rotating cases to show that the three-dimensional instabilities in the latter configuration can indeed lead to chaotic stirring and efficient mixing. We first discuss three-dimensional particle paths in the two systems to underscore the significant differences in dynamics. Subsequently, we illustrate the ability of the counter-rotating configuration to induce transport across the entire container. We also illustrate the increase in the richness of dynamics with Reynolds number for the counter-rotating configuration by comparing Poincaré maps for Re =40, 80 and 100.

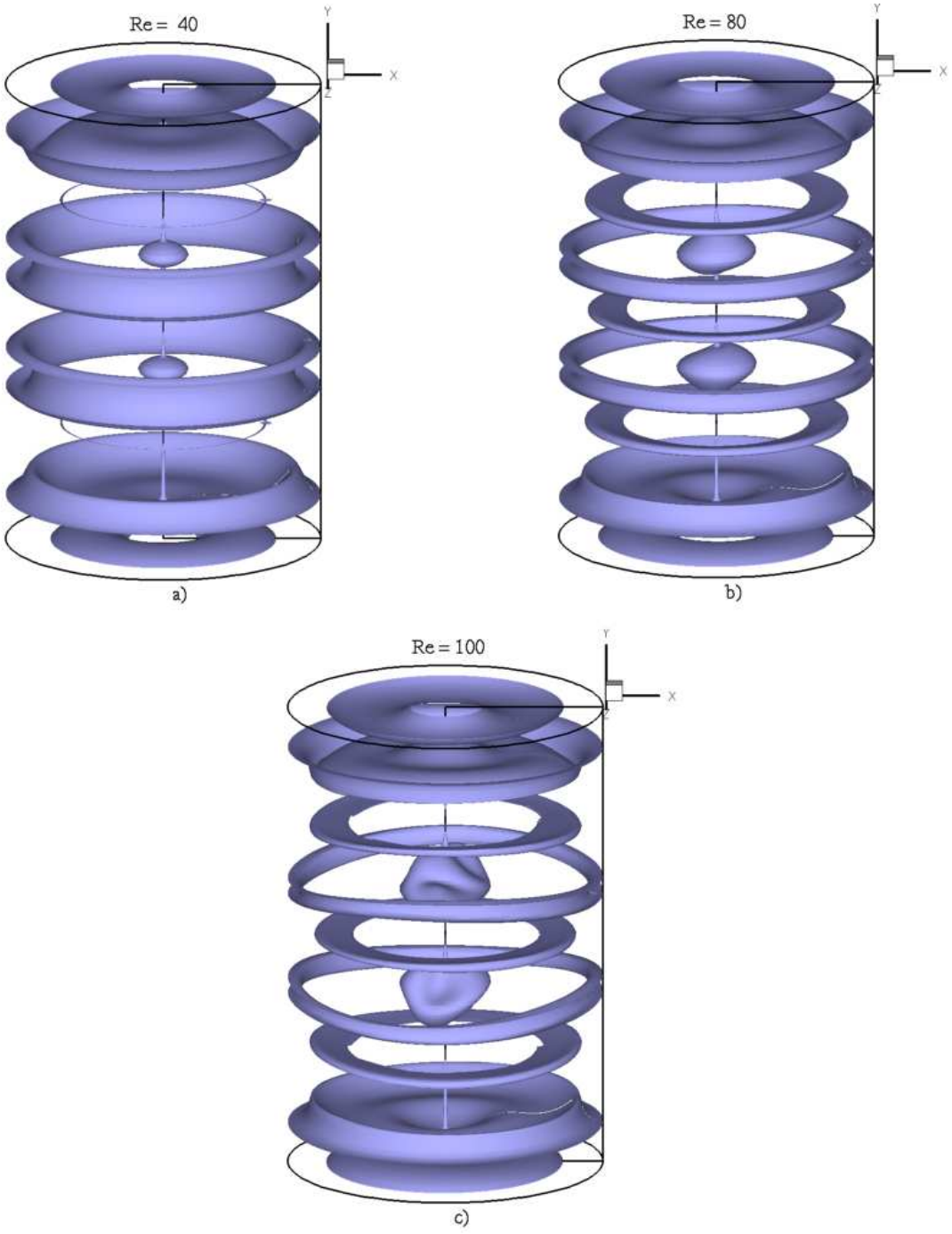

Figure 7.7 Iso-surface of vorticity magnitude for Re = 40, 80, and 100 counter-rotating disk flows.

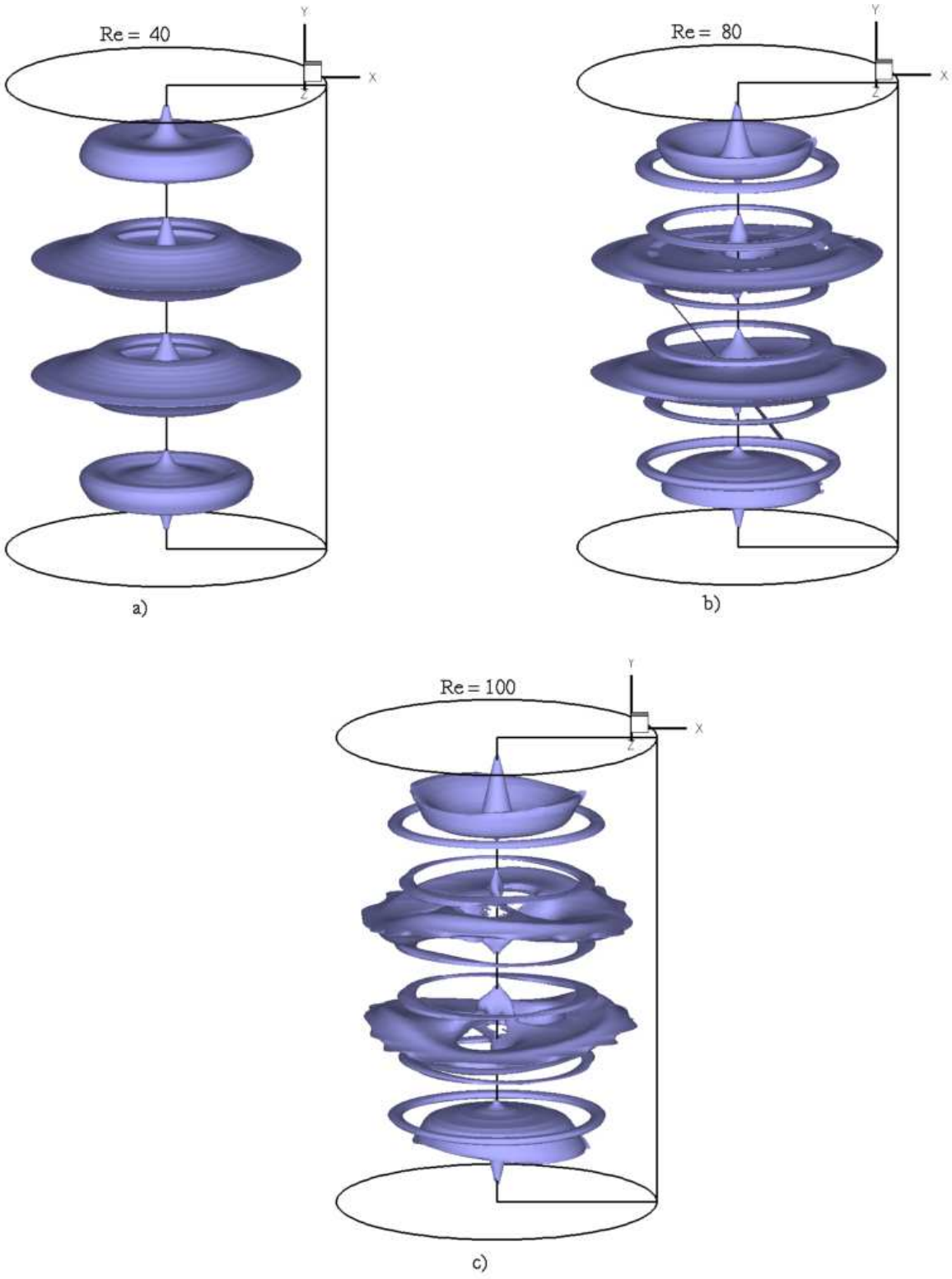

Figure 7.8 Iso-surface of normalized helicity for Re = 40, 80, and 100 counter-rotating disk flows.

The base axisymmetric flow for both the co- and counter-rotating tanks, as described in the previous sections, consists of toroidal stream-surfaces. It has been shown in previous investigations of the co-rotating case (Zalc et al 2001, Zalc et al 2002) that as perturbations are introduced into the flow the outer tori begin to break. This is also consistent with our findings from the previous chapter. In figure 7.9, we plot a series of three-dimensional particle paths that originate along the outer edges of the toroidal structures in the upper portion of the container. For the co-rotating case the flow remains axisymmetric for both Re = 40 and 80. Consequently, for both Reynolds numbers the particles follow trajectories that remain confined on their respective invariant streamsurfaces in the upper half of the flow domain. For the counter-rotating flows, the dynamics are simple and integrable for the Re=40 case with the particles remaining trapped on toroidal streamsurfaces. However, as the Reynolds number is increased to Re=80 and the flow becomes three dimensional, the invariant regions begin to break and the particles escape and start exploring the entire container region. The ability of particles to move throughout the container can be easily understood in terms of the vertical velocity contours at SL1 and SL2 planes shown earlier in figure 7.5. Recall, that for the counter-rotating case the onset of the shear layer instability is accompanied by the growth of non-zero vertical velocity field at the disk mid-planes. As discussed above, this feature allows for transport across the entire container and as shown in figure 7.9 such transport does indeed take place for the counter-rotating case.

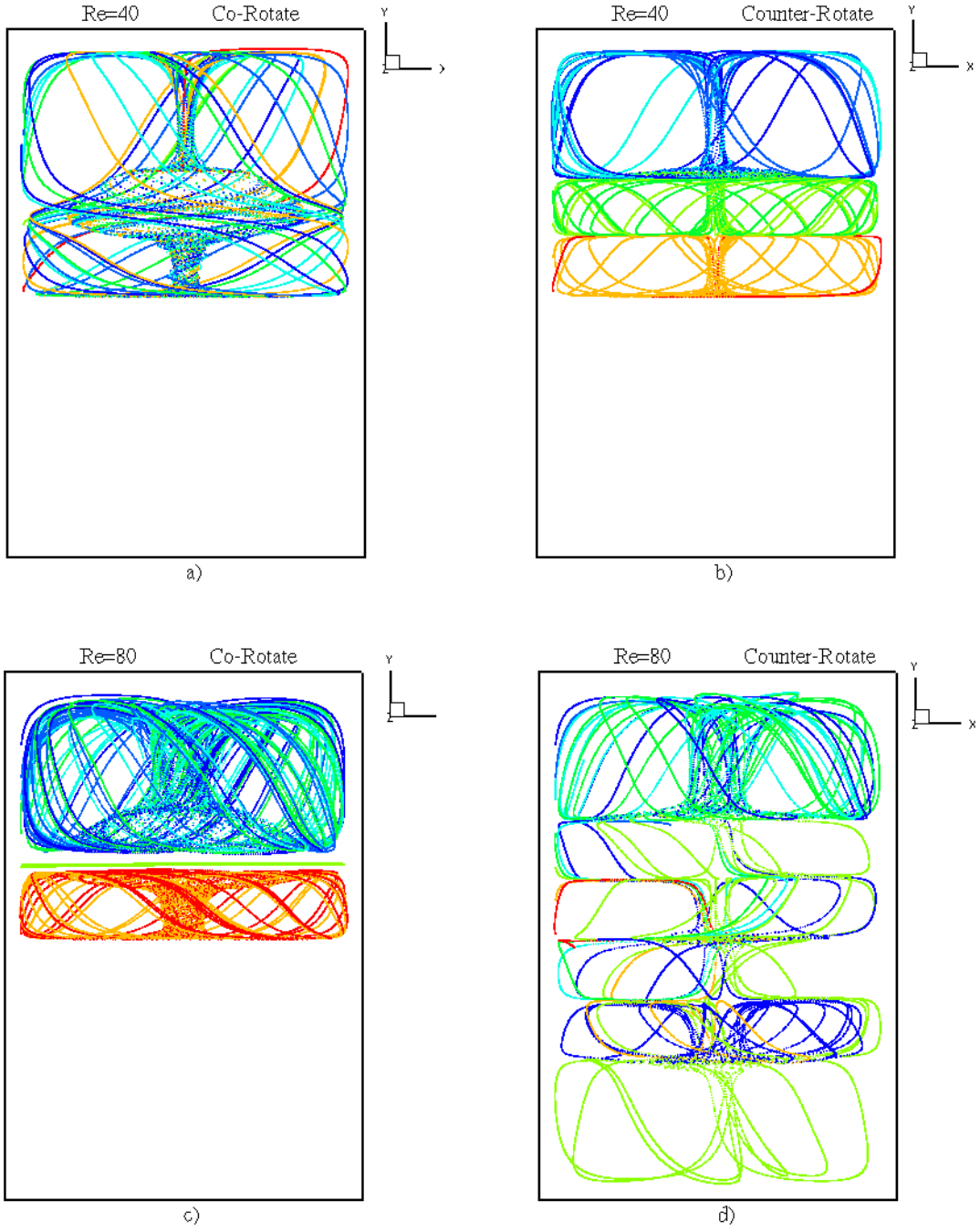

Figure 7.9 Three-dimensional particle paths originating along the toroidal outer edges for Re=40 and 80, co- and counter-rotating flows.

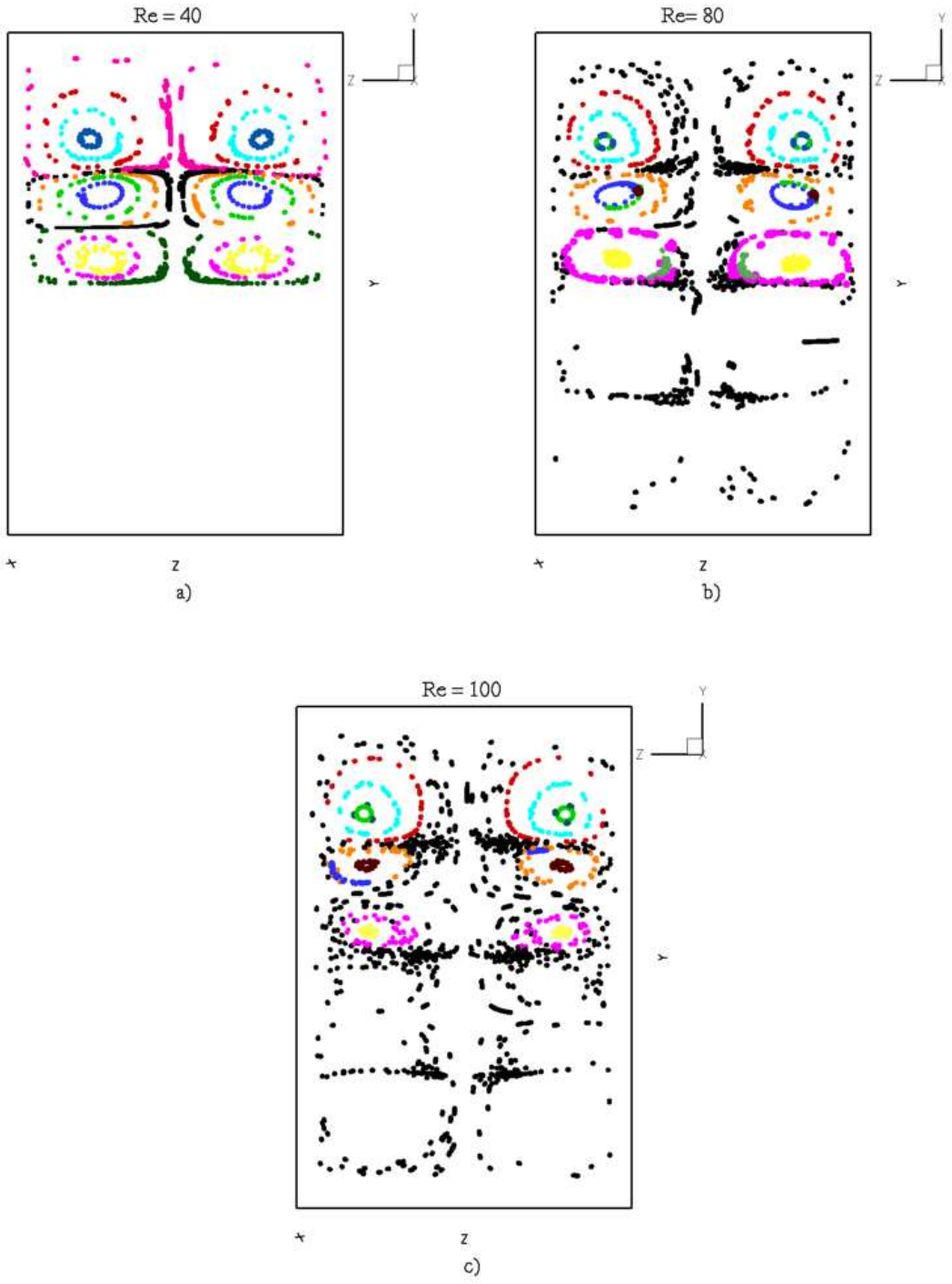

Figure 7.10 Poincarè maps for Re=40,80, and 100 counter-rotating disk flows.

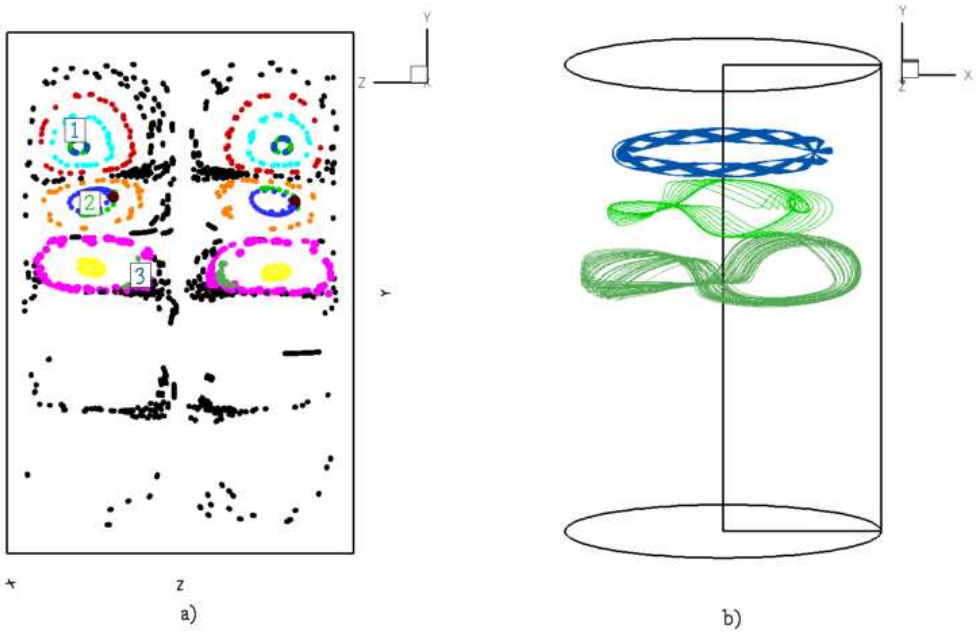

Figure 7.11 a) Re=80 Poincarè map with marked flow regions b) streamtraces originating in the marked flow regions, corresponding to the color indicated.

To underscore the effect of the shearing instability on the Lagrangian dynamics of the counter-rotating disk flow, we show in figure 7.10 Poincaré maps for the three Reynolds numbers. Particles are placed in several regions of the flow. Black markers are particles placed initially in the outer flow region and all other colors are particles placed in invariant flow areas. For the Re = 40 case the flow is axisymmetric and the Poincaré map consists, as one would expect, of invariant tori. Tracers remain trapped in the region of the container they originated and global stirring is not possible. As the Reynolds number increases to 80, it is evident that the invariant streamsurfaces begin to break and tracers wander chaotically throughout the container. Invariant regions (KAM-tori) and periodic islands occupy a large portion of the flow. By inspecting the Poincaré map for this case we can readily conclude that even though there are regions in the flow were

chaotic transport is possible a significant portion of the flow domain is still occupied by trajectories with integrable dynamics. However, it is clearly evident from figure 7.10c that as the Reynolds number increases the invariant areas shrink and the chaotic regions increase considerably. In addition, it is evident that some invariant regions have rather complex topology and are shown in figure 7.11 which displays particle paths for Re=80 case.

To demonstrate the increased mixing efficiency of the counter-rotating configuration, we show in figures 7.12. and 7.13 snapshots from the temporal evolution of a blob of particles in each configuration for Re = 80. For both cases a blob of 1000 particles is introduced near the outer wall of the container in between Disks 1 and 2 and their trajectories are integrated for 40 disk revolutions. For the co-rotating case the blob remains always in the region of the container it originated from and undergoes a rather slow stretching process. The particles retain their coherency even as they pass through the saddle focus on the upper side of Disk 2 (see *t = 5* and *15* in figure 7.12) for several times. It takes over 40 disk revolutions to begin to observe some significant stretching of the initial blob and even then no particle has escaped from the container region it originated. A striking different picture emerges for the counter-rotating case. The blob undergoes exponential stretching as it passes through the disk saddle focus and its length grows rapidly with each disk revolution. After approximately 10 disk rotations the initial blob has lost any coherency as it starts spreading rapidly throughout the entire container. It is important to emphasize that the final snapshot at t = 40 (see figure 7.13f) is a bit deceiving as at first glance it appears to suggest that global mixing has been achieved. Clearly this cannot be so, since as shown in the Poincaré map in figure 7.9 there are

several invariant regions that have survived the onset of the shear-layer instability for this case. The presence of invariant areas is also evident in figure 7.13f as regions that have remained devoid of particles even after 40 disk rotations. Comparing figures 7.12f with 7.13f, however, clearly shows the dramatic improvement in the stirring performance of the counter-rotating configuration. We find this comparison between the co- and counter-rotating cases extremely encouraging. A simple modification of the co-rotating stirred tank by counter-rotating the middle disk alters drastically the Lagrangian properties of the flow and creates a significant subset of the flow domain where chaotic stirring and, thus, efficient mixing is possible.

Finally to demonstrate that arbitrarily close initial conditions in chaotic regions of the flow separate exponentially in time for the counter-rotating, we show in figure 7.14 the time evolution of the separation of two particle trajectories that initially started at a distance $\Delta x = .0001d$ apart for the Re=80 case. Figure 7.14a shows the particle paths of two trajectories that initiated in the chaotic flow region and figure 7.14b shows initial positions placed in the invariant flow region. In figure 7.14c we plot σ versus time on a semi-log scale, where σ is the magnitude of the distance between the particles given by:

$$\sigma = \left| \mathbf{x}_1 - \mathbf{x}_2 \right| \qquad (7.1)$$

where $\mathbf{x_i}$ is the position vector for each particle. For particles initiated in chaotic regions, the particles separate erratically and exponentially as expected until they reach a point in which their separation is approximately the axial distance of the container. This is the maximum distance possible. Particle trajectories initiated in the invariant flow region separate initially quickly, and then slow to a gradual periodic rate of separation.

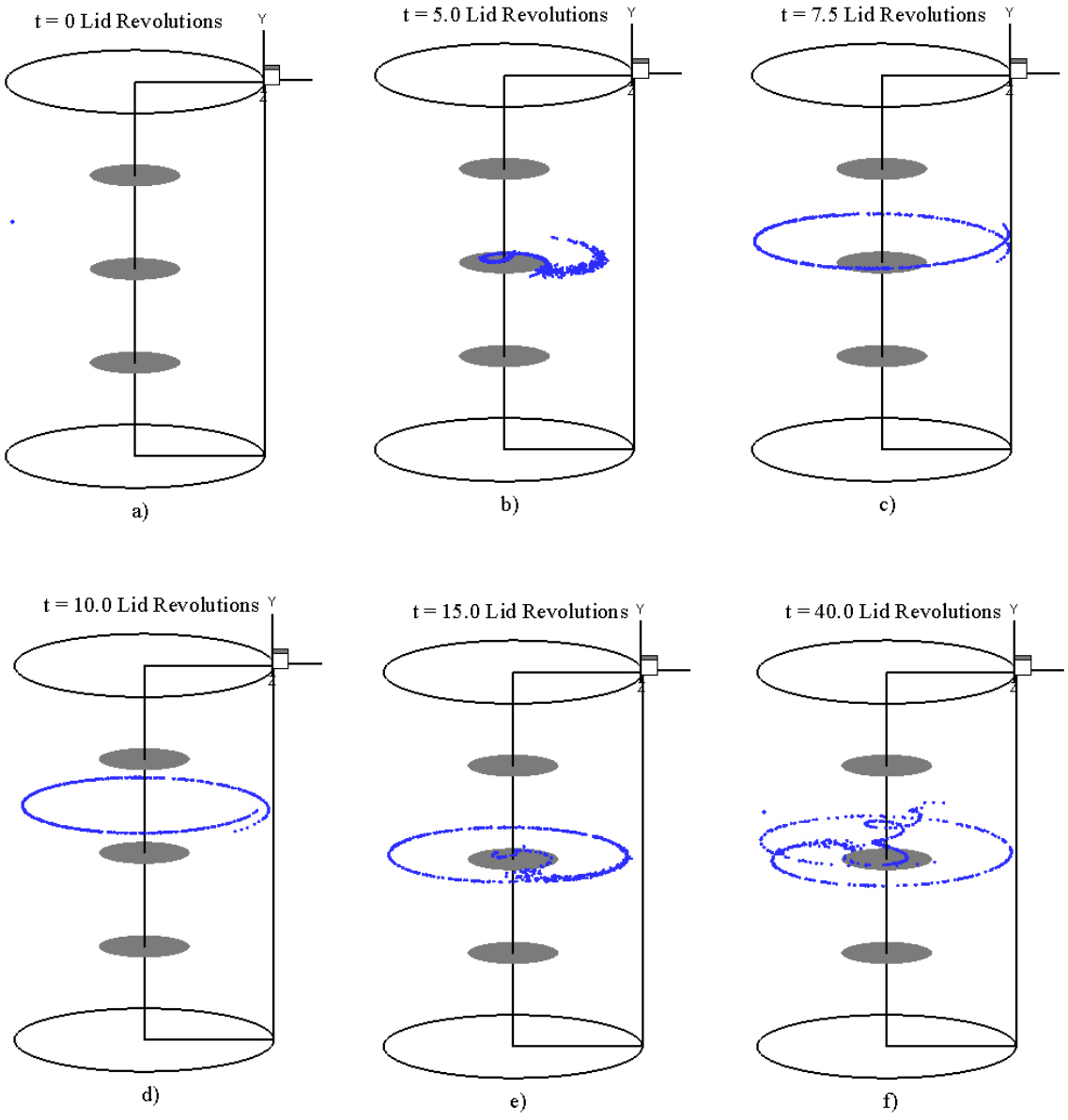

Figure 7.12 Snapshots of stirring of 1000 particle tracers placed in Re=80 co-rotating flow.

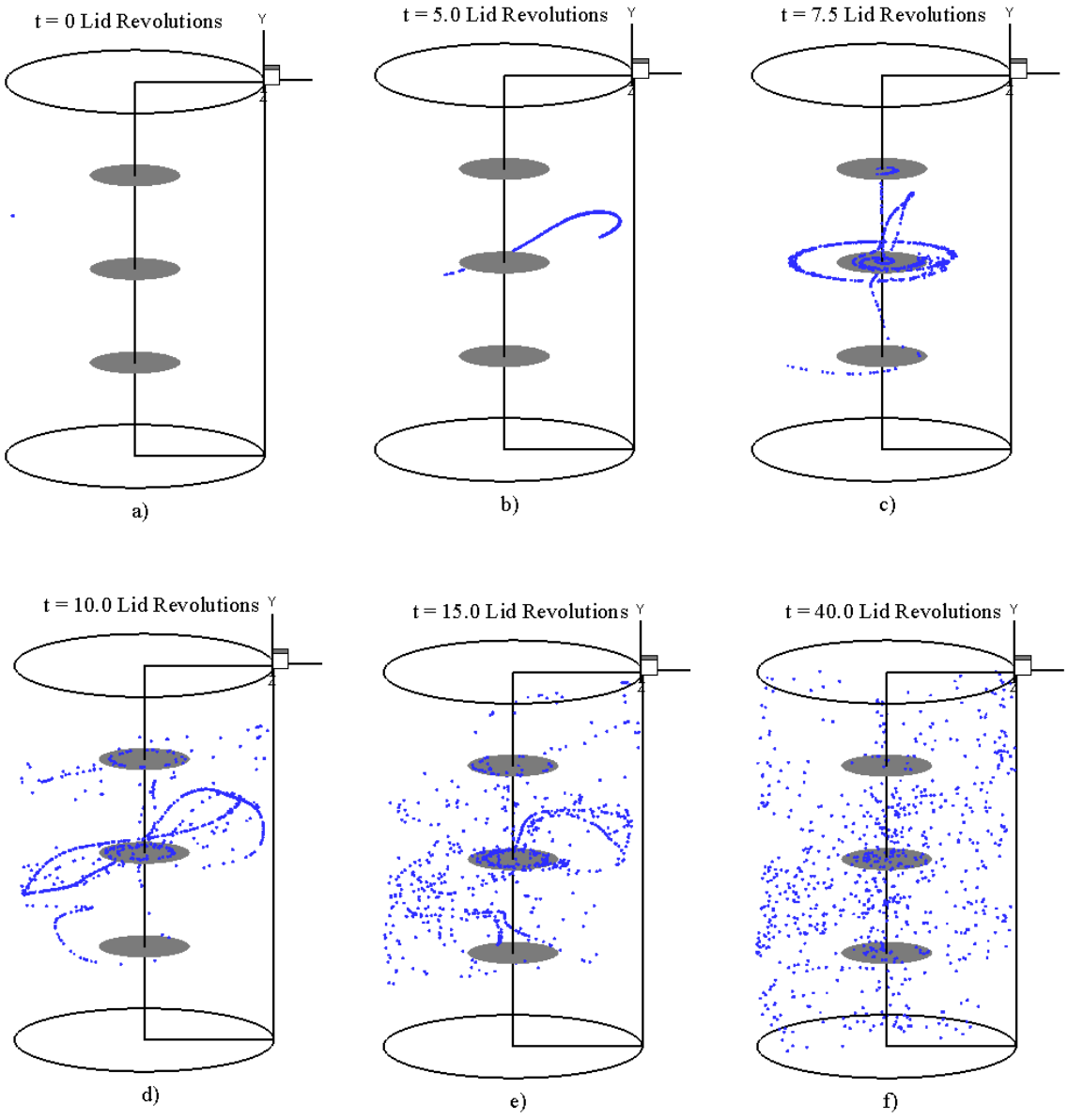

Figure 7.13 Snapshots of stirring of 1000 particle tracers placed in Re=80 counter-rotating flow.

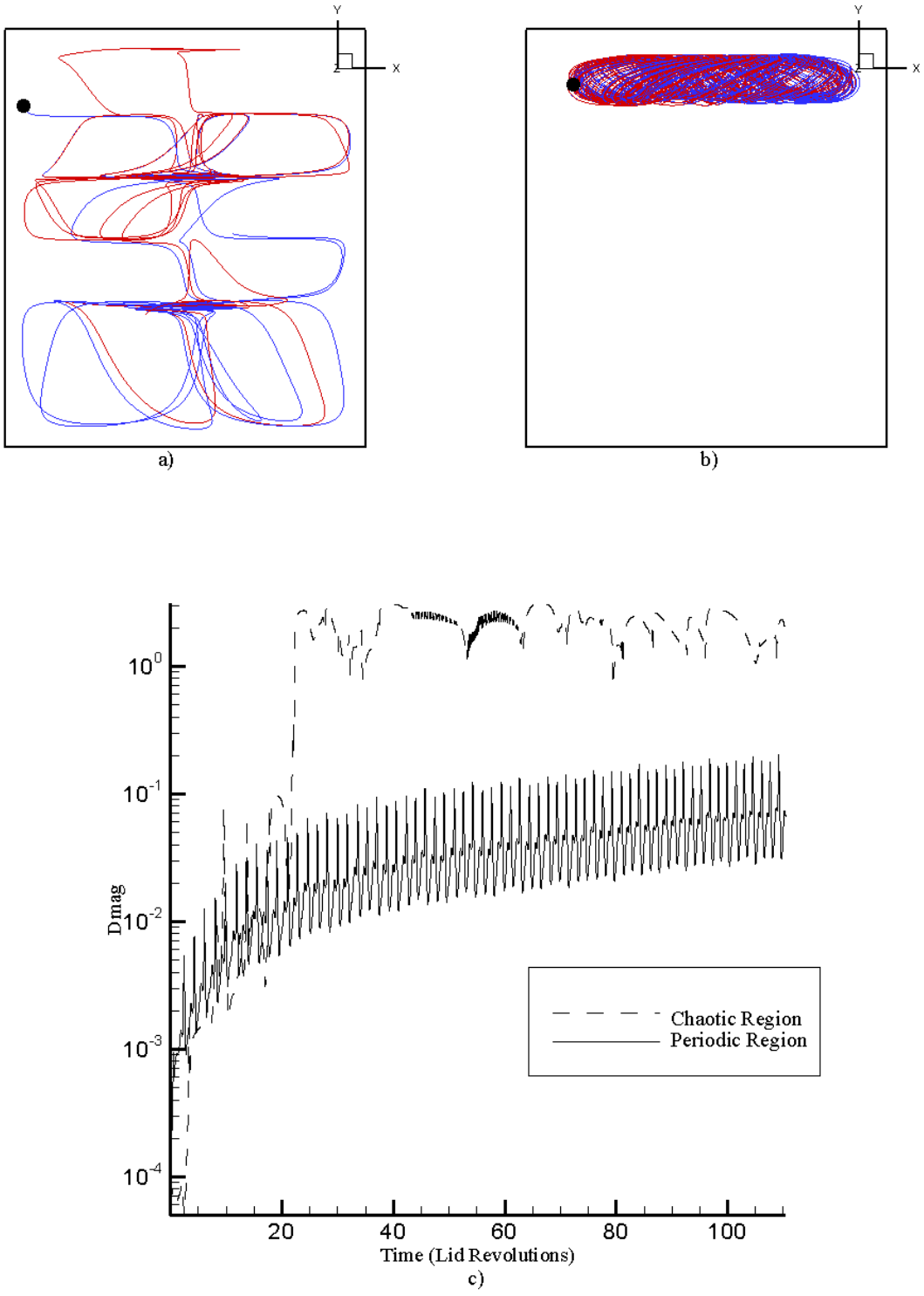

Figure 7.14 Re=80 counter-rotating flow; a) Particle paths of two trajectories initiated in chaotic flow region b) Particle paths of two trajectories initiated in invariant flow region. c) the magnitude of the distance between the trajectories.

7.5 Summary

In this chapter we provide a direct engineering application to the knowledge of innate flow instabilities due to counter-rotation discussed in the previous chapter. This is accomplished using a stirring tank with counter-rotating disks. Our findings show that by making a simple design change to the co-rotating stirred tank, by replacing the middle disk with a counter-rotating disk, it is possible to excite above a threshold Re the three-dimensional instabilities at the shear layers and create a three-dimensional flow with rich Lagrangian properties. The proposed stirred-tank design, however, promising as it may be requires significant further analysis to quantify its mixing performance with Reynolds number. Nevertheless we have shown for the first time in this work that counter rotation of the middle disk can create a flow with large chaotic regions without the need to resort to exotic impeller designs to break the symmetry and integrability of the flow. The results presented herein serve to demonstrate that fundamental studies of chaotic mixing are important as they can lead to valuable technological breakthroughs.

CHAPTER 7

STIRRED TANK FLOW WITH COUNTER-ROTATING DISKS

It has been estimated (Harnby et al. 1992, Alvarez et al. 2002) that the lack of fundamental knowledge of the physics of mixing in industrial systems, which naturally results in inefficient mixing devices, costs the industry in North America alone nearly ten billion dollars per year. In this chapter we seek to demonstrate that fundamental studies of mixing in simple model systems, such as that reported in the previous chapter, are not important only from an academic standpoint. The fundamental understanding gained from such studies can lead to specific improvements and design modifications of standard mixing devices, which can drastically enhance mixing performance. More specifically, we seek to demonstrate that the shear-layer instability between two counter-rotating disks can be exploited to modify and enhance the performance of a widely used industrial mixing device, that of a stirred tank.

Stirred tanks are employed to mix just about everything: from household items when preparing a cake, to pharmaceutical products, such as insulin and penicillin, to nuclear waste products during treatment. A stirred tank consists of a container filled with fluid and one or more agitators that take the form of rotating impellers or disks. The simplest example of such an agitator is the hand-mixer used to blend cake materials in the

kitchen. More sophisticated agitators are used in industrial mixers, which consist of multiple impellers of disks mounted along a rotating shaft. As the agitators rotate, they set up a three-dimensional flow, which could exhibit chaotic particle paths and lead to efficient mixing. Quite often baffles are also used in stirred tanks to enhance its mixing performance. These are obstacles that are positioned parallel to the agitator arm at the edge of the tank to enhance the three-dimensionality of the flow and promote chaotic stirring and mixing.

Although mixing in stirred tanks has been studied since the 1950's, starting with the early work of Rushton (Rushton et al 1950) on the so-called Rushton Turbine, many of these early studies were performed under the assumption that the flow could be thoroughly mixed only by increasing mechanical energy, i.e. direct agitation and turbulence. However in many industrial applications, such as in the pharmaceutical and food industries, it is necessary to achieve good mixing under laminar flow conditions. Examples range from the mixing of highly viscous fluids in the food processing industries (pastes, dough, yogurt, etc.) to low velocity mixing in bio-reactors where low levels of shearing stresses are required to avoid harming living cells. Under such conditions, efficient mixing can only be achieved via chaotic advection (Harvey et al 2000, Alvarez et al 2001, Zalc et al 2001, etc…).

A typical stirred tank configuration consists of an impeller shaft, located along the central axis of the container, with one or more co-rotating disks or impellers (see figure 7.1). When disks are used the flow remains axisymmetric and mixing efficiency is very poor. Figure 7.1 shows some experimental results of scalar mixing in a co-rotating disk stirred tank performed by Alvarez et al (2002). The top half of the container shows the

lack of mixing either between or within the nested tori by the unmixed different colored dye streaks that were injected with needles into the container. The bottom half of the figure shows a slice through the tank axis, displaying the perfectly axisymmetric invariant tori. Many attempts to break the symmetry of this configuration and thereby promote chaotic mixing have been reported in the literature. These efforts have included among others attempts to displace the shaft away from the axis and/or add additional shafts with disks (Ascanio et al 2002). A different approach for breaking the symmetry is to replace the disk with bladed impellers (Recknagle and Shekarriz 1998, Zalc et al 1999, Alvarez et al 2002a & 2002b, Zalc et al 2002,etc…). While these approaches have succeeded in inducing chaotic mixing, they require more complex machinery and are thus more susceptible to wear.

In this work we look specifically at the flow geometry within a cylindrical container with three rotating disks. The co-rotating disk version of this flow has been studied both numerically and experimentally by Zalc et al (2001, 2002) who utilized this as a base flow for their investigation of mixing using three Rushton turbines. The resulting flows in this device are steady and axisymmetric and, thus, mixing is very slow as it can only be affected by molecular diffusion. In this chapter we apply the concepts of innate flow instabilities developed due to counter rotation of the disks. We seek to show that by simply reversing the rotation of the central disk, the Lagrangian properties of the flow are drastically altered—due to the effect of the shearing instabilities discussed in detail in the last chapter—and mixing is dramatically enhanced.

This chapter will proceed as follows. First we review previous research on mixing in stirring tanks. Subsequently we describe the geometry of the co-rotating and

counter-rotating stirred tank configurations and the various computational details of our simulations. This is followed by the discussion of the computed results for the co-rotating and counter-rotating cases from the Eulerian standpoint. Finally we analyze and compare the Lagrangian characteristics of the various flowfields.

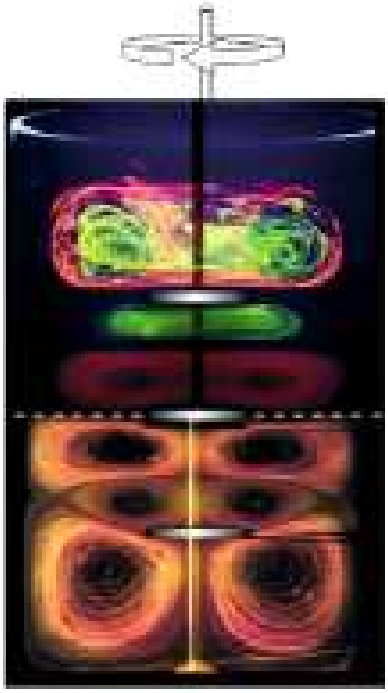

Figure 7.1 Experimental results of scalar mixing in a stirred tank with three co-rotating disks. Top) Unmixed different colored dye streaks injected with needles. Bottom) Slice through tank axis, displaying invariant tori. (Alvarez 2002).

7.1 Previous Research

The stirred tank mixer is perhaps the most commonly used industrial mixer. Early experiments on this device focused primarily on performance and mixing times (O'Connell and Mack 1950, Rushton et al 1950a, 1950b) and were performed under the assumption that mixing performance is proportional to the mechanical energy of the impeller. For the most part, these works were oriented towards creating power curves for different impeller configurations under various operating conditions and did not delve deeply into the dynamics of the flow and the physical mechanisms, which enhanced mixing. In subsequent years various methods for quantifying mixing in stirred tanks were developed. Norwood and Metzer (1960) carried out a series of neutralization experiments to visually determine mixing times. Other methods for measuring mixing times were based on the variance of pH or using conductivity equipment (Sano and Usui 1985).

In recent years the advancement of non-intrusive experimental techniques, such as PIV and LIF, has allowed for the first time detailed and simultaneous measurements of velocity profiles and scalar concentration in mixing devices. Furthermore, the ability to generate numerical solutions to the complex flowfields using CFD has provided an additional method for determining the Lagrangian and Eulerian aspects of such flows. Ranada (1997) computed laminar flowfields in a baffled stirred tank with a single Rushton turbine. However in this work, they do not solve the full time-dependent flow equations. Instead they compute a quasi-steady flowfield for any momentary impeller position by taking an instantaneous "snapshot" of the time-dependent three-dimensional

flow. The resulting averaged velocity fields were compared with experimental data and found in general to have good agreement. However this type of investigation would be insufficient for in-depth mixing studies. Bakker et al (1996) computed the laminar flow field in a stirred tank with a single pitched blade turbine. In this study also, the results they obtained using CFD agreed in general with experimental results, but these first CFD studies were not centered on understanding mixing mechanisms.

Much of the research in mixing in stirred tanks over the years involved turbulent flows (Norwood and Metzner 1960, Bakker et al 2000, Compolo et al 2003) where the focus is primarily on the method of capturing the various scales of flow structures. As the importance of such devices for mixing in the laminar regime has become evident, however, many studies in the last decade have considered low Reynolds number flows (i.e. Re<500) and employed the theory of chaotic advection to understand and enhance mixing rates. Lamberto et al (1996) proposed to enhance mixer performance by introducing periodic fluctuations to their agitation, thus, making their flow time dependent. They studied both baffled and un-baffled systems and concluded that the size and location of unmixed areas in the flow are dependent on the Reynolds number. This work was continued (Lamberto et al 1999, 2000) in their experimental and numerical investigation of this one impeller system. However, using their numerical technique, they only calculated one-sixth of the flow geometry due to the inherent symmetry of the tank. They characterized mixing in the flow using Poincare maps and by developing stretching distributions and were able to visualize the two ring unmixed structures that appear above and below the blades. Tanguy et al (1997) proposed to enhance mixing using a combination of Rushton impeller and helical ribbon turbine mounted on the same shaft.

They found that by rotating these two different impeller types at different speeds, they were able to out perform either one of the impellers alone. A ribbon impeller was also studied by de la Villeon et al (1998) who performed a numerical investigation of that geometry and calculated stretching lengths and Lyapunov exponents. This type of study was continued by Harvey III et al 1997 who used four different impellers of varying sizes on the same shaft, obtaining velocity profiles and streamline plots to characterize mixing. Recknagle and Shekarrize (1998) investigated the effect of the pitch blade impeller system. They showed that laminar mixing correlates with rotational speed for both Newtonian and Non-Newtonian fluids. Additional unconventional configurations were adopted by Ascanio et al (2002) who studied varying combinations of Rushton impellers and hydrofoil impellers. In addition they also considered time dependent perturbations to the flow and off-center placement of the impeller shaft. They found that creating dynamic perturbations was sufficient to enhance mixing in small size tanks. For larger mixing tanks, however, it would be extremely challenging to implement unsteady forcing as that would require the installation of a variable direction control for the motor and also perhaps magnetic breaks.

Harvey III et al (2000) performed a milestone experiment when they began to rigorously look at flow visualization of the unmixed regions of the flow in a stirring tank with multiple impellers. Using CFD, they also constructed Poincaré maps to visualize the unmixed regions of the flow. This work was the first to simulate numerically the full laminar flow fields in an unbaffled stirring tank with multiple impellers and paved the way for a series of other experiments—Zalc et al 2001, Shrinbrot et al 2001, Alvarez et al 2002a, Alvarez et al 2002b, Zalc et al 2002. In these works, the investigators report on

the use of Rushton impellers to improve mixing in stirred tanks. They show a series of results in which they describe the mixing that occurs in the base flow (flow with co-rotating disks) becoming greatly improved as small perturbations to the integrable flow are introduced which lead to the emergence of 3D horseshoes. Poincaré maps as well as stretching maps are computed numerically and compared to experimental visualization techniques that are used to differentiate between the mixed and unmixed regions of the flow.

In all the previously discussed stirred tank configurations, co-rotating disks/impellers have been used. The primary emphasis of these studies has been on approaches for perturbing the base axisymmetric flow and inducing chaotic advection either by breaking the symmetry of the flow (using impellers and various unconventional configurations) or by introducing time dependent perturbations. In this work, we instead, consider the effect of counter-rotation of the disks to exploit innate flow instabilities in the system and instigate chaotic mixing.

7.2 Flow Geometry and Computational Details

We study flow in a closed cylindrical container of diameter D and height H driven by three, co-axial rotating disks of diameter d. The centers of all disks are located on the container centerline as shown in the schematic of figure 7.2. We consider two cases: 1) co-rotating disks, where all three disks rotate in the same direction with constant angular velocity Ω; and 2) counter-rotating disks, where all three disks rotate with constant angular velocity Ω but the middle disk rotates in the opposite direction from the top and

bottom disks. For both cases the diameter of the container is three times the size of the disks ($D = 3\times d$). The container aspect ratio ($AR = R/H$, where R=D/2) is set equal to 1/3 and the three disks are spaced .25H apart. This specific configuration is selected because it is identical to the co-rotating case studied extensively by Zalc et al. (2002), whose work will serve to validate our computations for the co-rotating case. The Reynolds number for both cases is based on the disk diameter and is defined as follows:

$$Re = \frac{\rho N d^2}{\mu} \qquad 7.1$$

where N is the disk speed expressed in rotations per sec (RPS), ρ is the density, and μ is the fluid viscosity.

For all cases the flow fields are generated by solving numerically the three-dimensional Navier-Stokes equations using the numerical method described in Appendix A. A polar/cylindrical grid with approximately 1.4 million nodes is used for all computations—61×161×141 nodes in the radial, axial, and circumferential directions, respectively (Figure 7.3). The grid is stretched, using the hyperbolic tangent function to cluster nodes at the three rotating disks and the stationary container lids. For all cases the disks are assumed to have zero thickness. Solutions for both co- and counter- rotation are calculated for *Re = 40* and *80*. For the counter-rotating case a solution at *Re = 100* has also been obtained.

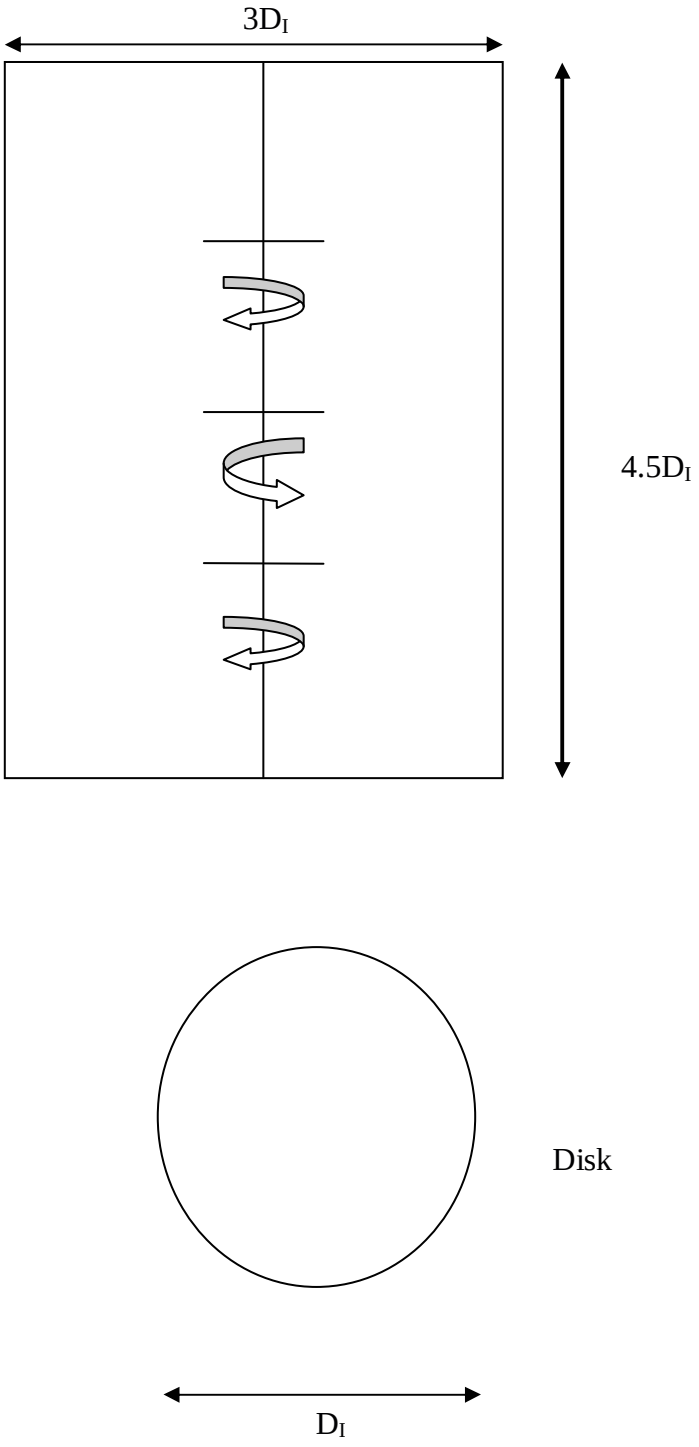

Figure 7.2 Schematic of counter-rotating disk system.

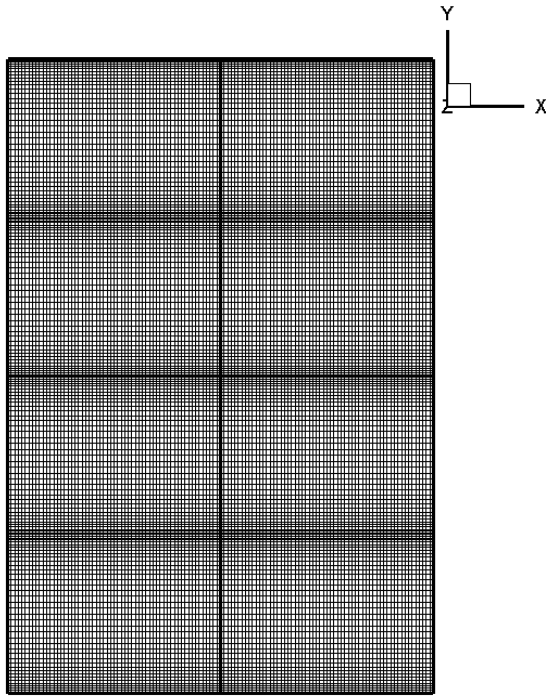

a)

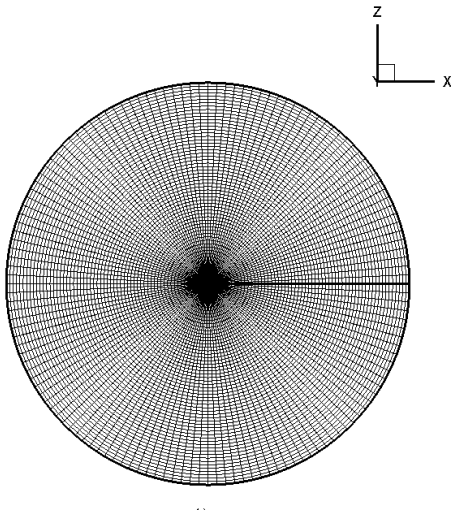

b)

Figure 7.3 Computational grid for flow with co- and counter-rotating disks.

7.3 Eulerian Flow Characteristics

In this section we investigate the Eulerian aspects of the co-rotating and counter-rotating flowfields in order to illustrate that the same shear-layer instability that was discussed in the previous chapter does occur for the latter case. We compare numerical solutions for the two configurations at Re = 40 and 80 and we also show results for the counter-rotating case for Re = 100. For the co-rotating case the flow is steady and axisymmetric for Re = 40 and 80. For the counter-rotating case, axisymmetric flow is obtained for Re = 40 but steady three-dimensional flows emerge at the two higher Reynolds numbers.

To aid the discussion of the flow, the following conventions are developed to refer to different flow regions. The upper most disk in the stirred tank is Disk 1. The middle disk is Disk 2 and the bottom disk is Disk 3. The equatorial plane between disks 1 and 2 is called Shear Layer 1 (SL1) and the equatorial plane between disks 2 and 3 is called Shear Layer 2 (SL2).

As the disks rotate, Ekman suction and pumping drives meridional recirculating regions in the flow. Fluid particles spiral outward in the vertical plane of the disks, are forced along the side walls of the container and then pushed back inwards towards the central axis of the container where the finally close the trajectories by moving up or down the axis back towards their origin. This creates a series of toroidal stream-surfaces in the co-rotating case and in the axisymmetric regime of the counter rotating case. In figure 7.4, the structure of these toroidal vortices for both systems are shown by plotting two-dimensional streamlines at a diametral plane for *Re = 40*.

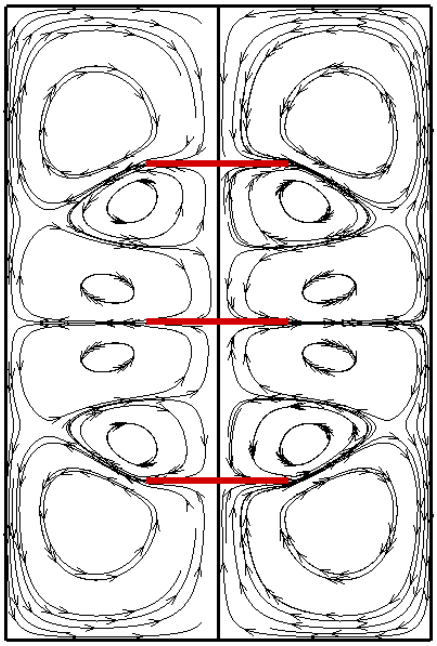

Co-rotating

a)

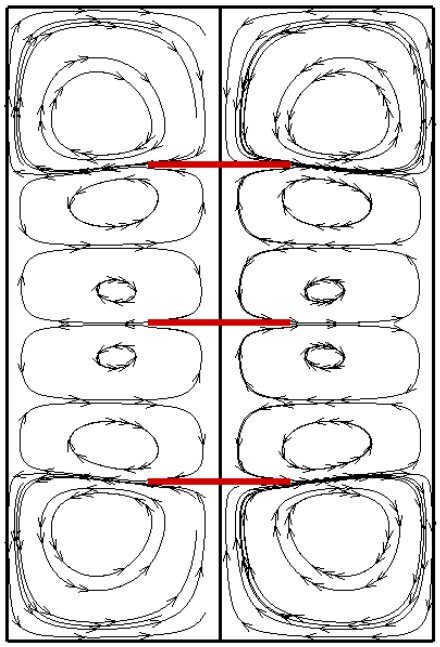

Counter-rotating

b)

Figure 7.4 Structure of toroidal surfaces for a) co-rotating and b) counter-rotating disk systems.

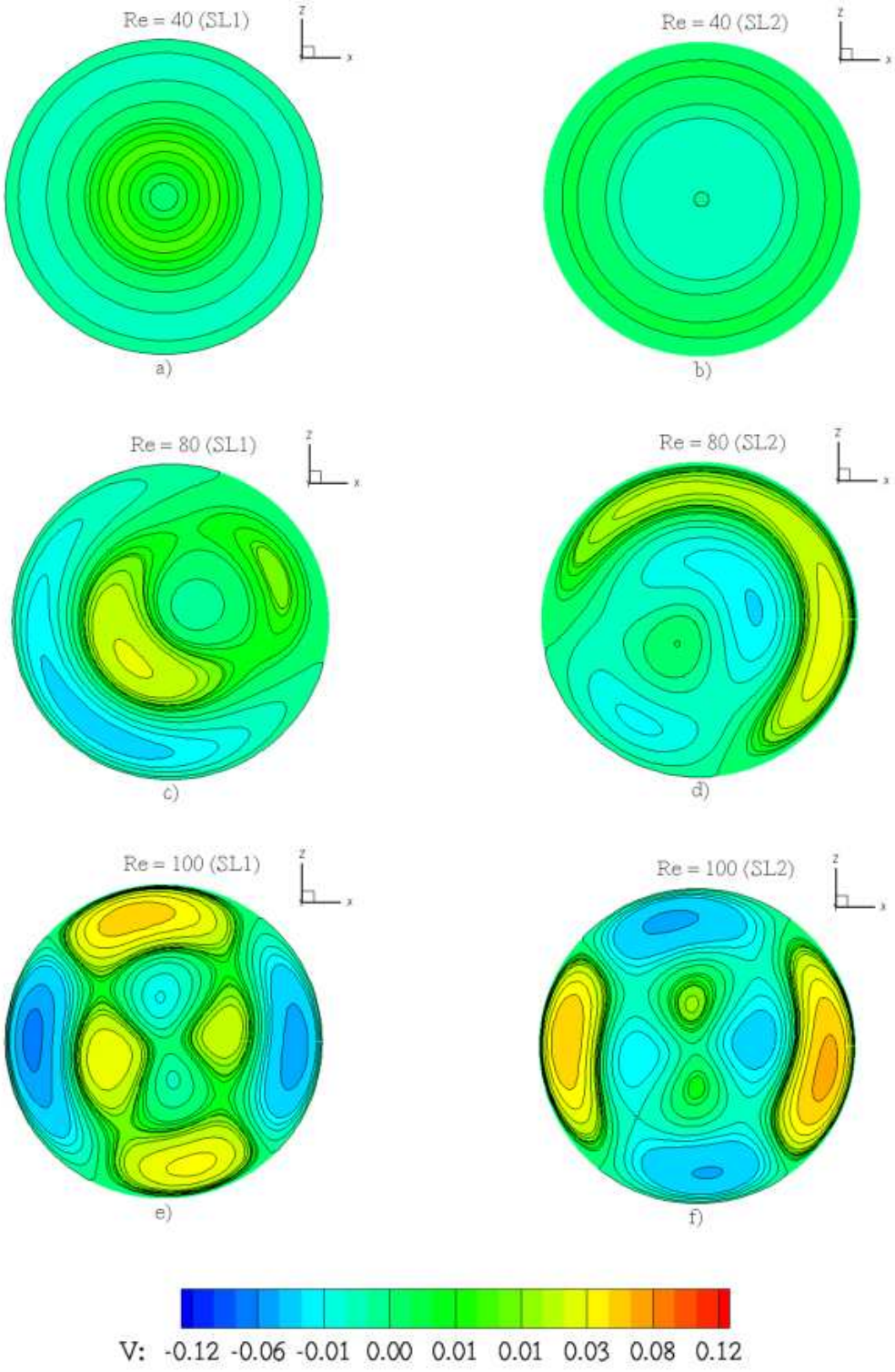

Figure 7.5 Vertical velocity contours at the shear layer planes for Re=40, 80, and 100 counter-rotating flows.

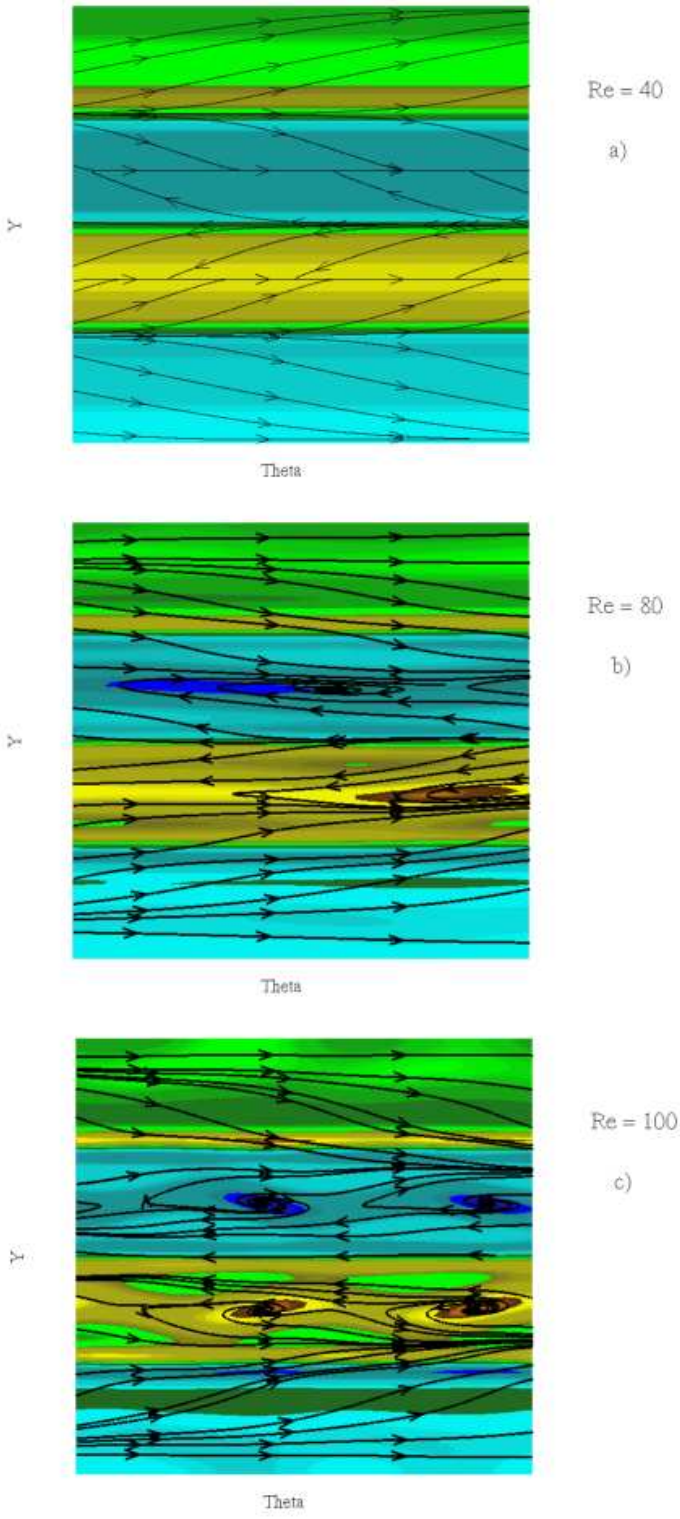

Figure 7.6 Surface streamlines and radial vorticity contours of unfolded radial plane.

The vertical velocity contours in figure 7.5 compare the flow at planes SL1 and SL2 for Re = 40, 80, and 100 for the counter rotating flow—as mentioned before the numerically simulated flowfields for the co-rotating case remain perfectly axisymmetry and are not shown here. Similar to the flow described in the previous chapter (container with exactly counter rotating lids), regions of alternating positive and negative vertical velocity appear at the mid-planes between the disks for Re = 80 and 100, marking the onset of the shear-layer instability. There are, however, some notable differences. Firstly, the figure shows the m = 1 and m=2 modes emerging for Re = 80 and 100, respectively, as opposed to the m = 3 mode that appeared in the simulations reported in the previous chapter. This discrepancy should not come as a surprise, however, as the stability work of Nore et al. (2004) clearly showed that the most critical azimuthal mode is a strong function of aspect ratio. In addition to differences in aspect ratio between the stirred tank configuration and the container flow, the fact that the disks do not extend all the way to the wall in the former case should also be expected to have a significant effect on the dynamics and stability characteristics of the flow.

Another important feature in the flowfields shown in Figure 7.5 is the fact that the mirror-image symmetry of the flow along the vertical direction also appears to break. For the Re=40 case (figure 7.5a), where the flow is axisymmetric, the vertical velocity contours at the SL1 and SL2 planes are essentially zero but even the very small contour levels retain the mirror-image symmetry that would be expected from the symmetry of the configuration. For the two higher *Re*, however, this mirror-image symmetry breaks as can be seen by comparing the contours at the SL1 and SL2 planes. The break of mirror-image symmetry in the streamwise direction should also be attributed to the presence of

the large gaps between the disks and the container wall ($d < D$) and should be expected to enhance transport in the entire container.

We argue that the symmetry break in the vertical direction is the result of a secondary instability, which is excited by the primary instability for this configuration: the formation of radial, cat's-eye vortices at SL1 and SL2. This is shown in figure 7.6, which depicts streamlines and radial vorticity contours on an unfolded plane of constant radius (similar format as that of figure 6.x in the previous chapter). For Re = 40 the flow is axisymmetric and SL1 and SL2 are marked by perfectly straight lines of convergence. The emergence of the m = 1 and m = 2 modes for the Re = 80 and 100 cases, respectively, is illustrated clearly in these figures by the appearance of radial vortices centered on each shear layer.

In figure 7.7 we show an iso-surface of vorticity magnitude for all three *Re* to further highlight the three-dimensional feature of the flow. For Re = 40, the flow is axisymmetric and a notable feature of the flow are the two small vorticity pockets centered around each saddle point at SL1 and SL2 planes, respectively. Near the container wall there are annular bands of vorticity, which mark areas where the fluid is pushed radially inward toward the centerline. For the Re=80 case shown in figure 7.7b, the bands along the outer wall of the container shrink in size and become azimuthally wavy and distorted as the m = 1 mode emerges. The distortion and three-dimensionality of the vorticity contours is even more pronounced for the Re = 100 case. It is worth noting in this case the increase in size and distortion of the pockets of vorticity around the two saddles at Sl1 and SL2. The patterns developing in these regions suggest the growth

of vertically inclined structures similar to those observed in the container case in the previous chapter.

Figure 7.8 show a positive and a negative iso-surface of normalized helicity (see eqn 6.1) for all three Reynolds numbers. Once again the effect of the shear layer instabilities become visible as the shape of the iso-surfaces evolves from the simple disk-like shapes in the Re=40 case to the topologically rich, three-dimensional structures seen in figures 7.8b and c. A pair of vortical structures resides along the axial plane on either side of each shearing plane. The shear layers are tilted upwards and downwards at the edges. These features are similar to those observed in similar plots for the container with counter-rotating lids.

7.4 Lagrangian Dynamics

In this section we analyze the Lagrangian characteristics of the co- and counter-rotating cases to show that the three-dimensional instabilities in the latter configuration can indeed lead to chaotic stirring and efficient mixing. We first discuss three-dimensional particle paths in the two systems to underscore the significant differences in dynamics. Subsequently, we illustrate the ability of the counter-rotating configuration to induce transport across the entire container. We also illustrate the increase in the richness of dynamics with Reynolds number for the counter-rotating configuration by comparing Poincaré maps for Re =40, 80 and 100.

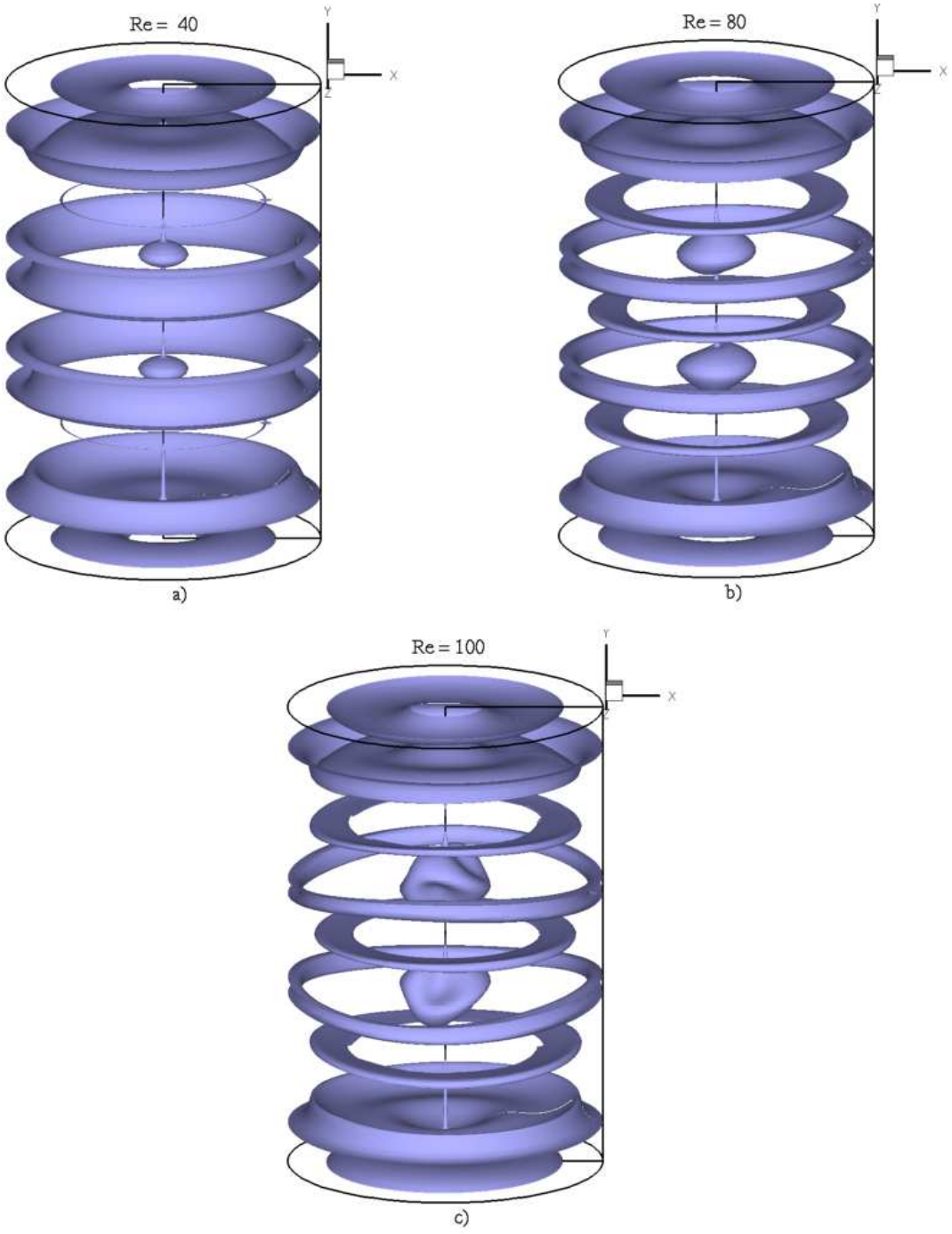

Figure 7.7 Iso-surface of vorticity magnitude for Re = 40, 80, and 100 counter-rotating disk flows.

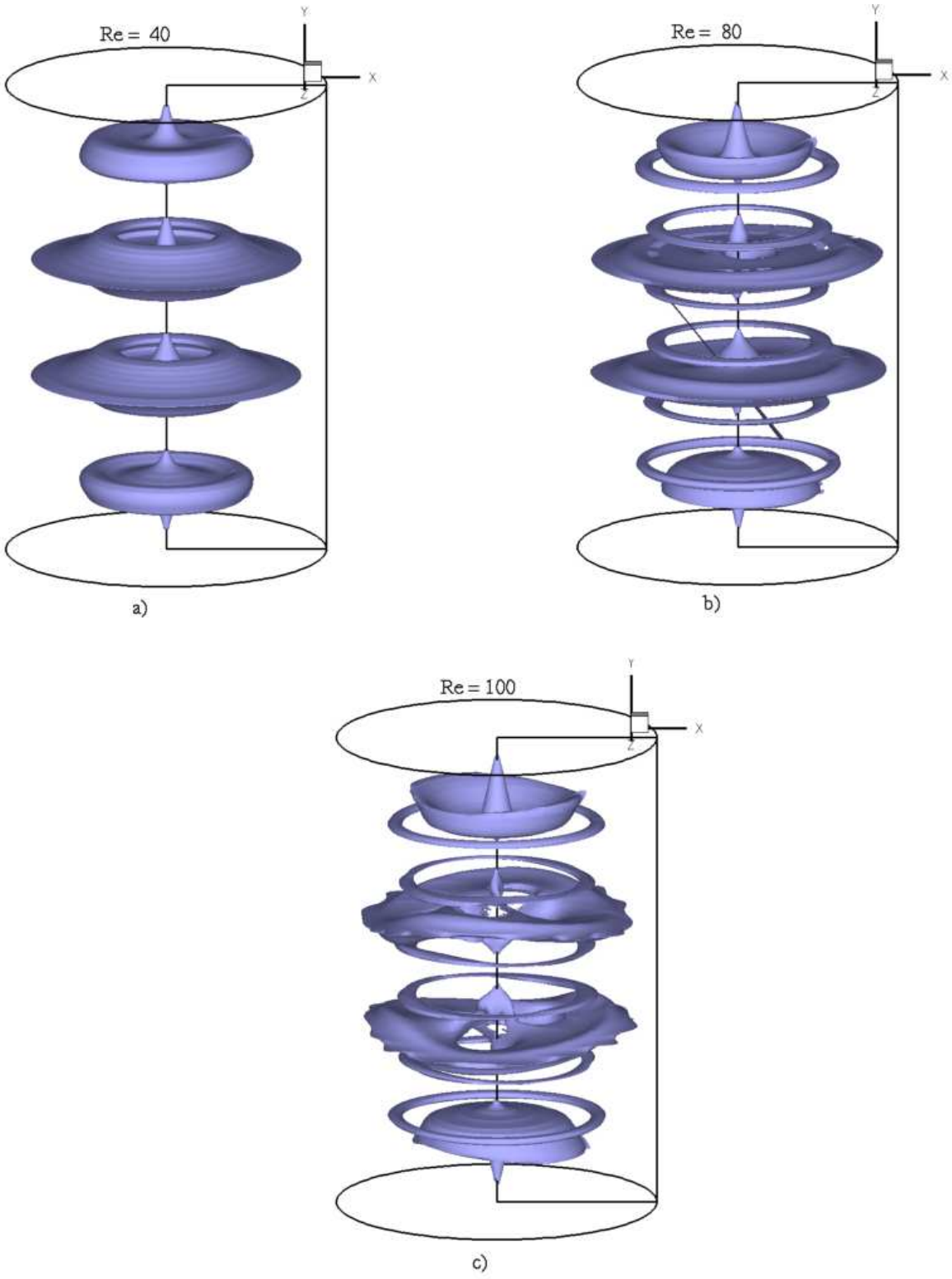

Figure 7.8 Iso-surface of normalized helicity for Re = 40, 80, and 100 counter-rotating disk flows.

The base axisymmetric flow for both the co- and counter-rotating tanks, as described in the previous sections, consists of toroidal stream-surfaces. It has been shown in previous investigations of the co-rotating case (Zalc et al 2001, Zalc et al 2002) that as perturbations are introduced into the flow the outer tori begin to break. This is also consistent with our findings from the previous chapter. In figure 7.9, we plot a series of three-dimensional particle paths that originate along the outer edges of the toroidal structures in the upper portion of the container. For the co-rotating case the flow remains axisymmetric for both Re = 40 and 80. Consequently, for both Reynolds numbers the particles follow trajectories that remain confined on their respective invariant streamsurfaces in the upper half of the flow domain. For the counter-rotating flows, the dynamics are simple and integrable for the Re=40 case with the particles remaining trapped on toroidal streamsurfaces. However, as the Reynolds number is increased to Re=80 and the flow becomes three dimensional, the invariant regions begin to break and the particles escape and start exploring the entire container region. The ability of particles to move throughout the container can be easily understood in terms of the vertical velocity contours at SL1 and SL2 planes shown earlier in figure 7.5. Recall, that for the counter-rotating case the onset of the shear layer instability is accompanied by the growth of non-zero vertical velocity field at the disk mid-planes. As discussed above, this feature allows for transport across the entire container and as shown in figure 7.9 such transport does indeed take place for the counter-rotating case.

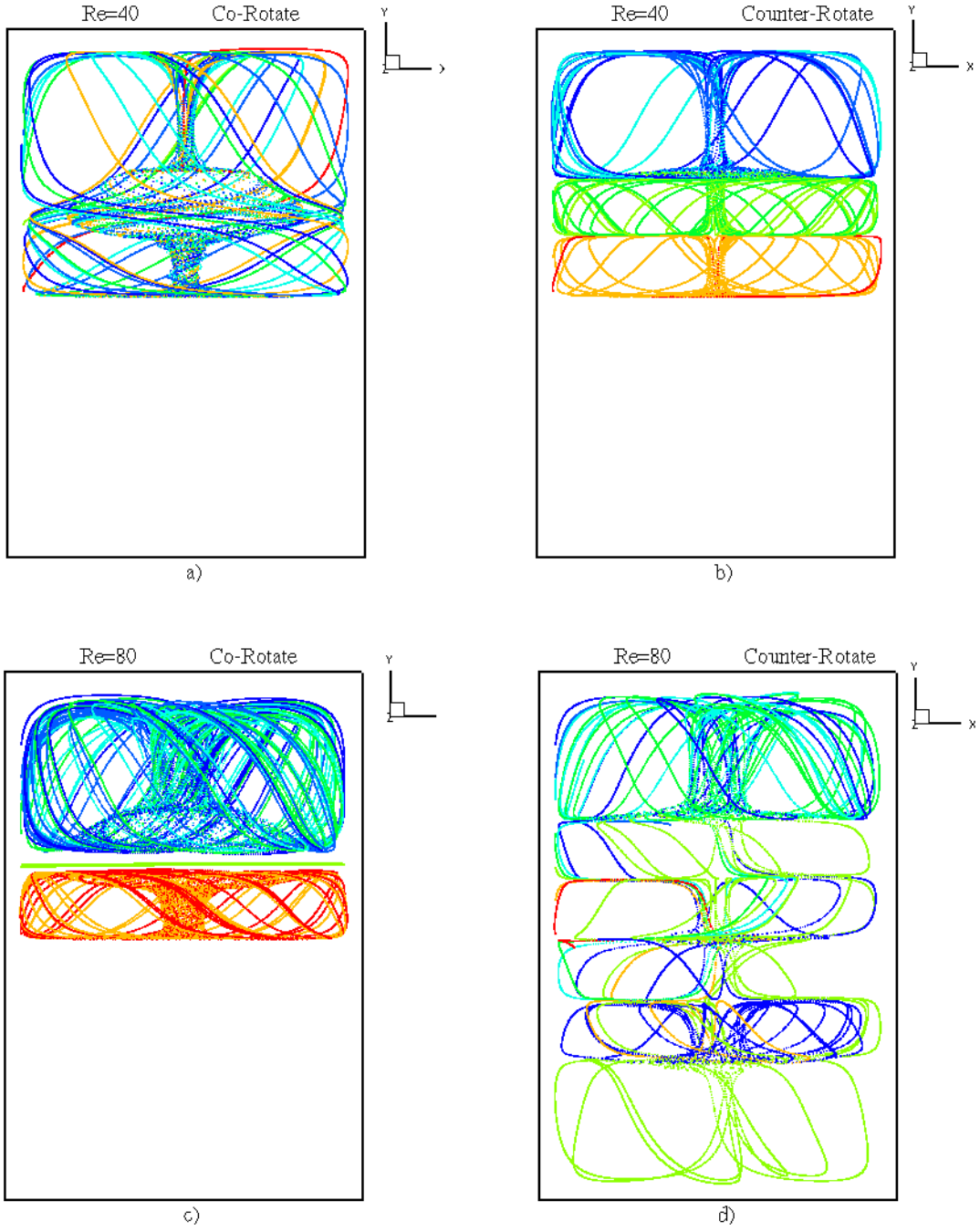

Figure 7.9 Three-dimensional particle paths originating along the toroidal outer edges for Re=40 and 80, co- and counter-rotating flows.

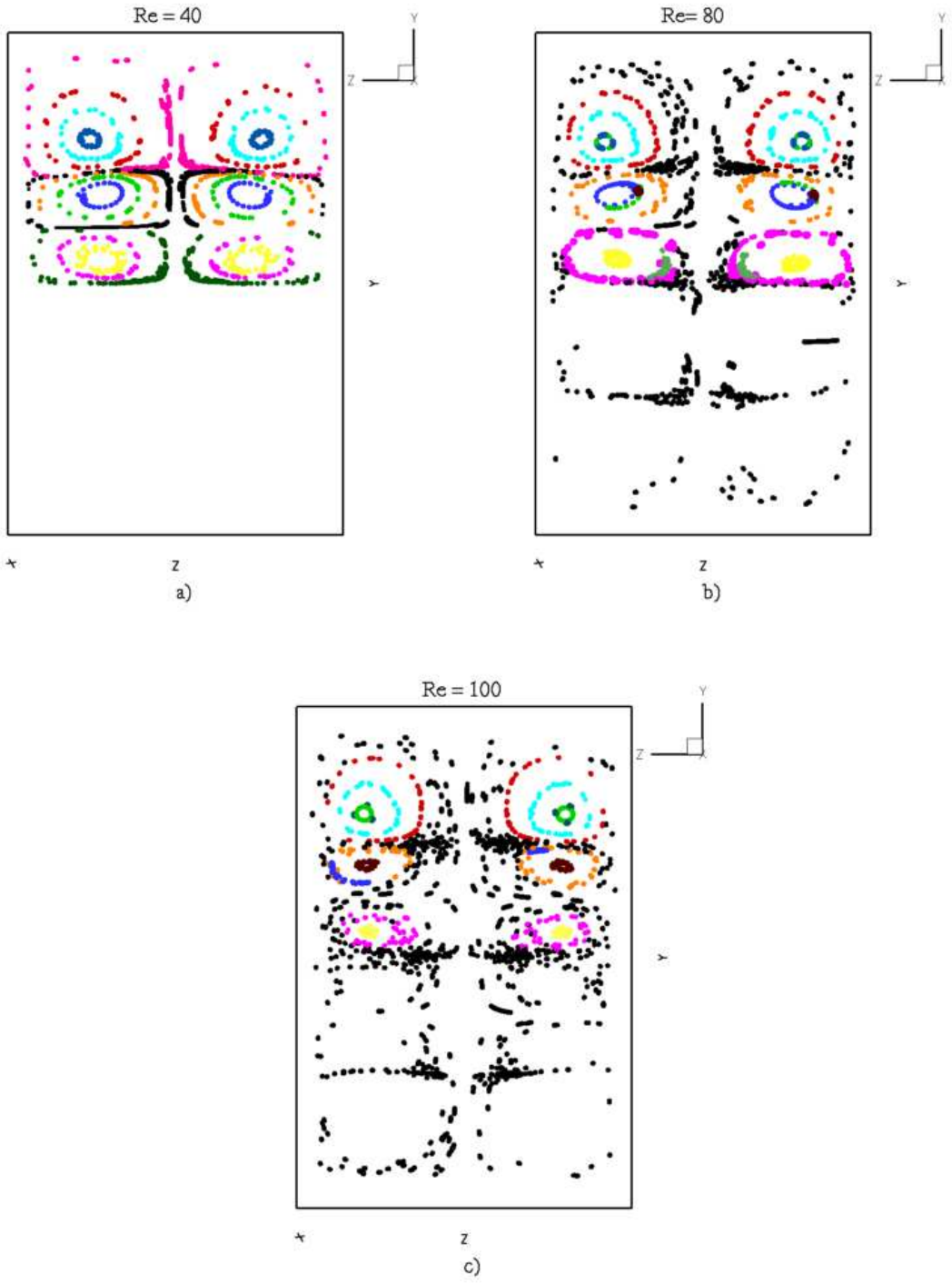

Figure 7.10 Poincarè maps for Re=40,80, and 100 counter-rotating disk flows.

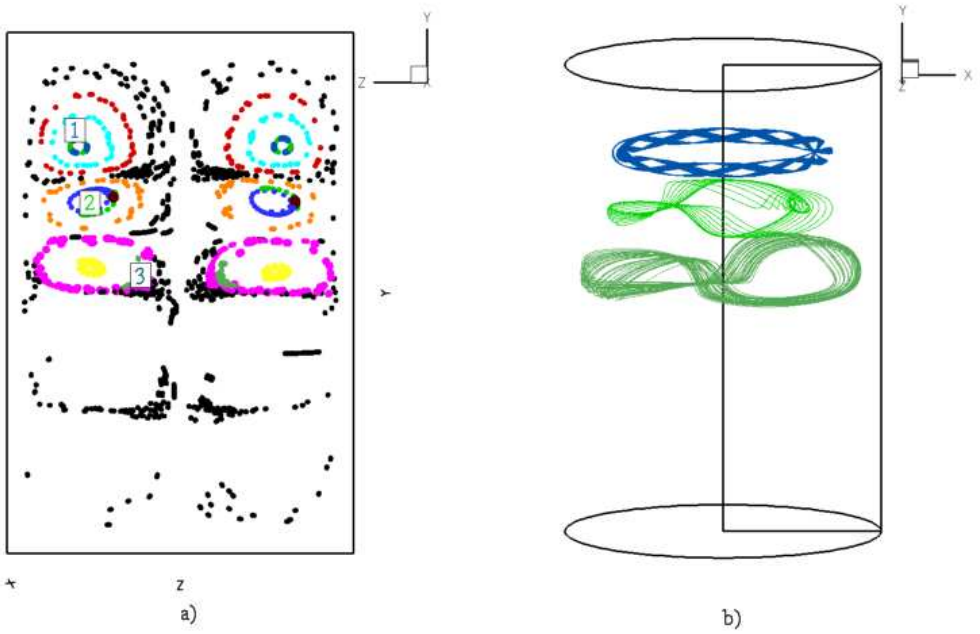

Figure 7.11 a) Re=80 Poincarè map with marked flow regions b) streamtraces originating in the marked flow regions, corresponding to the color indicated.

To underscore the effect of the shearing instability on the Lagrangian dynamics of the counter-rotating disk flow, we show in figure 7.10 Poincaré maps for the three Reynolds numbers. Particles are placed in several regions of the flow. Black markers are particles placed initially in the outer flow region and all other colors are particles placed in invariant flow areas. For the Re = 40 case the flow is axisymmetric and the Poincaré map consists, as one would expect, of invariant tori. Tracers remain trapped in the region of the container they originated and global stirring is not possible. As the Reynolds number increases to 80, it is evident that the invariant streamsurfaces begin to break and tracers wander chaotically throughout the container. Invariant regions (KAM-tori) and periodic islands occupy a large portion of the flow. By inspecting the Poincaré map for this case we can readily conclude that even though there are regions in the flow were

chaotic transport is possible a significant portion of the flow domain is still occupied by trajectories with integrable dynamics. However, it is clearly evident from figure 7.10c that as the Reynolds number increases the invariant areas shrink and the chaotic regions increase considerably. In addition, it is evident that some invariant regions have rather complex topology and are shown in figure 7.11 which displays particle paths for Re=80 case.

To demonstrate the increased mixing efficiency of the counter-rotating configuration, we show in figures 7.12. and 7.13 snapshots from the temporal evolution of a blob of particles in each configuration for Re = 80. For both cases a blob of 1000 particles is introduced near the outer wall of the container in between Disks 1 and 2 and their trajectories are integrated for 40 disk revolutions. For the co-rotating case the blob remains always in the region of the container it originated from and undergoes a rather slow stretching process. The particles retain their coherency even as they pass through the saddle focus on the upper side of Disk 2 (see *t = 5* and *15* in figure 7.12) for several times. It takes over 40 disk revolutions to begin to observe some significant stretching of the initial blob and even then no particle has escaped from the container region it originated. A striking different picture emerges for the counter-rotating case. The blob undergoes exponential stretching as it passes through the disk saddle focus and its length grows rapidly with each disk revolution. After approximately 10 disk rotations the initial blob has lost any coherency as it starts spreading rapidly throughout the entire container. It is important to emphasize that the final snapshot at t = 40 (see figure 7.13f) is a bit deceiving as at first glance it appears to suggest that global mixing has been achieved. Clearly this cannot be so, since as shown in the Poincaré map in figure 7.9 there are

several invariant regions that have survived the onset of the shear-layer instability for this case. The presence of invariant areas is also evident in figure 7.13f as regions that have remained devoid of particles even after 40 disk rotations. Comparing figures 7.12f with 7.13f, however, clearly shows the dramatic improvement in the stirring performance of the counter-rotating configuration. We find this comparison between the co- and counter-rotating cases extremely encouraging. A simple modification of the co-rotating stirred tank by counter-rotating the middle disk alters drastically the Lagrangian properties of the flow and creates a significant subset of the flow domain where chaotic stirring and, thus, efficient mixing is possible.

Finally to demonstrate that arbitrarily close initial conditions in chaotic regions of the flow separate exponentially in time for the counter-rotating, we show in figure 7.14 the time evolution of the separation of two particle trajectories that initially started at a distance $\Delta x = .0001d$ apart for the Re=80 case. Figure 7.14a shows the particle paths of two trajectories that initiated in the chaotic flow region and figure 7.14b shows initial positions placed in the invariant flow region. In figure 7.14c we plot σ versus time on a semi-log scale, where σ is the magnitude of the distance between the particles given by:

$$\sigma = \left| \mathbf{x}_1 - \mathbf{x}_2 \right| \qquad (7.1)$$

where $\mathbf{x_i}$ is the position vector for each particle. For particles initiated in chaotic regions, the particles separate erratically and exponentially as expected until they reach a point in which their separation is approximately the axial distance of the container. This is the maximum distance possible. Particle trajectories initiated in the invariant flow region separate initially quickly, and then slow to a gradual periodic rate of separation.

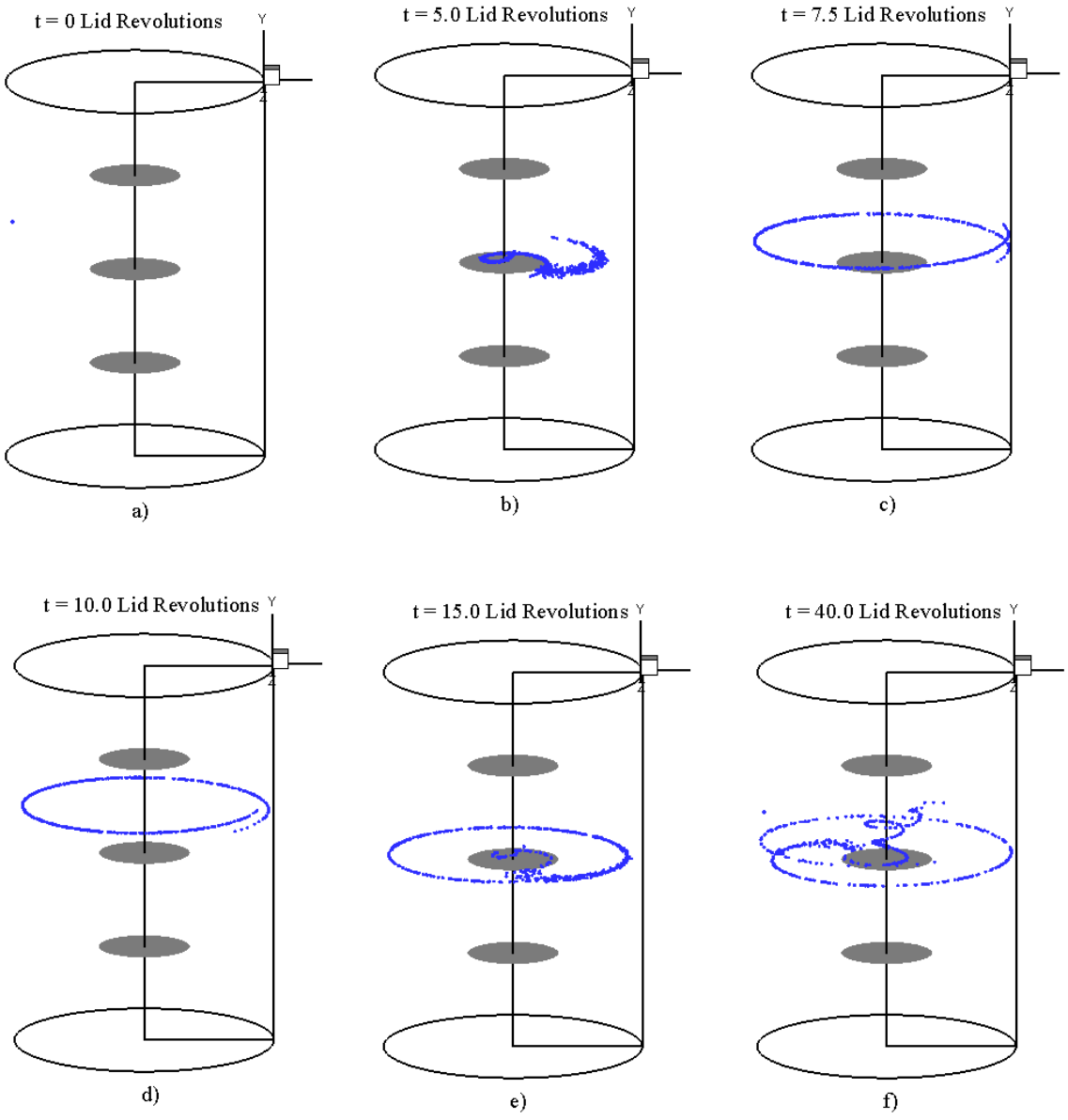

Figure 7.12 Snapshots of stirring of 1000 particle tracers placed in Re=80 co-rotating flow.

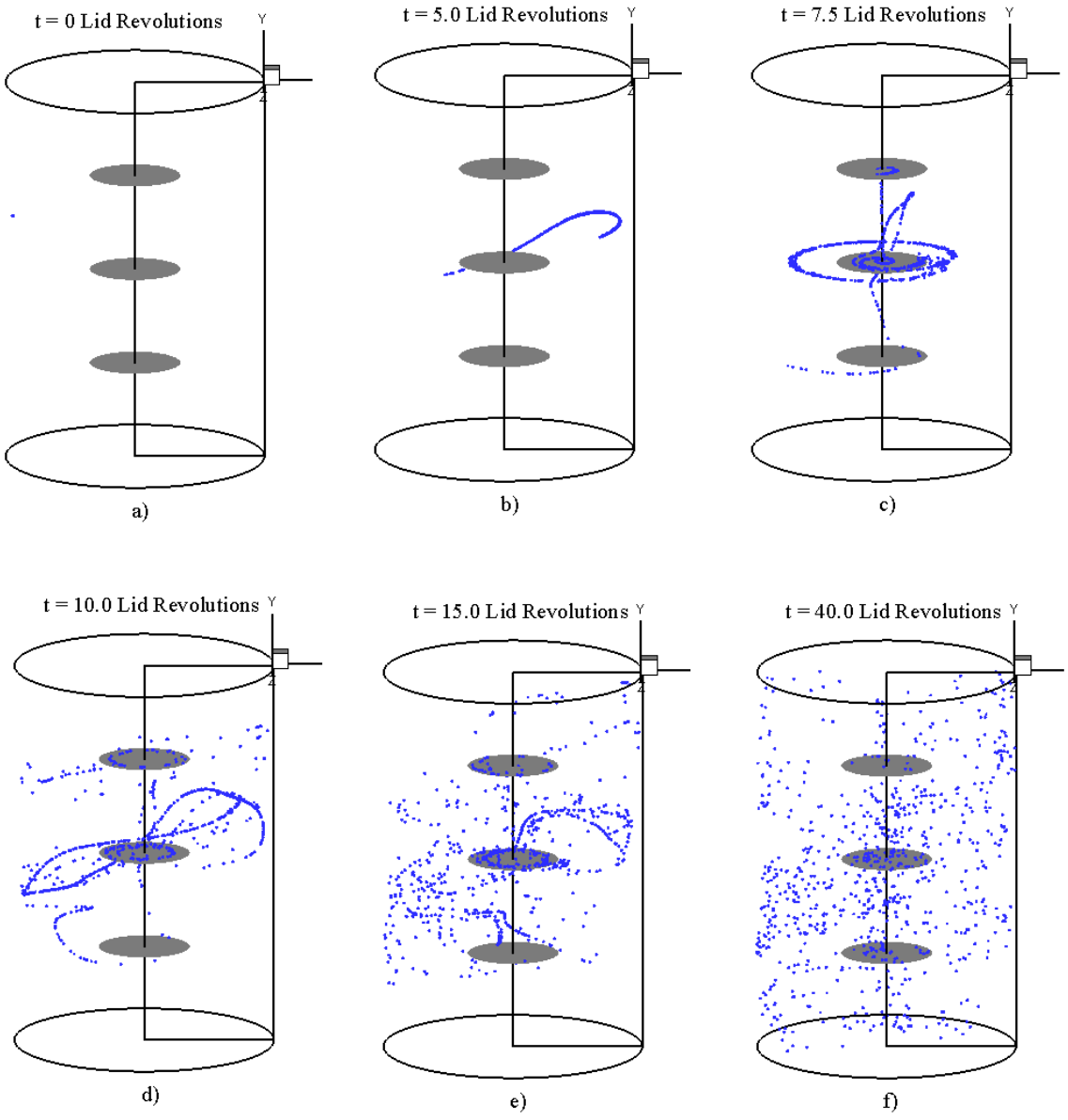

Figure 7.13 Snapshots of stirring of 1000 particle tracers placed in Re=80 counter-rotating flow.

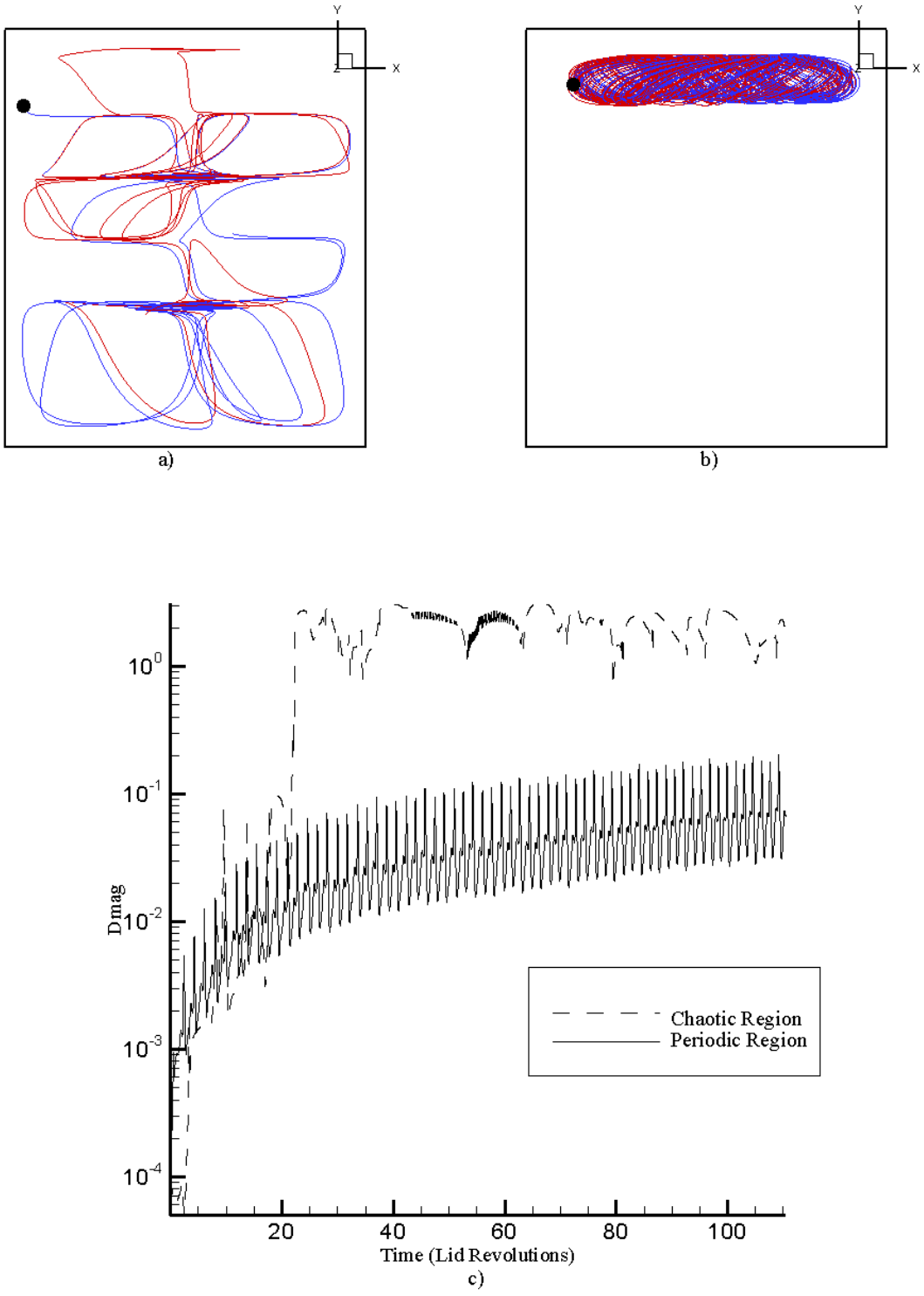

Figure 7.14 Re=80 counter-rotating flow; a) Particle paths of two trajectories initiated in chaotic flow region b) Particle paths of two trajectories initiated in invariant flow region. c) the magnitude of the distance between the trajectories.

7.5 Summary

In this chapter we provide a direct engineering application to the knowledge of innate flow instabilities due to counter-rotation discussed in the previous chapter. This is accomplished using a stirring tank with counter-rotating disks. Our findings show that by making a simple design change to the co-rotating stirred tank, by replacing the middle disk with a counter-rotating disk, it is possible to excite above a threshold Re the three-dimensional instabilities at the shear layers and create a three-dimensional flow with rich Lagrangian properties. The proposed stirred-tank design, however, promising as it may be requires significant further analysis to quantify its mixing performance with Reynolds number. Nevertheless we have shown for the first time in this work that counter rotation of the middle disk can create a flow with large chaotic regions without the need to resort to exotic impeller designs to break the symmetry and integrability of the flow. The results presented herein serve to demonstrate that fundamental studies of chaotic mixing are important as they can lead to valuable technological breakthroughs.

CHAPTER 8

SUMMARY, CONCLUSIONS, AND RECOMMENDATIONS

In this chapter we summarize the work reported in this thesis and present the major findings and conclusions of this research. We also discuss a number of future research topics that arose as part of the present work.

8.1 Chapter Summaries

Chapter 1 provided an introduction to chaotic mixing and the motivation for this research. In this chapter we described the necessity for understanding the Lagrangian properties of flows in the laminar regime. In many engineering applications involving mixing of highly viscous fluids or mixing at micro-scales, efficient mixing is required under laminar flow conditions. In addition, in many turbulent atmospheric and oceanic flows, large scale, determinist flow structures account for a considerable portion of total transport and mixing. In such flows the concept of chaotic advection along with the theory of non-linear dynamical systems comprise a rigorous and powerful framework for understanding, quantifying, and optimizing mixing in the absence of turbulence. In this thesis chaotic advection is studied numerically in three, steady, three-dimensional flows: 1) steady vortex breakdown flow in a cylindrical container with bottom rotating lid, 2)

flow in a cylindrical container with exactly counter rotating lids, and 3) flow in a model stirred-tank with counter-rotating disks.

Chapter 2 reviewed basic background concepts from the theory of dynamical systems and chaotic advection in order to facilitate the interpretation of the computational findings of our work. The chapter also described specific dynamical systems tools that can be applied to visualize and quantify transport in chaotically advected flows.

Chapter 3 reviewed previous experimental, theoretical, and computational research in the area of chaotic advection. An overview of chaotic advection for two-dimensional flows was given but emphasis was placed on work on experimentally realizable, chaotically advected three-dimensional flows. The chapter provided a comprehensive look at the broad range of previously studied flows but also discussed the important parameters and tools that have been used in the past, such as Poincaré Maps, stretching fields, and Lyapunov exponents. The main conclusion of the chapter was that relative to two-dimensional flows, few studies have been devoted to three-dimensional, experimentally realizable flows presumably due to their complexity. This conclusion naturally placed the work reported in this thesis in context and underscored its potential significance.

Chapter 4 described the numerical particle tracking algorithm. Here we discussed the various aspects of the numerical algorithm we developed to track passive particles in chaotically advected flows. The particle location, interpolation, and integration

algorithms are all described in detail. Numerical experiments with a model flow were also carried out to select an optimal time integration scheme.

Chapter 5 discussed the Lagrangian properties of steady vortex breakdown bubbles in a cylindrical container with rotating bottom lid. The effect of arbitrarily small non-axisymmetric perturbations on the Lagrangian properties of the integrable axisymmetric flow was discussed in detail. Firm links were established with the theory of volume-preserving dynamical systems, which underscored the significance of the Šil'nikov mechanism in breaking the invariance of the bubble surface. Poincaré maps, residence time maps, and concepts from fractal geometry were employed to elucidate the richness of dynamics for various Reynolds number and aspect ratios. The dynamics of multiple breakdown bubbles was investigated and was shown that sufficiently high swirl numbers can have a profound stabilizing effect on the chaotic dynamics. Results were presented for Reynolds numbers ranging from 1492 to 1900 and aspect ratios of 1.75 and 2.0.

Chapter 6 presented a computational investigation of steady flow in a cylindrical container with exactly counter-rotating lids. Calculations are reported for one aspect ratio over a range of Reynolds numbers in the steady flow regime. The computations confirm recent stability findings, which showed that above a threshold Re the shear layer at the container mid-plane loses stability to three-dimensional disturbances in the form of radial cat's eye vortices. The computed flowfields are analyzed to clarify for the first time the three-dimensional structure of the flow and to show that streamwise vortical structures inclined in the azimuthal direction also develop along with the radial vortices.

The Lagrangian dynamics of the flow are investigated and it is shown that a chaotic flow with rich dynamics emerges following the onset of the three-dimensional instability. Above a threshold Re, however, unmixed regions begin to appear in the flow, which cause a dramatic decline of mixing rate with Reynolds number. This striking effect is in agreement with a recent theory of chaotic advection, which predicted that mixing rate will indeed decline with increasing Re assuming that the flow remains steady and free of additional instabilities.

Chapter 7 shows how the fundamental understanding gained in Chapter 6 can be exploited to propose and demonstrate the potential of a modified stirred tank configuration whose mixing performance is dramatically increased relative to the basic design. Typical stirred tanks employ multiple co-rotating disks or impellers. Here it is proposed to make the middle disk of a three-disk stirred tank counter-rotate. Numerical computations show that the same shear layer instability found in the container flow is also excited in the counter-rotating stirred tank flow above a threshold Reynolds number. Following the onset of instability, chaotic areas develop in the flow, which allow for passive tracers to disperse globally throughout the entire container. A comparison was made between the new counter-rotating stirred tank and the standard co-rotating design and the potential of the new design was clearly demonstrated.

8.2 Conclusions and Contributions

8.2.1 Vortex breakdown flow in a cylindrical container with rotating bottom

We have shown computationally that the upstream and downstream fixed hyperbolic points of a perturbed, steady vortex breakdown bubble are of spiral focus type and argued that the Šil'nikov mechanism is responsible for the destruction of the invariant axisymmetric bubble surface and the chaotic stirring of upstream originating particles (Šil'nikov's 1965). We constructed Poincaré sections to clarify the very rich dynamics of the flow in the interior of vortex breakdown bubbles. The picture that emerged is consistent with what we would generically anticipate for a perturbed, three-dimensional, volume-preserving system. The dynamics are characterized by a sequence of nested KAM-tori and cantori with the gaps between adjacent tori populated by periodic islands embedded within large regions of chaotic motion.

We calculated residence times of non-diffusive Lagrangian tracers and argued that there exists a Cantor set of initial conditions leading to arbitrarily long residence times within the breakdown region. We also showed that the rate at which upstream originating particles exit the breakdown region exhibits a Devil's staircase distribution. The fractal nature of this curve was established rigorously by computing the fractal dimension of the Cantor set associated with its construction. We presented results for two aspect ratios and a total of three Reynolds numbers, which show that the chaotic dynamics within the bubble (number of un-mixed islands and the extent of the chaotic and quasi-periodic

regions) and the fractal dimension of the Devil staircase depend strongly on the Reynolds number and container aspect ratio.

We showed that a simple Eulerian quantity, the swirl ratio, is the key parameter that determines the complexity of the Lagrangian dynamics. Vortex breakdown bubbles occurring at sufficiently high swirl intensities can exhibit integrable, quasi-periodic dynamics, even though they form within a three-dimensional Eulerian flow. This finding explains the apparent axisymmetric appearance of the steady vortex breakdown bubble that forms in the wake of the first bubble in the two-bubble regime. The circumferential velocity does not change significantly along the container axis but the axial velocity in the wake of the first bubble is orders of magnitude smaller than that upstream of the first bubble. Consequently the second vortex breakdown bubble exists under a much higher swirl ratio, which explains its integrable dynamics.

Holmes's (1984) ingenious prediction of a spatially chaotic flowfield in which particles enter the breakdown region and recirculate arbitrarily many times before they finally exit, is essentially the type of Lagrangian motion we find herein. An important difference between our findings and Holmes's arguments is that he discussed the effects of an arbitrarily small, time-periodic, non-axisymmetric mode on a steady, axisymmetric vortex breakdown bubble. Our results, on the other hand, suggest that even stationary non-axisymmetric perturbations suffice to drastically alter the integrable dynamics of the axisymmetric flow and lead to the onset of chaotic particle paths. It is important to recognize that such a scenario is not new in the dynamical systems literature. Its

theoretical foundations, in the context of an autonomous, three-dimensional, dynamical system whose dynamics closely mimic those of a stationary vortex breakdown bubble, were first laid out by Broer and Vegter (1984)—see also the more recent discussion in Wiggins (1990). Our results are also entirely consistent with the more recent theoretical predictions by MacKay (1994

Our work along with our earlier contribution (Sotiropoulos and Ventikos 2000) and the recent experimental study of Spohn et al. (1998), clarify the origin of the asymmetries observed in all laboratory visualization experiments and resolve conclusively the fifteen-year old controversy regarding the fundamental nature of the bubble-type mode of vortex breakdown in the container problem. The asymmetric folds that invariably appear at the downstream end of the bubble (see, among others, Escudier 1984; Fujimura et al. 1995; Spohn et al. 1998) are due to the very complex topology of trajectories in the vicinity of the spiral-in saddle.

The present computational findings in conjunction with previous theoretical work in the area of non-linear dynamical systems (Broer and Vetger 1984; Wiggins 1990; MacKay 1994) explain clearly the reason why previous axisymmetric computations have succeeded in predicting most Eulerian features of the flow reasonably well (Lopez 1990; Gelfgat et al. 1996; Brons et al. 1999; etc.). The non-axisymmetric component of the flow in the vicinity of real-life vortex breakdown bubbles is indeed very small and, thus, the Eulerian flow can be well approximated by the axisymmetric assumption. Yet this small three-dimensional perturbation has a profound effect on the Lagrangian

characteristics of the flow. In other words, even though the real-life and ideal (axisymmetric) flowfields are very similar from the Eulerian standpoint, their Lagrangian descriptions are as fundamentally different as order and chaos.

Our findings concerning the fractal structure of the residence-time maps and the Devil's staircase, which essentially confirm and help clarify Holmes's and MacKay's theoretical predictions, are both spectacular examples of the physical relevance of the Cantor set. Note, for instance, that the concept of arbitrarily long residence times appears counter-intuitive from the standpoint of conservation of volume in an incompressible fluid. Yet when linked to a Cantor-set of release conditions, this apparent physical contradiction is removed. By definition a Cantor set is not dense at any interval, and, thus, the total tracer flow rate that emanates from points leading to arbitrarily long residence times is in fact zero.

8.2.2 Steady flow in a cylindrical container with exactly counter-rotating lids

Our computations have described in detail for the first time the complex vortical structures in this flow and confirmed the findings of recent linear stability studies for this flow. We have shown that above a threshold Reynolds number the equatorial shear layer loses stability to stationary, three-dimensional modes in the form of radial, cat's eyes vortices. The resulting three-dimensional flow, however, is far more complex than originally thought. Upon the onset of the three-dimensional instability, the azimuthal pressure gradients that develop in the flow redistribute radial vorticity in the axial

direction causing the formation of axial vortices inclined in the azimuthal direction. Helicity and vorticity iso-surfaces along with two-dimensional streamline plots have elucidated for the first time the resulting intricate and strikingly complex web of vortical structures.

We have developed a host of new computational tools for visualizing and quantifying chaotic advection in complex three-dimensional flow. To the best of our knowledge our study reports the first application of Lagrangian averaging in a complex, three-dimensional flow. Lagrangian averaging was shown to be a very effective computational technique for identifying unmixed regions and should be used more extensively in numerical studies of chaotic advection. Even though in principle one could also identify such regions using standard Poincaré maps, the complexity and richness of the present flow would necessitate a long and tedious, trial-and-error search over an extensive region of initial conditions. Note that Poincaré maps work well in mildly perturbed flows where upon perturbation many of the invariant surfaces in the flow survive and, thus, one has some indication of where to search for chaotic regions and unmixed island chains. In the present flow, however, following the onset of the shear-layer instability a very complex, highly three-dimensional flow arises and only few KAM surfaces survive. As a result, the topology of the unmixed, higher period tori is very complex and highly three-dimensional. The Lagrangian time-averaging algorithm allows the straightforward identification of these regions.

We also developed a new computational algorithm for quantifying mixing rate computationally. The algorithm is inspired by a widely used technique in LIF experimental studies, which quantify the mixing rate in terms of the rate of decay of the variance of concentration of light intensity fields. In our approach a discrete concentration field is calculated by counting the number of particles in each mesh volume. This algorithm can be applied in a full three-dimensional manner by defining three-dimensional control volumes around its computational node. A far more efficient approach, however, is obtained by collapsing all azimuthal or all axial planes in one single plane. We showed that all three approaches, full 3D, azimuthal collapse, and axial collapse, yield very similar stirring rates. The 2D approaches, however, require an order of magnitude less particles as compared to the full three-dimensional approach and are, thus, preferable in computational studies of mixing in complex flows.

We investigated the Lagrangian dynamics of the flow using the numerical tools described above. We showed that following the onset of the three-dimensional instability a very complex chaotic flow emerges. Most invariant regions disappear and only two small toroidal regions remain in the vicinity of the two lids. The appearance of the axial vortical structures in the flow further leads to the formation of pairs of saddle-foci at the equatorial mid-plane, which serve to enhance global transport and stirring throughout the entire container.

A rather striking finding of our work is that above a threshold Reynolds number, unmixed island chains of complex, three-dimensional topology begin to appear in the

flow. The islands appear to expand in size as the Reynolds number increases and have a detrimental effect on the global stirring rate. This was conclusively shown by calculating and plotting the variation of stirring rate with Reynolds number. The stirring rate increased from zero at the critical Re for the onset of the three-dimensional instability up to Re = 500 where it attained its maximum value. For higher Re the mixing declined monotonically. This striking finding has obviously important implications for optimizing mixing in industrial mixing devices that operate in the laminar flow regime as it clearly shows that great care needs to be taken to understand the dynamics of the device so that it can be operated as close to its respective optimal Reynolds number as possible.

The existence of an optimal Reynolds at which mixing efficiency is optimized has been predicted by a recent theory of 3D chaotic advection by Mezić (2001). Mezić argued that since an Euler flow is in general integrable and viscous effects in wall bounded flows are confined within a layer whose thickness is of order $Re^{-1/2}$, the chaotic regions in the flow will shrink with Reynolds number assuming that the flow remains steady and instability free. Using the Melnikov theory he further made a prediction that the chaotic stirring will decay at the same rate as the boundary layer thickness, i.e. at a rate of $Re^{-1/2}$. In his work he presented some evidence for the wavy Taylor-Couette flow, which indeed showed a sustained decline of mixing rate above a threshold Reynolds number. The rate of decay was initially very close to the -0.5 rate predicted by the theory but became much steeper at higher *Re*. Our results also show the same trend. Between Re = 500 to 800 the calculated stirring rates decay at a rate, which is in good agreement with the theoretical value. For Re>800 a significantly higher rate of decay is calculated. Unfortunately in

our simulations it became increasingly difficult to obtain steady solutions for Re>800 and, thus, only one data point (Re = 850) is available, which exhibits this increase in the rate of decay of mixing rate with Reynolds number. This notwithstanding, however, our results establish clearly the existence of a Reynolds number at which stirring rate is maximized, which is in agreement with the theory.

8.2.3 Flow in a stirred tank with counter rotating disks

Stirred tanks typically employ two or more co-axial and co-rotating disks or impellers. The base axisymmetric configuration, which consists of disks, leads to very poor mixing as the flow remains steady and axisymmetric over a broad range of Reynolds numbers. Consequently the disks are usually replaced with impellers of complex shape to break the axial symmetry and enhance chaotic advection. In this work we showed for the first time that the base configuration with disks can, in fact, be made to induce chaotic advection if the middle disk is made to counter-rotate relative to the other two. Our simulations showed that this simple design modification excites the same type of three-dimensional instabilities as the container flow with radial, cat's eyes vortices forming at the equatorial plane between each disk pair above a threshold Reynolds number. For the range of Reynolds numbers studied in this work (Re = 40, 80, and 100) and for the aspect ratio considered, the azimuthal modes one and two where excited.

Lagrangian analysis of the flow showed that as the Reynolds number increases for the counter-rotating stirred tank the integrable toroidal region between each pair of disks

begins to shrink and the chaotic areas grow in size. Since the objective of this study is to demonstrate the feasibility of a counter-rotating stirred tank design, we did not attempt to identify the Reynolds number, which optimizes the stirring rate. Yet, based on the results presented in the previous chapter there is little doubt that such Reynolds number must exist.

The comparisons between the co-rotating and counter-rotating stirred tanks were pretty striking. At a given Reynolds number the flow in the former remains axisymmetric and the trajectories remain confined in their respective axisymmetric streamsurfaces. For the latter, however, trajectories were shown to diverge exponentially in time and explore the entire container.

Our results clearly show that fundamental studies of mixing, such as those reported in the Chapters 5 and 6 in this thesis, are not important only from a fundamental standpoint but when their conclusions are properly exploited can lead to important technological innovations. As should be evident from this work and previous studies in the literature, mixing in the absence of turbulence is a very difficult and multi-faceted problem. Inducing three-dimensionality in the flow does not by itself guarantee efficient mixing as was shown both for the vortex breakdown bubbles and the counter-rotating disk flow. Thus, the design of efficient mixing devices at low Reynolds numbers requires a close synergy between theory, computations, and, of course, experiments.

8.3 Recommendations for Future Research

This thesis has made a number of significant and novel contributions, which have advanced the state of understanding of chaotic advection in complex, three-dimensional, steady flows. The findings of this work, however, have led to a number of new questions and identified significant areas for further work.

The finding that the swirl parameter controls chaotic stirring intensity in vortex breakdown bubbles points to the need for further theoretical and experimental studies to gain a more quantitative understanding of this effect. Such work could lead to a rigorous framework for controlling mixing in vortex breakdown bubbles. It could, thus, impact the design of a number of engineering mixing devices, such as combustors and swirl burners, which rely on vortex breakdown to stabilize flame by enhancing the residence times of fuel in the core of the flame. Work is also needed to understand the Lagrangian properties of vortex breakdown bubbles in open systems, such as diffusers, and in the unsteady regime.

The finding that there is a Reynolds number at which stirring intensity is optimized in the cylinder flow with counter-rotating lids deserves considerable further work and investigation. Even though this phenomenon has also been documented before for the wavy Taylor-Couette vortex flow, it is important to demonstrate more conclusively that this is indeed a universal property of 3D, confined, chaotically advected flows as suggested by Mezić's theory. In the context of the counter-rotating disk flow future work

should quantify the relationship of stirring rate and Reynolds numbers for different accept ratios as well as for configurations with differentially counter-rotating disks. Experiments should also be carried out to confirm the computational findings for this flow.

Much work remains to be done for the counter-rotating stirred tank design proposed in this work. First the mixing performance of the base axisymmetric geometry (with disks) needs to be quantified over a broad range of Reynolds numbers and aspect ratios. Calculations and experiments should be carried out to identify the optimal Reynolds numbers for various tank and disk-placement configurations. The effect of combining non-axisymmetric perturbations, say by using impellers instead of disks, unsteady forcing and counter-rotation on mixing efficiency needs to be also understood and quantified.

Finally, the work we have reported in this thesis as well as most previous work in the literature has focused on the Lagrangian properties of passive tracers in chaotically advected flows. Yet in many engineering applications the tracer to be mixed cannot be characterized as passive and inertia effects could become important, especially in rotating flows. Future work should be carried out to examine the transport of small inertial particles in the flows studied in this work in order to quantify the effects that properties of the particles, such as mass, density, shape, etc., have on their advection by the flow. The computational tools we developed in this thesis are general enough and can be readily applied, with relatively small algorithmic modifications, to account for such effects.

APPENDIX A

NUMERICAL METHOD

In this appendix we present the numerical method used for solving the three-dimensional incompressible Navier-Stokes equations. These equations are solved using a scheme that combines a fractional step method with an ADI (alternate-direction-implicit) solver and is second order accurate in space. This method has been utilized in previous work (Stewart 2003) to obtain two-dimensional axisymmetric solutions for simulating selective withdrawal in temperature stratified flows. This method is used in this work to provide computational solutions to the flow in a cylindrical container with exactly counter rotating lids and the flow driven by counter-rotating disks. The appendix proceeds as follows. First we present the governing equations in both Cartesian and an then their transformation to general curvilinear coordinates. Next we describe the numerical technique, including the discretization algorithms. Finally we discuss boundary conditions, convergence acceleration techniques, and other numerical implementation details.

A.1 Governing Equations

The three-dimensional incompressible Navier-Stokes equations formulated in Cartesian coordinates in tensor notation (where repeated in dices imply summation) read as follows:

Continuity

$$\frac{\partial u_i}{\partial x_i} = 0 \tag{A.1}$$

Momentum

$$\frac{\partial u_i}{\partial t} + u_j \frac{\partial u_i}{\partial x_j} + \frac{\partial p}{\partial x_i} - \frac{1}{Re} \frac{\partial^2 u_i}{\partial x_j \partial x_j} = 0 \tag{A.2}$$

where x_1, x_2, and x_3 are the x, y, and z coordinates, respectively, p is the pressure divided by the fluid density and Re is the Reynolds number of the flow. These equations are then transformed to generalized, non-orthogonal curvilinear coordinates $\{\xi_i\}$ using a partial transformation $\{x_i\} \rightarrow \{\xi_i\}$ and can be formulated as follows:

Continuity

$$\mathbf{J} \frac{\partial}{\partial \xi_i} \left(\frac{U^i}{\mathbf{J}} \right) = 0 \tag{A.3}$$

Momentum

$$\frac{\partial \mathbf{Q}}{\partial t} + A^j \frac{\partial \mathbf{Q}}{\partial \xi^j} + \mathbf{H} - J \frac{\partial}{\partial \xi^j} \left[\frac{1}{J} \frac{1}{Re} \left[g^{mj} \frac{\partial \mathbf{Q}}{\partial \xi^m} \right] \right] = 0 \tag{A.4}$$

where,

$$\mathbf{Q} = [u_1, u_2, u_3]^T, \tag{A.5}$$

$$\mathbf{H} = \left(\xi^j_{x_1} \frac{\partial p}{\partial \xi^j} \quad \xi^j_{x_2} \frac{\partial p}{\partial \xi^j} \quad \xi^j_{x_3} \frac{\partial p}{\partial \xi^j} \right)^T$$

$$J = \left| \frac{\partial(\xi^1, \xi^2, \xi^3)}{\partial(x_1, x_2, x_3)} \right|. \tag{A.6}$$

$$\mathbf{A}_j = diag(U^j, U^j, U^j) \tag{A.7}$$

Here, $\xi^j_{x_j}$ are the metrics of the geometric transformation, U^j are the contravariant velocity components $(U^j = u_i \xi^i_{x_j})$, g^{ij} are the components of the contravariant metric tensor $(g^{ij} = \xi^i_{x_k} \xi^j_{x_k})$, and *J* is the Jacobian of the geometric transformation.

A.2 Numerical Method

An implicit fractional-step (or projection) method is used to integrate the Navier-Stokes equations in time. The time integration is carried out in two steps. The first step is the convection-diffusion step and is used to compute a velocity field based on the current pressure field. After which a projection step (which is also called the continuity step) is carried out. In this step the gradient of a pressure correction field, calculated by solving a Poisson equation so that the incompressibility constraint is satisfied, is added to the

velocity field, thereby projecting the new velocity field into the divergence free vector space.

An alternate-direction-implicit (ADI) method is used to solve the momentum equations. The three-dimensional equations are solved in a sequence of one-dimensional spatial operations along each direction. These can be inverted by solving tri-diagonal matrices.

A.2.1 Spatial Discretization

In this section we describe the spatial discretization of the various terms in the NS equation. The continuity equation is discretized with the three-point, second-order accurate, central differencing scheme. The momentum equations are discretized in space using three-point central-finite-differencing for the pressure gradient and viscous terms. Second-order upwind-differencing is used for the convective terms. The upwind differencing is used to stabilize the numerical algorithm and eliminates the need for explicitly adding artificial dissipation terms to the right hand side of the moment equations because it has an inherent amount of dissipation. Figure A.1 shows the schematic of the two-dimensional version of the computational cell on which the discrete approximations are made. In the figure the filled circles refer to half nodes (i+1/2) and the open circles are whole nodes (i+1)

Continuity Equation:

$$J\left[\delta_{\xi}^{q}\left(\frac{U^{q}}{J}\right)\right]_{i,j,k}=0 \tag{A.8}$$

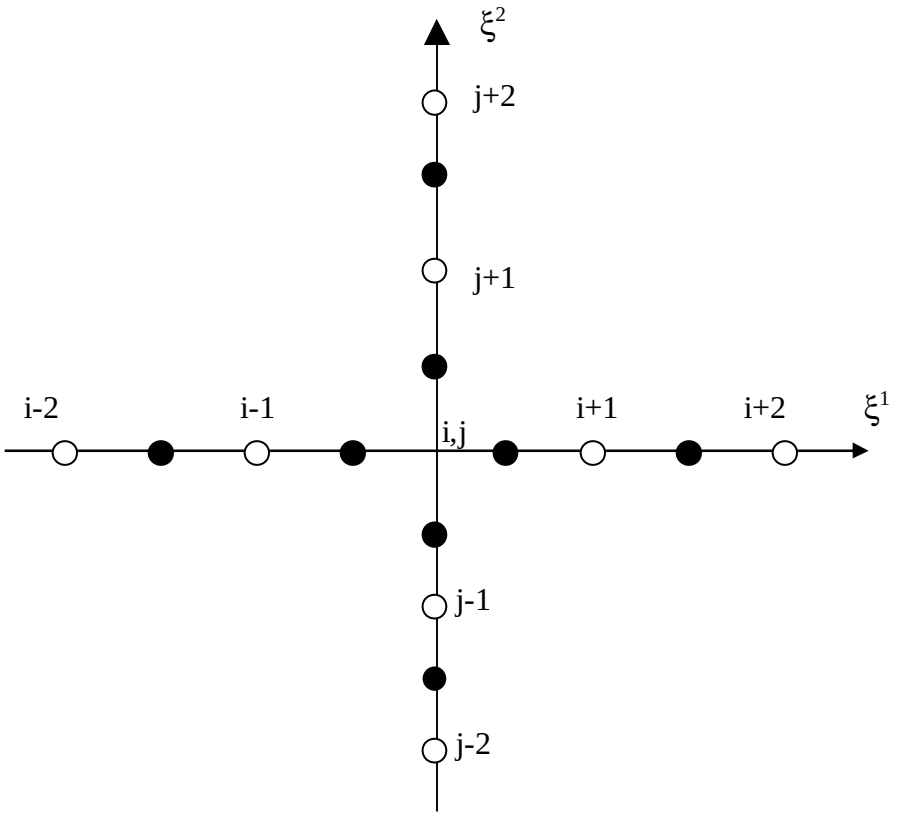

Figure A.1 – Two-dimensional version of a finite-difference computational cell. The filled circles (●) are the half nodes (i+1/2) and the open circles (○) are whole nodes (i+1).

The various terms in the momentum equations are discretized as follows:

Convective Terms:

$$C_{\xi^1}=\left[U^{1}\frac{\partial u_1}{\partial \xi^{1}}\right]_{i,j,k}\cong U_{i,j,k}^{1+}\delta_{\xi^1}^{-}\left(u_1\right)_{i,j,k}+U_{i,j,k}^{1-}\delta_{\xi^1}^{+}\left(u_1\right)_{i,j,k} \tag{A.9}$$

Pressure Gradient:

$$G_{\xi^1} = \left[\xi_{x_1} \frac{\partial p_1}{\partial \xi^1} \right]_{i,j,k} \cong \left(\xi_{x_1} \right)_{i,j,k} \delta_{\xi^1} (p)_{i,j,k} \tag{A.10}$$

Viscous Terms:

$$D_{\xi^1} = \left\{ J \frac{\partial}{\partial \xi^1} \left[\frac{g^{11}}{J \,\mathrm{Re}} \frac{\partial u_1}{\partial \xi^1} \right] \right\}_{i,j,k} \cong \left\{ J \tilde{\delta}_{\xi^1} \left[\frac{g^{11}}{J\,Re} \tilde{\delta}_{\xi^1} (u_1)_{i,j,k} \right] \right\} \tag{A.11}$$

where the various difference operators are defined as follows

$$\delta^{\pm}_{\xi^1} (\;)_{i,j,k} = \pm \frac{1}{2\Delta \xi^1} \left[-3(\;)_{i,j,k} + 4(\;)_{i+1,j,k} - (\;)_{i\pm 2,j,k} \right] \tag{A.12}$$

$$\delta_{\xi^1} (\;)_{i,j,k} = \frac{1}{2\Delta \xi^1} \left[(\;)_{i+1,j,k} - (\;)_{i-1,j,k} \right] \tag{A.13}$$

$$\tilde{\delta}_{\xi^1} (\;)_{i,j,k} = \frac{1}{\Delta \xi^1} \left[(\;)_{i+\frac{1}{2},j,k} - (\;)_{i-\frac{1}{2},j,k} \right] \tag{A.14}$$

and the plus/minus contravariant velocity terms are determined by

$$U^{i\pm} = \frac{1}{2} \left[U^i \pm \left| U^i \right| \right], \text{ (for } i\text{=1,2,3)} \tag{A.15}$$

To facilitate our subsequent discussion of the fractional step method we introduce the following notation for the discrete convective, pressure gradient, and viscous operators, respectively:

$$C[\ ]=\sum_{i=1}^{3} C_{\xi^i} \quad ; \; G[\ ]=\sum_{i=1}^{3} G_{\xi^i} \; ; \; D[\ ]=\sum_{i=1}^{3} D_{\xi^i} \tag{A.16}$$

A.2.2 Fractional Step Method

The fractional step (or projection) method was introduced independently by Chorin (1968) and Temam (1969). In this work we employ a fractional step approach that handles the viscous and convective terms are implicitly. The NS equations are discretized in time by introducing an intermediate pseudo-velocity $\mathbf{Q}^*$, which does not satisfy the continuity equation, as follows:

$$\frac{\mathbf{Q}_{i,j,k}^{n+1}-\mathbf{Q}_{i,j,k}^{*}}{\Delta t}+\frac{\mathbf{Q}_{i,j,k}^{*}-\mathbf{Q}_{i,j,k}^{n}}{\Delta t}+C\left[\mathbf{Q}_{i,j,k}^{*}\right]-D\left[\mathbf{Q}_{i,j,k}^{*}\right]+G\left[P_{i,j,k}^{n+1}\right]=0 \tag{A.17}$$

The velocity vector $\mathbf{Q}^*$ and the pressure $\mathbf{P}^{n+1}$ are linearized in time as:

$$P_{i,j,k}^{n+1}=P_{i,j,k}^{n}+\Delta P_{i,j,k} \tag{A.18}$$

$$\mathbf{Q}_{i,j,k}^{*}=\mathbf{Q}_{i,j,k}^{n}+\overline{\Delta\mathbf{Q}}_{i,j,k} \tag{A.19}$$

These terms are then placed into A.17 to obtain:

$$\frac{\mathbf{Q}_{i,j,k}^{n+1}-\mathbf{Q}_{i,j,k}^{*}}{\Delta t}+\frac{\overline{\Delta\mathbf{Q}}_{i,j,k}}{\Delta t}+C\left[\mathbf{Q}_{i,j,k}^{n}+\overline{\Delta\mathbf{Q}}_{i,j,k}\right]-D\left[\mathbf{Q}_{i,j,k}^{n}+\overline{\Delta\mathbf{Q}}_{i,j,k}\right]+G\left[P_{i,j,k}^{n}+\Delta P_{i,j,k}\right]=0 \tag{A.20}$$

This equation can be split into two separate equations as:

$$\frac{\overline{\Delta\mathbf{Q}}_{i,j,k}}{\Delta t}+C\left[\overline{\Delta\mathbf{Q}}_{i,j,k}\right]-D\left[\overline{\Delta\mathbf{Q}}_{i,j,k}\right]=-\left\{C\left[\mathbf{Q}_{i,j,k}^{n}\right]-D\left[\mathbf{Q}_{i,j,k}^{n}\right]+G\left[P_{i,j,k}^{n}\right]\right\} \tag{A.21}$$

$$\frac{\mathbf{Q}_{i,j,k}^{n+1}-\mathbf{Q}_{i,j,k}^{*}}{\Delta t}+G\left[\Delta P_{i,j,k}\right]=0 \tag{A.22}$$

such that the sum of A.21 and A.22 is A.20.

The fractional step method is then carried out by first performing the convection-diffusion step to advance the solution to $\mathbf{Q}^{*}$. Equation A.21 is rewritten as

$$\left\{1+\Delta t\left(C\cdot-D\cdot\right)\right\}\left[\overline{\Delta\mathbf{Q}}_{i,j,k}\right]=-\Delta t\left\{C\left[\mathbf{Q}_{i,j,k}^{n}\right]-D\left[\mathbf{Q}_{i,j,k}^{n}\right]+G\left[P_{i,j,k}^{n}\right]\right\} \tag{A.23}$$

Here $\overline{\Delta\mathbf{Q}}_{i,j,k}$ is obtained by inverting the above equation using the ADI method (see below) and $\mathbf{Q}_{i,j,k}^{*}$ is obtained using eqn (A.19). Next a projection step is performed to

project $\mathbf{Q}^{*}_{i,j,k}$ into the divergence-free vector space, so that continuity is satisfied. Equation A.22 can be written as

$$\mathbf{Q}^{n+1}_{i,j,k} = \mathbf{Q}^{*}_{i,j,k} - \Delta t G\left[\Delta P_{i,j,k}\right] \tag{A.24}$$

This equation can be combined with the continuity equation which states that the final velocity should be divergence free:

$$\nabla \cdot \left[\mathbf{Q}^{n+1}_{i,j,k}\right] = 0 \tag{A.25}$$

Inserting equation A.24 into equation A.25 gives us

$$\nabla \cdot \left\{\Delta t G\left[\Delta P_{i,j,k}\right]\right\} = \nabla \cdot \left[\mathbf{Q}^{*}_{i,j,k}\right] \tag{A.26}$$

This equation can be solved for ΔP. Once this value is determined, the velocity field is advanced to the n+1 time level using equation A.24.

A.2.3 Solution of the Convection-Diffusion Equation

Employing the ADI factorization, the operator in the left-hand side of (A-23) can be split into three directions and described as

$$\left\{1+\Delta t\left[U^{1+}\delta_{\xi^1}^{-}+U^{1-}\delta_{\xi^1}^{+}-\frac{J}{Re}\delta_{\xi^1}\left(g^{11}\right)\delta_{\xi^1}\right]\right\}$$

$$\left\{1+\Delta t\left[U^{2+}\delta_{\xi 2}^{-}+U^{2-}\delta_{\xi^2}^{+}-\frac{J}{Re}\delta_{\xi^2}\left(g^{22}\right)\delta_{\xi^2}\right]\right\} \qquad \text{(A.27)}$$

$$\left\{1+\Delta t\left[U^{3+}\delta_{\xi^3}^{-}+U^{3-}\delta_{\xi^3}^{+}-\frac{J}{Re}\delta_{\xi^3}\left(g^{33}\right)\delta_{\xi^3}\right]\right\}\overline{\Delta\mathbf{Q}}=$$

$$-\Delta t\left\{C\left[\mathbf{Q}^n\right]-D\left[\mathbf{Q}^n\right]+G\left[P^n\right]\right\}$$

This equation is solved in three consecutive sweeps along the ξ^i (i=1,2,3) directions using the Thomas algorithm. The convection terms on the left-hand side of this equation are discretized using first-order accurate upwind differencing so that inversions of tri-diagonal matrices are required. This approximation has no real effect on the accuracy of the final result since the method is used to obtain steady state solutions and, thus, the left hand side vanishes at convergence.

`

A.2.4 Continuity Step

In the projection step, we solve equation A.22 whose discrete form can be defined in terms of the following discrete Laplacian operator L as

$$L_{\xi^1}=\delta_{\xi^1}\left(\frac{1}{J}g^{11}\Delta t\right)_{i,j,k}\delta_{\xi^1} \qquad \text{(A.28)}$$

It can be shown based on the definition of the gradient and the divergence that this operator is exactly equal to the operator seen in the left hand side of equation A.26, so that

$$\nabla \cdot \{\Delta t G[\ ]\} = L[\ ] \tag{A.29}$$

Therefore we can say that

$$L[\Delta P] = \frac{1}{\mathbf{J}} \nabla \cdot [\mathbf{Q}^*] \tag{A.30}$$

Introducing a pseudo-time derivative of the pressure in (A.30), we obtain the equation

$$-\beta \frac{\Delta P_{i,j,k}}{\Delta t} + L[\Delta P] = \frac{1}{\mathbf{J}} \nabla \cdot [\mathbf{Q}^*] \tag{A.31}$$

where β is a positive preconditioning constant introduced to accelerate the convergence to steady state. In this work β is set to one. This step ultimately, has no effect on the steady-state solution of the pressure equation since its left-hand side vanishes at steady state. Further simplification of (A.31) yields

$$\Delta P_{i,j,k} - \frac{\Delta t}{\beta} L[\Delta P_{i,j,k}] = -\frac{\Delta t}{\beta} \left[\frac{1}{J} \nabla \cdot [\mathbf{Q}^*] \right] \tag{A.32}$$

Application of the ADI approximation factorization method to (A.32) gives

$$\left[1-\frac{\Delta t}{\beta}\delta_{\xi^1}\left(\frac{1}{J}g^{11}\Delta t\delta_{\xi^1}\right)_{i,j,k}\right]\left[1-\frac{\Delta t}{\beta}\delta_{\xi^2}\left(\frac{1}{J}g^{11}\Delta t\delta_{\xi^2}\right)_{i,j,k}\right]\left[1-\frac{\Delta t}{\beta}\delta_{\xi^3}\left(\frac{1}{J}g^{11}\Delta t\delta_{\xi^3}\right)_{i,j,k}\right]\Delta P_{i,j,k}$$

$$=-\frac{\Delta t}{\beta}\left[\frac{1}{J}\nabla\cdot\left[\mathbf{Q}^*\right]\right] \tag{A.33}$$

This equation is solved similarly to equation (A.27), using the Thomas algorithm.

A.3 Local Time Stepping

The rate of convergence of the above iterative algorithm to steady state is accelerated using local time stepping. The time increment is computed and stored for every grid node as follows:

$$\Delta t_{i,j,k}=\frac{CFL}{\max\left(\sqrt{g_{11}},\sqrt{g_{22}},\sqrt{g_{33}},\right)} \tag{A.34}$$

where g_{ii} are the components of the covariant metric tensor and CFL is the Courant-Friedrich-Lewis number. Most computations reported herein have been carried out using CFL = 0.1.

A.4 Boundary Conditions

A.4.1 Container with Exactly Counter Rotating Lids

The no-slip condition is imposed on all walls, thereby requiring the velocity components at all stationary walls to be zero. The velocity components at all rotating surfaces are set equal to the velocity of the wall. The pressure at all walls is extrapolated from the interior of the solution domain using linear extrapolation.

Since we employ a cylindrical/polar mesh to discretize the container domain a coordinate singularity point exists along the centerline axis of the container. At this point the Cartesian velocity components and pressure are computed using circumferential averaging of the respective variables at the next radial grid point off the axis. That is, assuming that the indices i, j, and k indicate the radial, axial, and circumferential directions, respectively, a flow variable S (where S is p, u, v, or w) on the axis is determined as follows:

$$S_{1,j,k} = \frac{\sum_{k=1}^{k\,max-1} S_{1,j,k}}{k_{max} - 1} \tag{A.35}$$

A.4.2 Counter Rotating Disk Driven Flow

The velocity components at all lids and walls are set to zero, enforcing the no slip condition. At the disks, the velocity is specified. Pressure is extrapolated from the interior solution. The disk has zero thickness and the grid-surface it coincides with represents a surface across which the pressure is discontinuous. The pressure at the top of each disk is extrapolated from coordinates above the disk and similarly pressure values at the bottom of each disk are extrapolated from points beneath the disk. The singularity

along the centerline axis is handled similarly to the previous description in the exactly counter rotating lids case.

The solution to equation A.27, using the ADI method requires a matrix inversion, as previously mentioned. Therefore special consideration must be taken for the case of rotating disks which exist within the midst of the flow. In these cases, blanking is used and the matrix coefficients along the diagonal are set to one and all off diagonal terms are set to zero on each disk.

REFERENCES

Acharya, N., Sen, M. and Chang, H. C. (1992) Heat-transfer enhancement in coiled tubes by chaotic mixing. Int. J. Mass Heat Transfer 35, 2475-2489.

Alvarez, M. M., Zalc, J. M., Shinbrot, T., Arratia, P. E., and Muzzio, F. J.(2002). Mechanisms of mixing and creation of structure in laminar stirred tanks, A.I.Ch.E. Journal, 48(10), 2135-2148.

Alvarez-Hernández, M. M., Shinbrot, T., Zalc, J.M. and Muzzio, F.J.(2002b) Practical chaotic mixing. Chemical Engineering Science, 57(17), 3749-3753.

Anderson, P. D. Galaktionov, O. S., Peters, G. W., Van de Vosse, F. N. and Meijer, H. E. (1999). Analysis of mixing in three-dimensional time-periodic cavity flows. 386, 149-166.

Angilella, J.R. and Brancher, J. P. (2003). Note on chaotic advection in an oscillating drop. Physics of Fluids 15(1), 261-264.

Aref, H. (1984). Stirring by chaotic advection. Journal of Fluid Mechanics. 143, 1-21

Aref, H. (2002). The Development of chaotic advection. Physics of Fluids. 14 (4), 1315-1325.

Arneodo, A., Coullet, P., and Tresser, C. (1982) Oscillators with chaotic behavior: an illustration of a theorem by Sil'nikov. J. Statist. Mech. 27, 171-182.

Arnold, V. I. (1965). Sur la topologte des ecoulements stationeries des fluids parfaits. C. R. Acad. Sci. Paris. 261, 17-20.

Arnold, V. I. (1978). Mathematical methods of classical mechanics. Springer-Verlag, New York.

Arter, W. (1983). Ergodic stream-lines in steady convection. Phys. Lett. A97, 171-174.

Ascanio, G., Brito-Bazán, M., Brito-De, E., Carreau, P. J., and Tanguy, P. (2002). Unconventional configuration studies to improve mixing times in stirred Tanks. The Canadian Journal of Chemical Engineering. 80, 558-565.

Ashwin, P. and King, G. P. (1995). Streamline topology in eccentric Taylor vortex flow J. Fluid Mech. 285, 215-247.

Ashwin and King (1997). A study of particle paths in non-axisymmetric Taylor-Couette flows. J. Fluid Mech. 338, 341-362.

Bajer, K. and Moffatt, H. K. (1990). On a class of steady confined Stokes flows with chaotic streamlines. J. Fluid Mech. 212, 337-363.

Bak, P. 1986. The devil's Staircase. Physics Today. 39(12), 38-45.

Bakker, A., Myers, K. J., Ward, R. W., and Lee, C. K. (1996). The laminar and turbulent flow pattern of a pitched blade turbine. Trans. IChemE. 74A, 486.

Bakker, A., Oshinowo, L. M., and Marshall E. M. (2000).. The use of large eddy simulation to study stirred vessel hydrodynamics. Proc. of the 10th Euro. Conf. on Mixing, Delft, The Netherlands, July 2-5, 2000. 247-254.

Barkley, D., Karniadakis, G. E., Kevrekidis, I. G. Smits, A. J and Shen, Z.H. (1991). Chaotic advection in a complex annular geometry. Phys. Fluids, 3(5), 1063.

Batchelor, G. K. (1951). Note on a class of solutions of the Navier-Stokes equations representing steady rotationally-symmetric flow. Q. J. Mech. Appl. Maths 4, 29-41.

Beerens, S. P., Ridderinkhof, H. , and Zimmerman, J. T. F. (1994). An analytical study of chaotic stirring in tidal areas. Chaos, Solitons, and Fractals. 4(6) 1011-1029.

Beigie, D., Leonard, A. and Wiggins, S. (1994). Invariant manifold templates for chaotic advection. Chaos, Solitons, and Fractals. 4(6) p749-868.

Benjamin, T. B. (1962) Theory of the vortex breakdown phenomenon. J. Fluid Mech. 14, 593-629.

Broer and Vetger (1984) Subordinate Sil'nikov bifurcations near some singularities of vector fields having low codimension. Ergod. Theor. Dyn. Syst. 4, 509-525.

Byrde, O. and Sawley, M. L. (1999). Parallel computation and analysis of the flow in a static mixer. Computers and Fluids. 28,1-18.

Cartwright, J. H. E., Feingold, M., and Piro, O. (1996) Chaotic advection in three-dimensional unsteady incompressible laminar flow. J. Fluid Mech. 316, 259--284.

Cartwright, J. H. E., Feingold, M., and Piro, O.(1999) An introduction to chaotic advection. Mixing: Chaos and Turbulence Eds. H. Chate, E. Villermaux, and J. M. Chomez, 307-342, Kluwer

Cerbelli, S., Zalc, J. M., and Muzzio, F. J. (2000). The evolution of material lines curvature in deterministic chaotic flows. Chem. Eng. Science. 55, 363-371.

Chaiken, J., Chevray, R., Tabor, M. and Tan, Q.M. (1986). Experimental study of Lagrangian turbulence in Stokes flow. Proc. R. Soc. Lond. A 408, 165-174.

Chen, X.-Q. and Pereira, J. C. F. (1999) A new particle-locating method accounting for source distribution and particle-field interpolation for hybrid modeling of strongly couple two-phase flows in arbitrary coordinates. Numerical Heat Transfer. Part B. 35, 41-63.

Chien, W. L., Rising, H. and Ottino, J. M. (1986). Laminar mixing and chaotic mixing in several cavity flows. J. Fluid Mech. 170, 355-377.

Chorda, R., Blasco, J. A. and Fueyo, N. (2002). An efficient particle-locating algorithm for application in arbitrary 2D and 3D grids. International Journal of Multiphase Flow. 28, 1565-1580.

Chorin, A. J. (1968). Numerical solution of the Navier-Stokes equations. J. Math. Comput. , 22, 745-762.

Compolo, M., Sbrizzai, F. , and Soldati, A. (2003). Time-dependent flow structures and Lagrangian mixing in Rushton-impeller baffled-tank reactor. Chem. Eng. Sci. 58, 1615-1629.

Darmofal, D. L and Haimes , R. (1996) An Analysis of 3D Particle Path Integration Algorithms. Journal of Computational Physics. 123, 182-195.

Davey, A., DiPrima, R. C. and Stuart, J.T. (1968) On the instability of Taylor vortices. J. Fluid Mech. 31, 17-52.

de La Villeon, J., Bertrand, F., Tanguy, P. A. , Labrie, R., Bousquet, J. and Lebouvier, D. 1998. Numerical investigation of mixing efficiency of helical ribbons. AIChE J. 44 972-977

Desmet, G., Verelst, H. and Baron, G. V. (1996) Local and global dispersion effects in Couette-Taylor flow-II. Quantitative measurements and discussion of the reactor performance. Chem. Engng. Sci. 51, 907-931.

Dijkstra, D. and Heijst, G. J. F. Van (1983). The flow between two finite rotating disks enclosed by a cylinder. J. Fluid Mech. 128, 123-154.

DiPrama, R. C. and Stuart, J.T. (1975) The nonlinear calculation of Taylor-vortex flow between eccentric rotating cylinders. J. Fluid Mech. 67, 85-111

Dombre, T., Frisch, U., Greene, J. M., Henon, M., Mehr, A. and Soward, A. M. (1986). Chaotic streamlines in the ABC flows. J. Fluid Mech. 167, 353-391.

Escudier, M. P. (1984) Observations of the flow produced in a cylindrical container by a rotating endwall. Exps. Fluids. 2, 189-196.

Escudier, M. P. (1988) Vortex breakdown: Observations and explanations. Prog. Aerospace Sci. 25, 189-229.

Fountain, G. O, Khakar, D. V. and Ottino, J. M. (1998). Visualization of three-dimensional chaos. Science. 281, 683-686.

Fountain, G. O. Khakar, D. V., Mezic, I. and Ottino, J. M. (2000). Chaotic mixing in a bounded three-dimensional flow. J. Fluid Mech. 417, 265-301.

Fujimura, K., Koyama, H. S., and Hyun, J. M. (1997) Time-dependent vortex breakdown in a cylinder with a rotating lid. Trans. ASME: J. Fluids Engng. 119(2), 450-453.

Gaspard, P. and Nicolis, G. (1983). What can we learn from homoclinic orbits in chaotic dynamics? J. Statist. Phys. 31, 499-518.

Gauthier, G., Gondret, P., Moisy, F. and Rabaud, M. (2002). Instabilities in the flow between co- and counter-rotating disks. J. Fluid Mech. 473, 1-21.

Gelfgat, A. Yu., Bar-Yoseph, P. Z., and Solan, A. (1996). Stability of confined flow with and without vortex breakdown. J. Fluid Mech. 311, 1-36.

Ghosh, S., Leonard, A. and Wiggins, S. (1998). Diffusion of a passive scalar from a no-slip boundary into a two-dimensional chaotic advection field. J. Fluid Mech. 372, 119-163.

Goverkhin,V. N., Morgulis, A., Yudovich,V. I. , and Zaslavsky, G. M.(1999). Chaotic advection in compressible helical flow. Physical Review E. 60 (3) 2788-2798

Grigoriev, R. and Schatz, M. (2004) Optically controlled mixing in microdroplets. Preprint.

Guyon, E., Hulin, J.P., Petit, L., and Mitescu, C. D. (2001). Physical hydrodynamics. Oxford University Press.

Harnby, N., Edwards, M. F., and Nienow, A. W. (1992). Mixing in the Process Industries, Butterworth-Heinemann. NY (1992).

Harvey III, A. D., Wood, Sp. P., and Leng, D. E. (1997). Experimental and computational study of multiple impeller flows, " Chem. Eng. Sci. 52, 1497

Harvey III, A. D., West, D. H., and Tufillaro, N. B. (2000). Evaluation of laminar mixing in stirred tanks using a discrete-time particle mapping procedure. Chem. Eng. Sci. 55, 667.

Helleman, R. G. H. (1980). Self generated chaotic behavior in nonlinear mechanics, Proceedings of the 5th International Summer School on Fundamental Problems in Statistical Mechanics, published in Fundamental problems in statistical mechanics V. Cohen, E. G. D. ed., pp 165-275, Amsterdan: North Holland.

Henon, M. (1966) Sur la topologie des lignes de courant dans un cas particulier. C.R. Acad. Sci. Paris A 262, 312-314.

Hobbs, D. M. and Muzzio, F. J. (1997). The Kenics static mixer: a three-dimensional chaotic flow. Chem. Eng. Journal. 67, 153-166.

Hobbs, D. M. and Muzzio, F. J. (1998a). Optimization of a static mixer using dynamical systems techniques. Chem. Eng. Sci. 53(18) 3199-3213.

Hobbs, D. M. and Muzzio, F. J. (1998b). The curvature of material lines in a three-dimensional chaotic flow. Physics of Fluids. 10(8) 1942-1950

Holmes, P. (1984). Some remarks on chaotic particle paths in time-periodic, three-dimensional swirling flows. Contemporary Mathematics 28, 393-404.

Holodniok, M. , Kubicek, M., and Hlavacek, V. (1977). Computation of the flow between two rotating coaxial disks: multiplicity of steady-state solutions. J. Fluid Mech. 108, 227-240.

Hourigan, K., Graham, L. J. W., and Thompson, M. C. (1995). Spiral streaklines in pre-vortex breakdown regions of axisymmetric swirling flows. Phys. Fluids. 7, 3126.

Hydon, P. E. (1994). Resonant and chaotic advection in a curved pipe. Chaos, Solitons and Fractals. 4(6) 941-954.

Jones, C. (1999). Static mixers for water treatment. PhD Thesis. Georgia Institute of Technology.

Jones, S. W. and Aref, H. (1988). Chaotic advection in pulsed source-sink systems. Phys. Fluids. 31, 469-485.

Jones, S. W., Thomas, O. M. and Aref, H. (1989). Chaotic advection by laminar flow in a twisted pipe. J. Fluid Mech. 209, 335-357.

Jones, S. W. and Young, W. R. (1994). Shear dispersion and anomalous diffusion by chaotic advection. J. Fluid Mech. 280, 149-172.

Joseph, B. and Swathi, P. S.(1999). Lagrangian particle transportation the Indian Ocean: A model study. J. Geophys. Research – Oceans 104, 5211-5224.

Kenwright and Lane (1996). Interactive time-dependent particle tracing using tetrahedral decomposition. IEEE Transaction on Visualization and Computer Graphics. 2(2), 120-129.

Khakhar, D. V., Franjione, J. G. and Ottino, J. M. (1987). A case study of chaotic mixing in deterministic flows. The partitioned pipe mixer. Chem. Engng. Sci. 42, 2909-2926.

Khakhar, Rising and Ottino, J. M. (1986). An analysis of chaotic mixing in two chaotic flows. J. Fluid Mech. 172, 419-451.

Kroujiline, D. and Stone, H. A. (1999). Chaotic streamlines in steady bounded three-dimensional Stokes flows. Physica D 130, 105-132.

Kusch, H. A. and Ottino, J. M. (1992). Experiments on mixing in continuous chaotic flows. J. Fluid Mech. 236, 319-348.

Lacis, S., Barci, J., Cebers, A., and Perzynski, R. (1997). Frequency locking and devil's staircase for a two-dimensional ferrofluid droplet in an elliptically polarized rotating magnetic field. Phys. Rev. E. 55, 2640-2648.

Lai, Y. C., Zyczkowski, K. and Grebogi, C. (1999) Universal behavior in the parametric evolution of chaotic saddles. Phys. Rev. E. 59, 5261-5265

Lamberto, D. J. , Muzzio, F. J, Swanson, PD., and Tonkovic, A. L. (1996). Using Time-Dependent RPM to Enhance Mixing in Stirred Vessels. Chem. Eng. Sci. 51, 733.

Lamberto, D. J, Alvarez, M. M. and Muzzio, F. J. (1999). Experimental and computational investigation of the laminar flow structure in a stirred tank. Chem. Eng. Sci. 54, 919-942.

Lamberto, D. J., Alvarez, M. M. and Muzzio, F. J. (2001). Computational analysis of regular and chaotic mixing in stirred tank reaction, " Chem. Eng. Sci. 56, 4887-4899.

Leibovich, S. 1978 The structure of vortex breakdown. Ann. Rev. Fluid Mech. 10, 221-246.

Leong, C. W. and Ottino, J.M. (1989). Experiments on mixing due to chaotic advection in a cavity. J. Fluid. Mech. 209, 463-499.

Lichtenberg, A. J. and Lieberman, M. A. (1992). Regular and Chaotic Dynamics. Springer-Verlag, New York.

Lin, F. and Sotiropoulos, F. (1997). Assessment of artificial dissipation models for three-dimensional, incompressible flow solutions. Trans. ASME: J. Fluids Engng. 119, 314-324.

Liu, M., Muzzio, F. J., and Peskin, R. L. (1994) Quantification of Mixing in Aperiodic Flows. Chaos, Solitons and Fractals. 4, 869-893.

Liu, R. H., Sharp, K. V., Olsen, M. G. Stremler, M. A. Santiago, J. G., Adrian, R. J., Aref, H. and Beebe, D. J. (2000) A Passive three-dimensional 'C-shape' helical miromixer. Journal of Microelecto-mechanical Systems. 9, 190-197.

Liu, Y. Z., Chen, H. P, and Koyama, H. S. (2000) Numerical and Experimental Investigation of Rotating Flow with Vortex Breakdown. Proc. ASME FEDSM'00, Boston, 11-15 June 16, 2000.

Lopez, J. M. and Brown, G. L. (1990) Axisymmetric vortex breakdown. Part 2: Physical mechanisms. J. Fluid Mech. (221), 553-576.

Lopez, J. M. , Hart, J. E., Marques, F. , Kittelman, S. and Shen, J. (2002). Instability and mode interactions in a differentially driven rotating cylinder. J. Fluid Mech. 462, 383-409.

Lugt, H. and Abboud, M. (1987). Axisymmetric vortex breakdown with and without temperature effects in a container with a rotating lid. J. Fluid Mech. 179, 179-200.

Lugt, H. and Haussling, H. J. (1973) Development of flow recirculation in a rotating tank. Acta Mech. 18, 255-272.

Lugt, H. and Haussling H. J. (1982) Axisymmetric vortex breakdown in rotating fluid within a container. Trans. ASME: J. Appl. Mech. 49, 921--922.

MacKay, Meiss, and Percival (1984). Transport in Hamiltonian systems. Physica D. 13, 55-81.

MacKay, R. S. (1994). Transport in 3D volume-preserving flows. J. Nonlinear Sci. 4, 329-354.

Melesahko, V. V. and Peters, G. W. M. (1996) Periodic points for two-dimensional Stokes flow in a rectangular cavity. Phys. Letters A. A(216), 87-96.

Mellor, G. L, Chapple, P. J. and Stokes, V. K. (1968). On the flow between a rotating and a stationary disk. J. Fluid Mech. 31, 95.

Mezić, I. (1994). On geometrical and statistical properties of dynamical systems: theory and applications. PhD. Thesis, California Institute of Technology.

Mezić, I. (2001). Three-dimensional chaotic advection in bounded Navier-Stokes flows. J. Fluid Mech. 431, 347-370.

Mezić and Wiggins (1994). On the integrability and perturbation of three-dimensional fluid flows with symmetry. J. Nonlinear Science 4, 157-194.

Mezić, I. and Wiggins, S. (1994). On the integrability and perturbation of three-dimensional fluid flows with symmetry. J. Nonlinear Sci. 4, 157-194.

Mezić I., Leonard, A., and Wiggins, S. (1998). Regular and chaotic particle motion near a helical vortex filament. Physica D 111, 179-201.

Mezić and Sotiropoulos (2002). Erogidc theory and experimental visualization of invariant sets in chaotically advected flows. Phys. Fluids 14, 2235-2243.

Moisy , F. Pasutto, T. and Rabaud, M. (2003) Instability patterns between counter-rotating disks. Nonlinear Processes in Geophysics. 10, 281-288.

Moser, J. (1968) On the theory of quasiperiodic motions. SIAM Review 8, 145-172.

Nagata, Shinji (1975) Mixing: Principles and Applications. Halsted press, New York.

Neishtadt, A.I., Vainshtein, D.L., Vasiliev, A.A. (1998). Chaotic advection in a cubic Stokes flow. Physica D 111, 227-242.

Nguyen, N. D., Ribault, J. P. and Florent, P. (1975). Multiple solutions for flow between coaxial disks. J. Fluid Mech. 68, 369.

Nore, C., Tuckerman, L. S., Daube, O. and Xin, S. (2003). The 1:2 mode interaction in exactly counter-rotating von Kármán swirling flow. J. Fluid Mech. 477, 51-88.

Nore, C., Tartar, M., Daube, O., and Tuckerman, L. S. (2004) Survey of instability thresholds of flow between exactly counter-rotating disks. J. Fluid Mech. 511, 45-65

Norwood, K. W. and Metzer, A. B. (1960). Flow Patterns and Mixing Rates in Agitated Vessels. AIChE J. 6, 432-437.

O'Connell, F. D. and Mack, D. E. (1950). Simple Turbines in Fully Baffled Tanks, Chem. Eng. Prog. 46, 358-362.

Ott, E. (1993) Chaos in Dynamical Systems. Cambridge University Press.

Ottino, J. M. (1989). The Kinematics of Mixing: Stretching, Chaos, and Transport. Cambridge University Press.

Paik, P., Pamula, V., and Fair, R. B. (2003). Rapid droplet mixers for digital microfluidic systems. Lab on a Chip 3(Advance Article)

Pao, H.-P. (1970) A numerical computation of a confined rotating flow. Trans. ASME: J. Appl. Mech. 37, 480-487.

Pasmanter, R. (1988) Deterministic diffusion, effective shear, and patchiness in shallow tidal flows. In Physical process in estuaries, J. Dronkers and W. Van Leussen, eds., Springer, New York, 42-52.

Peerhossaini, H., Castelain, C., and Guer, Y. Le. (1993) Heat Exchanger Design Bsed on Chaotic Advection. Experimental Thermal and Fluid Science. 7, 333-344.

Petersen, K. (1983). Ergodic Theory. Cambridge University Press. Cambridge.

Pierce, R. B. and Fairlie, T. D. A. (1993). Chaotic advection in the stratosphere.: Implications for the dispersal of chemically perturbed air from the polar vortex. Journal of Geophys. Res. Atmos. 98 (D10), 18589

Pierrehumbert, R. T. and Yang, H. (1993). Global Chaotic Mixing on Isentrophic Surfaces. Journal of Atmos. Sci. 50, 2462-2480.

Ranada V. V. (1997) An efficient computational model for simulating flow in stirred vessels: a case of Rushton turbine. Chem. Eng. Sci. 52 (24) 4473-4484.

Recknagle, K. P. and Shekarriz, A. (1998). Laminar Impeller Mixing of Newtonian and Non-Newtonian Fluids: Experimental and Computational Results. Proc. of FEDSM '98, 1-11

Reinchhardt, C. and Nori, F. (1999). Phase locking, devil's Staircase, Farey Tress, Arnold tongues in driven vortex lattices with periodic pinning. Phys. Rev. Lett. 82, 414-417.

Reynolds, O. (1894) Study of fluid motion by means of coloured band. Nature, 50, 161-164. This is a transcript of a Friday 2, 1893 evening presentation given by Professor Osborne Reynolds at the Royal Institution (also published in the Notices of the Proceedings at the Meeting of the Members of the Royal Institution of great Britain, Vol. XIV, 1893-1895, pp. 129-138).

Rom-Kedar, Leonard, and Wiggins (1990). An analytical study of transport, mixing and chaos in an unsteady vortical flow. J. Fluid Mech. 214, 347-394.

Ronnenberg, B. (1977). Ein selbstjustierendes 3-Komponenten-Laserdoppleranemometer nach dem Vergeichsstrahlvefahren, angewandt auf Untersuchungen in einer stationaren zylinder- symmetrischen Drehstromung mit einen Ruckstromgebiet. Max-Planck-Institut fur Stromungsfors-chung, Gottingen, Bericht 19.

Rudman, M. (1998). Mixing and particle dispersion in the wavy vortex regime of Taylor Couette flow. AIChE J. 44, 1015-1026.

Rudolph, M., Shinbrot, T. and Lueptow, R. M.(1998). A model of mixing and transport in wavy Taylor-Couette flow. Physica D 121, 163-174.

Rushton, J.H. Costich, E. W. and Everett, H. J. (1950). Power characteristics of mixing impellers: Part I. Chem. Engng. Prog. 46, 395-404.

Rushton, J.H. Costich, E. W. and Everett, H. J. (1950). Power characteristics of mixing impellers: Part II. Chem. Engng Prog. 46, 467-476.

Saatdjian, E. Midoux, N. Gastou Chassaing, M. I, Leprevost, J. C., and Andre, J. C (1996) Chaotic mixing and heat transfer between confocal ellipses: Experimental and numerical results. Phys. Fluids 8(3) 677-691.

Saatdjin, E. and Leprevost, J. C (1998). Chaotic heat transfer in a periodic two-dimensional flow. Physics of Fluids. 10(8), 2102-2104

Samelson, R. M. (1996). Chaotic transport by mesoscale motions. Stochastic Modelling and Physical Oceanography.

Sano, Y., and Usui, H. (1985) Interrelations among mixing time, power number and disharge flow rate number in baffled mixing vessels. J. Chem. Eng. Japan 18, 47-52.

Shepherd, T.G., Koshyk, J.N. and Ngan, K. On the nature of large-scale mixing in the stratosphere and mesosphere. J.Geophys.Res. **105** 12433-12446.

Shinbrot, T. , Alvarez, M. M., Zalc, J. M, and Muzzio, F. J. (2001) Attraction of minute particles to invariant regions of volume preserving flows by transients. Physical Review Letters. 86(7) 1207-1210.

Sil'nikov, L. P. (1965). A case of the existence of a denumerable set of periodic motions. Sov. Math. Dokl. 6, 163-166.

Smale, S. (1963). Diffeomorphism with many periodic points. Differential and Combinatorial Topology, ed. Cairns, S. S. Princeton University Press, Princeton.

Solomon, T. H., Weeks, E. R., Swinney, H. L. (1994). Chaotic advection in a two-dimensional flow: Levy flights and anomalous diffusion. Physica D 76, 70-84.

Sorensen, J. N. (1992) Visualization of rotating fluid flow in a closed cylinder.
Report No. AFM 92--06, Department of Fluid Mechanics, Technical University of Denmark.

Sotiropoulos, F. and Ventikos, Y. (1998) Transition from bubble-type vortex breakdown to columnar vortex in a confined swirling flow. Intl J. Heat and Fluid Flow. 19, 446-458.

Sotiropoulos, F. and Ventikos, Y. (2001). The three-dimensional structure of confined swirling flows with vortex breakdown. J. Fluid Mech. 426, 155-175.

Sotiropoulos , F., Ventikos, Y. and Lackey, T. C. (2001). Chaotic advection in three-dimensional stationary vortex-breakdown bubbles: Sil'nikov's chaos and the Devil's Staircase. J. Fluid Mech. 444, 257-297.

Sotiropoulos, F., Webster, D. and Lackey, T. C. (2003) Experiments on lagrangian transport in steady vortex-breakdown bubbles in a confined swirling flow. J. Fluid Mech. 66, 215-248.

Spohn, A., Mory, M., and Hopfinger, E.J. (1993) Observations of vortex breakdown in an open cylindrical container with rotating bottom. Exps. Fluids. 13, 70-77.

Spohn, A., Mory, M., and Hopfinger, E.J. (1998) Experiments on vortex breakdown in a confined flow generated by a rotating disk. J. Fluid Mech. 370, 73-99.

Stevens, J. L., Lopez, J. M., and Cantwell, B. J. (1999) Oscillatory flow states in an enclosed cylinder with a rotating endwall. J. Fluid Mech. 389, 101-118.

Stewart, K. (2002) Numerical simulation of selective withdrawal in stably stratisfied flows. Master's Thesis. Georgia Institute of Technology.

Stewartson (1951) On the flow between two rotating coaxial disks. Proc. Camb. Phil. Soc. 49, 333-341.

Stokes, J. R. and Boger, D. V. (2000) Mixing of viscous polymer liquids. Physics of Fluids. 12 (6) 1411-1416.

Stone, H. A., Nadim, A. and Strogatz, S. H. (1991). Chaotic streaklines inside drops immersed in steady linear flows. J. Fluid Mech. 232, 629-646.

Swanson, P.D. and Ottino, J. M. (1990). A comparative computational and experimental study of chaotic mixing of viscous fluids. J. Fluid Mech. 213, 227-249.

Tang, X. Z. and Booz, A. H. (1999). A Lagrangian analysis of advection-diffusion equation for a three-dimensional chaotic flow. Physics of Fluids. 11(6) 1418-1434.

Tanguy, P., Thibault, F., Brito-Del La Fuete, E., Espinosa-Solares, T. and Tecante, A. (1997). Mixing performance induced by coaxial flat blade-helical ribbon impellers rotating at different speeds. Chem. Eng. Sci. 52, 1733-1741.

Temam, R. (1969). Sur l'approximation de la solution des equations de Navier-Stokes par la methode des pas fractionaries ii. Arch Rat. Mech. Anal, 33, 377-385.

Vogel, H. U. (1968) Experimentelle Ergebnisse uber die laminare Stromung in einem zylinderischen Gehause mit darin rotierender Scheibe. MPI Bericht 6.

Vogel, H. U. (1975) Ruckstromungsblasen in Drallstromungen. Festschrift 50 Jahre Max-Planck-Institut fur Stromungsforschung 1925-1975.

Voth, G. A. , Saint, T. , Dobler, G., Gollub, J. (2003) Mixing rates and symmetry breaking in 2D chaotic flow. Physics of Fluids. 15(9), 2560-2566.

von Karman, T. (1921). Laminar und turbulente reibung. Z. Angew. Math 1, 233-252.

Ward, T. and Homsy, G. M. (2003). Electrohydrodynamically driven chaotic mixing in a translating drop.. Physics of Fluids 13 (12), 3521-3525.

Ward, T. and Homsy, G. M. (2003). Electrohydrodynamically driven chaotic mixing in a translating drop. II. Experiments. Physics of Fluids 15 (10), 2987-2994.

Welander, P. (1955). Studies of the general development of motion in a two-dimensional ideal fluid. Tellus 7, 141-156.

Wereley, S. T. and Lueptow, R. M. (1998). Spatio-temporal character of non-wavy and wavy Taylor-Couette flow. J. Fluid Mech. 364, 59-80.

Wiggins, S. (1990). Introduction to Applied Nonlinear Dynamical Systems and Chaos. Springer.

Wiggins, S. 1991 Chaotic Transport in Dynamical Systems. Springer-Verlag, New York.

Yannacopoulos, T., Mezić, I., King, G. P. and Rowlands, C. (1998). Eulerian diagnostics for Lagrangian chaos in three dimensional Navier-Stokes flows. Physical Review E 57, 482-490.

Yeung, P. K. and Pope, S. P (1988). An algorithm for tracking fluid particles in Numerical Simulations of Homogeneous Turbulence. J. Comp. Physics, 79, 373.

Zalc, J. M., Alvarez, M. M. Arik, B. E. and Muzzio, F. J. (2001). Extensive validation of computed laminar flow fields in a stirred tank equipped with three Rushton turbines, AIChE. Journal, 47(10), 2144-2154.

Zalc, J. M., Szalai, E. S., Alvarez, M. M. (2002). Using CFD to understand chaotic mixing in laminar stirred tanks. AIChE J. 48(10), 2124-2134

Zheligovsky, V. A. (1993). A kinematic magnetic dynamo sustained by a Beltrami flow in a sphere. Geophys. Astrophys. Fluid Dyn. 73, 217-254.

Zhou, Q., and Leschziner, M. A. (1999). An improved particle-locating algorithm for Eulerian-Lagrangian computations of two-phase flows in general coordinates. International Journal of Multiphase Flow. 25, 813-825.

VITA

Tahirih Charryse Lackey was born May 26, 1976, in Jackson, Mississippi in the United States. Attending elementary and secondary education in Mississippi, she matriculated to Jackson State University in 1993 where she pursued an undergraduate Physics degree. At the culmination of her undergraduate career, during which she received numerous awards, including Valedictorian Class of 1997 and All USA Today Academic Team, Honorable Mention, Ms. Lackey entered the graduate Civil Engineering program at the Georgia Institute of Technology in Atlanta, Ga. joining the Department of Environmental Fluid Mechanics and Water Resources where she received a Masters of Science degree in Civil Engineering in 2000. Ms. Lackey continued her work there in pursuit of her doctoral degree during which time she published work investigating complex three-dimensional flows using computational fluid dynamics including: "*Chaotic advection in three-dimensional stationary vortex-breakdown bubbles: Sil'nikov's chaos and the Devil's Staircase."* (JFM. 444, 257-297) and "*Experiments on Lagrangian transport in steady vortex-breakdown bubbles in a confined swirling flow*" (JFM 66, 215-248). Ms. Lackey remains an active member of the Baha'i Faith, spending much of her time involved in service projects such as teaching community children's classes and the organization of the Annual College Park Race Amity Conference.